Impairment Mitigation for High-speed Optical Communication Systems

ZHAO, Jian

A Thesis Submitted in Partial Fulfillment of the Requirements
for the Degree of Doctor of Philosophy

in

Information Engineering

©The Chinese University of Hong Kong

July 2007

The Chinese University of Hong Kong holds the copyrights of this thesis. Any person(s) intending to use a part or whole of the materials in the thesis in a proposed publication must seek copyright release from the Dean of the Graduate School.

UMI Number: 3295078

INFORMATION TO USERS

The quality of this reproduction is dependent upon the quality of the copy submitted. Broken or indistinct print, colored or poor quality illustrations and photographs, print bleed-through, substandard margins, and improper alignment can adversely affect reproduction.

In the unlikely event that the author did not send a complete manuscript and there are missing pages, these will be noted. Also, if unauthorized copyright material had to be removed, a note will indicate the deletion.

UMI®

UMI Microform 3295078

Copyright 2008 by ProQuest Information and Learning Company.

All rights reserved. This microform edition is protected against unauthorized copying under Title 17, United States Code.

ProQuest Information and Learning Company
300 North Zeeb Road
P.O. Box 1346
Ann Arbor, MI 48106-1346

Acknowledgements:

The work described in this thesis was conducted with the help and support of many people to whom I would like to express my thanks.

First of all, I would like to give my earnest gratitude to my supervisor, Prof. Lian-Kuan Chen, for his fruitful guidance and continuous support during my three year's research life pursuing the degree of Doctor of Philosophy in the Chinese University of Hong Kong. His in-depth knowledge in optical communications and dedications to research inspired my research ideas and sharpened my right research attitude. Discussions with him are always invaluable.

Many thanks are also to Prof. Chun-Kit Chan and Prof. Chinlon Lin, whose ways of learning and thinking enlightened me a lot in my studies. Their valuable advice and enormous help strengthened my understanding in researches and greatly enhanced my abilities to solve problems.

In addition, I feel fortunate to be able to work with so many talented post-doctors and postgraduate students. They include Dr. Huo Li, Dr. Zhaoxin Wang, Dr. Vincent Hung, Dr. Kit Chan, Dr. Guowei Lu, Mr. Jordan Tse, Mr. Jam Ku, Mr. Ning Deng, Mr. Siu-Sun Pun, Mr. Siu-Ting Ho, Mr. Clement Cheung, Mr. Chi-Man Lee, Mr. Xiaofeng Sun, Mr. Bo Zhang, Mr. Qiguang Zhao, Mr. Zhenchang Xie, and Mr. Yin Zhang. Without their generous support, my research would have never borne fruit.

Finally, I am sincerely grateful to my father, my mother, and my sister for their long term encouragement and solicitude. Their dedications are part of the most important impetuses for my tolerance, which invigorated me to affront difficulties in my studies.

Abstract:

The increasing bandwidth demands have aroused a myriad of industry and academic activities to develop cost-effective optical communication systems with data rates of 10 Gbit/s and beyond. However, as the capacity grows, many signal degradation effects become prominent and seriously limit the data rate and the transmission distance. The mitigation of the impairments inevitably increases the operation complexity and implementation cost. The focus of this thesis is to develop new impairment mitigation approaches to improve the impairment compensation performance and/or to reduce the operation complexity and cost. As a result, cost-effective high-speed optical communication systems are enabled.

Electronic equalization has recently attracted considerable interest for impairment compensation for its significant cost saving and adaptive compensation capability. In this thesis, we propose novel maximum-likelihood sequence estimation (MLSE) structures for various advanced modulation formats. Electronic equalization of advanced modulation formats further extends the transmission reach and relaxes the speed limitation of electronic devices. We also propose novel application of MLSE for mitigation of timing misalignment between the pulse carver and data modulator in return-to-zero (RZ) systems.

In access networks, we focus on the achievement of centralized light source (CLS) wavelength-division-multiplexing passive optical networks (WDM-PON) with data rate of 10 Gbit/s for both downstream and upstream signals. The previous CLS WDM-PON schemes at 10 Gbit/s suffer from chromatic dispersion (CD) and/or asynchronous upstream modulation. We propose two solutions to mitigate these impairments. By eliminating the modulation synchronization module and all-optical CD compensation module, the proposed methods greatly reduce the cost and operation complexity of high-speed WDM-PON.

To freely enable the employment of advanced modulation formats for optical communications, we propose all-optical conversion from 40-Gbit/s RZ signal to 40-Gbit/s inverse-RZ/10-Gbit/s differential-phase-shift-keying orthogonal modulation

signal to interface high-speed transmission systems using RZ format with networks using orthogonal modulation format. We also propose a novel all-optical coding and decoding scheme for 20-Gbit/s four-amplitude-shift-keying signal.

In the monitoring for impairment compensation, we propose a polarization-insensitive monitoring scheme for synchronized phase re-modulation by using a narrowband optical-passband filter (OBPF). With the optimal central wavelength of the OBPF, high monitoring sensitivity is achieved.

摘要

對數據頻寬的日益增加的需求引發了各式各樣的致力於開發低成本，高速率（數據率在10Gbit/s以上）光網絡和光傳輸系統的工業和學術活動。然而，隨著數據量的增加，許多光纖和光器件中的有害機制變得越發突出，嚴重限制了光傳輸系統的數據率和傳輸距離。爲了緩解這種有害機制而採取的措施不可避免地增加網絡運作的複雜性和實施費用。這篇論文的重點就在於開發探討出新的能夠提高傳輸系統性能以及降低運作複雜度和成本費用的方法。一旦這些方法加以實施，實現網絡傳輸系統的高速度，低成本運作便成爲可能。

電子均衡器最近引起了極大的研究興趣。因爲它可以大規模生產以降低成本而且有很強的自適應補償的能力，所以很適合用於光通訊系統中的有害機制的補償。在這篇論文中，我們提出了對高級調製格式的最大似然估計均衡器的設計。對高級編碼格式的電子均衡將進一步延伸傳輸系統所能達到的傳輸容量和距離，並且緩解了用來做高速光傳輸的電子設備的速度限制。此外，我們還研究了最大似然估計均衡器的新的應用，把它應用在歸零調製系統中以緩解脈衝切割器和數據調製器之間的不同步所帶來的有害效應。

在接入網方面，我們致力於實現上行和下行數據率都為10Gbit/s的集中式光源波分復用無源光網絡。在以前的方案中，色散和上行綫路的非同步調製嚴重限制了網絡性能。在這篇論文中，我們提出兩种方法來緩解這些有害機制。通過避免使用用於上行數據調製同步的模塊和全光色散補償的模塊，我們的方法可以大大的減少集中式光源波分復用無源光網絡的成本和運作複雜度。

爲了能夠在全光網絡中靈活的使用高級編碼格式，我們提出了一種從40Gbit/s歸零碼轉換成40Gbit/s翻轉歸零/10Gbit/s差分相位正交調製碼的全光方法。這種方法可用于接口使用歸零碼的高速傳輸系統和使用正交調製碼的光網絡。我們還提出了一種新穎的4強度調製碼的全光編碼和解碼方法。

在為達到對有害機制的自適應補償而使用的監控方面，我們提出了一種用於同步相位重調的基於光帶通濾波器的簡單且對偏振不敏感的監控方法。在優化光帶通濾波器中心頻率的條件下，這種監控方法有很高的敏感度。

Table of Contents

1. Introduction

During the past decade, we have been witnessing tremendous demands for high-speed telecommunication networks, as shown in Fig. 1.1 [1]. In addition, a significant change in the dominant type of traffic from voice to data and other new services such as video on demand, electronic distance learning, multimedia gaming, YouTube applications and electronic business will further increase the traffic in broadband networks [2]. Therefore, carriers will be required to increase the bandwidth of the networks to match the increase in traffic.

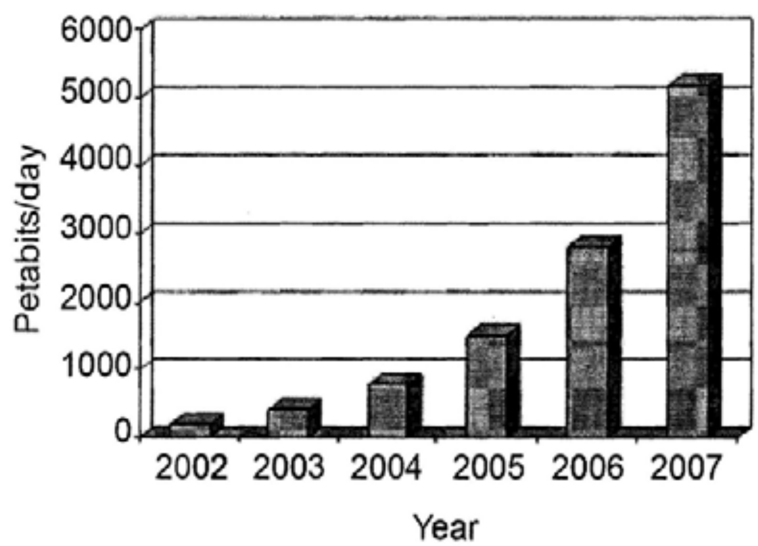

Fig. 1.1: Global bandwidth demands from end-users [1]

The enormous potential bandwidth of optics drives the worldwide development and deployment of optical communication systems. With the carrier frequency around 200 THz, more than 10,000 times increase of information capacity is expected for optical communication systems compared to microwave systems [3]. Nowadays, 10-Gbit/s wavelength division multiplexing (WDM) networks have been deployed and systems operating at 40 Gbit/s or beyond have been experimentally demonstrated in research labs [4]. The data rate of 100 Gbit/s has been adopted by IEEE 802.3 working committee for next generation Ethernet in 2006 [5].

1.1. Network Architectures

Optical communication systems can be classified into three broad categories: long-haul networks, metropolitan area networks, and local area networks.

1.1.1. Long-Haul Networks

Long-haul networks were the first to experience the impact of increasing data traffic in the last few years. Such systems are used for high-speed transmission with a link length of up to several thousand kilometers. A longer distance and a larger bandwidth are important factors in the design of long-haul systems.

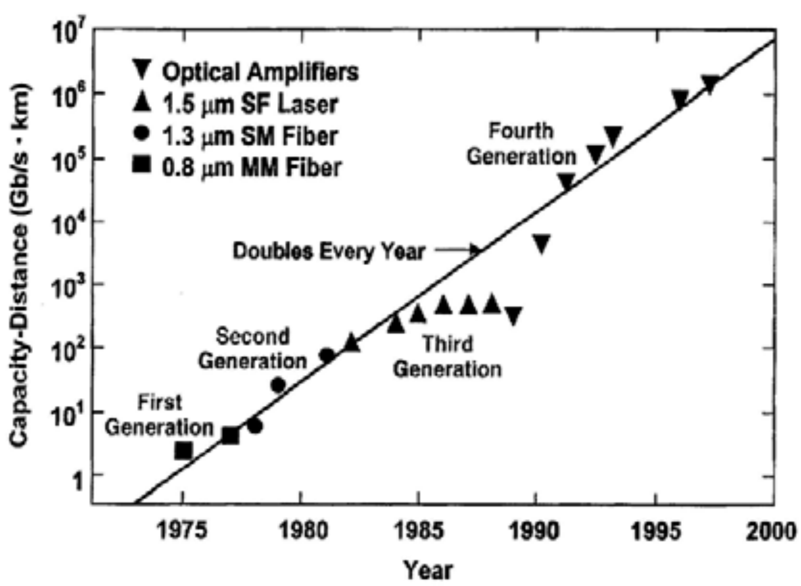

Fig. 1.2: Exponential BL during the period between year 1975 and year 2000. [6]

Starting in 1980 when the first generation optical systems operating near 800 nm at a bit rate of 45 Mbit/s were available commercially, the capacity has jumped by a factor of more than 10,000 over a period of 20 years. Fig. 1.2 shows the increase in the *BL* product over the period of 1975 to 2000 [6]. *B* and *L* are the bandwidth and the distance of the optical communication systems respectively. The progress over these years can be grouped into several distinct generations.

The product was 1 (Gbit/s)-km for the first generation systems operating near 850 nm [7]. However, it was soon clear that by operating the optical systems in the wavelength region near 1300 nm, the fiber loss can be reduced to below 1 dB. Furthermore, the use of single-mode fiber, which exhibits minimum dispersion in this wavelength region, largely overcomes the limitation by the dispersion. By 1987, second-generation systems at the bit rate of 1.7 Gbit/s with a repeater spacing of 50 km were commercially available.

The repeater spacing of the second-generation lightwave systems was limited by the fiber losses at the operating wavelength of 1300 nm. Losses of silica fibers become minimum near 1550 nm. However, large fiber dispersion exhibits when the systems operate at 1550 nm. The dispersion problem can be overcome by using dispersion-shifted fibers in the third generation lightwave systems, which are capable of operating at a bit rate of up to 10-Gbit/s.

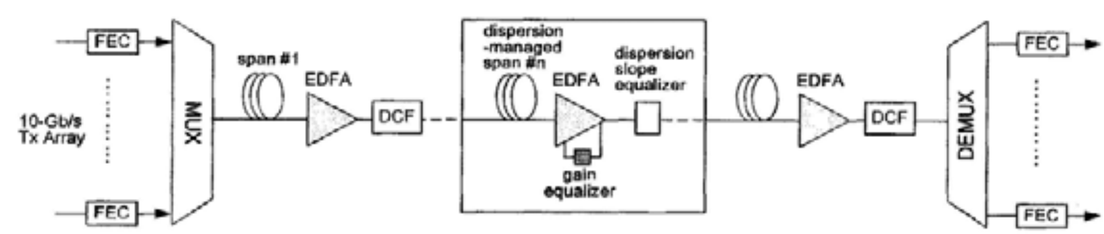

Fig. 1.3: Architecture of long-haul WDM networks; FEC: forward-error correction encoder/decoder, DCF: dispersion compensation fiber, EDFA: Erbium-doped fiber amplifier

A drawback of third generation 1550 nm systems is that the signal is regenerated periodically by using electronic repeaters spaced apart typically by 60-70 km. The fourth generation of optical systems makes use of optical amplifications for increasing the repeater spacing and the technology of WDM for increasing the bandwidth. Fig. 1.3 shows a typical transport network link configuration for WDM systems with optical amplification. The advent of WDM led to lightwave systems operating with *BL* product of more than 25,000 (Tbit/s)-km [8].

The fifth-generation systems attempt to extend the wavelength range over L, C, and S bands as well as to increase the bit rate of each channel. Many experiments have demonstrated the transmission with channel capacity of 40 Gbit/s [4]. However, as the capacity of the optical networks/transmission systems grows, many signal degradation effects, such as chromatic dispersion (CD) and polarization mode dispersion (PMD), become prominent and require careful compensation. Optical compensation methods like dispersion compensating fiber (DCF) with optical amplifiers have enabled high capacity transmission systems [9], but those components are bulky, inflexible and expensive. Electronic signal processing provides a cost-effective solution to mitigate the impairments in optical transmission systems [10]-[12], which has attracted much attention in recent years.

The existing commercial optical systems are mostly based on non-return-to-zero (NRZ) modulation format. However, in such modulation format, further bandwidth demands are severely hindered by the maximum operating speed of electrical and optical components, and also by the rapidly reduced signal reach limited by CD and PMD. At 40 Gbit/s, the signal reach over single mode fiber (SMF) is typically two to five kilometers, and it is further reduced to 500 meters at 100 Gbit/s [3]. Advanced modulation formats such as differential quadrature phase shift keying (DQPSK) are promising candidates of the next generation high-capacity signaling formats because they have enhanced CD and PMD tolerance and relax the speed limitation of the optical and electrical components [13]-[25]. Most of the recorded long-haul experimental demonstrations recently are based on advanced modulation formats. For example, in 2007, 1.1 Tbit/s, 50 GHz spaced RZ-DQPSK transmission over 2375 km was demonstrated [26].

The combination of electronic signal processing and advanced modulation formats is promising to further enhance the transmission reach/capacity of the long-haul transmission systems. However, few studies have been performed on this issue. In Chapter 2, we will propose novel electronic signal processing structures for advanced modulation formats.

In addition, the existing optical systems use direct detection. Coherent detection of optical communication signals has been well known to offer several performance advantages over direct detection, such as better receiver sensitivity approaching to the Shannon limit and the capability to detect phase-encoded modulation formats like QPSK and quadrature amplitude modulation (QAM) [27]-[31]. But to date, it has not been deployed in fiber optical networks because coherent detection is sensitive to polarization of the optical signal. Furthermore, it is required to recover the phase of the signal for synchronous detection. Recently, there has been renewed interest in coherent detection due to the development of high-speed electronic digital signal processing (DSP) technology. The DSP technology has emerged in the past fiber year and it has been successfully applied in commercial 10-Gbit/s direct detection transceivers to compensate CD. The application of this technology to coherent detection brings more benefits than to direct detection. The challenging operations of coherent detection, such as phase estimation and alignment of polarizations, can be done digitally [32]-[42]. The electronic DSP offers more flexibility and new functionality. If it can be sold in volume, it is expected to be cost effective. Therefore, it has attracted much attention in these two years. In 2007, the transmission of 42.8 Gibt/s QPSK signal over 6400 km of standard fiber with no optical dispersion compensation has been demonstrated [42]. Such topic will be one of focuses in my future works.

Orthogonal-frequency-division-multiplexing (OFDM) is an alternative solution for cost-effective long-haul optical transmission in the future [43]-[56]. In this modulation, a single data stream is transmitted over a number of lower-data-rate orthogonal subcarriers. Recently, such technique has been shown to be robust to CD and PMD. In 2007, an experimental demonstration of coherent OFDM systems in which 128 OFDM subcarriers with a nominal data rate of 8-Gbit/s was successfully processed and recovered after 1000-km single-mode fiber transmission [54].

1.1.2. Metropolitan Area Networks

Compared with long-haul transmission systems, the challenges faced by metropolitan area networks (MANs) is far diverse. The clients connected to MANs are access networks with increasing bandwidth demand as well as high-end users with advanced switching/routing gears capable of direct line-rate input into metro core. MANs must cope with not only the increase in traffic demand but also the burstiness of data traffic and time-dependant nature of traffic pattern.

To enhance the bandwidth and the transmission distance of the MANs, efforts are required to overcome the transmission impairments such as CD, PMD, and nonlinearities. Traditional methods of CD compensation use links that incorporate lengths of fiber with dispersion of opposite sign, DCF, to that of the main link fiber. These fibers often have high loss and do not allow dynamic adaptation of the link dispersion map. This may be adequate in long-haul links where link length and characteristics suffer small and gradual change. But in fast switched MANs, this may be an incomplete solution as CD may change frequently due to the time-varying effects of different routing paths. Electronic equalization is cost-effective for impairment mitigation compared to all-optical compensation. The use of digital signal processing to extend the reach of optical links beyond their dispersion limit is a vibrant research topic. This offers a solution without the use of expensive high loss optical compensation and with fast adaptation [57]-[64]. Note that although electronic equalizers with the same structure can be applied to both long-haul transmission and MANs, the designed parameters are different. For example, in MANs where the required transmission distance is relatively shorter than that in long-haul systems, the taps in the feed-forward equalizer (FFE) / decision feedback equalizer (DFE) or the memory length of maximum likelihood sequence estimation (MLSE) are much relaxed. Also similar to long-haul transmission systems, advanced modulation formats are also promising methods for extending the transmission reach of the MANs.

Compared to the long-haul application, the employment of advanced modulation formats are more flexible in MANs due to the shorter required transmission distance. For example, in addition to differential phase shift keying (DPSK) and DQPSK etc., four-amplitude shift keying (4-ASK) format and ASK/DPSK orthogonal modulation format can also be used in MANs. The combination of electronic equalization and advanced modulation formats can further improve the transmission performance. However, little work has been done in this field. We have performed considerable study in this topic. Such issue will be discussed in detail in Chapter 2 of this thesis.

Although the single wavelength channel transmission speed can reach 10 Gbit/s or even Tbit/s, the speed of optical-to-electrical conversion, transmission speed of electronics connections, and switching speed of electronic gates have not matched the transmission speed in optical fibers. To enhance the flexibility, next generation MANs will be based on an optical packet burst switching paradigm, in which data packet intended for a remote network node is forwarded and routed in optical domain without OEO conversion while routing decision is made packet-by-packet using control information sent along with the packets [65]-[68]. To achieve this goal, a lot of signal processing in network intermediate node must be implemented all optically, such as all-optical label swapping and routing. As discussed above, advanced optical modulation formats are one of the most promising technologies to significantly alleviate the transmission impairments and increase the capacity of MANs. They are also capable for enabling various applications for signal processing in all-optical networks. For example, orthogonal modulation format has attracted a lot of interest to carry optical payload / label in optical networks concurrently. Synchronous phase re-modulation of phase-encoded formats can be employed in all-optical label swapping, as discussed in Section 1.2.4. To freely enable the employment of advanced modulation formats for high-speed optical communication in all-optical networks, all-optical format conversion and coding/decoding for advanced modulation formats are essential. In Chapter 4, we will give detailed investigation to this topic.

1.1.3. Local Access Networks

Fig. 1.4 shows a topology of optical access networks. Multiple optical network units (ONUs) located at customer premises are connected to a remote node (RN) through fiber-optic connections. The RN, which is physically located in close proximity to ONU's, is connected to network operator's central office (CO) through a longer fiber link (feeder fiber). This arrangement provides significant cost saving when compared with the case in which each ONU is directly connected to the CO [69]. Among all optical network proposals, passive optical network (PON) has received increasing amount of attention in recent year [70]. This class of optical access network uses passive optical components between CO and ONU. Thus no power supply will be needed in the field and network maintenance can be effectively reduced.

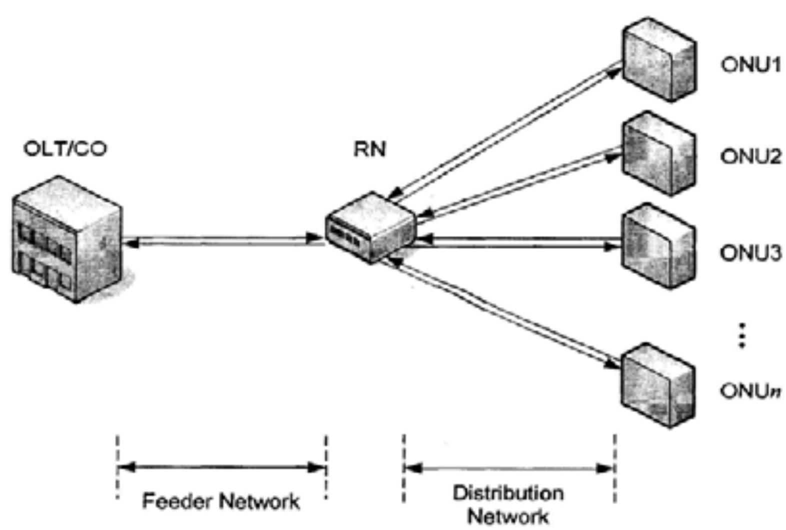

Fig. 1.4: A topology of optical access networks

Wavelength division multiplexing passive optical network (WDM-PON) has aroused much attention for next-generation broadband access architecture, due to its large bandwidth and upgrade flexibility [71]-[72]. The architecture of WDM-PON is shown in Fig. 1.5. In such kind of PON, CO communicates with each ONU using a dedicated set of wavelength channels. Thus each ONU can enjoy a secure and scalable downstream communication channel. If each ONU uses a different wavelength for upstream transmission, there is no ranging problem which exists in traditional power splitting PON. All upstream wavelengths can be multiplexed at RN using WDM multiplexer, thus no data collision will occur.

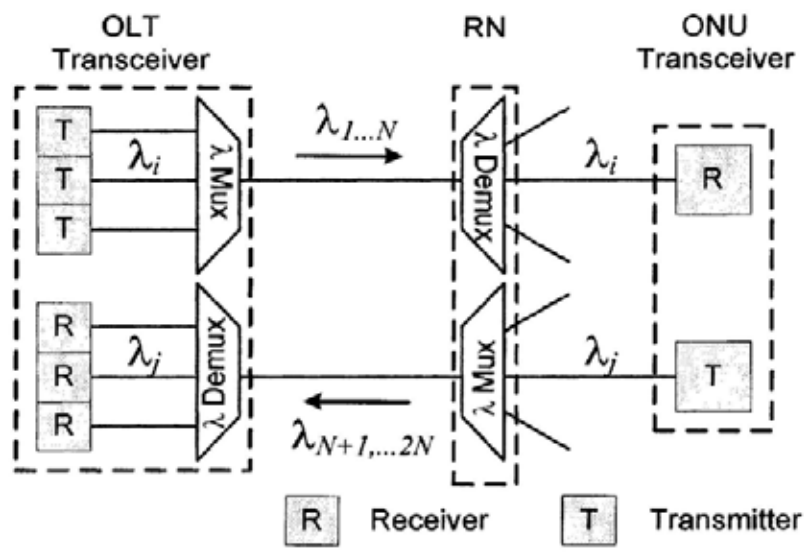

Fig. 1.5: Architecture of WDM-PON

The main problem of WDM-PON architecture in Fig. 1.5 is that multiple temperature-controlled laser sources at different wavelength are needed at both CO side and ONU side. Besides the component cost, the network maintenance and backup component management also become very complicated. Another challenge arises from the use of AWG-based wavelength router. As the AWG is deployed at the RN, which is assumed to be passive, consequently, there is no active temperature control. With a silica-based AWG, the temperature sensitivity is around 0.011 nm/°C, and so over a range of temperature fluctuation from -20°C to +55°C, there is a passband drift of ~0.8 nm, which corresponds to a typical DWDM channel spacing of 100 GHz. Without proper wavelength control on all sources at CO and ONU to align the wavelengths with the passband center of the AWG at RN, the network would not operate properly.

Centralized light source (CLS) WDM-PON can overcome these challenges [73]-[79]. With this scheme, all the wavelength-controlled light sources are located at

CO. The carriers of the upstream signals are provides by the downstream signal or the CW light from CO. As a result, such scheme features well-controlled wavelength spacing and management-cost reduction by eliminating wavelength-specific transmitters at ONUs. In [76], 10-Gbit/s downstream signal and 2.5-Gbit/s upstream signal over 50-km SMF was demonstrated. However, as the demands for data bandwidth increase and the emerging new applications such as Bit Torrent (BT) and PPlive, it is much desirable to upgrade not only the downstream capacity but also the upstream capacity of WDM-PON. Therefore, the primary objective of my work is to achieve high-speed colorless CLS WDM-PON with data rates of 10 Gbit/s for both downstream and upstream signals. In the existing CLS schemes, the ones using re-modulation technique and supercontinuum generation are two promising architectures to achieve a high-speed CLS WDM-PON with upstream transmission capacity up to 10 Gbit/s [75]-[79]. However, the previous CLS WDM-PON schemes at 10 Gbit/s suffer from chromatic dispersion (CD) and/or asynchronous upstream modulation. We propose two solutions to mitigate these impairments. By eliminating the modulation synchronization module and all-optical CD compensation module, the proposed methods greatly reduce the cost and operation complexity of high-speed CLS WDM-PON.

1.2. Impairments in Optical Transmission Systems and Optical Networks

As we mentioned, impairments in optical communication systems can cause serious signal degradation. As a result, the capacity and the transmission distance are severely limited. The design of fiber-optic communication systems requires a clear understanding of the limitations imposed by various impairments. The impairments can be from the transmitter side, the transmission link, the receiver side, and the intermediate node of the all-optical networks. Classified according to the dynamic characteristics, the impairments can be deterministic or random. In this section, we will introduce the impairments relevant to this thesis.

1.2.1. Noise

There are many kinds of noise in optical systems. Transmitters have laser phase noise and laser intensity noise. Optical amplifier in the fiber link introduces amplified spontaneous emission (ASE) noise. In receivers, there are two fundamental noise mechanisms responsible for current fluctuations, the shot noise and the thermal noise. Despite many noise sources, optical systems generally operate in either of the following two regions: (1) without optical amplification, the receiver becomes thermal noise limited; (2) For optically pre-amplified receivers, the receiver operates in optical signal to noise ratio (OSNR) limited region. In this section, we will discuss more about these two noises.

At a finite temperature, electrons move randomly in any conductor. Random thermal motion of electrons in a resistor manifests as a fluctuating current even in the absence of an applied voltage. The load resistor in the front end of an optical receiver adds such fluctuations to the current generated by the photodiode. This additional noise component is referred to as thermal noise. Mathematically, thermal noise is modeled as a stationary Gaussian random process with a spectral density that is frequency independent up to 1 THz and is given by [3]:

$$S_T(f) = 2k_B T / R_L \tag{1.1}$$

where k_B is the Boltzmann constant. T is the absolute temperature, and R_L is the load resistor.

The spontaneous emission in erbium-doped fiber amplifier (EDFA) is a random process and the emitted photons are in all directions. Some spontaneous emission is captured and amplified as it propagates along fiber. The ASE noise appears at the output of the EDFAs. Assume an optical amplifier with uniform gain G over an optical bandwidth B. The ASE spectral density in a single polarization is [3]:

$$N_0 = n_{sp} h\nu (G-1) \tag{1.2}$$

where n_{sp} is the spontaneous emission noise factor and $h\nu$ is the photon energy.

As the ASE noise can be modeled as additive white Gaussian noise and the ASE noise is typically unpolarized, the total ASE noise power in bandwidth B is given as:

$$P_{ASE} = 2n_{sp}h\nu(G-1)B \tag{1.3}$$

1.2.2. Chromatic Dispersion

CD is a relatively small impairment in optical links operating at data rates below 10 Gbit/s but it grows quickly as the data rate increases and becomes serious at 10 Gbit/s and beyond. The origin of CD is from the fact that the group velocity associated with the fundamental mode is frequency dependent. As a result, different spectral components of the pulse travel at slightly different group velocities, which will limit the performance of the optical communication systems by broadening optical pulses.

Mathematically, CD can be viewed as a linear filter in optical domain with the transfer function of

$$H_{out}(\omega) = H_{in}(\omega)e^{\frac{(\omega-\omega_0)^2\beta_2}{2}} \tag{1.4}$$

where $H_{in}(\omega)$ and $H_{out}(\omega)$ are the spectrums of the input and output optical signals. ω_0 is the carrier's central frequency. β_2 is the group velocity dispersion (GVD) parameter. CD is usually characterized by the CD parameter $D=-2\pi c\beta_2/\lambda^2$. The pulse broadening from CD for a fiber length L is given by

$$\Delta T = DL\Delta\lambda \tag{1.5}$$

where $\Delta\lambda$ represents the wavelength width. The broadened pulses disperse into adjacent bits as the signal propagates along the fiber, which leads to detection errors.

Several optical techniques exist to control dispersion. One of them is the use of lasers with a wavelength in the region around 1310 nm, where CD reaches a minimum. However, in long-haul and metro links, wavelength in the 1550 nm region, where the fiber attenuation is minimum and significantly lower than at 1310nm, are generally preferred. CD can also be compensated by the use of DCFs [9]. These are fibers where the slope of the delay versus wavelength curves has an opposite sign compared with normal fibers. Reels of appropriate lengths of DCF are placed at certain points in the link to compensate dispersion. Unfortunately, DCFs also cause significant attenuation, and their length has to be manually adjusted to achieve proper compensation, so link provisioning become expensive and time consumption. Although other optical techniques to compensate dispersion exist, in general they suffer from the problems of being costly and requiring manual adjustment.

Electronic solution has the advantage of higher integration and easier and faster adaptation of the compensation. Its application to compensate CD alleviates the need for DCFs and other costly optical dispersion compensation techniques. It also benefits from the automatic adaptation of the equalizer, thus eliminating the need for manual adjustment of optical compensation elements [80]-[82].

Various advanced modulation formats can also be used to enhance the CD tolerance. For example, optical duobinary modulation is a method of pre-compensation of the transmitted signal. It allows the reach to be approximately doubled compared to that of non-return-to-zero format. Multi-bit per symbol modulation formats, including DQPSK, ASK/DPSK orthogonal modulation, and 4-ASK, also exhibit enhanced tolerance to CD due to the reduced symbol rate. Furthermore, multi-bit per symbol modulation formats relax the speed limitation of optical and electrical components [23]-[24]. The techniques of electronic equalization and advanced modulation formats for CD compensation will be studied in Chapter 2.

In addition, coherent detection with digital signal processing and OFDM are also promising techniques for CD compensation. These two techniques arise in recent two years and can in principle support optical signal transmission up to several thousand kilometers without optical dispersion compensation. These interesting research topics will be one of my research areas in the future.

1.2.3. Polarization Mode Dispersion

PMD which occurs as a result of birefringence in the optical fiber also becomes important at high data rates. Birefringence is caused by manufacturing defects and by stress, vibration, and other mechanical effects on the fiber. A typical manifestation of

PMD is pulse splitting. As a result of its dependence on stress and vibration, as well as on random changes in the state of polarization of the laser, PMD is nonstationary. The time-averaged DGD along a fiber link is given by:

$$DGD = D_{PMD}\sqrt{L} \tag{1.6}$$

where L is the fiber length. D_{PMD} is the fiber PMD parameter measured in ps/km$^{1/2}$.

Adaptive optical devices at a bit rate of 40 Gbit/s for polarization mode dispersion compensation have been demonstrated. Those devices, however, are expensive since they make use of sophisticated technologies and are not yet in volume production.

Adaptive digital signal processing techniques are ideally suited to PMD compensation [60]-[85]. Such method is cheap and flexible. 43-Gbit/s adaptive electronic equalizer with control feedback by using both eye monitoring and pseudo-error count have been proposed [63]. Similar to CD compensation, advanced modulation formats are also capable for PMD tolerance enhancement [23]-[24].

1.2.4. Component Synchronization

Synchronization is an essential issue for optical communication systems and is required in various components.

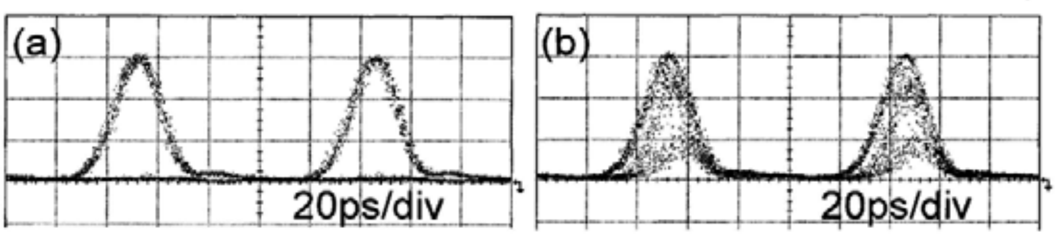

Fig. 1.6: Eye diagrams of RZ signal when the pulse carver and data modulator are (a) synchronized and (b) asynchronous.

At the transmitter for return-to-zero (RZ) signal generation, a continuous-wave light is first carved by a pulse carver and then modulated by NRZ data in the data modulator. For proper generation of the RZ signal, it is essential to locate the pulse peak in the middle of the NRZ data bit slot [86]-[87]. When timing is misaligned, the generated signal is severely distorted. Fig. 1.6 shows the eye diagrams of the RZ signal when the pulse carver and data modulator are (a) synchronized and (b) asynchronous. In Chapter 2, we will show that such impairment can be generalized as intersymbol interference (ISI) and can be compensated by electronic equalization.

Similar problem also appears for the generation of multi-bit per symbol modulation formats, where concatenation of several modulators is usually required. In such case, time alignment between modulators should be carefully adjusted for proper operation.

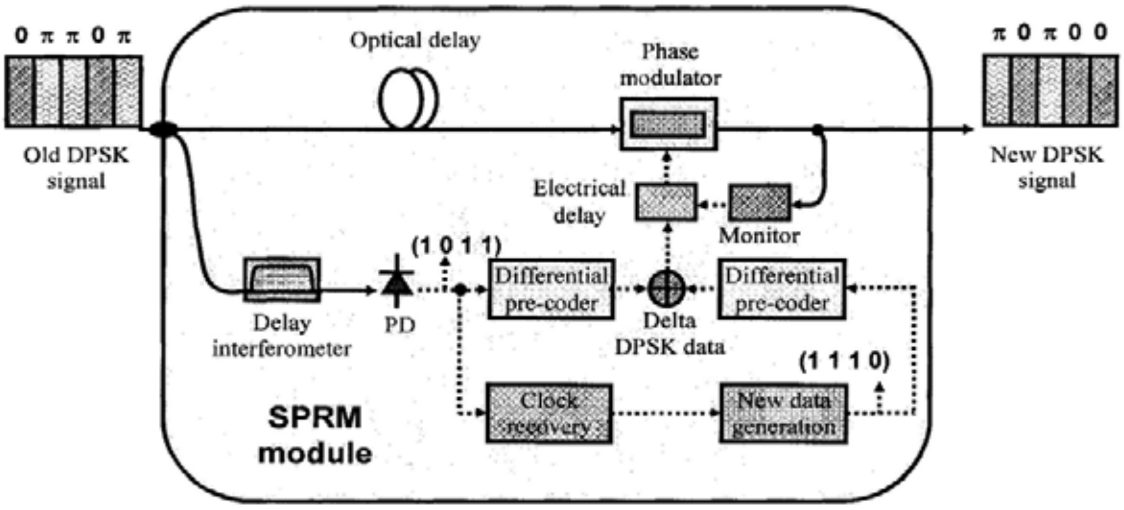

Fig. 1.7: Principle of SPRM

At the intermediate node of the optical networks, synchronization is also required in many optical signal processing. Synchronized phase re-modulation (SPRM) is a crucial signal processing technique to erase the original and write the new phase information simultaneously for phase-encoded modulation formats [88]-[89]. Such technique has been employed in optical label swapping in optical networks. Fig. 1.7 shows the principle of the SPRM. In the figure, it can be found that to properly achieve SPRM, the electrical delta DPSK data should be superimposed onto the time slot center of the old optical DPSK signal. Asynchronous phase re-modulation leads to severely signal degradation, as discussed in Chapter 5 in detail.

At the receiver side, the data decision is sensitive to the sampling phase. Sampling with improper sampling phase largely increases the detection errors. Such impairment, discussed in more detail in Chapter 2, can be reduced by using maximum likelihood sequence estimation with two or more samplings per bit.

1.2.5. Nonlinear Effect in Optical Fibers and Devices

All devices exhibit only a limited range for linear operation. Devices will become non-linear when, for example, the input signal's power level is too high or too many carriers are injected into the same device at the same time. This kind of degradation is not only confined to electronic components.

Non-linear effect in the fiber induces various types of crosstalk. There are two categories of fiber nonlinearities. The first one is due to the scattering between the input signal and the phonons in the silica medium. Stimulated Brillouin scattering (SBS) and stimulated Raman scattering (SRS) belong to this category [90]. These two effects would cause transfer of power from the original wavelength to another wavelength and would consequently cause power reduction and channel crosstalk. The second category is due to the fact that the refractive index of a fiber depends on the optical power. Four-wave mixing (FWM), self-phase modulation (SPM) and cross-phase modulation (XPM) fall to this category. FWM would generate new frequency components, inducing crosstalk, while SPM and XPM would cause spectral broadening and therefore increase the chromatic dispersion penalties.

Semiconductor optical amplifier (SOA) also exhibits nonlinear effects [91]. It is principally caused by carrier density changes induced by the amplifier input signals. The four main types of nonlinearity are cross gain modulation, cross phase modulation, self-phase modulation, and four-wave mixing. On the other hand, cross-absorption modulation effect exhibits in electron-absorption modulator (EAM). These nonlinearity effects may causes impairments but may be used for optical signal processing in some cases. In Chapter 4, we will employ the nonlinearity effects in SOA and EAM for all-optical signal processing of advanced modulation formats.

1.3. Methods for Impairment Mitigation

Impairments significantly limit the performance of high bit rate optical communication systems. Hence, it is very important to develop cost-effective impairments mitigation techniques. Classified by the positions, compensation schemes can be grouped to be pre-compensation schemes, in-line compensation schemes, and post-compensation schemes.

1.3.1. Pre-Compensation Techniques

The idea of this approach is to perfect the characteristics of the input pulses at the transmitter before they are launched into the fiber link. Such method can be used to mitigate not only the impairments at the transmitter side, e. g. timing misalignment between the pulse carver and data modulator in RZ systems, but also the impairments in the fiber link and at the receiver side.

As discussed previously, the RZ signals are highly degraded when the pulse carver and the data modulator do not synchronize. In the laboratory, pulse carver and data modulator alignment is accomplished using microwave line stretchers that are manually adjusted by a person. However, if such systems are to make their way into the field, a more low cost automatic approach must be obtained. Several timing alignment techniques were proposed [86]-[87]. These systems employ a monitoring stage. The monitoring signal is fed back to control a delay line for automatic synchronization. As a result, the potential penalty induced by timing misalignment between the pulse carver and the data modulator is avoided.

The stabilization for the wavelength of the optical sources is another important issue, especially for WDM-PON. As a result, temperature-controller embedded feedback loop is required for laser sources. This method may be acceptable for metro/long-haul transmission systems. However, in WDM-PON, besides the component cost, the network maintenance and backup component management become very complicated. CLS WDM-PON can overcome these challenges [73]-[78]. With this scheme, all the wavelength-controlled light sources are located at CO. The carriers of the upstream signals are provided by the downstream signal or the CW light from CO. As a result, wavelength-specific transmitters at ONUs are eliminated.

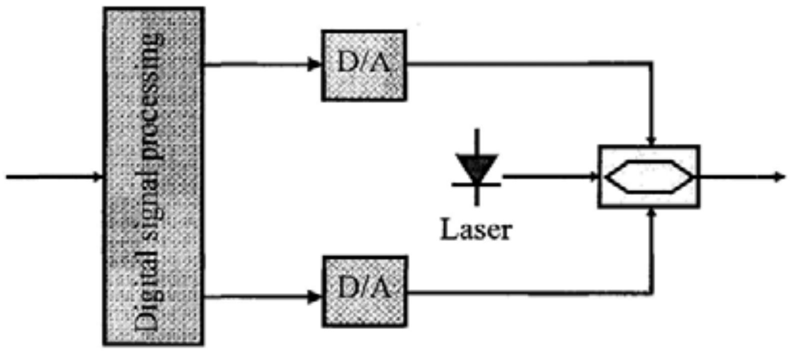

Fig. 1.8: Block diagram of a pre-distorted transmitter

Recently, electronic pre-distortion technique has attracted much attention for dispersion compensation and has been applied to practical transmission systems [92]-[97]. Fig. 1.8 shows a block diagram of a pre-distortion transmitter, in which the amplitude and phase waveforms of the transmitted data are pre-distorted. The digital signal processor generates the pre-distorted real and imaginary parts of the optical signal according to the amount of dispersion to be compensated. After digital-to-analog converters, the real and imaginary parts are modulated independently by a dual-drive modulator. The pre-distortion in the transmitter can be adjusted by digital signal processing. Up to now, 5120 km transmission without optical dispersion compensation was demonstrated for a 10-Gbit/s DPSK system [95]. Recently, studies on pre-distortion have been moving to implementation issues. The memory required for various modulation formats was reported. However, in such technique, the pre-distortion parameters are preset according to the information given the fiber dispersion for each link. However, the preset parameters are often inaccurate. Furthermore, the optimum setting often changes due to unpredictable residual dispersion and waveform changes due to fiber nonlinearity and transmitter chirps. Therefore, adaptive optimization is necessary in practice. However, because the errors are detected at the receiver end, the time for feedback is unacceptable due to the long round-trip distance. In order to precisely and quickly optimize the dispersion compensation, collaboration of the pre-distortion at the transmitter with a post-equalizer at the receiver end was recently proposed [96]. With the pre-distortion preset approximately and the accumulated dispersion of the transmission link compensated coarsely, the residual waveform distortion would be finely tuned at the receiver end by the post equalizer.

1.3.2. In-Line Compensation Techniques

The most common in-line compensation technique is regeneration. The system transmission limits stem from a combined effect of amplifier noise accumulation, fiber dispersion, fiber nonlinearity, and inter/intrachannel interactions. There are two solutions for signal regeneration. The first is to segment the systems into independent trunks, with full electronic repeater/transceivers at interfaces. The second solution, all-optical regeneration, performs the same signal-restoring functions as the electronic approach, but with far reduced complexity and enhanced capabilities. In regeneration, the three basic signal-processing functions are reamplifying, reshaping, and retiming.

A special kind of fiber, dispersion compensating fiber (DCF), has been developed for dispersion compensation along the transmission line in a periodic fashion. The use of DCF provides an all-optical technique that is capable of compensating the fiber GVD completely if the average optical power is kept low enough that the nonlinear effects are negligible. Unfortunately, DCFs also cause significant attenuation, and their length has to be manually adjusted to achieve proper compensation, so link provisioning become expensive and time consumption.

Conventional OOK format is not robust to transmission impairments. Advanced optical modulation format is one of the most promising technologies to significantly alleviate the transmission impairments and increase the capacity of the optical communication systems. DPSK format was experimentally demonstrated to exhibit higher tolerance to fiber nonlinear effects compared to on-off keying (OOK) format. Multilevel modulation formats, with reduced symbol rate, are also robust to dispersion. In addition, OFDM is an alternative solution for cost-effective long-haul optical transmission in the future. Such technique has been shown to be robust to CD and PMD. This method also features simpler DSP implementation complexity compared to electronic equalization in long-haul transmission [98]. However, OFDM is sensitive to nonlinear effects in the fiber and devices, which requires stricter requirement for optical components.

1.3.3. Post-Compensation Techniques

Electronic techniques can be used for compensation of dispersion within the receiver. In early 1990s, Winters et al. proposed for the first time to use electronic equalization in optical communication system to mitigate the transmission distortion including chromatic dispersion and PMD [10]-[11]. However, due to the lack of high speed microelectronics, electronic equalization in optical systems has not been applied until the late 1990s. The network upgrade from 2.5 Gbit/s to 10 Gbit/s in the late 1990s urged efficient solutions for compensating transmission distortions. At the same time, the development of high speed microelectronics enables the applications of electronic equalization in optical communication systems at 10 Gbit/s or beyond. For example, digital signal processors, analog-to-digital and digital to analog converters make the use of electronic dispersion compensation increasingly feasible. 22 GSamples/s, 6-bit D/A has been implemented. Integrated circuits for 10 Gbit/s and even 40 Gbit/s signal processing has been demonstrated for CD and PMD compensation [99]-[101]. The receiver-side electronic techniques can be classified into several categories:

- Feed-forward equalizer (FFE). In such filter, the signal is delayed by a taped delay line. The delayed signal is then weighted by the tap coefficients and summed together [59]-[60]. The FFE is realized by tuning the tap coefficients. However, because a linear FFE enhances the noise, a pure FFE is less preferable.
- Decision feedback equalizer (DFE). DFE is a nonlinear filter which eliminates post-cursors of distorted signals. It consists of a decision circuit and a feedback path. The feedback signal from the decision circuit is delayed by one bit period, weighted and subtracted from the original input signal. This technique does not introduce noise enhancement but has little capability to reduce the influence of precursors. A preferred method is to employ DFE to take into account the

postcursors while using a FFE before the DFE to compensate the interference from the precursors.

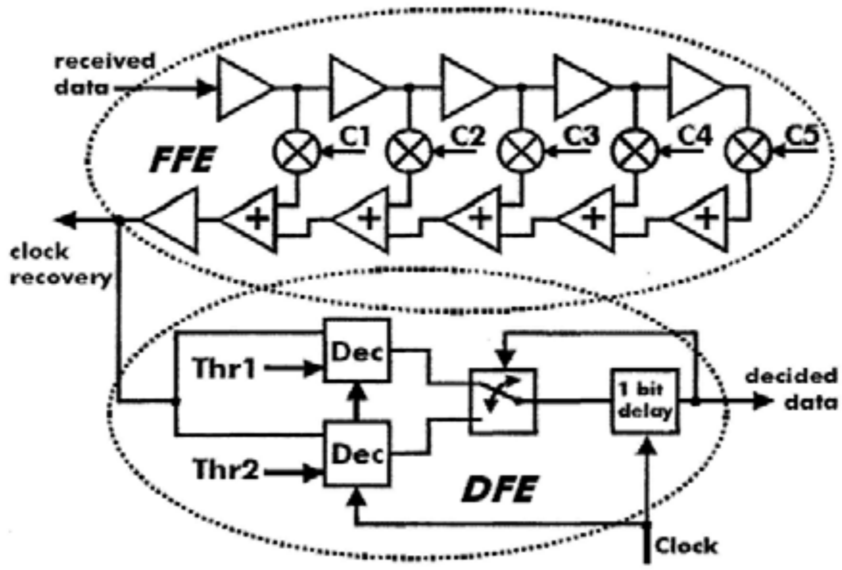

Fig. 1.9: Structure of an FFE+DFE equalizer

- Feed-forward equalizer + Decision feedback equalizer (FFE+DFE). Fig. 1.9 illustrates the structure of an FFE+DFE equalizer. The combination of FFE and DFE takes advantages of the two equalizers and has better performance [62]-[63]. For NRZ format, the CD tolerance at 3-dB OSNR penalty is about 2000 ps/nm. The PMD tolerance at 3-dB OSNR penalty is 70 ps. However, despite the effectiveness to extend the transmission reach of OOK modulation format, conventional electronic equalizer provides limited CD tolerance improvement for DPSK format [102]-[103]. FFE+DFE can also adaptively compensate the impairments. 43-Gbit/s adaptive electronic equalizer with control feedback by using both eye monitoring and pseudo-error count have been proposed [63].

- Maximum likelihood sequence estimation (MLSE). MLSE is regarded as the most efficient electronic equalizer and has better performance than DFE and FFE [104]-[105]. Fig. 1.10 shows the principle of MLSE. The detected signal is firstly A/D converted. Then MLSE algorithms with pure digital signal processing are performed in DSP. The implementation of 10-Gbit/s MLSE has been reported

[101]. Detailed study has been performed to investigate the performance of MLSE for impairment compensation in conventional OOK format. It was shown that conventional MLSE exhibits 3-dB OSNR penalty for 80-ps DGD and CD tolerance of 3100 ps/nm at 10 Gbit/s [85]. However, similar to FFE+DFE, the conventional MLSE structure has limited performance improvement for the DPSK format [106]. Furthermore, the design of MLSE for advanced modulation formats, such as ASK/DPSK orthogonal modulation and 4-ASK, to extend the transmission reach has not been systematically investigated yet. The optimal design of MLSE structures for different advanced modulation formats is different. In Chapter 2, we will design novel MLSE structures with high impairment compensation performance and low cost for different advanced modulation formats.

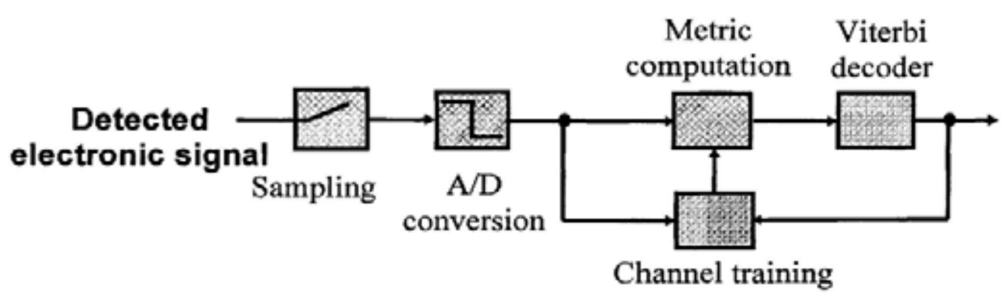

Fig. 1.10: Principle of MLSE

The existing receiver-side electronic equalizers are based on the direct detection, where all phase information is lost. As a result, the compensation is not perfect. In recent two years, another two advanced electronic equalization techniques are proposed. The first method employs the combination of delay interferometer (DI) and direct detector to reconstruct the full-field of the optical signal and to compensate the distortion by using not only the power information but also the phase information [107]-[110]. The second method uses coherent detection followed by electronic signal processing for impairment mitigation. The digital signal processing can also solve the challenges of coherent detection, such as phase estimation and alignment of polarizations. By exploiting both the amplitude and the phase of the optical signal, these two techniques outperform conventional equalizers but at the expense of the increase of implementation complexity [32]-[42].

1.3.4. Optical Compensation vs. Electronic Compensation

Electronic compensation has attracted much attention recently and will be one of focuses in this thesis. Therefore, it is necessary to discuss its advantages compared to optical compensation:

- Reduce costs by eliminating the need for optical dispersion compensation modules (DCMs). The removal of DCMs will reduce the first-installed cost including the cost of DCMs and the associated cost for compensating the loss from the DCMs, simplify the deployment and configuration, and reduce the linear impairments caused by optical filtering.
- Offer flexible and adaptive compensation which will be required in future dynamic optical networks.
- Easy to be integrated in transmitter and receiver

1.4. Objective and Main Contributions of the Thesis

The objective of the thesis is to develop new impairment mitigation approaches to improve the performance and/or to reduce the operation complexity and the cost. As a result, cost-effective high-speed optical transmission systems and optical networks are enabled.

The original contributions of the thesis are listed below:

(1). Propose and investigate several novel MLSE techniques/structures for various advanced modulation formats, including DPSK, ASK/DPSK orthogonal modulation, DQPSK, and 4-ASK.

(2). Propose novel application of MLSE to overcome the problem of the TM between the pulse carver and the data modulator for RZ/CSRZ signal and develop a simple and effective analytical method for the performance evaluation of MLSE for TM mitigation.

(3). Propose a novel re-modulation techniques for high-speed CLS WDM-PONs where ASK format with low extinction ratio is used for downstream transmission and the ASK downstream signal is re-modulated by the DPSK signal for upstream transmission. Experiments are carried out to show that the proposed scheme can significantly enhance the tolerance to CD and asynchronous upstream modulation.

(4). Apply MLSE for 10-Gbit/s upstream signal detection in centralized SC BLS WDM-PON and show that MLSE can effectively reduce the impairments from asynchronous upstream modulation at ONUs and CD in the fibers.

(5). Propose an all-optical format conversion from 40-Gbit/s RZ signal to 40-Gbit/s inverse RZ (IRZ) / 10-Gbit/s DPSK orthogonal modulation signal to interface high-speed transmission system using RZ format with networks using orthogonal modulation format. Error-free 40-km SMF transmission of the converted 40-Gbit/s IRZ/10-Gbit/s DPSK orthogonal modulation signal is experimentally demonstrated.

(6). Propose an all-optical multilevel 4-ASK coding and decoding technique. The proposed scheme encodes two input on-off-keying signals all optically into a 4-ASK signal using cross absorption modulation in an EAM and employs fiber-based all-optical approach for 4-ASK data decoding.

(7). Propose and experimentally investigate a simple monitoring technique for synchronized phase re-modulation using a narrowband optical filter. This technique can be applied for optical label swapping in optical packet switched networks, and the re-modulation of the downstream signal for upstream transmission in WDM-PONs.

1.5. Outline of the Thesis

The outline of this thesis is as follows:

Chapter 2 presents the technologies of MLSE for impairment compensation. In the first part of this chapter, we propose novel MLSE structures with high impairment compensation performance and low cost for different advanced modulation formats, including DPSK, ASK/DPSK orthogonal modulation, DQPSK, 4-ASK. In the second part of this chapter, we discuss novel applications of MLSE. We characterize the impairment from TM between the pulse carver and the data modulator in RZ systems as ISI and propose to use MLSE for TM mitigation. We also propose a simple analytical method for performance evaluation of MLSE for TM mitigation.

Chapter 3 investigates the schemes for impairment mitigation in CLS WDM-PON. The primary objective of the work is to achieve high-speed CLS WDM-PON with data rates of 10 Gbit/s for both downstream and upstream signals. We show that in the existing schemes at such high data rate, the upstream signals are sensitive to CD in the fibers and/or asynchronous upstream modulation at ONUs. We propose two solutions to mitigate the impairments from CD and asynchronous modulation. By eliminating the modulation synchronization module and all-optical CD compensation module, the proposed methods greatly reduce the cost and operation complexity of high-speed CLS WDM-PON.

Chapter 4 investigates the signal processing of advanced modulation formats in all-optical networks. Firstly, we propose an all-optical format conversion from 40-Gbit/s RZ signal to 40-Gbit/s IRZ / 10-Gbit/s DPSK orthogonal modulation signal. Error-free 40-km SMF transmission of the converted 40-Gbit/s IRZ/10-Gbit/s DPSK orthogonal modulation signal was demonstrated. Secondly, we demonstrate an all-optical 4-ASK coding and decoding technique.

Chapter 5 investigates a simple and polarization-insensitive monitoring scheme for synchronized phase re-modulation by using a narrowband OBPF.

Finally, summary and future works are described.

2. Maximum Likelihood Sequence Estimation for Impairment Compensation

As the capacity of the transmission systems increases, many signal degradation effects, such as chromatic dispersion (CD) and polarization mode dispersion (PMD), become prominent and seriously degrade the performance of the optical communication systems. Maximum likelihood sequence estimation (MLSE) has recently attracted considerable interest for impairment compensation because of its significant cost saving via volume production and adaptive compensation capability required in future dynamic optical networks [111]-[115]. Advanced optical modulation formats such as differential phase shift keying (DPSK) are alternative methods to extend the capacity and the transmission reach of the communication systems [13]-[26]. However, few studies have been performed to extend the transmission reach by combining advanced modulation formats and MLSE [102], [106], [115]. The optimal design of MLSE structures is different for different advanced modulation format.

In the first part of this chapter, we will review our recent work on the design of novel MLSE structures with high impairment compensation performance and low cost for different advanced modulation formats, including DPSK, amplitude shift keying/DPSK (ASK/DPSK) orthogonal modulation, differential quaternary phase shift keying (DQPSK), and 4-ASK. After evaluating the performance and the complexity of the proposed schemes, we can then determine the most cost-effective solution given the requirements of a transmission system.

(a) Multi-Chip DPSK MLSE for CD and PMD Compensation

In the DPSK format, we review our recently proposed 3-chip DPSK MLSE for CD and PMD compensation. Such method exploits the phase difference between not only the adjacent optical bits but also the bits that have one bit slot apart for sequence estimation of the DPSK data. The proposed 3-chip DPSK MLSE significantly outperforms conventional MLSE in CD and PMD compensation. We show that 3-chip DPSK MLSE can enhance the CD tolerance of 10-Gbit/s DPSK signal to 2.5 times of that by using 2-chip DPSK MLSE and can bound the penalty for 100-ps differential group delay (DGD) by 1.4 dB.

We further investigate 4-, 5-, and 6-chip DPSK MLSEs and show that these structures can provide further performance improvement but at the expense of the implementation complexity increase. We suggest that in practice, 3- or 4-chip DPSK MLSE is optimal in terms of the performance and the complexity.

(b) Joint MLSE (J-MLSE) and Decision-Feedback J-MLSE (DF-J-MLSE) for CD Compensation in ASK/DPSK Orthogonal Modulation

In ASK/DPSK orthogonal modulation, we firstly determine the fundamental impairment mechanism in CD-limited ASK/DPSK orthogonal modulation format both experimentally and numerically. Based on the fundamental finding, we show that conventional MLSE which only considers intra-tributary interference of the ASK and DPSK tributaries separately fails to improve the overall CD tolerance of the ASK/DPSK signal despite the increase of the MLSE's memory length. J-MLSE exploits the correlation information between the detected ASK and DPSK signals and can improve the CD tolerance of the ASK/DPSK signal significantly.

However, a J-MLSE has the implementation complexity which is proportional to $2^{2\times(m+1)}$, whereas a conventional MLSE's complexity is proportional to 2^{m+1}, where m is the MLSE's or J-MLSE's memory length. Therefore, we further propose a novel DF-J-MLSE. We show that DF-J-MLSE has the same implementation complexity as a conventional MLSE while preserving the overall CD tolerance of the ASK/DPSK signal under the J-MLSE.

(c) 3-Chip DQPSK J-MLSE for CD and PMD Compensation

In DQPSK format, we firstly show that separate equalization of the two tributaries of the DQPSK signal provides limited CD tolerance improvement while J-MLSE can significantly improve the CD tolerance of the DQPSK signal. Then we propose a novel 3-chip DQPSK J-MLSE. The 3-chip DQPSK J-MLSE searches the most probable path through the trellis for data sequence estimation by exploiting the phase difference between not only the adjacent optical bits but also the bits that have one bit slot apart. The proposed scheme significantly outperforms conventional MLSE and J-MLSE in CD and PMD compensation. We show that the proposed 3-chip DQPSK J-MLSE can enhance the CD tolerance of 20-Gbit/s DQPSK signal to 1.5 times of that by using J-MLSE and exhibits 0.8-dB penalty for 100-ps DGD at 10-Gsym/s.

(d) 4-ASK MLSE for CD Compensation

In 4-ASK format, we show that due to the increased number of levels, such format is sensitive to intersymbol interference (ISI) from optical filtering, electronic filtering, and CD. We optimize the optical/electronic receiver bandwidth and multilevel spacing of 4-ASK format. We find that the optimal level spacing of the 4-ASK signal changes with the CD values and improper level spacing design leads to significant CD tolerance reduction. As a result, level spacing optimization is difficult in CD-varying 4-ASK optical systems, in which the CD constantly changes due to the time-varying effects of the installed fibers and different routing paths. We propose 4-ASK MLSE for signal detection. It is shown that 4-ASK MLSE can effectively alleviate the sensitivity of CD tolerance to level spacing, therefore, relax the difficulty of level spacing optimization. By using MLSE, the CD tolerance of the 4-ASK signal is significantly enhanced by a factor of at least two.

As a general post-detection solution to ISI, MLSE compensates ISI regardless of its origins. Therefore, in additional to the transmission impairments such as CD and PMD, MLSE is capable to mitigate other impairments characterized as ISI. Furthermore, a versatile and cost-effective MLSE can also achieve simultaneous compensation of distortions with shared electrical devices. Hence the number of the required compensation components can be reduced [85].

In the second part of this chapter, we characterize the impairment from timing misalignment (TM) between the pulse carver and the data modulator in RZ systems as ISI. We propose to use MLSE for TM mitigation. Not specific to a certain type of ISI, MLSE can achieve simultaneous compensation of TM and PMD. We develop a theory to evaluate the performance of MLSE for compensation of TM without and with the presence of PMD in both OSNR limited and thermal-noise limited operation regions. The developed theory for MLSE's performance evaluation, employing decorrelation of noise components and the steepest decent method as well as Karhunen-Loeve expansion and saddlepoint approximation, is applicable to arbitrary input signal pulse shape, optical and electrical filtering. Monte Carlo simulations are demonstrated and agree with the prediction of the theory well.

2.1. Novel MLSE Structures for Impairment Compensation in Advanced Modulation Formats

2.1.1. Multi-Chip DPSK MLSE for CD and PMD Compensation

DPSK format is one of the most desirable formats for high-speed optical transmission due to its 3-dB optical signal to noise ratio sensitivity improvement and higher tolerance to fiber nonlinear effects compared to OOK format. However, despite the effectiveness to extend the transmission reach of OOK modulation format, conventional electronic equalizer provides limited CD tolerance improvement for the DPSK format [102]-[103].

Recently, a new family of DPSK, multi-chip DPSK (MC-DPSK), was ported from wireless communication to optical communication [116]-[118]. By exploiting the phase difference between not only the adjacent optical bits but also the bits that have one or several bit slots apart, MC-DPSK soft detection improves the quantum limit sensitivity of incoherently detected DPSK approaching to that of coherently detected PSK. Furthermore, MC-DPSK soft detection is more robust to nonlinear phase noise compared to conventional 2-chip DPSK hard decision [117]. However, MC-DPSK soft detection is based on block-by-block decision and does not consider inter-block interference. Therefore, it provides only slight improvement in CD and PMD tolerance compared to 2-chip DPSK hard decision.

In this section, we introduce the design of a novel multi-chip DPSK MLSE that exploits the phase difference between both the adjacent optical bits and the bits that have one or several bit slot apart for sequence estimation rather than block-by-block estimation. We show that the proposed scheme can significantly enhance the CD and PMD tolerance of the DPSK signal.

2.1.1.1. Principle of 3-Chip DPSK MLSE

Firstly, we study the principle of the least simple scheme, 3-chip DPSK MLSE. Fig. 2.1 shows the simulation model and the structures of 3-chip DPSK soft detection and the proposed 3-chip DPSK MLSE. Matlab programming was used for the simulation. This tool was also employed in other simulations in the following sections. A continuous wave light is phase modulated by a 10-Gbit/s DPSK data train using a Mach-Zehnder modulator (MZM). The DPSK data train consists of 500,000 raised-cosine shaped bits with 40 samples per bit. The generated DPSK signal is launched into a piece of fiber. In the fiber link, the DPSK signal is split into two orthogonal polarization modes with γ=0.5 being the relative power in the fast principal state of polarization. The sources for signal degradation, CD and PMD, are included. At the receiver, the signal is optically pre-amplified and filtered by a 50-GHz

Gaussian-shaped optical bandpass filter (OBPF). Optical noise from optical preamplifier is modeled as complex additive white Gaussian noise with zero mean and a power spectral density of N_0 for each polarization component. The signal is then split into two branches by a 50/50 coupler. The signals of the two branches are demodulated by delay interferometers (DIs) with one- and two-bit delays respectively and detected by balanced detectors. After O-E conversion, the detected signals, $q_T(t)$ and $q_{2T}(t)$, are electronically amplified, filtered by 7-GHz 4th-order Bessel electronic filters (EFs), and sampled.

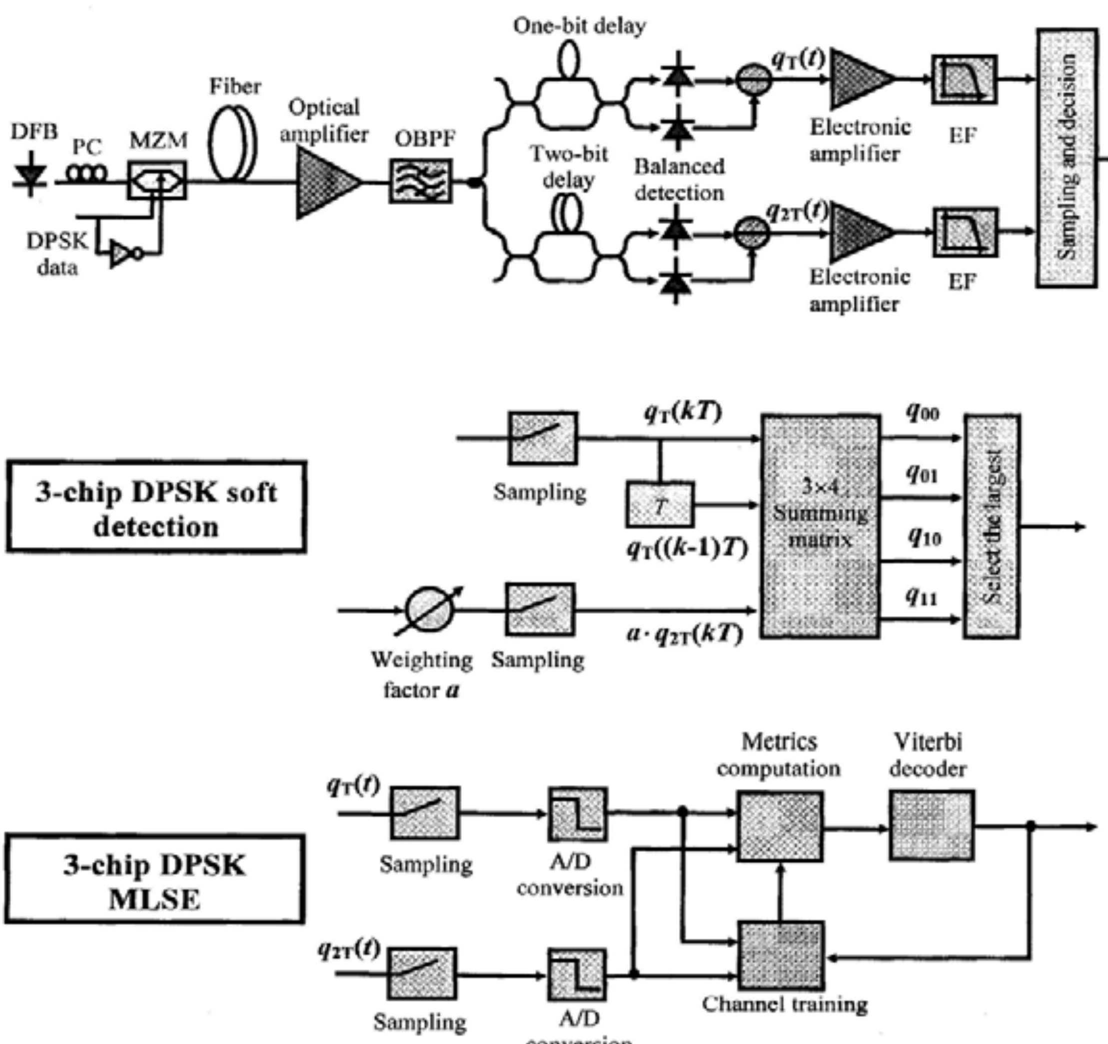

Fig. 2.1: Simulation model and the structures of 3-chip DPSK soft detection and the proposed 3-chip DPSK MLSE.

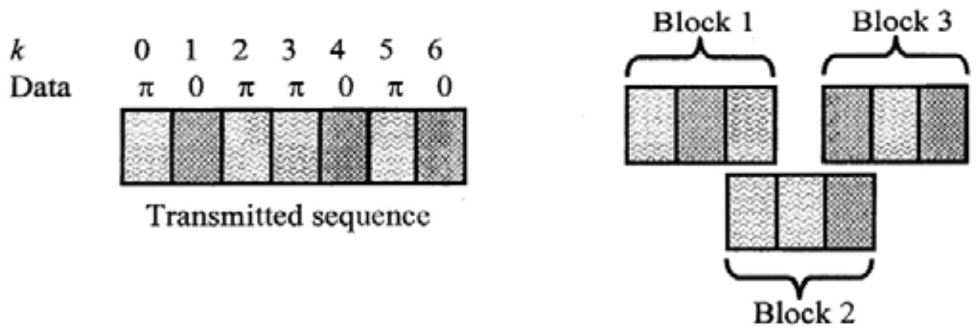

	$q_T(kT)$	$q_T((k\text{-}1)T)$	$q_{2T}(kT)$	q_{00}	q_{01}	q_{10}	q_{11}	Decision
Block 1 (k=2)	-1	-1	1	-1	-1	-1	3	11
Block 2 (k=4)	-1	1	-1	-1	3	-1	-1	01
Block 3 (k=6)	-1	-1	1	-1	-1	-1	3	11

Weighting factor *a* is assumed to be 1

Fig. 2.2: An example of 3-chip DPSK soft detection.

For 3-chip DPSK soft detection, maximum likelihood principle is employed for block-by-block decision [116]. An example with a transmitted pattern (π 0 π π 0 π 0) is used to illustrate 3-chip DPSK soft detection in Fig. 2.2. Three signals $q_T(kT)$, $q_T((k\text{-}1)T)$, and $a{\cdot}q_{2T}(kT)$ are used as the inputs to a 3×4 summing matrix, where a is the weighting factor to evaluate the importance of $q_{2T}(kT)$ in data decision [118]. The matrix outputs, q_{ij}, $i, j \in \{0, 1\}$, are

$$\begin{aligned} q_{00} &= q_T(kT) + q_T((k-1)T) + a \cdot q_{2T}(kT), \quad q_{01} = -q_T(kT) + q_T((k-1)T) - a \cdot q_{2T}(kT), \\ q_{10} &= q_T(kT) - q_T((k-1)T) - a \cdot q_{2T}(kT), \quad q_{11} = -q_T(kT) - q_T((k-1)T) + a \cdot q_{2T}(kT) \end{aligned} \tag{2.1}$$

Maximum-likelihood decision is to find the largest q_{ij}, and its corresponding indexes are the best estimation of the 2-bit DPSK data (b_{k-1}, b_k). Although 3-chip DPSK soft detection is optimal in the sense of block-by-block detection, it does not consider the inter-block interference.

On the other hand, sequence estimation is employed in the proposed scheme. $q_T(t)$ and $q_{2T}(t)$ are sampled with two samples per bit and analog-to-digital (A/D) converted with resolution of 5 bits. The samples from both $q_T(t)$ and $q_{2T}(t)$ are simultaneously exploited in the initial channel training and the metrics computation. The metric of

3-chip DPSK MLSE, $PM(b_k)$, is

$$PM(b_k) = PM(b_{k-1}) - \sum_{t_j} \log(p(q_T(t_j) \mid b_{k-m},...,b_k)) - a \cdot \sum_{t_j} \log(p(q_{2T}(t_j) \mid b_{k-m},...,b_k)) \quad (2.2)$$

For $q_T(t_j)$, $t_j=(k-m/2)T$, $(k-(m+1)/2)T$, or $(k-(m-1)/2)T$. For $q_{2T}(t_j)$, $t_j=(k-m/2)T$, $(k-(m-1)/2)T$, or $(k-(m-2)/2)T$. $p(q_i(t_j) \mid b_{k-m},\ldots,b_k)$, with i being T or $2T$, is the probability of the sampled $q_i(t)$ signal value at $t=t_j$ given the DPSK logical data $b_{k-m},\ldots,b_k$. m is the memory length. The initial metrics in the channel training table are obtained using nonparametric histogram method by a 200,000-bit training sequence. Because 2^{m+1} metrics have to be calculated after the detection of each bit and each metric requires the sum of two input branches, therefore, the complexity of the metrics computation is proportional to $2\times2^{m+1}$. On the other hand, the complexity of the Viterbi decoding is proportional to the state number, 2^m. The performance is evaluated in terms of required E_b/N_0 (required photon number per bit before pre-amplification) to achieve bit error rate (BER) of 10^{-4}, where E_b is the optical average power in one bit slot after optical pre-amplification.

2.1.1.2. Performance of 3-Chip DPSK MLSE

Firstly, the effect of the weighting factor a on the performance of 3-chip DPSK signals is investigated. Fig. 2.3(a) shows the required E_b/N_0 (dB) versus CD by using 3-chip DPSK soft detection (circles) and 3-chip DPSK MLSE with m=4 (triangles) under a=1 (solid) and optimal a value for each CD value (dashed). From the figure, it is shown that by using 3-chip DPSK MLSE, the CD tolerance of the DPSK signal is significantly enhanced compared to that by using 3-chip DPSK soft detection. The CD tolerance of the DPSK signal under a=1 (solid) is very close to that under optimal a value (dashed) irrespective of 3-chip DPSK detection methods. Fig. 2.3(b) depicts the required E_b/N_0 (dB) versus a by using 3-chip DPSK soft detection (circles) and 3-chip DPSK MLSE with m=4 (triangles) when the CD values are 1250 ps/nm (solid) and 2500 ps/nm (dashed). From the figure, it is shown that the optimal a values change with CD values. For example, for 3-chip DPSK soft detection, optimal a values are 0.75 and 0.25 when the CD values are 1250 ps/nm and 2500 ps/nm, respectively.

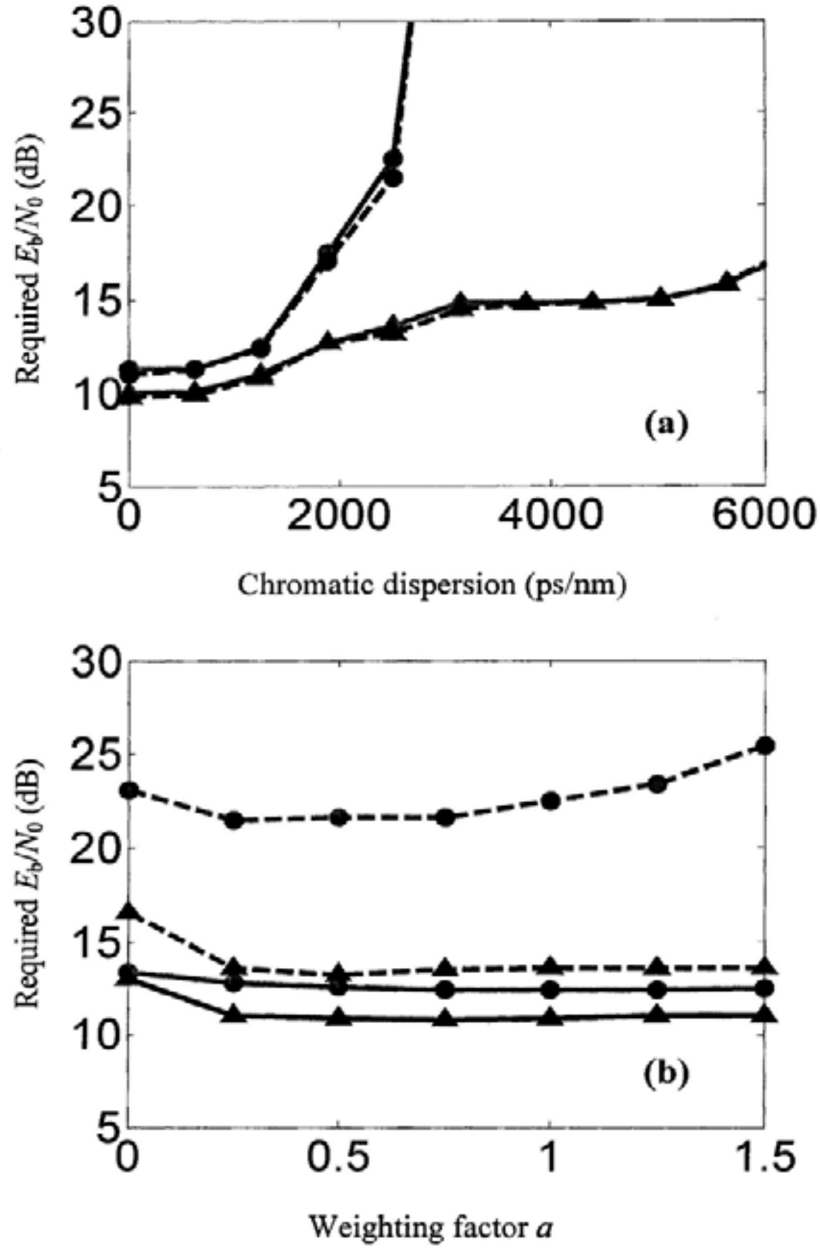

Fig. 2.3: (a) The required E_b/N_0 (dB) versus CD by using 3-chip DPSK soft detection (circles) and 3-chip DPSK MLSE with m=4 (triangles) under a=1 (solid) and optimal a value for each CD value (dashed); (b) the required E_b/N_0 (dB) versus a by using 3-chip DPSK soft detection (circles) and 3-chip DPSK MLSE with m=4 (triangles) when the CD values are 1250 ps/nm (solid) and 2500 ps/nm (dashed).

Similar conclusions from Fig. 2.3(a) & (b) can also be obtained for PMD tolerance of the DPSK signal. Fig. 2.4(a) shows the required E_b/N_0 (dB) versus DGD by using 3-chip DPSK soft detection (circles) and 3-chip DPSK MLSE with m=4 (triangles) under a=1 (solid) and optimal a value for each DGD value (dashed). Fig. 2.4(b) depicts the required E_b/N_0 (dB) versus a by using 3-chip DPSK soft detection (circles) and 3-chip DPSK MLSE with m=4 (triangles) when the DGD values are 40 ps (solid) and 80 ps (dashed). From Fig. 2.3 and Fig. 2.4, for both 3-chip DPSK detection methods, it is concluded that a=1 can be used to eliminate the complexity of weighting factor optimization yet with negligible performance degradation.

To further show the advantages of the proposed scheme in CD and PMD compensation, Fig. 2.5(a) shows the required E_b/N_0 (dB) versus CD for 2-chip DPSK signal (solid) and 3-chip DPSK signal under the weighting factor a=1 (dashed). Circles, triangles, and squares represent the detection methods without MLSE (2-chip DPSK optimal threshold detection / 3-chip DPSK soft detection), with MLSE under memory length m=2, and with MLSE under m=4, respectively. From the figure, it is shown that compared to 2-chip DPSK optimal threshold detection (circles and solid), 3-chip DPSK soft detection (circles and dashed) exhibits only slight CD tolerance improvement because it does not consider inter-block interference, i.e. the interference from the adjacent blocks. By employing sequence estimation, 2-chip DPSK MLSE (triangles and solid, or squares and solid) achieves higher CD tolerance than 3-chip DPSK soft detection. However, its performance in CD compensation for the DPSK signal is still limited, with CD tolerance about 1900 ps/nm at E_b/N_0 of 15 dB irrespective of 2-chip DPSK MLSE's memory length. In contrast, by introducing redundant detection information for sequence estimation, 3-chip DPSK MLSE (triangles and dashed, or squares and dashed) significantly outperforms conventional 2-chip DPSK MLSE in CD compensation. At E_b/N_0 of 15 dB, the CD tolerance by using 3-chip DPSK MLSE is enhanced to 2800 ps/nm and 5000 ps/nm for memory length m=2 and 4, respectively. These values are about 1.5 times and 2.5 times of those by using conventional 2-chip DPSK MLSE.

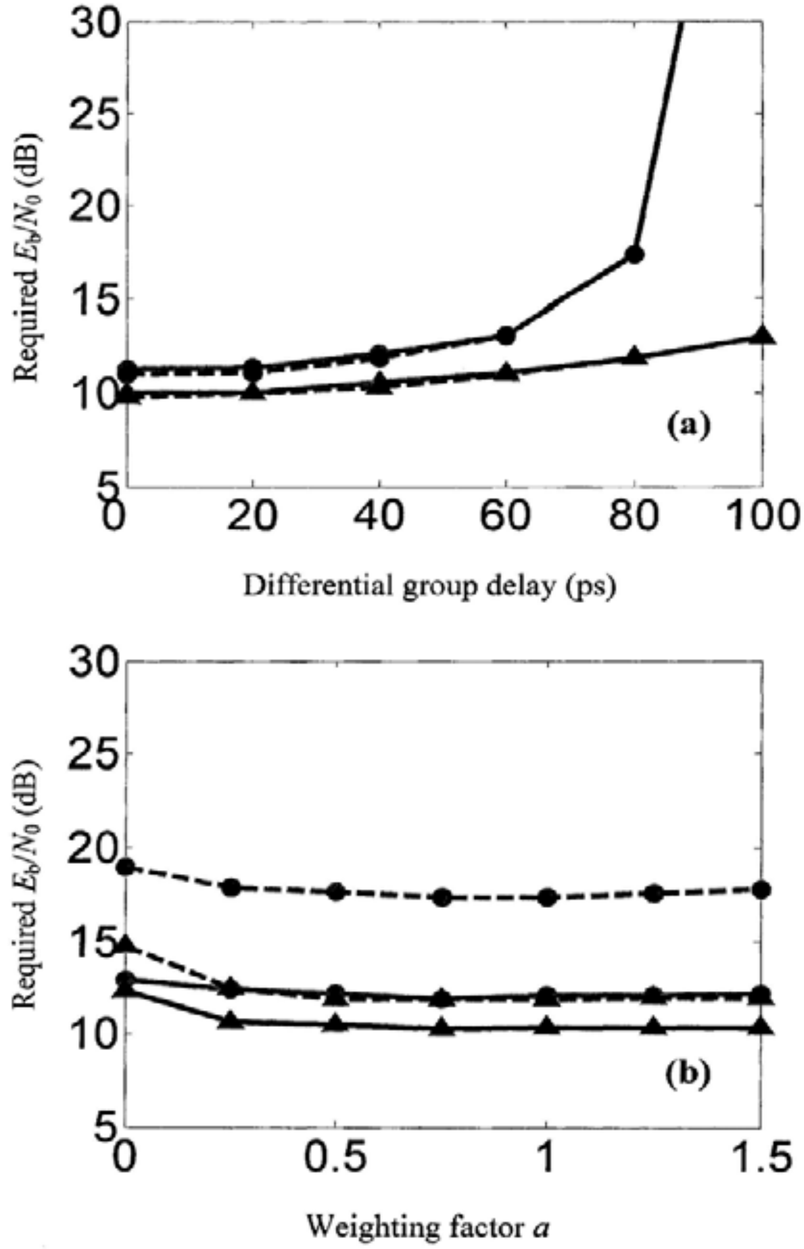

Fig. 2.4: (a) The required E_b/N_0 (dB) versus DGD by using 3-chip DPSK soft detection (circles) and 3-chip DPSK MLSE with m=4 (triangles) under a=1 (solid) and optimal a value for each DGD value (dashed); (b) the required E_b/N_0 (dB) versus a by using 3-chip DPSK soft detection (circles) and 3-chip DPSK MLSE with m=4 (triangles) when the DGD values are 40 ps (solid) and 80 ps (dashed).

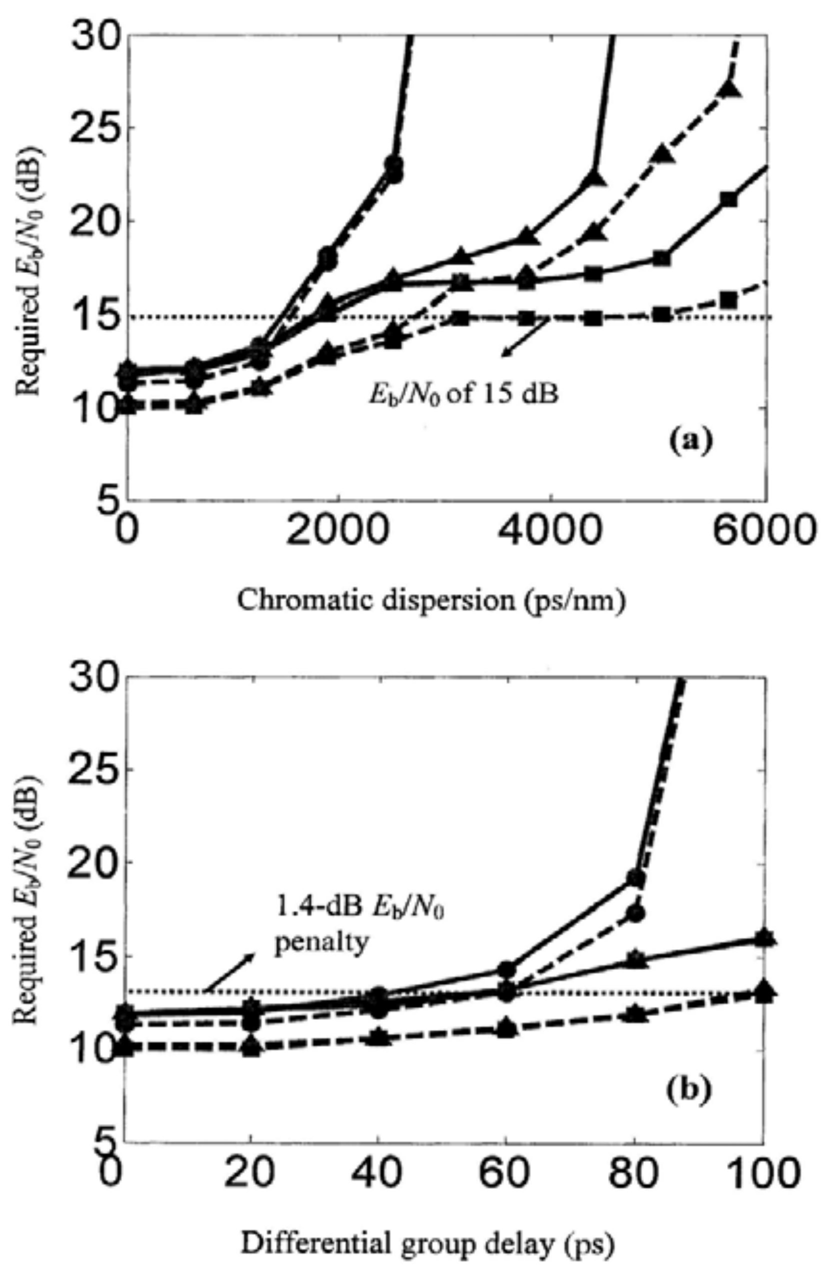

Fig. 2.5: The required E_b/N_0 (dB) versus (a) CD and (b) DGD for 2-chip DPSK signal (solid) and 3-chip DPSK signal under the weighting factor a=1 (dashed). Circles, triangles, and squares represent the detection methods without MLSE (2-chip DPSK optimal threshold detection / 3-chip DPSK soft detection), with MLSE under memory length m=2, and with MLSE under m=4, respectively.

Next, the performance of the proposed 3-chip DPSK MLSE for 1st-order PMD compensation is investigated. Fig. 2.5(b) shows the required E_b/N_0 (dB) versus DGD for 2-chip DPSK signal (solid) and 3-chip DPSK signal under a=1 (dashed). Circles, triangles, and squares represent the detection methods without MLSE, with MLSE under m=2, and with MLSE under m=4, respectively. From the figure, it is shown that similar to Fig. 2.5(a), 3-chip DPSK MLSE significantly outperforms the other detection methods in PMD compensation. For DGD of 100 ps, the E_b/N_0 penalties by using 3-chip DPSK MLSE with m=2 and 4 are bounded by 1.6 dB and 1.4 dB respectively, which correspond to 2.6-dB and 2.8-dB penalty reduction compared to those by using 2-chip DPSK MLSE, where the E_b/N_0 penalty is with respect to the back-to-back E_b/N_0 (E_b/N_0=11.8 dB) of 2-chip DPSK optimal threshold detection. Therefore, the proposed method is an effective way to extend the transmission reach of the DPSK signal.

2.1.1.3. Principle and Performance of Multi-Chip DPSK MLSE

Next, we consider the more general structure of L-chip DPSK MLSE, as shown in Fig. 2.6. The simulation parameters are the same as those in 3-chip DPSK MLSE. The DPSK signal is demodulated by (L-1) DIs and detected by balanced detectors. $q_T(t)\ldots q_{(L-1)T}(t)$ are sampled with two samples per bit and A/D converted with 5-bit resolution. The samples from $q_T(t)\ldots q_{(L-1)T}(t)$ are simultaneously exploited in the initial channel training and the metrics computation. The metric of L-chip DPSK MLSE, $PM(b_k)$, is

$$PM(b_k) = PM(b_{k-1}) - \sum_{i=1}^{L-1}\sum_{t_j}\log(p(q_{iT}(t_j)\,|\,b_{k-m},\ldots,b_k)) \tag{2.3}$$

$p(q_{iT}(t_j)\mid b_{k-m},\ldots,b_k)$, with $i\in\{1,\ldots L\text{-}1\}$, is the probability of the sampled $q_{iT}(t)$ signal value at $t=t_j$ given the DPSK logical data $b_{k-m},\ldots,b_k$. The design of memory length m is dependent on L with $m+2\geq L$. In the investigation, m is assumed to be 4. Therefore multi-chip DPSK MLSEs with $L\leq6$ are studied. Because in L-chip DPSK MLSE, the calculation of each metric requires the sum of (L-1) input branches, therefore, the complexity of metrics computation is proportional to $(L\text{-}1)\times 2^{m+1}$. On the other hand, the complexity of the Viterbi decoding does not change with L and is still proportional to the state number, 2^m. The performance is evaluated in terms of required E_b/N_0 to achieve BER of 10^{-4}.

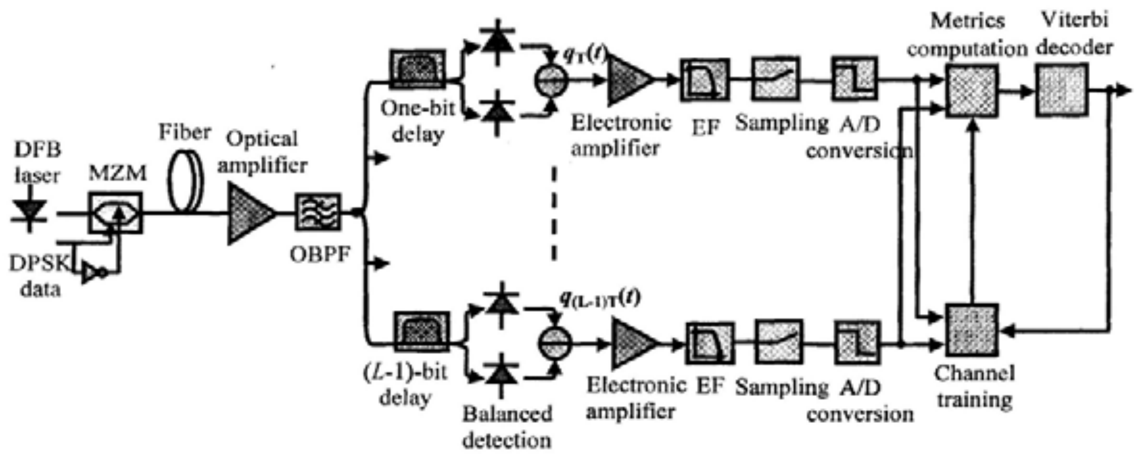

Fig. 2.6: Structure of L-chip DPSK MLSE

Fig. 2.7(a) shows the required E_b/N_0 (dB) versus CD for 2-chip DPSK without MLSE (circles), with 2- (triangles), 3- (squares), 4- (diamonds), 5- (crosses), and 6-chip (pluses) DPSK MLSE. From the figure, it is shown that compared to 3-chip DPSK MLSE, 4-, 5-, and 6-chip DPSK MLSEs provide further performance improvement. At E_b/N_0 of 15 dB, the CD tolerances for 4-, 5-, and 6-chip DPSK MLSEs are 5600 ps/nm, 6300 ps/nm, and 7200 ps/nm respectively. However, notice that the computation complexity of multi-chip DPSK MLSE increases with the chip number. Furthermore, the required number of DIs and detectors is also linearly proportional to L. Therefore, we suggest that in practice, 3- or 4-chip DPSK MLSE is optimal in terms of the performance and the complexity. Next, the performance of the L-chip DPSK MLSE for 1st-order PMD compensation is investigated. Fig. 2.7(b) shows the required E_b/N_0 (dB) versus DGD for 2-chip DPSK without MLSE (circles), with 2- (triangles), 3- (squares), 4- (diamonds), 5- (crosses), and 6-chip (pluses) DPSK MLSE. From the figure, it is shown that similar to Fig. 2.7(a), 4-, 5-,and 6-chip DPSK MLSEs provide further PMD tolerance improvement compared to 3-chip DPSK MLSE. For DGD of 100 ps, the E_b/N_0 penalties by using 3-, 4-, 5-, and 6-chip DPSK

MLSEs are bounded by 1.4 dB, 0.3 dB, -0.3 dB, and -0.8 dB respectively. Therefore, the proposed method is an effective way for CD and PMD compensation to extend the transmission reach of the DPSK signal in high-speed optical transmissions.

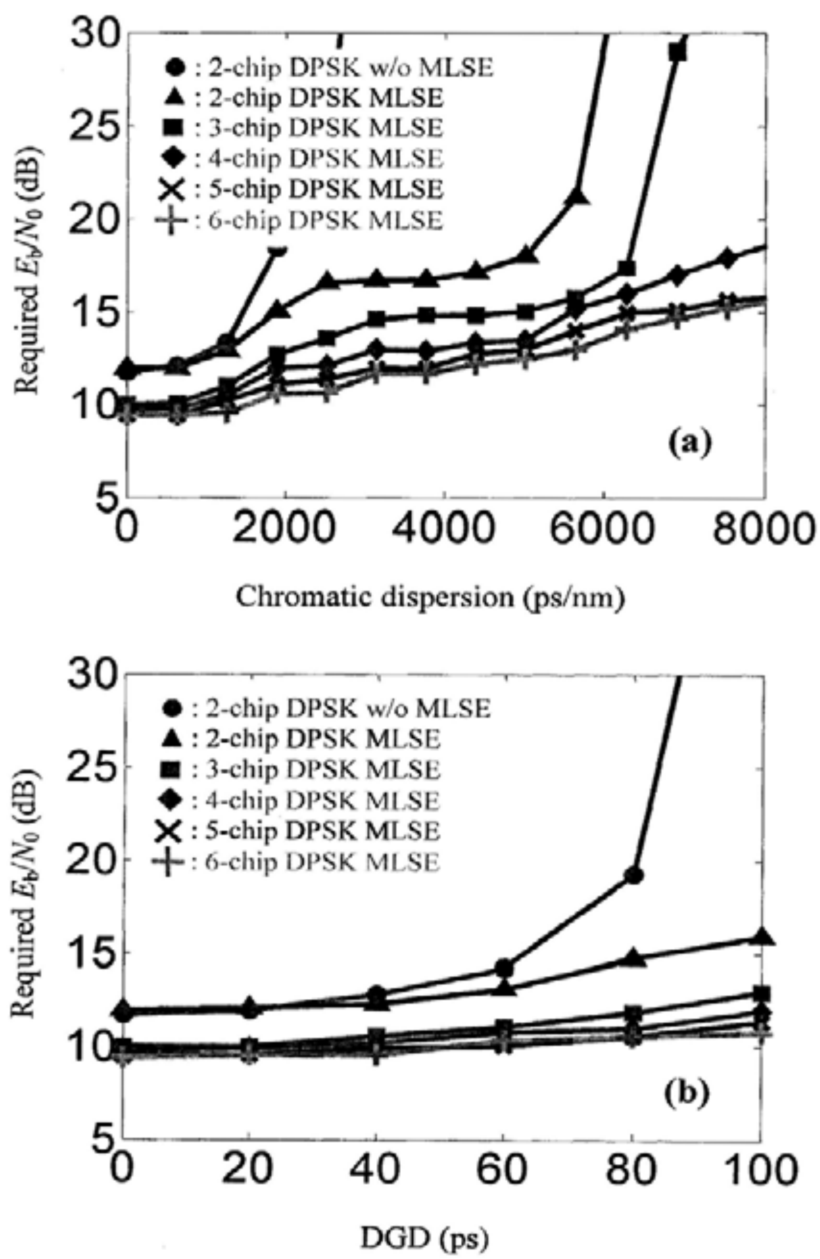

Fig. 2.7: Required E_b/N_0 (dB) versus (a) CD and (b) DGD for 2-chip DPSK without MLSE (circles), with 2- (triangles), 3- (squares), 4- (diamonds), 5- (crosses), and 6-chip DPSK MLSE (pluses).

2.1.1.4. Summary

In summary, we have proposed the design of a novel multi-chip DPSK MLSE to extend the transmission reach of the DPSK signal in high-speed optical transmission applications. The proposed technique significantly outperforms conventional 2-chip DPSK MLSE in CD and 1st-order PMD compensation. We show that at E_b/N_0 of 15 dB, 3-chip DPSK MLSE can enhance the CD tolerance of 10-Gbit/s DPSK signal to 5000 ps/nm, 2.5 times of that by using 2-chip DPSK MLSE. For PMD compensation, 3-chip DPSK MLSE can bound the E_b/N_0 penalty for 100-ps DGD by 1.4 dB, a 2.8-dB penalty reduction compared to that by using 2-chip DPSK MLSE. We further investigate 4-, 5-, and 6-chip DPSK MLSEs and show that these structures can provide further performance improvement but at the expense of the implementation complexity increase. We suggest that in practice, 3- or 4-chip DPSK MLSE is optimal in terms of the performance and the complexity.

2.1.2. J-MLSE and DF-J-MLSE for CD Compensation in ASK/DPSK Orthogonal Modulation Format

ASK/ DPSK orthogonal modulation format is an attractive spectral efficient multi-bit per symbol modulation format to enable close channel spacing in dense wavelength-division multiplexing (DWDM) transmission, to carry optical payload / label in optical networks, and to provide capacity upgrade without component replacement [119]-[122]. However, despite many experimental demonstrations of this format in the applications, few studies have been performed to investigate its CD tolerance [119]-[120]. In [119] where phase modulator (PM) is employed for DPSK tributary modulation, it is shown that the DPSK tributary of the ASK/DPSK signal has much better CD tolerance than the ASK tributary. Such great difference of the CD tolerance between the two tributaries, however, is not manifest in [120], where MZM is used for DPSK tributary modulation in the ASK/DPSK transmitter. Despite their contributions, these papers have not revealed the fundamental mechanism that limits the transmission distance in CD-limited ASK/DPSK orthogonal modulation format.

Electronic dispersion compensation has attracted considerable interest because of its cost effectiveness and adaptive equalization capability. The implementation of 10-Gbit/s conventional MLSE has been reported [101]. However, there is little prior work for the investigation of electronic device to extend the transmission reach of ASK/DPSK orthogonal format. Electronic equalization of multi-bit per symbol format relaxes the speed limitation of electronic devices for high speed optical transmission.

In this section, we firstly determine the fundamental transmission limitation of the ASK/DPSK orthogonal format. It is found that for the two different implementation schemes of the DPSK tributary generation (PM or MZM), the transmission distance of the ASK/DPSK signal is limited by the ASK tributary and the intrinsic limitation mechanism is from the interaction between the two tributaries. Therefore, conventional MLSE which only considers intra-tributary interference of the two tributaries separately cannot improve the CD tolerance of the ASK/DPSK signal. We show that J-MLSE makes full use of the correlation information between the two tributaries and can effectively improve the CD tolerance of the ASK/DPSK signal.

However, a J-MLSE has higher implementation complexity which is proportional to $2^{2\times(m+1)}$, whereas a conventional MLSE's complexity is proportional to 2^{m+1}, where m is the MLSE's or J-MLSE's memory length. Therefore, we further propose a novel DF-J-MLSE. We show that DF-J-MLSE has the same implementation complexity as a conventional MLSE while preserving the overall CD tolerance of the ASK/DPSK signal under the J-MLSE.

2.1.2.1. Fundamental Transmission Limitation in CD-Limited ASK/DPSK Orthogonal Modulation

Fig. 2.8 shows the simulation model. A continuous wave light is phase modulated by a 10-Gbit/s DPSK data train using a PM or an MZM. The following 10-Gbit/s intensity modulation with finite extinction ratio (ER) is implemented in another MZM. The DPSK and ASK data trains both consist of 500,000 raised-cosine shaped bits with 40 samples per bit. The generated ASK/DPSK signal is amplified and launched into an optical fiber where CD is introduced. Before detection, the signal is filtered by a 50-GHz Gaussian-shaped OBPF. The ASK tributary is directly detected while the DPSK tributary is demodulated by a DI and detected by a balanced detector. After O-E conversion, the detected DPSK or ASK signal is electrically amplified, filtered by a 7-GHz 4th-order Bessel EF, sampled, and compared with the optimal threshold. The system is in thermal-noise limited operation region. The performance is evaluated in terms of receiver power penalty at BER of 10^{-4}, which can be corrected below 10^{-15} using forward error correction.

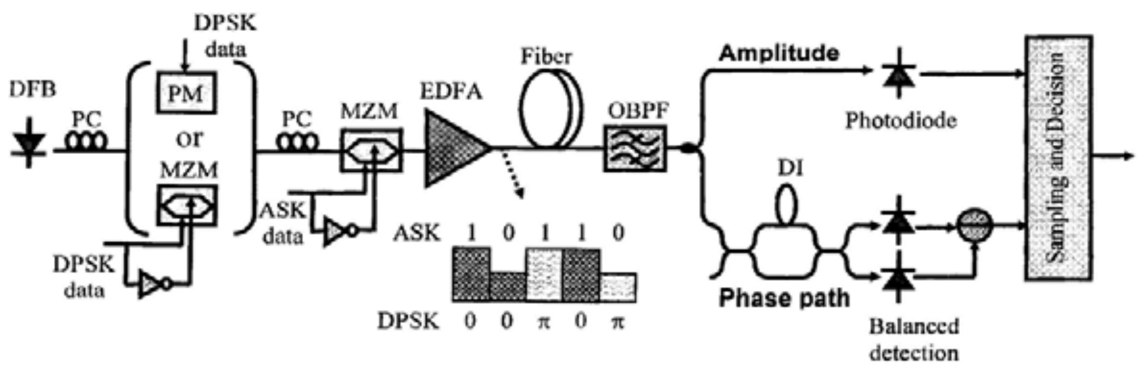

Fig. 2.8: Simulation model for fundamental transmission limitation investigation

The dependence of the receiver power penalty of the ASK (circles) and DPSK (triangles) tributaries on the ER of the ASK tributary is shown in Fig. 2.9(a). Note that the receiver power penalty is with respect to the back-to-back receiver sensitivity of the ASK tributary at ER of 4.9 dB, and this reference is used throughout this section. From the figure, it is shown that at this ER, the receiver sensitivities of the ASK tributary and the DPSK tributary are almost the same [119]. Fig. 2.9(b) depicts the CD tolerance of the ASK (circles) and DPSK (triangles) tributaries of 10-Gsym/s ASK/DPSK signal at ER of 4.9 dB when the DPSK tributary is generated by MZM. The CD tolerance of 20-Gbit/s pure ASK signal with infinite ER (squares) is also given in Fig. 2.9(b) for comparison. From the figure, it is shown that despite its 1.6 dB back-to-back penalty, ASK/DPSK orthogonal modulation format outperforms pure ASK format for cumulative CD larger than 400 ps/nm.

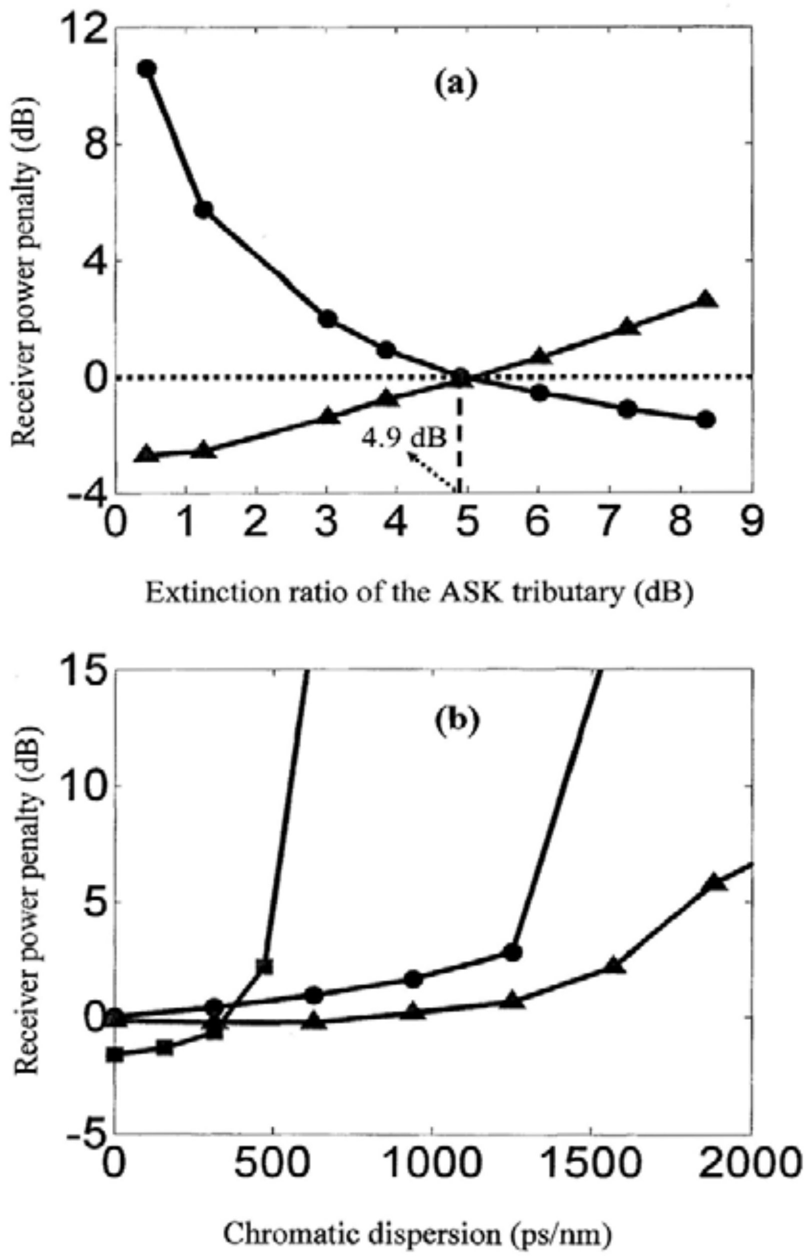

Fig. 2.9: (a) Receiver power penalty of the ASK (circles) and DPSK (triangles) tributaries of the ASK/DPSK signal versus the ER of the ASK tributary. (b) Receiver power penalty of the ASK (circles) and DPSK (triangles) tributaries of 10-Gsym/s ASK-DPSK signal versus CD for ER of 4.9 dB when the DPSK tributary is generated by MZM. Squares represent the CD tolerance of 20-Gbit/s pure ASK signal with infinite ER.

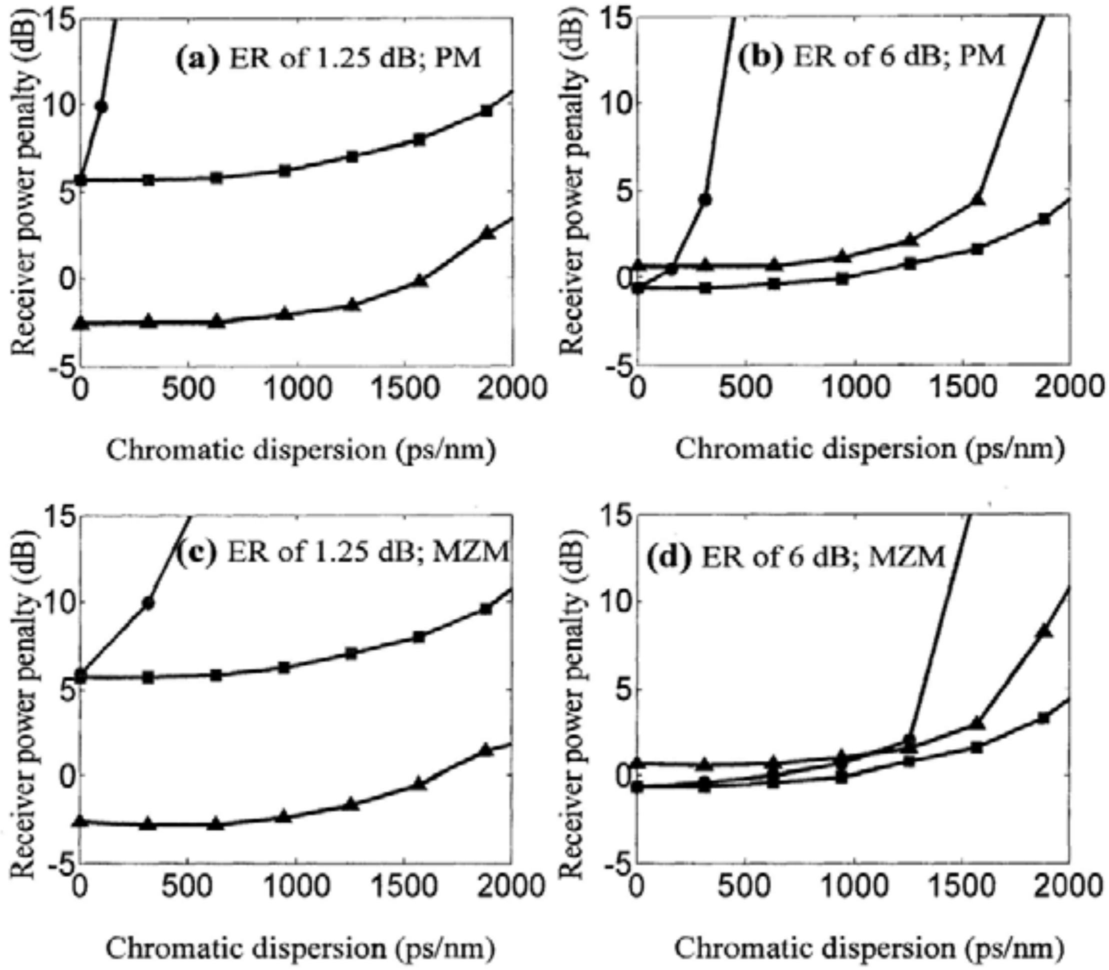

Fig. 2.10: Receiver power penalty versus CD for (a) ER of 1.25 dB and DPSK tributary generation by PM; (b) ER of 6 dB and DPSK tributary generation by PM; (c) ER of 1.25 dB and DPSK tributary generation by MZM; and (d) ER of 6 dB and DPSK tributary generation by MZM. Circles and triangles represent the ASK and DPSK tributaries of the ASK/DPSK signal, respectively. Squares represent the pure ASK signal in the absence of the DPSK tributary at the ER of 1.25 dB for (a) & (c) and 6 dB for (b) & (d).

To determine the intrinsic transmission limitation mechanism and find out the extrinsic parameters on which the CD tolerance of the ASK/DPSK format depends, Fig. 2.10 shows the receiver power penalty versus CD for (a) ER of 1.25 dB and DPSK tributary generation by PM; (b) ER of 6 dB and DPSK tributary generation by PM; (c) ER of 1.25 dB and DPSK tributary generation by MZM; and (d) ER of 6 dB and DPSK tributary generation by MZM. Circles and triangles represent the ASK and DPSK tributaries of the ASK/DPSK signal, respectively. Squares represent the pure ASK signal in the absence of the DPSK tributary at the ER of 1.25 dB for Fig. 2.10(a) & (c) and 6 dB for Fig. 2.10(b) & (d). From the figure, two conclusions can be drawn. First, compared to that of the pure ASK signal in the absence of the DPSK tributary, the CD tolerance of the ASK tributary in the ASK/DPSK signal is significantly reduced. Such phenomenon is even more severe for small ER value and is also related to the choice of PM or MZM for phase modulation. When the DPSK tributary is generated by PM, the imperfect phase modulation in data transition region induces chirp, which limits the CD tolerance of the ASK tributary below several hundreds ps/nm. In contrast, for the DPSK generation by MZM, phase in data transition region jumps instantaneously and the transmission reach is extended. Second, the DPSK tributary of the ASK/DPSK signal has much better CD tolerance than the ASK tributary. Therefore, it is the ASK tributary that limits the overall transmission distance of the ASK/DPSK signal and the intrinsic limitation mechanism is from the interaction between the ASK and DPSK tributaries.

We also confirm our conclusions experimentally. Fig. 2.11 shows the experimental setup. PM was employed for DPSK tributary generation. The ER of the ASK tributary was set at 4.9 dB. Fig. 2.12 depicts the ASK (solid) and DPSK (dotted) tributaries of 10-Gsym/s ASK/DPSK signal. In addition, we show the CD tolerance of 10-Gbit/s pure ASK signal at ER of 4.9 dB in the absence of the DPSK tributary (dashed) by switching off the PM. Insets show the eye diagrams for the ASK tributary, pure ASK signal without the DPSK tributary, and the DPSK tributary after 10-km SMF transmission. From the figures, it is shown that clear eye is exhibited for the pure ASK signal after 10-km SMF transmission. However, in the presence of the DPSK tributary, the CD tolerance of the ASK tributary (solid) is severely reduced. On the other hand, the presence of the ASK tributary has little impact on the CD tolerance of the DPSK tributary. Therefore, it is the ASK tributary that limits the overall transmission distance of the ASK/DPSK signal, and the intrinsic impairment mechanism is not from the intra-tributary interference but from the interaction between the two tributaries.

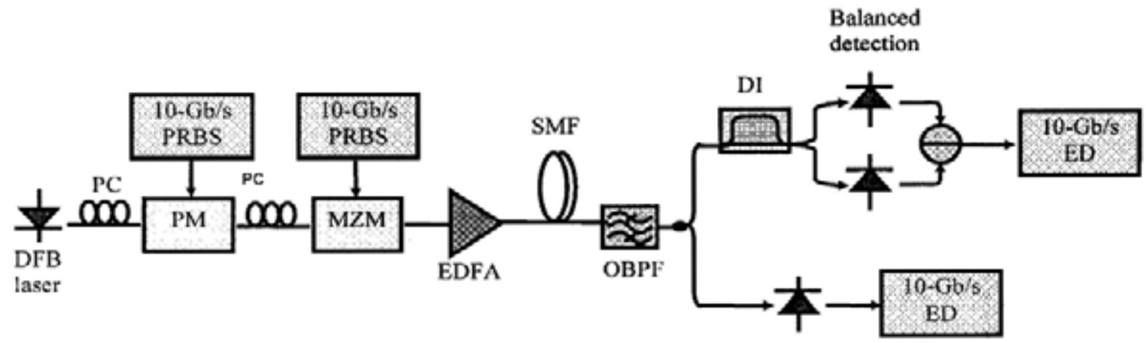

Fig. 2.11: Experimental setup

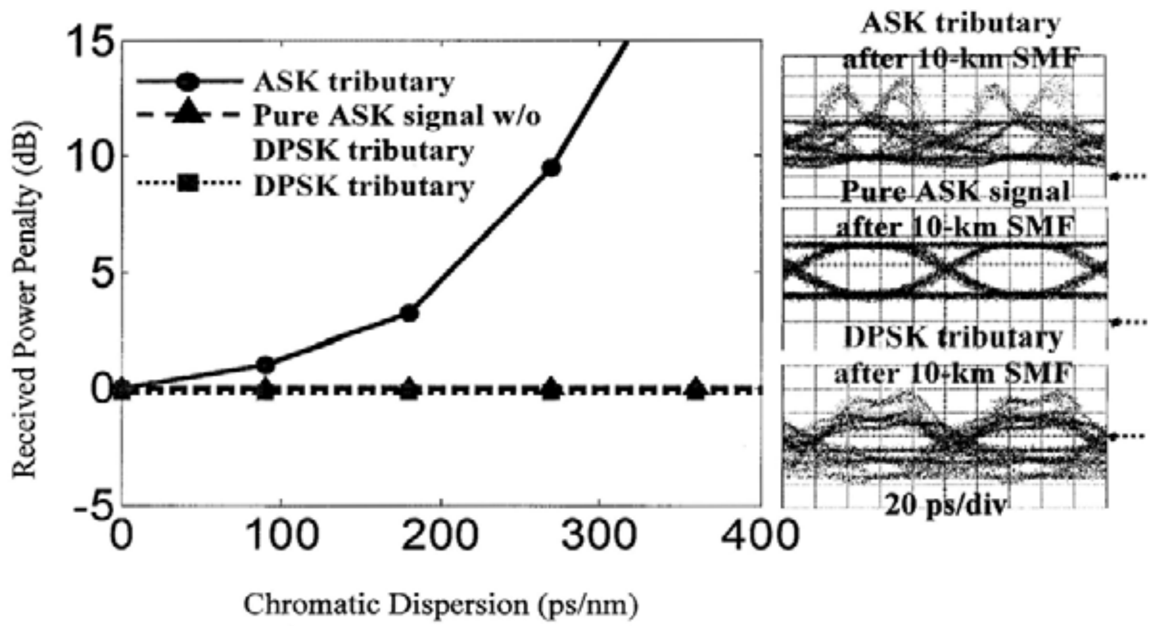

Fig. 2.12: Received power penalty versus CD

2.1.2.2. Principle of J-MLSE

Next, we investigate the performance of MLSE for CD compensation. We consider two schemes, as shown in Fig. 2.13. The first scheme applies two separate 10-Gbit/s MLSEs to the detected ASK and DPSK signals, respectively. The ASK or the DPSK signal is amplified, filtered, sampled, and A/D converted with resolution of 5 bits. MLSE operates with two samples per bit. The metric of MLSE, $PM(b_{i,n})$, i being ASK or DPSK, is

$$PM(b_{i,n}) = PM(b_{i,n-1}) - \sum_{t_j} \log(p(I_i(t_j) \mid b_{i,n-m},\ldots,b_{i,n})) \quad (2.4)$$

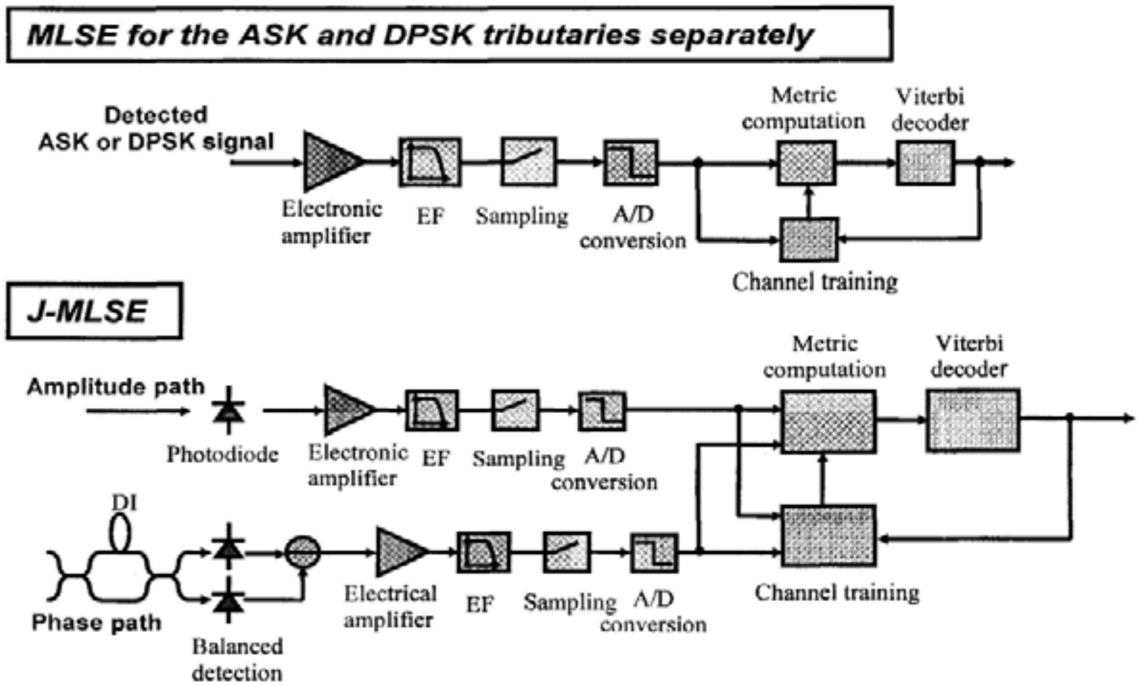

Fig. 2.13: Structure of conventional MLSE and J-MLSE

where $t_j \in \{(n-m/2)T\ (n+1/2-m/2)T\}$. $b_{i,n}$ and $p(I_i(t_j) \mid b_{i,n-m},\ldots,b_{i,n})$ are the n^{th} ASK or DPSK logical data and the probability of the sampled ASK or DPSK signal value at time t_j giving the logical data $b_{i,n-m},\ldots,b_{i,n}$, respectively. m is the memory length. The initial metric in the channel training table is obtained using nonparametric histogram method by a 200,000-bit training sequence. The second scheme, J-MLSE, exploits the detected ASK and DPSK signals simultaneously in both initial channel training and metric computation. The metric of two-sample per bit J-MLSE is:

$$\begin{aligned} PM(b_{ASK,n}, b_{DPSK,n}) &= PM(b_{ASK,n-1}, b_{DPSK,n-1}) \\ &\quad -\sum_{i}\sum_{t_j}\log(p(I_i(t_j) \mid b_{ASK,n-m},\ldots,b_{ASK,n}, b_{DPSK,n-m},\ldots,b_{DPSK,n})) \end{aligned} \tag{2.5}$$

Note that the complexities of one J-MLSE and two conventional MLSEs are proportional to 4^m and 2×2^m, respectively. In the investigation, J-MLSE is assumed to be a 16-state machine with memory length m of 2 while each MLSE in the second scheme has 8 states for fair comparison. The other system parameters are the same as those in Fig. 2.8. The system is thermal-noise limited. The performance is evaluated in terms of receiver power penalty at BER of 10^{-4}.

2.1.2.3. Performance of J-MLSE

Fig. 2.14 depicts the receiver power penalties versus CD by using conventional detection (circles), MLSE for the ASK and DPSK tributaries separately (triangles), and J-MLSE (squares). In the figure, ER is 4.9 dB and the DPSK tributary is generated by (a) PM, and (b) MZM. The solid lines and the dashed lines represent the ASK tributary and the DPSK tributary, respectively. From Fig. 2.14, for both (a) and (b), individual MLSE for the two tributaries cannot improve the CD tolerance of the ASK tributary, and thus the overall CD tolerance of the ASK/DPSK signal. It is because the transmission distance is not limited by the intra tributary interference. By employing J-MLSE, however, the performances of the ASK tributary are effectively improved. The reason is twofold. First, because different ASK data lead to different amplitude levels in the detected DPSK signal [119], the knowledge of the detected DPSK signal definitely helps the decision of the ASK data. Second, because the transmission limitation is from the interaction between the ASK and DPSK tributaries, a J-MLSE that considers both ASK and DPSK data is effective for CD compensation. Therefore, from the figure, it is shown that at ER of 4.9 dB, negative receiver power penalty of the ASK tributary is achieved for cumulative CD less than 160 ps/nm in Fig. 2.14(a) and 1200 ps/nm in Fig. 2.14(b) by using J-MLSE. The CD tolerance of the ASK tributary at 1-dB receiver power penalty is enhanced by J-MLSE from 120 ps/nm to 300 ps/nm in Fig. 2.14(a) and from 640 ps/nm to 1400 ps/nm in Fig. 2.14(b). Because the main transmission limit of the ASK/DPSK signal is from the ASK tributary, as a result, the overall transmission reach of such format is enhanced by J-MLSE.

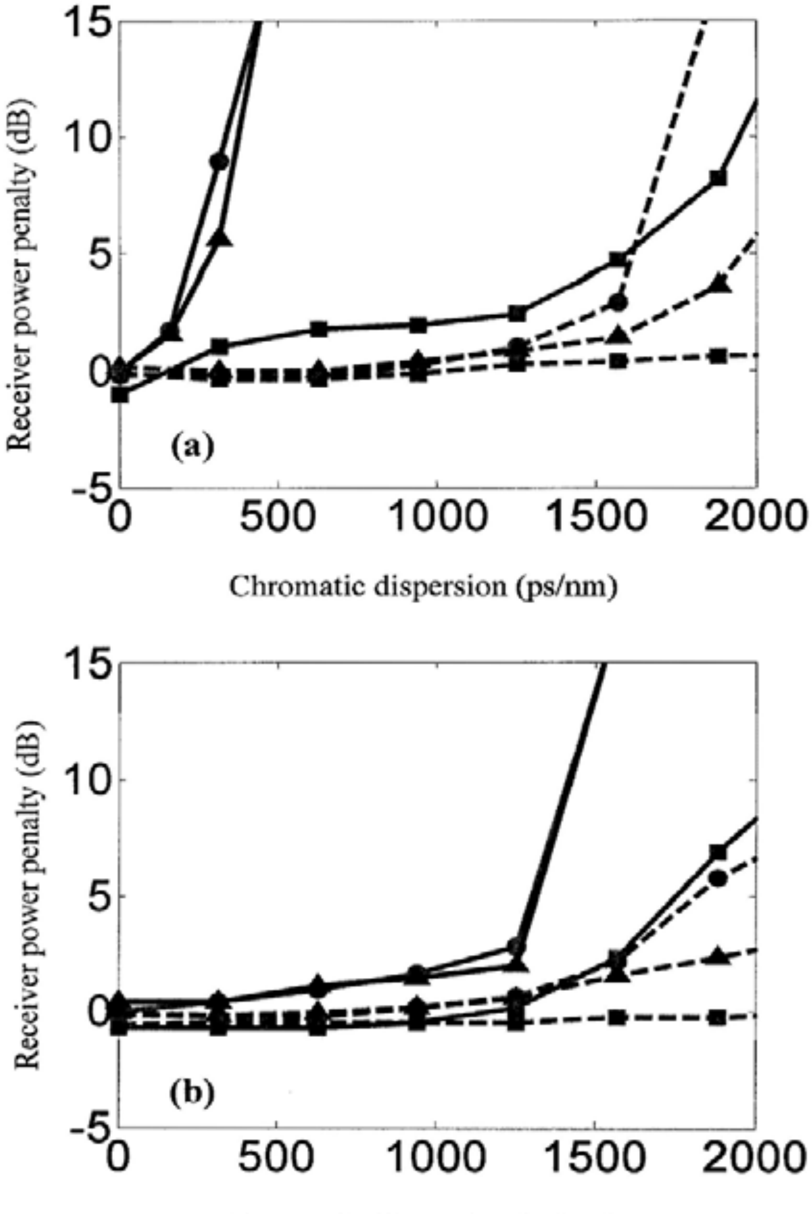

Fig. 2.14: Receiver power penalty versus CD by using conventional detection (circles), MLSE for the ASK and DPSK tributaries separately (triangles), and J-MLSE (squares) at ER of 4.9 dB when the DPSK tributary is generated by (a) PM, and (b) MZM. The solid lines and the dashed lines represent the ASK tributary and the DPSK tributary of the ASK/DPSK signal respectively.

2.1.2.4. Principle of DF-J-MLSE

Although J-MLSE exploits the correlation information between the detected ASK and DPSK signals and can improve the CD tolerance of the ASK-DPSK signal significantly, a J-MLSE has higher implementation complexity which is proportional to $2^{2\times(m+1)}$, whereas a conventional MLSE's complexity is proportional to 2^{m+1}, where m is the MLSE's or J-MLSE's memory length. Therefore, we will further propose a novel MLSE structure, DF-J-MLSE, for CD compensation in ASK/DPSK modulation format. We show that DF-J-MLSE has the same implementation complexity as a conventional MLSE while preserving the overall CD tolerance of the ASK/DPSK signal by the original J-MLSE.

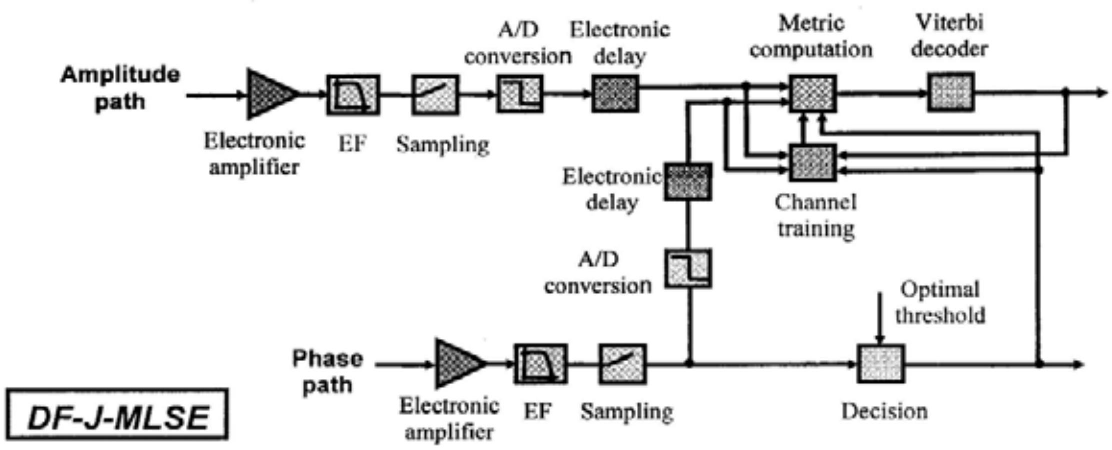

Fig. 2.15: Structure of the proposed DF-J-MLSE.

Fig. 2.15 shows the structure of the proposed DF-J-MLSE. In the simulation, the ER of the ASK tributary was set at 4.9 dB. The 10-Gbit/s ASK and DPSK data trains both consisted of 500,000 raised-cosine shaped bits with 40 samples per bit. The detected ASK and DPSK signals were filtered by 7-GHz 4^{th}-order Bessel EFs, and sampled.

For the ASK tributary, because its intrinsic transmission limitation is from its interaction with the DPSK tributary, therefore, only the joint MLSE structure which exploits the information of both ASK and DPSK tributaries can improve its CD tolerance. The detected ASK and DPSK signals are A/D converted with resolution of

5 bits and utilized in the channel training and the metrics computation. The metric, $PM(b_{ASK,n})$, is:

$$PM(b_{ASK,n}) = PM(b_{ASK,n-1}) - \sum_{i}\sum_{t_j}\log(p(I_i(t_j) \mid b_{ASK,n-m},\ldots,b_{ASK,n},b_{DPSK,n-m},\ldots,b_{DPSK,n})) \quad (2.6)$$

where i is ASK or DPSK. t_j is the sampling phase. For two samples per bit, $t_j=(n-m/2)T$ or $(n+1/2-m/2)T$. $b_{i,n}$ and $p(I_i(t_j) \mid b_{ASK,n-m},\ldots,b_{ASK,n}, b_{DPSK,n-m},\ldots,b_{DPSK,n})$ are the n^{th} ASK or DPSK logical data and the probability of the sampled ASK or DPSK signal value at time t_j given the logical data $b_{ASK,n-m},\ldots,b_{ASK,n}$, $b_{DPSK,n-m},\ldots,b_{DPSK,n}$, respectively. m is the memory length. The initial metrics in the channel training table are obtained using nonparametric histogram method by a 200,000-bit training sequence. Notice that in (1), different from conventional J-MLSE, the logical data $b_{DPSK,n-m},\ldots,b_{DPSK,n}$ are obtained not by Viterbi decoding but from the feedback of the DPSK tributary. Therefore, the metric number of the DF-J-MLSE is only 2^{m+1}, rather than $2^{2\times(m+1)}$. In this section, m is set to be 2. Therefore, DF-J-MLSE has 8 metrics, only one eighth of that of a conventional J-MLSE.

On the other hand, because the overall CD tolerance of the ASK/DPSK is not limited by the DPSK tributary, electronic devices for CD compensation of the DPSK tributary can be saved. The DPSK tributary data are decided using optimal threshold detection and fed back into a J-MLSE structure, which is imperative for effective CD compensation of the ASK tributary.

The system is assumed thermal-noise limited. The performance is evaluated in terms of receiver power penalty at BER of 10^{-4}.

2.1.2.5. Performance of DF-J-MLSE

Firstly, we investigate why DF-J-MLSE is effective for CD compensation in ASK/DPSK modulation format. We observe the results in Fig. 2.14. From Fig. 2.14, it is shown that for the ASK tributary (solid), irrespective of the generation methods (PM or MZM) of the DPSK tributary and the number of sample per bit, only the

J-MLSE structure which also exploits the information of the DPSK tributary is able to improve its CD tolerance. In contrast, the CD tolerance of the DPSK tributary using conventional optimal threshold detection is much better than that of the ASK tributary using conventional optimal threshold detection. It is even better than or comparable to that of the ASK tributary using the original J-MLSE method, except for the cumulative CD larger than 1600 ps/nm in Fig. 2.14(a). As a result, electronic devices for CD compensation of the DPSK tributary can be saved. The DPSK tributary data are decided using conventional optimal threshold detection and fed back into a J-MLSE structure, which is imperative for effective CD compensation of the ASK tributary as shown before. The feedback from the DPSK tributary eliminates the need of logical data estimation of the DPSK tributary in the J-MLSE, thus exponentially reducing the J-MLSE's complexity. On the other hand, the decision errors of the DPSK tributary are also fed back to the ASK tributary and may degrade the performance of the DF-J-MLSE. To investigate such error propagation effect, we have additional simulation where the DF-J-MLSE is operated by feeding back the original DPSK tributary data without errors. The result of this simulation shows that without error propagation effect, the performance of the ASK tributary under the DF-J-MLSE is almost the same as that under the original J-MLSE in Fig. 2.14, irrespective of the generation methods (PM or MZM) of the DPSK tributary and the number of sample per bit. Fig. 2.16 shows the receiver power penalties versus CD by using conventional optimal threshold detection (circles), and DF-J-MLSE (triangles) with error propagation effect when (a) the DPSK tributary is generated by PM; and (b) the DPSK tributary is generated by MZM. The solid lines and the dashed lines represent the ASK tributary and the DPSK tributary, respectively. By comparing Fig. 2.14 and Fig. 2.16, it is shown that except for the cumulative CD larger than 1600 ps/nm in Fig. 2.16(a), the performance of the ASK tributary under the DF-J-MLSE in Fig. 2.16 is almost the same as that under the original J-MLSE in Fig. 2.16. Therefore, error propagation effect is negligible except for the cumulative CD larger than 1600 ps/nm in Fig. 2.16(a). Therefore, DF-J-MLSE is an effective electronic device with simple implementation to extend the transmission reach of the ASK/DPSK signal.

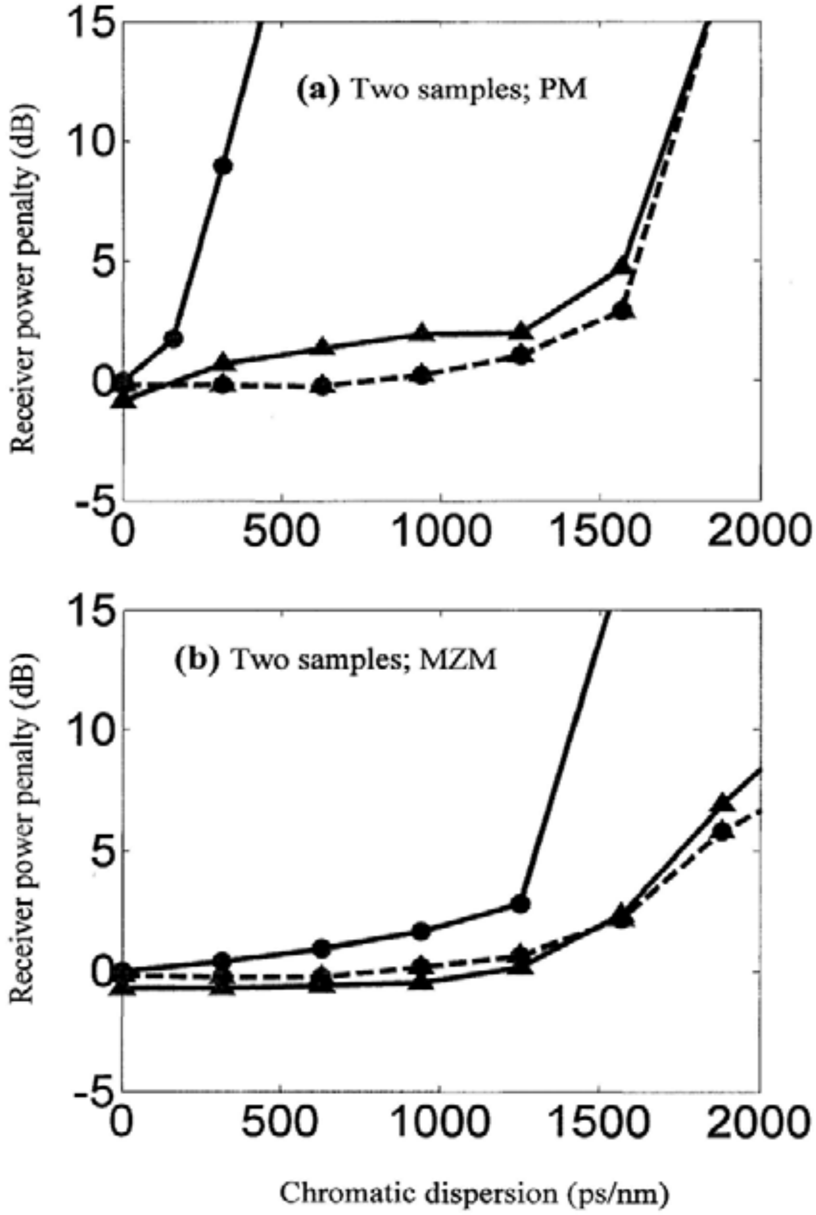

Fig. 2.16: Receiver power penalties versus CD by using conventional optimal threshold detection (circles), and DF-J-MLSE (triangles) with error propagation effect when (a) the DF-J-MLSE is two samples per bit and the DPSK tributary is generated by PM; and (b) the DF-J-MLSE is two samples per bit and the DPSK tributary is generated by MZM. The solid lines and the dashed lines represent the ASK tributary and the DPSK tributary, respectively.

2.1.2.6. Summary

In summary, we determine the fundamental impairment mechanism in the CD-limited hybrid ASK/DPSK orthogonal modulation format. It is found that the transmission distance of the ASK/DPSK signal is limited by the ASK tributary and the intrinsic limitation mechanism is from the interaction between the ASK and DPSK tributaries. Therefore, conventional MLSE which only considers intra-tributary interference of the two tributaries separately cannot improve the overall CD tolerance of the ASK/DPSK signal. J-MLSE makes full use of the correlation information between the two tributaries and is numerically shown to improve not only the back-to-back receiver sensitivity but also the CD tolerance of the ASK/DPSK signal significantly. J-MLSE has a higher implementation complexity. We further propose a novel DF-J-MLSE which reduces the implementation complexity of the J-MLSE for the ASK tributary from $2^{2\times(m+1)}$ to 2^{m+1}. We have numerically shown that, with the reduced complexity the same as that of a MLSE, DF-J-MLSE can still achieve the same performance as that by the J-MLSE method and provide twofold increment of the overall CD tolerance for the ASK-DPSK signal at 1-dB receiver power penalty.

2.1.3. 3-Chip DQPSK J-MLSE for CD and PMD Compensation

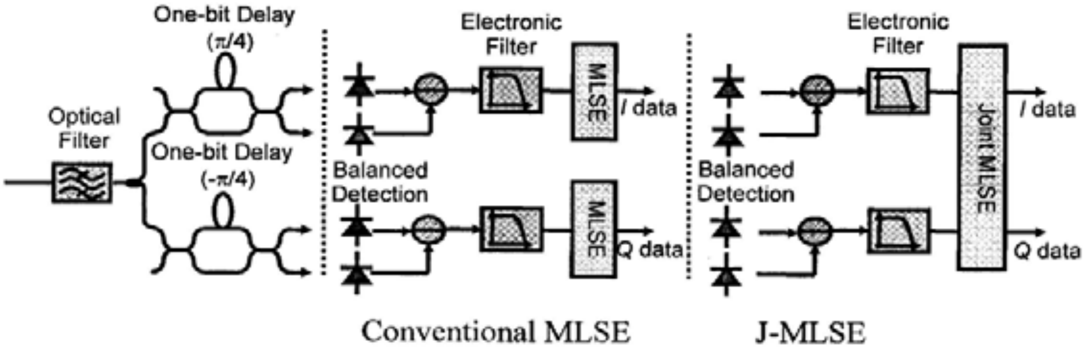

Fig. 2.17: Structure of conventional MLSE and J-MLSE

DQPSK has recently attracted much attention for high-speed optical transmission due to its better spectral efficiency and higher tolerance to CD and PMD compared to DPSK format [123]. To enhance the transmission reach of the DQPSK signal, a design of electronic equalizer was investigated, as shown in Fig. 2.17 [106]. It was shown that separate equalization of the two tributaries of the DQPSK signal provides limited CD tolerance improvement. J-MLSE, which exploits the samples of the two DQPSK's tributaries simultaneously, can significantly improve the CD tolerance. In this section, we investigate our proposed novel 3-chip DQPSK J-MLSE for CD and PMD compensation. The proposed method exploits the phase difference between not only the adjacent bits but also the bits that have one bit slot apart in optical domain and subsequently uses the detected information simultaneously for data sequence estimation in electrical domain. 3-chip DQPSK J-MLSE significantly outperforms conventional MLSE and conventional J-MLSE in CD and PMD compensation. We show that the proposed scheme provides twofold CD tolerance enhancement compared to conventional J-MLSE and exhibits 0.8-dB penalty for 100-ps DGD at 10 Gsym/s.

2.1.3.1. Principle of 3-Chip DQPSK J-MLSE

Fig. 2.18 shows the simulation model and the structure of the proposed 3-chip DQPSK J-MLSE. A continuous wave light is first modulated to phase 0 or π by a dual-drive MZM and then modulated by a PM with a modulation depth of $\pi/2$. Data 1 and data 2 are both 10 Gbit/s and consist of 500,000 raised-cosine shaped bits with 40 samples per bit. The generated DQPSK signal is launched into a piece of fiber where the signal is split into two orthogonal polarization modes with γ=0.5 being the relative power in the fast principal state of polarization. The signal degradation sources, CD and PMD, are included. At the receiver, the signal is optically pre-amplified and filtered by a 50-GHz Gaussian-shaped OBPF. Optical noise from optical preamplifier is modeled as complex additive white Gaussian noise with the power spectral density of N_0 for each polarization component.

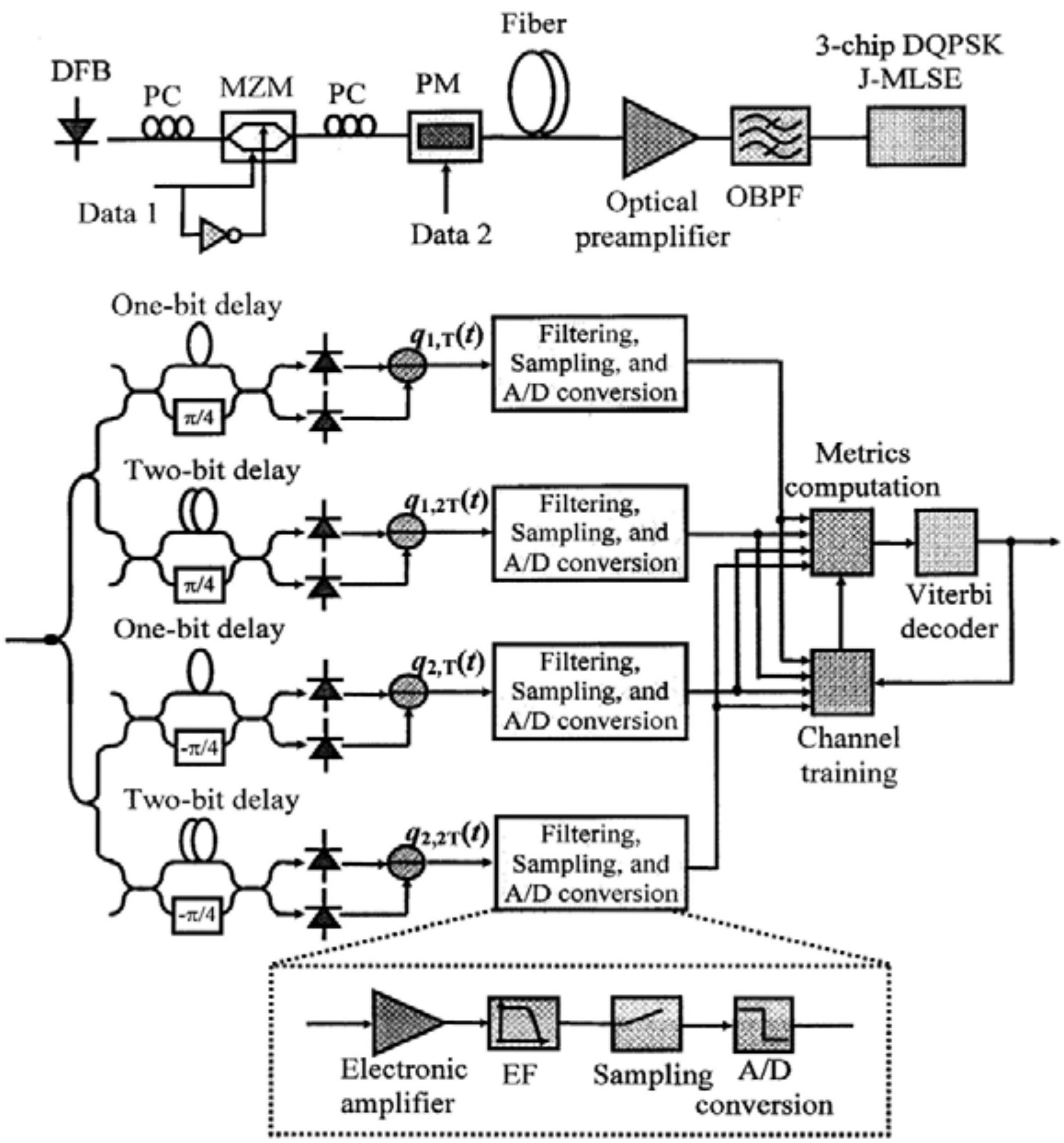

Fig. 2.18: Simulation model and the structure of the proposed 3-chip DQPSK J-MLSE

3-chip DQPSK J-MLSE demodulates the two tributaries of the DQPSK signal by using DIs with π/4 and -π/4 phase shift, respectively. For each tributary, two DIs with one-bit delay and two-bit delay are employed to exploit the phase difference between both the adjacent optical bits and the bits that have one bit slot apart [116]. Four differentially detected signals, $q_{1,T}(t)$, $q_{1,2T}(t)$, $q_{2,T}(t)$, and $q_{2,2T}(t)$ are electronically amplified, filtered by 4th-order Bessel EFs, and sampled. A/D conversion has 5-bit resolution. The samples of the four branches are simultaneously exploited in the channel training and metrics computation. The metric of 3-chip DQPSK J-MLSE is:

$$PM(b_k) = PM(b_{k-1}) - \sum_{i=1}^{2}\sum_{r=1}^{2}\sum_{t_j} \log(p(q_{i,rT}(t_j) \mid b_{k-m},...,b_k)) \tag{2.7}$$

where t_j is the sampling phase. For one sample per bit, $t_j=(k-m/2)T$. For two samples per bit, $t_j=(k-m/2)T$ or $(k+1/2-m/2)T$. b_k and $p(q_{i,rT}(t_j) \mid b_{k-m},\ldots,b_k)$ are the k^{th} DQPSK logical data and the probability of the sampled values of $q_{i,rT}(t)$ at time t_j given the logical data $b_{k-m},\ldots,b_k$, respectively. m is the memory length and is assumed to be 2. The initial metrics in the channel training table are obtained using nonparametric histogram method by a 200,000-bit training sequence. Because 4^{m+1} metrics have to be calculated after the detection of each bit and each metric requires the sum of two input branches, therefore, the complexity of the metrics computation is proportional to $2\times4^{m+1}$. On the other hand, the complexity of the Viterbi decoding is proportional to the state number, 4^m. The performance is evaluated in terms of required E_b/N_0 to achieve BER of 10^{-4}, where E_b is the optical average power in one bit slot.

2.1.3.2. Performance of 3-Chip DQPSK J-MLSE

Fig. 2.19 shows the required E_b/N_0 (dB) versus CD without MLSE (circles), with conventional MLSE for the two tributaries separately (triangles), with J-MLSE (squares), and with 3-chip DQPSK J-MLSE (diamonds) in the cases of (a) one sample per bit; and (b) two samples per bit. From the figure, it is shown that separate conventional MLSE for the two tributaries (triangles) provides limited CD tolerance improvement irrespective of sample number per bit. J-MLSE exploits the correlation information between the two DQPSK's tributaries and can effectively improve the CD tolerance. At E_b/N_0 of 18 dB, the CD tolerance by using one- and two-sample per bit J-MLSE are 1000 and 1600 ps/nm respectively. On the other hand, 3-chip DQPSK J-MLSE significantly outperforms conventional MLSE and conventional J-MLSE. At E_b/N_0 of 18 dB, the proposed scheme enhances the CD tolerance to 1800 ps/nm and 3000 ps/nm for one and two samples per bit, respectively. These values are twice of those by using conventional J-MLSE.

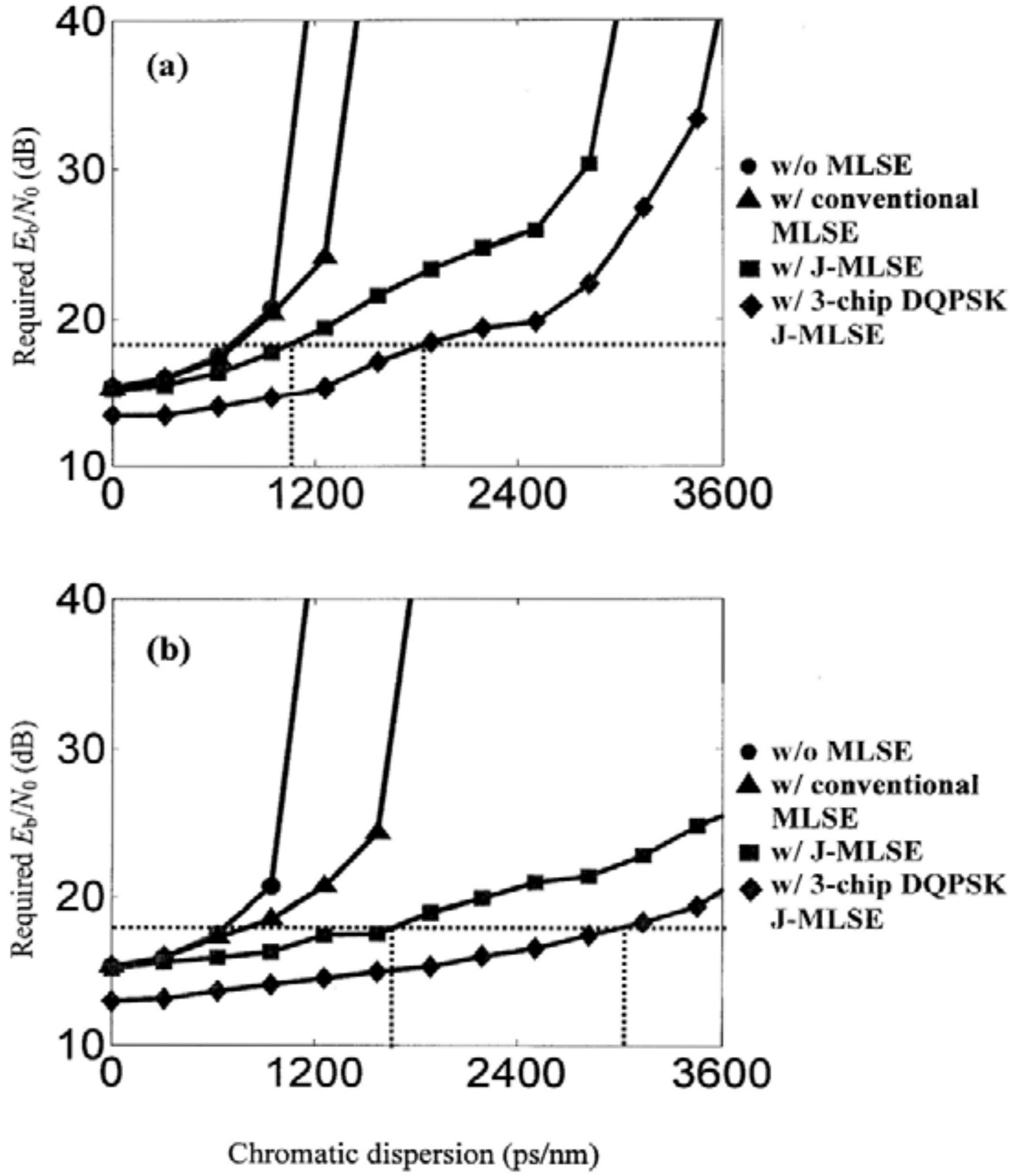

Fig. 2.19: Required E_b/N_0 versus CD when the MLSE, J-MLSE, and the proposed 3-chip DQPSK J-MLSE are (a) one sample per bit; and (b) two samples per bit. Circles, triangles, squares, and diamonds represent the cases without MLSE, with conventional MLSE for the two tributaries separately, with J-MLSE (squares), and with 3-chip DQPSK J-MLSE

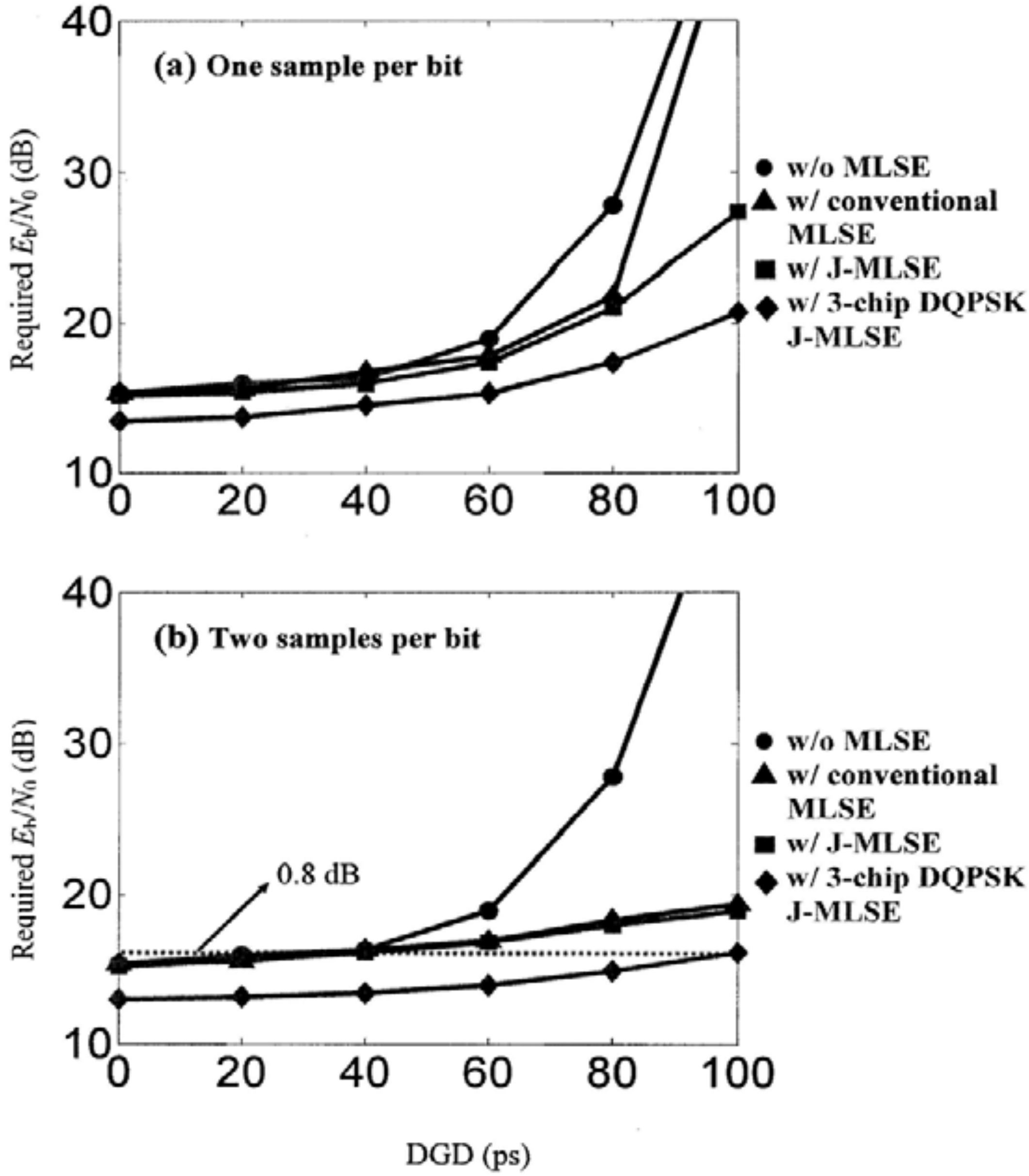

Fig. 2.20: Required E_b/N_0 versus DGD when the MLSE, J-MLSE, and the proposed 3-chip DQPSK J-MLSE are (a) one sample per bit; (b) two samples per bit. Circles, triangles, squares, and diamonds represent the cases without MLSE, with conventional MLSE for the two tributaries separately, with J-MLSE (squares), and with 3-chip DQPSK J-MLSE

Fig. 2.20 shows the required E_b/N_0 versus DGD without MLSE (circles), with conventional MLSE for the two tributaries separately (triangles), with J-MLSE (squares), and with 3-chip DQPSK J-MLSE (diamonds) in the cases of (a) one sample per bit; and (b) two samples per bit. From the figure, it is shown that for all electronic equalization methods, two samples per bit significantly outperform one sample per bit. For two samples per bit, conventional MLSE and conventional J-MLSE have similar performance of PMD compensation, with 4-dB and 3.6-dB E_b/N_0 penalty for 100-ps DGD respectively. In comparison, the proposed 3-chip DQPSK J-MLSE exhibits only 0.8-dB E_b/N_0 penalty for 100-ps DGD.

2.1.3.3. Summary

In summary, we have proposed a novel 3-chip DQPSK J-MLSE for CD and PMD compensation. The proposed scheme significantly outperforms conventional MLSE and conventional J-MLSE. We show that 3-chip DQPSK J-MLSE provides twofold CD tolerance enhancement compared to conventional J-MLSE and exhibits 0.8-dB E_b/N_0 penalty for 100-ps DGD at 10 Gsym/s. Therefore, it is a promising technique to extend the transmission reach of the DQPSK format for high-speed optical transmission.

2.1.4. 4-ASK MLSE for CD Compensation

4 amplitude shift keying (4-ASK) is a promising cost-effective spectral-efficient modulation format to extend the transmission capacity. By operating at only half of the bit rate, 4-ASK not only improves the tolerance to CD compared to on off keying format [13], but also alleviates the speed limitation of electrical and optical components. 4-ASK signal only requires one optical modulator and receiver for signal generation and detection. Therefore, such format is more cost-effective than DQPSK and ASK/DPSK orthogonal modulation. Furthermore, it can also be coded and decoded all optically, as will be discussed in Chapter 4.

However, due to the increased number of levels, 4-ASK format suffers from the OSNR degradation. Furthermore, such modulation format is sensitive to ISI from optical filtering, electronic filtering, and CD, which may weaken the superior CD tolerance of 4-ASK over binary coding. Therefore, accurate optimizations of optical/electronic receiver bandwidth and the multilevel spacing are required to reach the fundamental OSNR-limited performance bound.

In the first part of this section, we will investigate the optimal optical/electronic receiver bandwidth and multilevel spacing of 4-ASK format. We will show the superior dispersion tolerance of such format compared to the OOK format. We find that the optimal level spacing of 4-ASK changes with the CD values and improper level-spacing design leads to significant CD tolerance reduction.

As the CD in optical networks may change frequently due to the time-varying effects of the installed fibers and different routing paths, the level-spacing optimization of the 4-ASK signal is difficult in CD-varying systems. In the second part of this section, we propose to use MLSE for 4-ASK signal detection. It is shown that MLSE can effectively alleviate the sensitivity of CD tolerance to level spacing, therefore, relax the difficulty of level-spacing optimization. By using MLSE, the CD tolerance of the 4-ASK signal is significantly enhanced by at least a factor of two.

2.1.4.1. Optimization of Optical/Electronic Filter Bandwidth and Level Spacing

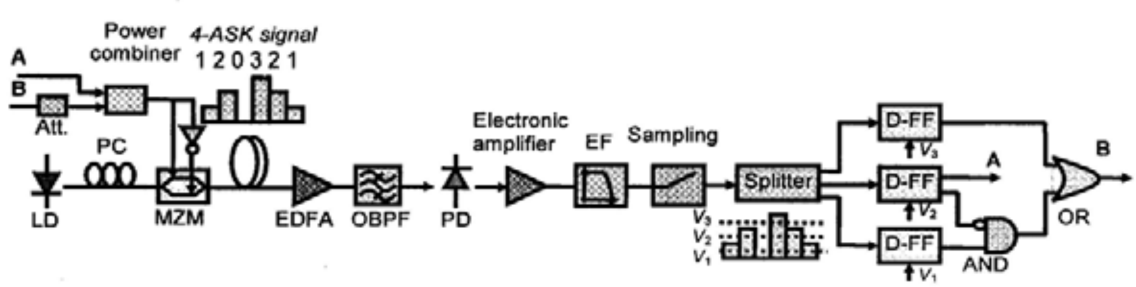

Fig. 2.21: Schematic diagram of system model

Fig. 2.21 shows the system model. 10-Gs/s 4-ary electrical signal is generated by combining two binary sources, A and B, using a power combiner. Attenuator is used before the source B to adjust the level spacing of the 4-ASK signal. A continuous wave light is modulated by the 4-ASK electrical signal using a MZM. The generated optical 4-ASK signal is fed into a piece of fiber where CD is introduced. At the receiver, the signal is optically pre-amplified, filtered by a Gaussian-shaped OBPF and detected. After O-E conversion, the electrical 4-ASK signal is amplified, filtered by a 4^{th}-order Bessel EF, sampled, and decoded.

Assume $I(t_n;\ a_{n-m},\dots,a_n)$, where a_n is the present logic data ($0 \le a_n \le 3$), is the detected electrical 4-ASK signal with t_n being the sampling time and m being the considered bit number of ISI, we can derive:

$$\begin{aligned} I(t_n;a_{n-m},\dots,a_n) &= (R|E_s(t;a_{n-m},\dots,a_n)|^2 \otimes h_e(t))\Big|_{t=t_n} + \boldsymbol{n}_{opt}^{T*}\boldsymbol{v}(t_n;a_{n-m},\dots,a_n) + \boldsymbol{v}^{T*}(t_n;a_{n-m},\dots,a_n)\boldsymbol{n}_{opt} + \boldsymbol{n}_{opt}^{T}\boldsymbol{Q}\boldsymbol{n}_{opt}^{*} \\ &= I_{sig}(t_n;a_{n-m},\dots,a_n) + \boldsymbol{z}_{opt}^{T*}\boldsymbol{b}(t_n;a_{n-m},\dots,a_n) + \boldsymbol{b}^{T*}(t_n;a_{n-m},\dots,a_n)\boldsymbol{z}_{opt} + \boldsymbol{z}_{opt}^{T}\boldsymbol{\Lambda}\boldsymbol{z}_{opt}^{*} \end{aligned} \tag{2.8}$$

where R, $E_s(t,\ a_{n-m},\dots,a_n)$ and $h_e(t)$ are the responsivity of the photo-detector, the optical 4-ASK signal field after the OBPF, and the impulse response of the EF, respectively. * stands for the conjugate. $\boldsymbol{n}_{opt}$ is a $2M$+1 column vector whose components are $n_{opt,\ p-M-1}$, $1 \le p \le 2M+1$, where $n_{opt,\ p-M-1}$ are the coefficients of the Karhunen-Loeve (KL) expansion for the ASE noise and are independent Gaussian variables with zero mean and the variances of the in-phase and quadrature components being $N_0/(2T_0)$. The parameters M and T_0 evaluate the bandwidth of the OBPF and the overall impulse response duration of the optical and the electrical filter, respectively. $\boldsymbol{v}(t_n;\ a_{n-m},\dots,\ a_n)$ is a $2M$+1 column vector whose p^{th}, $1 \le p \le 2M+1$, component is

$$RH_0{}^*((p-M-1)/T_0)\cdot((E_s(t;a_{n-m},\dots,a_n)\exp(-2\pi j(p-M-1)t/T_0))\otimes h_e(t))\big|_{t=t_n} \tag{2.9}$$

where $H_0(f)$ is the transfer function of OBPF. $\boldsymbol{Q}$ is a $(2M+1)\times(2M+1)$ matrix whose p^{th}-row, q^{th}-column element is:

$$RH_0((p-M-1)/T_0)H_0{}^*((q-M-1)/T_0)\cdot(\exp(2\pi j(p-q)t/T_0)\otimes h_e(t))\big|_{t=t_n} \tag{2.10}$$

where $1 \le p,q \le 2M+1$. $\boldsymbol{Q}$ is Hermitian symmetric, therefore its eigenvalues λ_p, $1 \le p \le 2M+1$, are real and the eigenvectors are orthogonal, e.g. $\boldsymbol{Q}=\boldsymbol{U}\boldsymbol{\Lambda}\boldsymbol{U}^{T*}$ with $\boldsymbol{\Lambda}=\mathrm{diag}\{\lambda_p\}$ and $\boldsymbol{U}$ being an orthogonal matrix. $\boldsymbol{z}_{xopt}$ is $\boldsymbol{U}^T\boldsymbol{n}_{opt}$ and $\boldsymbol{b}_x(t_n; a_{n-m},\ldots, a_n)$ is $\boldsymbol{U}^T\boldsymbol{v}_x(t_n; a_{n-m},\ldots, a_n)$. The moment generating function (MGF) of $I(t_n;a_{n-m},\ldots, a_n)$ is obtained as:

$$M(s;a_{n-m},...,a_n)=\exp(-sI_{sig}(t_n;a_{n-m},...,a_n))\cdot\prod_{p=1}^{2M+1}\frac{\exp(s^2\left|b_p(t_n;a_{n-m},...,a_n)\right|^2 N_0/(T_0(1+s\lambda_p N_0/T_0)))}{(1+s\lambda_p N_0/T_0)} \tag{2.11}$$

where $b_p(t_n; a_{n-m},\ldots, a_n)$, $1 \le p \le 2M+1$, is the p^{th} component of $\boldsymbol{b}_x(t_n; a_{n-m},\ldots, a_n)$. BER probability can be calculated from the MGF by using saddlepoint approximation:

$$P_e=\frac{1}{4}\sum_{p=1}^{3}E_\delta\{\frac{\exp(\psi_p(s_{p,0};a_{n-m},...,a_{n-1},a_n=p-1))}{\sqrt{2\pi\psi_p''(s_{p,0};a_{n-m},...,a_{n-1},a_n=p-1)}}+\frac{\exp(\psi_p(s_{p,1};a_{n-m},...,a_{n-1},a_n=p))}{\sqrt{2\pi\psi_p''(s_{p,1};a_{n-m},...,a_{n-1},a_n=p)}}\} \tag{2.12}$$

where E_δ is the ensemble average with δ being the set of all possible $[a_{n-m}\ldots a_{n-1}]$. $\psi_p(s; a_{n-m},\ldots, a_n)=\ln(M(s; a_{n-m},\ldots, a_n))+sV_p-\ln|s|$, $p=1,2,3$. $s_{p,0}$ and $s_{p,1}$ are the negative and positive saddlepoints of $\psi_p(s; a_{n-m},\ldots, a_n)$, respectively. The optimal thresholds V_p, $p=1,2,3$, were determined numerically in practical operation.

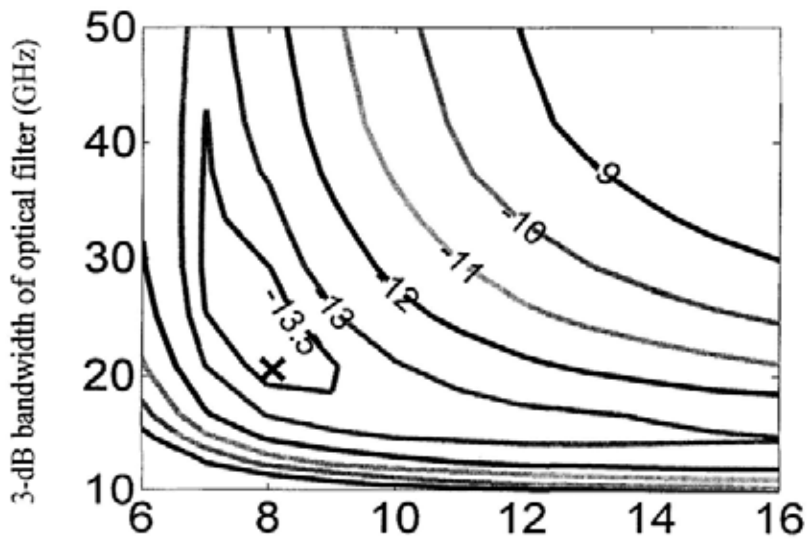

Fig. 2.22: BER versus optical and electrical filter bandwidth at E_b/N_0 of 28dB

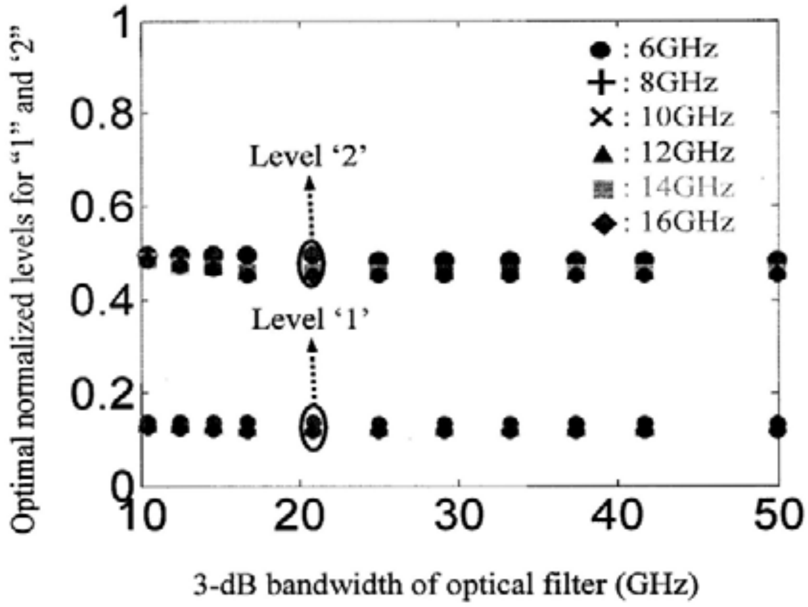

Fig. 2.23: Optimal normalized levels for "1" and "2" versus optical and electrical filter bandwidth at E_b/N_0 of 28dB

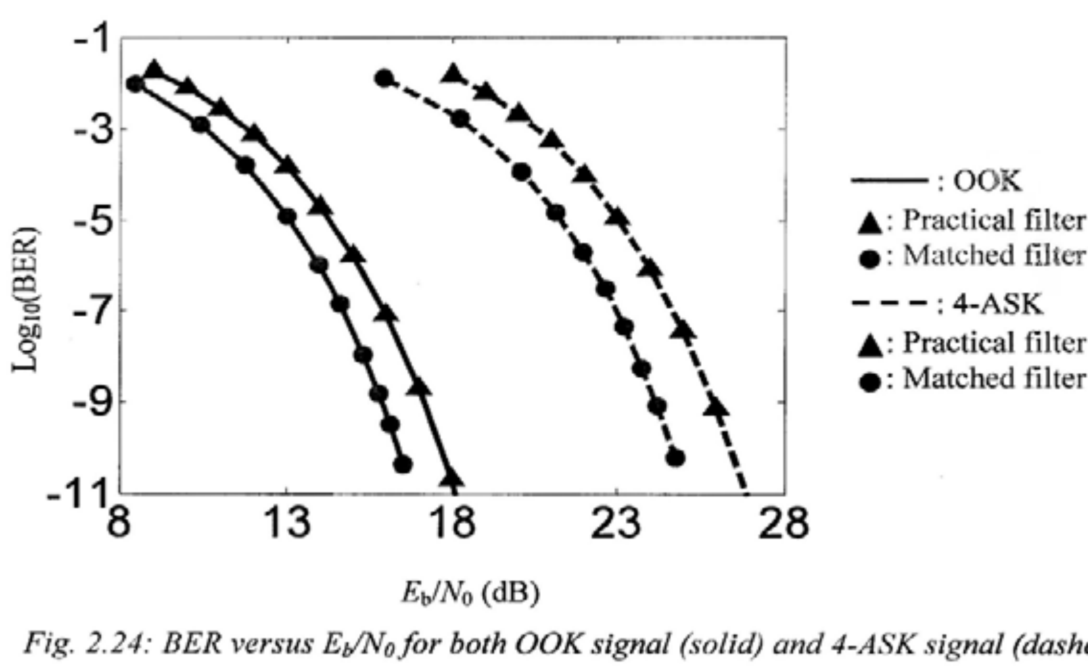

Fig. 2.24: BER versus E_b/N_0 for both OOK signal (solid) and 4-ASK signal (dashed) under the matched filter (circles) and the optimal practical filter (triangles)

Fig. 2.22 shows the $\log_{10}$(BER) versus the optical and the electrical receiver bandwidth at E_b/N_0 of 28 dB for 20Gbit/s 4-ASK signal (10Gbit/s symbol rate), where

E_b is the average power in one bit slot. In the investigation, the optical filter is chosen as Gaussian-shaped OBPF and the electrical filter is the 4^{th}-order Bessel filter. The multilevel spacing is optimized for each optical/electrical bandwidth pair. The point with the lowest BER in the figure is marked by '×'. From the figure, it is shown that the optimal optical and electrical receiver bandwidths are 8 GHz and 20 GHz respectively. At those receiver bandwidths, a balance between the noise and the ISI is achieved. Fig. 2.23 shows the optimal power magnitude for level '1' and '2' normalized by that of level '3' in 4-ASK signals. From the figure, it is observed that the optimal multilevel spacing is not sensitive to the bandwidth of and the OBPF and EF by using Gaussian-shaped OBPF and 4^{th}-order Bessel filter. Additional results show that when Butterworth EF is employed, the optimal level spacing is much sensitive to the electronic filter bandwidth. From the figure, it is also shown that under the optimal optical and electrical filter bandwidth, the optimal level spacing is around 0:1:4:9. To find out the OSNR-limited performance bound of 4-ASK signal, the $\log_{10}$(BER) versus E_b/N_0 for both the matched filter (circles) and the optimal practical filter (triangles) is shown in Fig. 2.24. The BER curves of 20Gbit/s OOK signal (solid) are also depicted in the figure for comparison. For the OOK signal under matched filter, the required photons per bit to achieve 10^{-9} is 38 (~ 16 dB). The employment of practical filter induces additional 2-dB penalty. However, such penalty only exhibits for NRZ signals. Additional results show that the penalty by using practical filters is negligible for RZ format. The 4-ASK reduces the symbol rate by a factor of two, but at the expense of 8-dB E_b/N_0 penalty, which is equivalent to 5-dB OSNR penalty considering two times symbol rate of the OOK signal. The required back-to-back E_b/N_0 for the adopted system at BER of 10^{-4} and 10^{-9} are around 22 dB and 26 dB.

2.1.4.2. Dependency of CD Tolerance on Level Spacing without MLSE

In this subsection, the optical and electrical filter bandwidths are optimized. Fig. 2.25 shows the optimal power for level '1' and level '2' versus CD, where the optical power is normalized by that of level '3'. From the figure, it is shown that optimal level spacing changes with CD values. Because the lower eyes of the 4-ASK signal is vulnerable to CD-induced ISI, higher powers are required for level '1' and level '2' as CD value increases. However, in practice, after the initial system design, the level spacing is usually fixed regardless of CD variations. Therefore, it is desirable to find out the CD tolerance under a fixed level spacing.

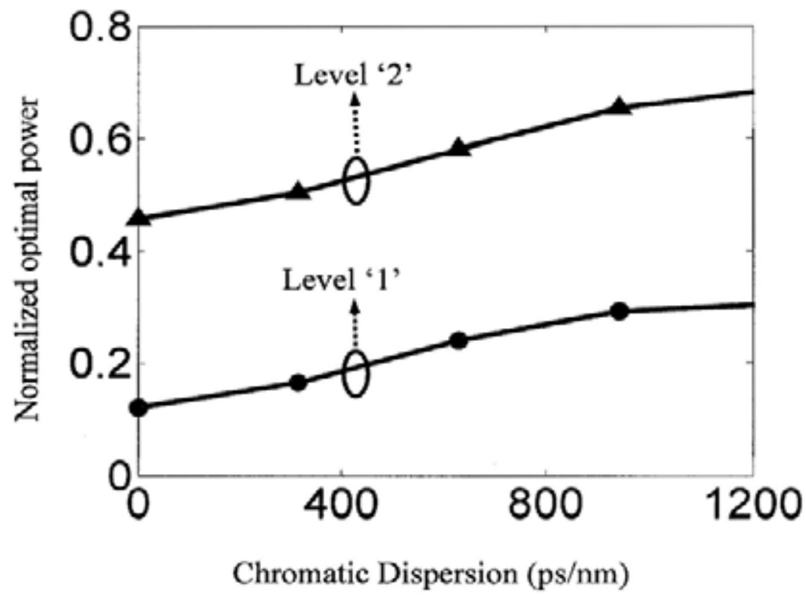

Fig. 2.25: Normalized optimal power for level '1' and level '2' versus CD at $BER=10^{-9}$. Magnitudes of level '0' and '3' are 0 and 1, respectively.

Fig. 2.26 depicts the CD tolerance of 20-Gbit/s OOK signal (solid line) and 10-Gsym/s 4-ASK signal (dashed lines) with level spacing optimized at (i) 0 ps/nm (circles), (ii) 700 ps/nm (triangles), and (iii) every CD value (diamonds) (the ideal case). It is shown that 4-ASK is more suitable for the CD-limited optical transmission than the OOK format irrespective of the level spacing design. The CD tolerance of the 4-ASK signal is strongly dependent on the level spacing design. From the figure, it is shown that the performance for case (i) is worse than that for case (ii) and (iii) when the CD values are larger than 400 ps/nm. For case (ii), the required E_b/N_0 for large CD value approaches to that with case (iii). However, compared to case (i), case (ii) has several dB's penalty for small CD values. Without MLSE, the performance trade-off for small and large CD values complicates the level-spacing optimization in CD-varying 4-ASK optical networks.

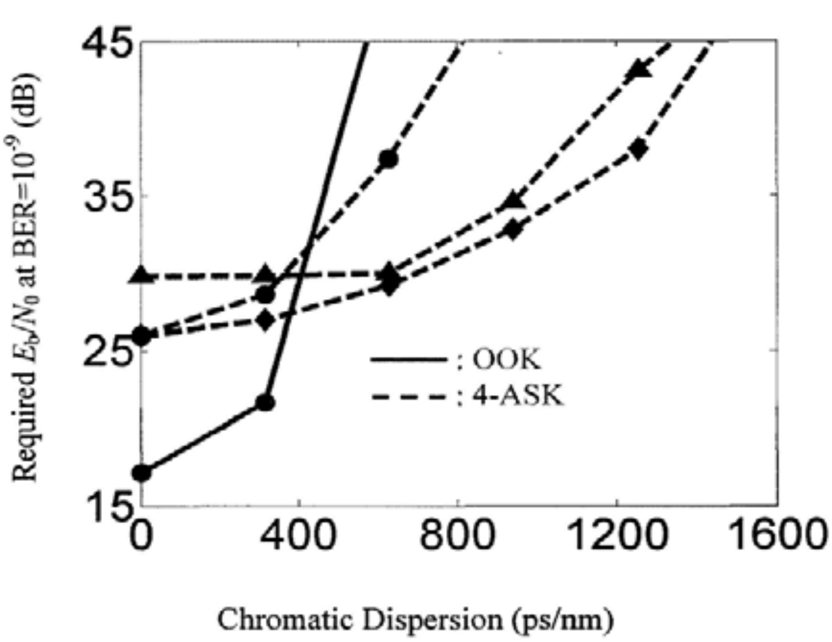

Fig. 2.26: Required E_b/N_0 versus CD for 20-Gbit/s OOK and 10-Gsym/s 4-ASK with level spacing optimized at 0 ps/nm (circles), at 700 ps/nm (triangle-ups), and at every CD value (diamonds).

2.1.4.3. Performance of MLSE for CD Compensation

Fig. 2.27 shows the system model. The generation of the 10-Gsym/s 4-ary signal is similar as Fig. 2.21. The generated optical 4-ASK signal is fed into a piece of fiber where CD is introduced. At the receiver, the signal is optically pre-amplified, filtered by a Gaussian-shaped OBPF and detected. After O-E conversion, the electrical 4-ASK signal is amplified, filtered by a 4^{th}-order Bessel EF, sampled, and decoded conventionally or by MLSE. The optical and electrical filter bandwidths are optimized and are 20 GHz and 8 GHz, respectively. A/D converter in MLSE has 5-bit resolution. MLSE is a 16-state machine and its metric, $PM(a_n)$, is:

$$PM(a_n) = PM(a_{n-1}) - \sum_{t_j} \log(p(I(t_j) \mid a_{n-m}, \ldots, a_n)) \tag{2.13}$$

For one sample per bit, $t_j=(n-m/2)T$. For two samples per bit, $t_j= (n-m/2)T$, or $(n-(m+1)/2)T$. a_n and $p(I(t_j) \mid a_{n-m}, \ldots, a_n)$ are the n^{th} 4-ASK logical data and the probability of the received signal value at $t=t_j$ given the logical data $a_{n-m}, \ldots, a_n$. m is the memory length. The initial metric of MLSE is obtained using nonparametric histogram method. The performance is evaluated in terms of required E_b/N_0 to achieve BER 10^{-4} for simulation.

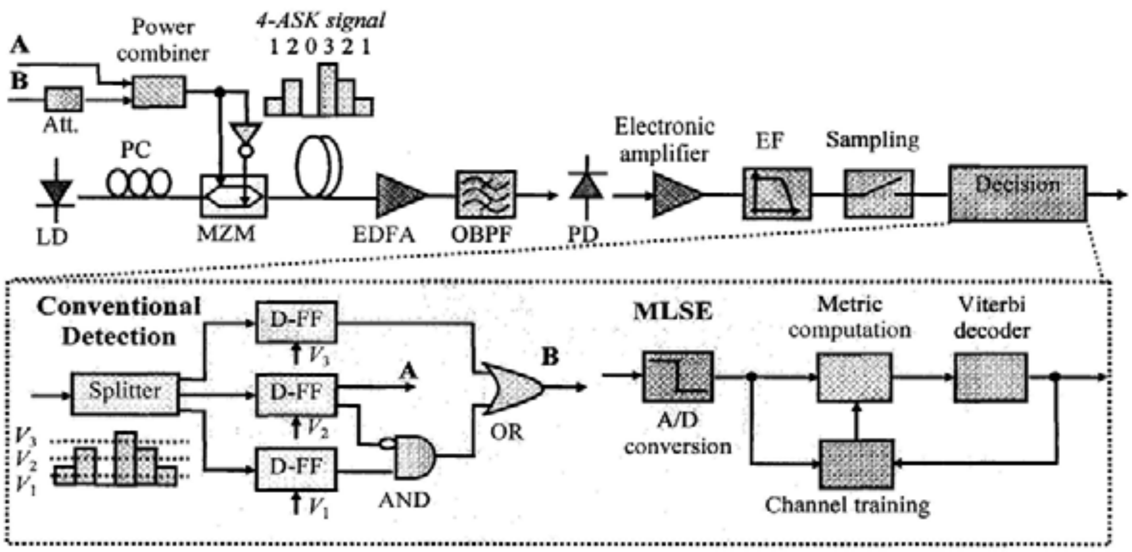

Fig. 2.27: System Model

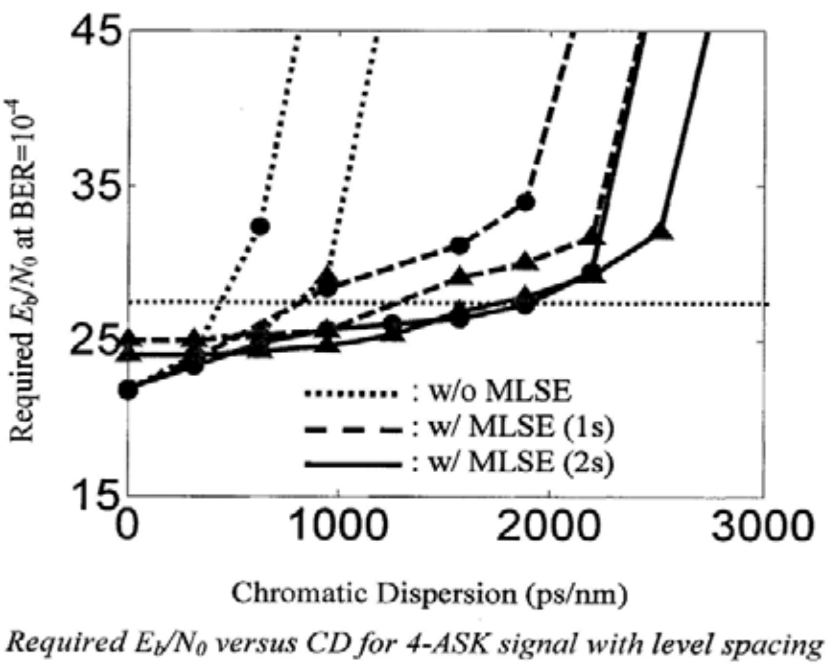

Fig. 2.28: Required E_b/N_0 versus CD for 4-ASK signal with level spacing optimized at 0 ps/nm (circles) and 700 ps/nm (triangles).

Fig. 2.28 shows the required E_b/N_0 versus CD for different level spacings without MLSE (dotted), with one-sample per bit MLSE (dashed), and with two-sample per bit MLSE (solid). Circles and triangles represent the level spacing optimized at 0 ps/nm and 700 ps/nm, respectively. From the figure, it is found that MLSE using one- or two-sample per bit can significantly enhances the CD tolerance of 4-ASK signal. For two-sample per bit MLSE, CD tolerance is improved by at least a factor of two for both level-spacing designs. Furthermore, with two-sample per bit MLSE, the back-to-back sensitivity of 4-ASK signal with level spacing optimized at 700 ps/nm is improved by 1 dB. At E_b/N_0 of 28 dB, the CD tolerances for the two different level-spacing designs are both around 2000 ps/nm, more than two times of that without MLSE. Therefore, by using two-sample per bit MLSE, the sensitivity of CD tolerance to level spacing is alleviated.

2.1.4.4. Summary

In summary, we have shown that optimal level spacing of 4-ASK signal changes with CD values and improper level-spacing design leads to significant CD tolerance reduction. As a result, level-spacing optimization is difficult in CD-varying 4-ASK optical systems. We propose MLSE for 4-ASK signal detection. It is found that MLSE can effectively alleviate the sensitivity of CD tolerance to the level spacing, thus relax the difficulty of level-spacing optimization. By using MLSE, the CD tolerance of 4-ASK format is significantly enhanced. At E_b/N_0 of 28 dB, MLSE can enhance the CD tolerance of the 4-ASK signal to 2000 ps/nm, more than two times of that without MLSE. Thus MLSE makes the cost-effective 4-ASK a promising format to extend the transmission capacity of optical networks.

2.1.5. Summary

We have designed novel MLSE structures for different advanced modulation formats. Table 1 summarizes the comparison between the existing schemes and the proposed schemes in terms of performance and complexity.

		DPSK	ASK/DPSK	DQPSK	4-ASK
The existing electronic equalization schemes		Conventional MLSE	No report (hard decision)	J-MLSE	No report (soft detection)
The proposed electronic equalization schemes		3-chip DPSK MLSE	DF-J-MLSE	3-chip DQPSK J-MLSE	4-ASK MLSE
The proposed schemes vs the existing schemes	B-B sensitivity	1.6-dB reduction	0.7-dB reduction	2.4-dB reduction	0- ~ 2-dB reduction
	CD tolerance	2.5 times	> 2 times	2 times	> 2 times
	PMD penalty at DGD=T	1.4 dB vs 4.2 dB	NA	0.8 dB vs 4.6 dB	NA
	Receiver complexity	2 times	The same	2 times	The same
	MLSE complexity	Comparable	NA	comparable	NA

Table 1: Performance improvement of our recently proposed schemes with respect to the existing schemes

In the table, T is the time period for one bit slot. The B-B sensitivity improvement of 4-ASK ranges from 0 to 2 dB with the value dependent on the level spacing design. From the table, we can find that the proposed schemes significantly outperform the existing schemes in terms of B-B sensitivity, CD and PMD tolerance, but without much complexity increase. Therefore, they are suitable for transmission impairment mitigation in long-haul/metropolitan area networks. In our future work, we will further investigate the capabilities of the proposed schemes for fiber nonlinear effects (self-phase modulation, cross-phase modulation etc.) compensation.

2.2. Novel Application of MLSE for TM Compensation and a Simple Analytical Method for MLSE Performance Evaluation

Besides CD and PMD, MLSE is capable to compensate other impairment characterized as ISI. Furthermore, a versatile and cost-effective MLSE can also achieve simultaneous distortion compensation with shared electrical devices. Hence the number and complexity of the compensation components can be reduced.

Return-to-zero (RZ) modulation format has been widely used in both long-haul optical communication systems and optical networks, including RZ format transmission, optical time-division multiplexing (OTDM), optical code-division multiple access (OCDMA) and wavelength division multiplexing passive optical networks (WDM-PON) [124]-[125]. Compared to non-return-to-zero (NRZ) format, it shows several-decibel improvement in receiver sensitivity and promises better tolerance against PMD [126]-[127].

The generation of RZ format can be implemented by using dual MZM configuration where a continuous-wave light is first carved by driving an MZM with a sinusoidal voltage at half of the bit rate and then modulated by NRZ data in the second MZM. For proper generation of the RZ signal, it is essential to locate the pulse peak in the middle of the data bit slot. However, the relative time delay of the optical and electrical devices drifts over time due to temperature variation and aging of devices, leading to timing misalignment (TM) between the pulse carver and the data modulator. To resolve the problem, several timing alignment techniques were proposed [86]-[87]. These systems, however, require an additional monitoring stage. Therefore the complexity and the cost of system implementation and maintenance are increased.

In this section, we will investigate the impact of TM on the performance of RZ systems. Our study shows that such distortion leads to ISI of the demodulated data. Therefore we propose to use MLSE for TM mitigation. Not specific to a certain type of ISI, MLSE can achieve simultaneous compensation of TM and PMD with shared electrical devices. We develop a simple theory to evaluate the performance of MLSE analytically for TM compensation without and with the presence of PMD in both OSNR limited and thermal-noise limited operation regions. The developed theory for MLSE's performance evaluation, employing Karhunen-Loeve expansion, saddlepoint approximation, and the steepest decent method, is applicable to arbitrary input signal pulse shape, optical and electrical filtering. Monte Carlo simulations are demonstrated and agree with the prediction of the theory well.

2.2.1. System Model and Principle of MLSE

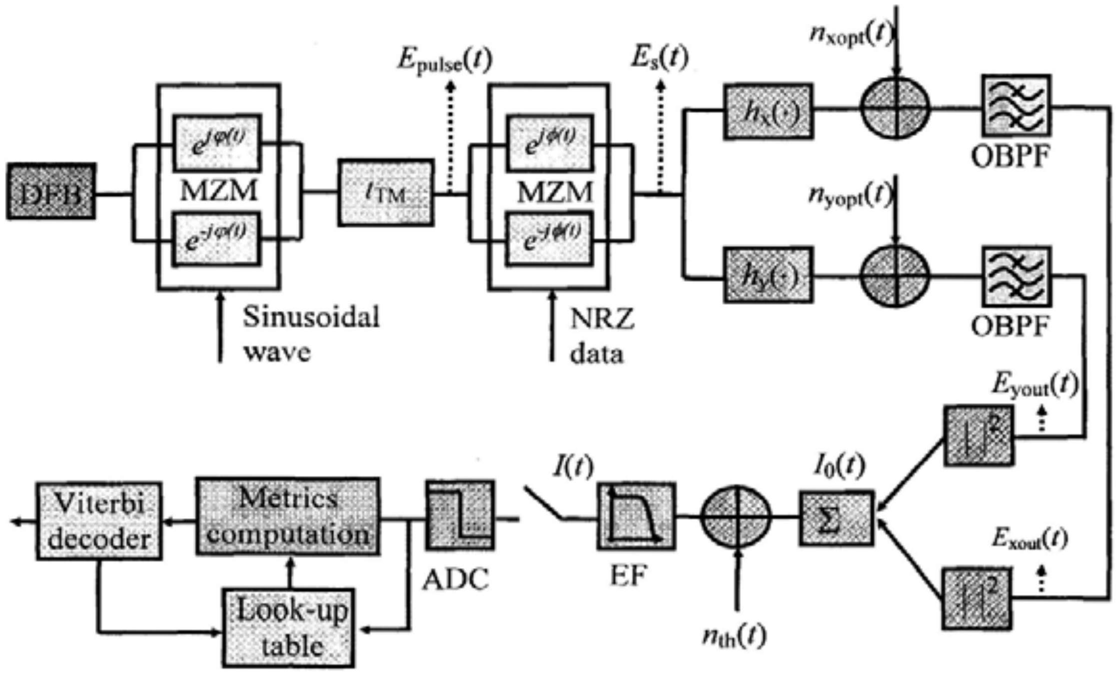

Fig. 2.29: System model in the analysis and simulations

Fig. 2.29 depicts the system model. The optical RZ pulse train $E_{\text{pulse}}(t)$ is obtained by driving the pulse carver with a sinusoidal voltage at half of the bit rate:

$$E_{pulse}(t) = E_{laser}(e^{j\varphi(t-t_{TM})} + e^{-j\varphi(t-t_{TM})})/2 = E_{laser}\cos(\frac{\pi}{2}\sin(\frac{\pi}{T}(t-t_{TM}))) \qquad (2.14)$$

where E_{laser}, $\varphi(t)$, and T are the optical field generated by the laser, the phase change in the pulse carver, and the bit period, respectively. t_{TM} is the misaligned time and is emulated by an optical delay line. The modulated signal $E_s(t)$ is obtained by feeding $E_{\text{pulse}}(t)$ into a data-driven MZM:

$$\begin{aligned} E_s(t) &= E_{pulse}(t)(e^{j\phi(t)} + e^{-j\phi(t)})/2 \\ &= E_{pulse}(t)\cos(\frac{\pi}{2}\sum_{n=0}^{\infty} a_n V_{NRZ}(t-nT) - \frac{\pi}{2}) = E_{pulse}(t)A(t) \end{aligned} \qquad (2.15)$$

where $\phi(t)$ and a_n are the phase change in the data modulator and the input logical data, respectively. $V_{\text{NRZ}}(t)$ is the raised cosine NRZ data pulse shape with α controlling the edge sharpness. Fiber transmission link is modeled as a single-input, two-output setup [81]. The initial RZ signal $E_s(t)$ is split into two orthogonal polarization modes with γ being the relative power in the fast principle state of polarization. $h_x(\gamma^{1/2}E_s(t))$ and $h_y((1-\gamma)^{1/2}E_s(t))$ denote the channel mapping of the two polarization modes and include the sources for signal degradation, e. g. PMD. Optical noises from optical amplifiers, $n_{xopt}(t)$ and $n_{yopt}(t)$, are modeled as independent additive white Gaussian noises (AWGN) with zero mean and a power spectral density of $N_0/2$ for each polarization's in-phase and quadrature components [128]. An OBPF with the impulse response of $h_o(t)$ is then employed to suppress the optical noise and yield the outputs of the transmission fiber, $E_{xout}(t)$ and $E_{yout}(t)$:

$$\begin{aligned} E_{xout}(t) &= (h_x(\gamma^{1/2}E_s(t)) + n_{xopt}(t)) \otimes h_o(t) = E_{s,x}(t) + n_x(t) \\ E_{yout}(t) &= (h_y((1-\gamma)^{1/2}E_s(t)) + n_{yopt}(t)) \otimes h_o(t) = E_{s,y}(t) + n_y(t) \end{aligned} \tag{2.16}$$

where $\otimes$ stands for the convolution operation. At the receiver, $E_{xout}(t)$ and $E_{yout}(t)$ are square-law detected and summed up to obtain the photo-current, $I_0(t)$, of the photo-detector:

$$I_0(t) = R(|E_{xout}(t)|^2 + |E_{yout}(t)|^2) \tag{2.17}$$

where R is responsivity of the photo-detector. Thermal noises $n_{th}(t)$ is also modeled as AWGN with the power spectral density of $N_{th}/2$. Finally, $I_0(t)$ is filtered by an EF with an impulse response of $h_e(t)$ before it is sampled. Assume that the sampling time for the n^{th} bit is t_n, the sampled discrete-time sequence can be written as ($I(t_0)$ $I(t_1)$… $I(t_{n-1})$ $I(t_n)$…) with:

$$I(t_n) = I(t)|_{t=t_n} = (I_0(t) \otimes h_e(t) + n_{th}(t) \otimes h_e(t))|_{t=t_n} \tag{2.18}$$

The sampled signal is A/D converted and is decoded by MLSE. The A/D conversion would introduce quantization noise, which, however, is found to be negligible for the AD conversion with more than 4-bit resolution [85]. The operation of MLSE realizes the optimal estimation of the input data sequence (a_0 a_1…a_{n-1} a_n). It requires the finding of a sequence (b_0 b_1… b_{n-1} b_n) which minimizes the metric of:

$$\begin{aligned} PM(I(t_n)) &= -\log(p(I(t_0), I(t_1), ..., I(t_{n-1}), I(t_n) \mid b_0, b_1, ..., b_{n-1}, b_n)) \\ &\approx PM(I(t_{n-1})) - \log(p(I(t_n) \mid b_0, b_1, ..., b_{n-1}, b_n)) \end{aligned} \tag{2.19}$$

where the '≈' is used instead of '=' because the assumption that $I(t_p)$, $0 \le p \le n$, are uncorrelated is not strictly satisfied in optical systems, where EF is only a noise limiting low-pass filter, instead of a whitened matched filter, in order to reduce the complexity of the MLSE front end. However, for RZ format, equation (2.19) is a near-optimal approximation because the bandwidth of EF is typically larger than the bit rate, leading to weak correlation among the values of $I(t_p)$, $0 \le p \le n$.

In practical systems, it is reasonable to assume that ISI affects a finite number of symbols, m. Therefore, $-\log(p(I(t_n)| b_0, b_1,..., b_{n-1}, b_n)) = -\log(p(I(t_n)| b_{n-m}, b_{n-m+1},..., b_{n-1}, b_n))$. MLSE can be modeled as a 2^m-state machine with state $S(b_n) = [b_{n-m}\ b_{n-m+1} \ldots b_{n-1}]$. The calculation of metric (2.19) is performed by employing the Viterbi algorithm, with an initial metric for different MLSE states in a look-up table obtained by using non-parametric histogram method.

2.2.2. Characterization of Impairments from TM and PMD

In this section, we first characterize TM as ISI and determine the parameters which influence the linear/nonlinear characteristic of TM. Then, the impairments from both TM and PMD are investigated.

2.2.2.1. TM without PMD

Firstly, we assume that the bandwidth of OBPF is sufficiently wide so that $E_{xout}(t) = \gamma^{1/2}E_s(t)$ and $E_{yout}(t) = (1-\gamma)^{1/2}E_s(t)$, therefore, $I_0(t)$ can be simplified as:

$$I_0(t) = R(\left|\gamma^{1/2}E_s(t)\right|^2 + \left|(1-\gamma)^{1/2}E_s(t)\right|^2) = R\left|E_{pulse}(t)\right|^2 A^2(t) \tag{2.20}$$

Table 2 gives the values of $A^2(t)$ and $I_0(t)$ within $-T \le t - n \times T \le 0$. Fig. 2.30(a), (b) and (c) depict $|E_{pulse}(t)|^2$, $A^2(t)$, and $I_0(t)$ for different data patterns in a 10-Gb/s RZ system, respectively. Misaligned time t_{TM}, α and R in the figures are -40 ps, 0.8 and 1, respectively. Define a notation $I_0(t; p, q)$, p, q =0, 1, which denotes the value of $I_0(t)$ for $a_{n-1}=p$ and $a_n=q$. Such kind of notation will be used throughout this section. Notice that $I_0(t;1,1)$- $I_0(t;1,0)$= $I_0(t;0,1)$- $I_0(t;0,0)$ for $-T \le (t-n \times T) \le 0$. Thus, TM would lead to linear ISI from the prior bit for negative t_{TM}. Also notice that $I(t)$ is the convolution of $I_0(t)$ and $h_e(t)$. As convolution is a linear operation, TM remains linear after electrical filtering and sampling, i.e. $I(t_n;1,1)=I(t_n;0,1)+I(t_n;1,0)$ considering $I(t_n;0,0)=0$. Similarly, a_n is corrupted by the posterior bit a_{n+1} for positive t_{TM}. In the following analysis, without loss of generality, negative misaligned time t_{TM} is assumed.

$(a_{n-1}\ a_n)$	(0 0)	(0 1)	(1 0)	(1 1)
$A^2(t)$	0	$\sin^2(\pi V_{NRZ}(t- n\times T)/2)$	$\cos^2(\pi V_{NRZ}(t- n\times T)/2)$	1
$I_0(t)$	0	$R\lvert E_{pulse}(t)\rvert^2 \times \sin^2(\pi V_{NRZ}(t- n\times T)/2)$	$R\lvert E_{pulse}(t)\rvert^2 \times \cos^2(\pi V_{NRZ}(t- n\times T)/2)$	$R\lvert E_{pulse}(t)\rvert^2$

Table 2: Values of $A^2(t)$ and $I_0(t)$, $-T \le t-n\times T \le 0$.

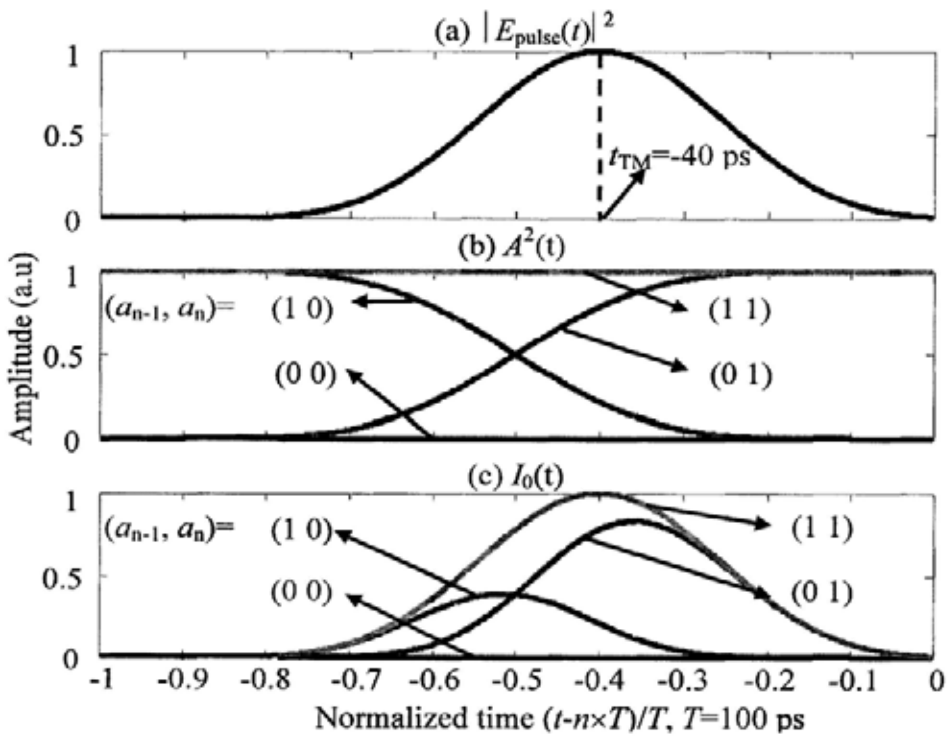

Fig. 2.30: (a) $|E_{pulse}(t)|^2$, (b) $A^2(t)$ and (c) $I_0(t)$ for different data patterns.

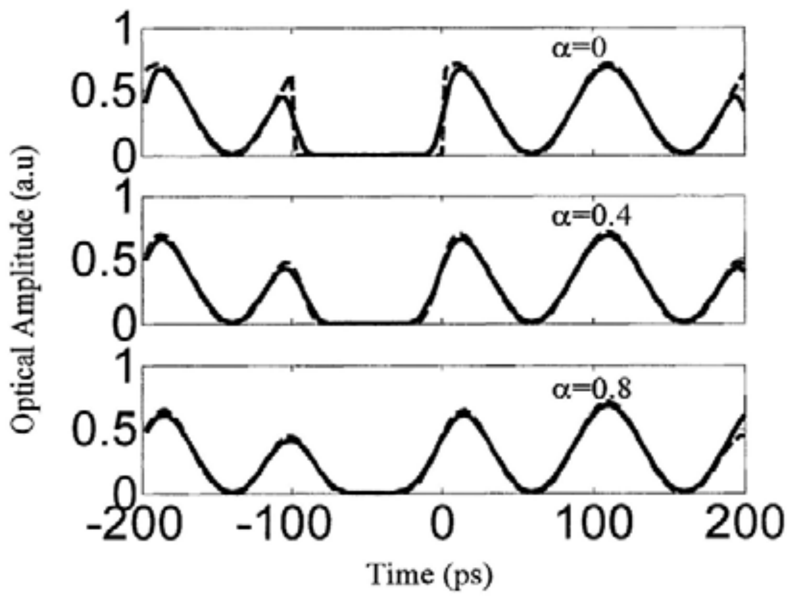

(a)

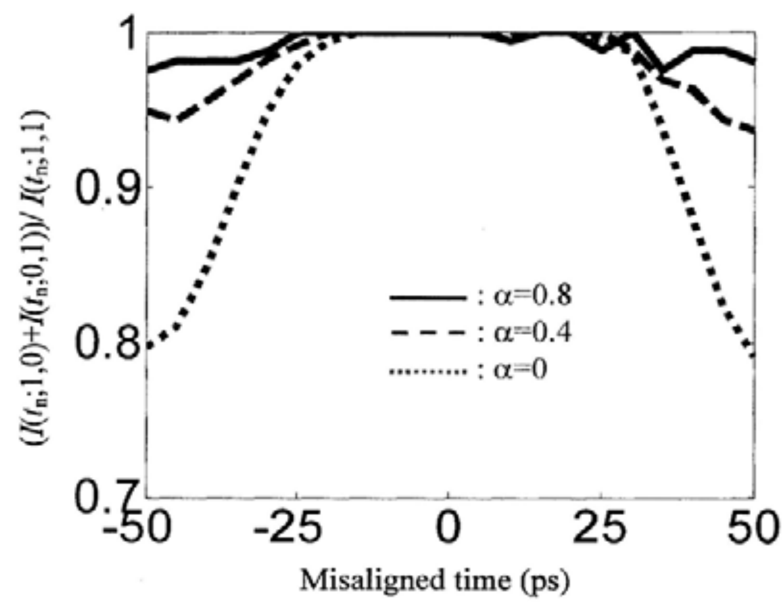

(b)

Fig. 2.31: (a) The optical signal before (dashed lines) and after (solid lines) OBPF for different NRZ data pulse shape and with misaligned time t_{TM}= -40 ps. (b) $(I(t_n;1,0)+I(t_n;0,1))/\ I(t_n;1,1)$ versus t_{TM}.

On the other hand, when OBPF-induced signal distortion is not negligible, TM is nonlinear. Fig. 2.31(a) shows the optical signal before (dashed lines) and after (solid lines) OBPF for different NRZ data pulse shape and with misaligned time t_{TM}=-40 ps. Fig. 2.31(b) depicts the values of $(I(t_n;0,1)+I(t_n;1,0))/I(t_n;1,1)$, which evaluates the linear/nonlinear characteristic of TM. In the figures, OBPF is Gaussian shaped with the bandwidth of 50 GHz. From Fig. 2.31, it is shown that for α=0.4 and 0.8 where OBPF-induced signal distortion is negligible, $(I(t_n;0,1)+I(t_n;1,0))/I(t_n;1,1) \approx 1$ and TM is linear. In contrast, TM is nonlinear for α=0 where the optical signal is distorted after the OBPF due to its sharp edge.

2.2.2.2. TM with PMD

When PMD is present, instead of ISI with m=1, the system induces ISI with the memory length m=2. For linear TM, which is applicable to most practical systems, $I(t_n; a_{n-1}, a_n)$ for TM can be written as $I(t_n; a_{n-1}, a_n)=f_{TM}(g_{-1}a_{n-1}+g_0a_n)$, where $g_{-1}+g_0=1$. On the other hand, PMD-induced ISI is also linear. $I(t_n; a_{n-1}, a_n)$ for PMD in RZ systems has the form of:

$$I(t_n;a_{n-1},a_n)=f^s_{a_{n-1}}a_{n-1}+(f^f_{a_n}+f^s_{a_n})a_n=f_{PMD}(r_{-1}a_{n-1}+r_0a_n),\ r_{-1}+r_0=1 \tag{2.21}$$

where $f^s_{a_{n-1}}$, $f^f_{a_n}$, and $f^s_{a_n}$ are the electric fields sampled from the slow mode (SM) of a_{n-1}, the fast mode (FM) of a_n, and the SM of a_n given $a_{n-1}=a_n=1$, respectively. The combined impairment from both PMD and TM can be proved to be linear ISI with $I(t_n; a_{n-2}, a_{n-1}, a_n)$ being:

$$\begin{aligned}&I(t_n;a_{n-2},a_{n-1},a_n)\\&=f^s_{a_{n-1}}(g_{a_{n-1},-1}{}^s a_{n-2}+g_{a_{n-1},0}{}^s a_{n-1})+f^f_{a_n}(g_{a_n,-1}{}^f a_{n-1}+g_{a_n,0}{}^f a_n)+f^s_{a_n}(g_{a_n,-1}{}^s a_{n-1}+g_{a_n,0}{}^s a_n)\\&=f_{both}(f_{-2}a_{n-2}+f_{-1}a_{n-1}+f_0a_n)\end{aligned} \tag{2.22}$$

where $f_{-2}+f_{-1}+f_0=1$. Here note that for a fixed sampling point in time, the relative sampling phases with respect to the SM of a_{n-1}, the FM of a_n, and the SM of a_n are different, leading to different values of TM coefficients, g_{-1} and g_0. In some special cases, for example when the DGD is T, we can simplify these coefficients as $f^s_{a_n}=0$, $g_{a_{n-1},-1}{}^s=g_{a_n,-1}{}^f=g_{-1}$ and $g_{a_{n-1},0}{}^s=g_{a_n,0}{}^f=g_0$ because only the SM of a_{n-1} and the FM of

a_n contribute to the sampled value and their relative sampling phase are the same. In those cases, f_{-2}, f_{-1}, and f_0 can be derived as $f_{-2}=g_{-1}r_{-1}$, $f_{-1}=g_{-1}r_0+g_0r_{-1}$, and $f_0=g_0r_0$.

2.2.3. A Simple Analytical Method for Performance Evaluation of MLSE for TM and PMD Compensation

Because both TM and PMD are characterized as ISI, therefore, MLSE is promising to compensate those impairments. To evaluate the performance of MLSE, we assume that in the sequence estimation using Viterbi algorithm, the estimated path ($b_0\ b_1 \ldots b_{n-1}\ b_n$) diverges from the correct path ($a_0\ a_1 \ldots a_{n-1}\ a_n$) at state k and remerges with the correct path at state $k+L$, i. e. $a_k \neq b_k$ and $a_{k+L-m-1} \neq b_{k+L-m-1}$, but $a_p = b_p$ for $k-m \leq p \leq k-1$ and $k+L-m \leq p \leq k+L-1$. Define two vectors to evaluate the error event in the estimation as $\varepsilon_c=[a_{k-m}\ a_{k-m+1} \ldots\ a_{k+L-2}\ a_{k+L-1}]$ and $\varepsilon_e=[b_{k-m}\ b_{k-m+1} \ldots\ b_{k+L-2}\ b_{k+L-1}]$. The BER of MLSE is written as [129]:

$$P_e \approx \sum_{\varepsilon_c \neq \varepsilon_e} P(\varepsilon_c \rightarrow \varepsilon_e) w(\varepsilon_c, \varepsilon_e) (\frac{1}{2})^{L+m} \tag{2.23}$$

where $P(\varepsilon_c \rightarrow \varepsilon_e)$ is the probability of the error event $\varepsilon_c \rightarrow \varepsilon_e$. $w(\varepsilon_c, \varepsilon_e)$ is the number of nonzero components in the vector of $[(b_k-a_k)\ (b_{k+1}-a_{k+1}) \ldots (b_{k+L-m-1}-a_{k+L-m-1})]^T$. In practice, P_e is dominated by the terms involving large $P(\varepsilon_c \rightarrow \varepsilon_e)$ as follows after thorough searching:

a) For m=1, i.e. only TM or PMD is present, two kinds of ε_c and ε_e contribute most to P_e: (1) one-bit error event with L=2 and $w(\varepsilon_c, \varepsilon_e)$=1, i. e. $\varepsilon_c=[a_{k-1}\ a_k\ a_{k+1}]$, $\varepsilon_e=[b_{k-1}\ b_k\ b_{k+1}]$, $b_p \in \{0\ 1\}$, $k-1 \leq p \leq k+1$, $a_{k-1}=b_{k-1}$, $a_k \neq b_k$, $a_{k+1}=b_{k+1}$; (2) ε_c and ε_e with arbitrary L>2, which satisfy i) $a_p \neq b_p$, $k \leq p \leq k+L-2$; and ii) the adjacent a_p, $k \leq p \leq k+L-2$, is different.

b) For m=2 when both TM and PMD are present, the dominating terms are: (1) one-bit error event, i. e. $\varepsilon_c=[a_{k-2}\ a_{k-1}\ a_k\ a_{k+1}\ a_{k+2}]$ and $\varepsilon_e=[b_{k-2}\ b_{k-1}\ b_k\ b_{k+1}\ b_{k+2}]$, $b_p \in \{0\ \ 1\}$, $k-2 \leq p \leq k+2$, $a_{k-2}=b_{k-2}$, $a_{k-1}=b_{k-1}$, $a_k \neq b_k$, $a_{k+1}=b_{k+1}$, and $a_{k+2}=b_{k+2}$; (2) two-bit error event and $a_k \neq a_{k+1}$, i. e. $\varepsilon_c=[a_{k-2}\ a_{k-1}\ a_k\ a_{k+1}\ a_{k+2}\ a_{k+3}]$ and $\varepsilon_e=[b_{k-2}$

$b_{k-1}\ b_k\ b_{k+1}\ b_{k+2}\ b_{k+3}]$, $b_p \in \{0\ 1\}$, $k\text{-}2 \le p \le k\text{+}3$, $a_{k-2}=b_{k-2}$, $a_{k-1}=b_{k-1}$, $a_k \ne b_k$, $a_{k+1} \ne b_{k+1}$, $a_{k+2}=b_{k+2}$, $a_{k+3}=b_{k+3}$, and $a_k \ne a_{k+1}$. (3) ε_c and ε_e with $L>3$ which satisfy i) $a_p \ne b_p$, $k \le p \le k+L\text{-}3$; and ii) the adjacent a_p, $k \le p \le k+L\text{-}3$, is different.

When the dominating terms are determined, the key to estimate P_e is to calculate the sequence-to-sequence error probability $P(\varepsilon_c \rightarrow \varepsilon_e)$, which should be based on bit-to-bit error probability of $I(t_n;\ a_{n-m}, \ldots, a_n)$. Therefore, we write KL expansion for $n_{xopt}(t)$ and $n_{yopt}(t)$, $t \in (t_n\text{-}T_0\ t_n)$, where T_0 is the overall impulse response duration of the optical and the electrical filters. Because $n_{xopt}(t)$ and $n_{yopt}(t)$ are both AWGN, Fourier orthonormal bases can be used for the expansion [130]. Thus, $n_{xopt}(t)$ and $n_{yopt}(t)$ are written as:

$$n_{xopt}(t) = \sum_{p=-\infty}^{\infty} n_{xopt},_p \cdot \exp(\frac{2\pi jpt}{T_0}),\ \ n_{yopt}(t) = \sum_{p=-\infty}^{\infty} n_{yopt},_p \cdot \exp(\frac{2\pi jpt}{T_0}),\ t \in (t_n\text{-}T_0\ t_n) \quad (2.24)$$

where $n_{xopt,p}$, and $n_{yopt,p}$ are independent Gaussian variables with zero mean and the variance of their in-phase and quadrature components being $N_0/(2T_0)$. After the OBPF, $n_x(t)$ and $n_y(t)$ are:

$$n_x(t) = \sum_{p=-M}^{M} H_o(\frac{p}{T_0}) n_{xopt},_p \cdot \exp(\frac{2\pi jpt}{T_0})$$
$$n_y(t) = \sum_{p=-M}^{M} H_o(\frac{p}{T_0}) n_{yopt},_p \cdot \exp(\frac{2\pi jpt}{T_0}), \qquad t \in (t_n\text{-}T_0\ t_n) \quad (2.25)$$

where $H_0(f)$ is the transfer function of the OBPF. The parameter M evaluates the finite bandwidth of the OBPF. From equation (2.16), (2.17), (2.18) and (2.25), $I(t_n;\ a_{n-m}, \ldots, a_n)$ can be written as:

$$\begin{aligned} I(t_n; a_{n-m}, \ldots, a_n) = {} & (R(\left|E_{s,x}(t; a_{n-m}, \ldots, a_n)\right|^2 + \left|E_{s,y}(t; a_{n-m}, \ldots, a_n)\right|^2) \otimes h_e(t))\Big|_{t=t_n} \\ & + \boldsymbol{n}_{xopt}^{T*} \boldsymbol{v}_x(t_n; a_{n-m}, \ldots, a_n) + \boldsymbol{n}_{yopt}^{T*} \boldsymbol{v}_y(t_n; a_{n-m}, \ldots, a_n) + \boldsymbol{v}_x^{T*}(t_n; a_{n-m}, \ldots, a_n) \boldsymbol{n}_{xopt} \\ & + \boldsymbol{v}_y^{T*}(t_n; a_{n-m}, \ldots, a_n) \boldsymbol{n}_{yopt} + \boldsymbol{n}_{xopt}^T \boldsymbol{Q} \boldsymbol{n}_{xopt}^{\ *} + \boldsymbol{n}_{yopt}^T \boldsymbol{Q} \boldsymbol{n}_{yopt}^{\ *} + n_{th\_EF}(t_n) \end{aligned} \quad (2.26)$$

where * stands for the conjugate. $n_{th\_EF}(t_n)$ with $n_{th\_EF}(t_n) = (n_{th}(t) \otimes h_e(t))|_{t=t_n}$, is AWGN with zero mean and the autocorrelation of

$$R_{n_{th\_EF}}(\tau) = N_{th}\int_{-\infty}^{+\infty} h_e(t)h_e^*(t+\tau)dt/2 \tag{2.27}$$

$\boldsymbol{n}_{xopt}$ (or $\boldsymbol{n}_{yopt}$) is a column vector whose $2M$+1 components are $n_{xopt,p-M-1}$ (or $n_{yopt,p-M-1}$), $1 \le p \le 2M+1$. $\boldsymbol{v}_x(t_n;\ a_{n-m},\ldots,\ a_n)$ (or $\boldsymbol{v}_y(t_n;\ a_{n-m},\ldots,\ a_n)$) is a column vector whose components are

$$RH_0*(\frac{p-M-1}{T_0})((E_{s,x}(t;a_{n-m},...,a_n)\exp(\frac{-2\pi j(p-M-1)t}{T_0}))\otimes h_e(t))\Big|_{t=t_n}, or$$
$$RH_0*(\frac{p-M-1}{T_0})((E_{s,y}(t;a_{n-m},...,a_n)\exp(\frac{-2\pi j(p-M-1)t}{T_0}))\otimes h_e(t))\Big|_{t=t_n}, 1\le p\le 2M+1 \tag{2.28}$$

$\boldsymbol{Q}$ is a $(2M+1)\times(2M+1)$ matrix whose p^{th}-row, q^{th}-column element is:

$$RH_0(\frac{p-M-1}{T_0})H_0*(\frac{q-M-1}{T_0})(\exp(\frac{2\pi j(p-q)t}{T_0})\otimes h_e(t))\Big|_{t=t_n}, 1\le p,q\le 2M+1 \tag{2.29}$$

Notice that $\boldsymbol{Q}$ is Hermitian symmetric, the eigenvalues λ_p, $1\le p\le 2M+1$, are real and the eigenvectors are orthogonal, i. e. $\boldsymbol{Q}=\boldsymbol{U}\boldsymbol{\Lambda}\boldsymbol{U}^{T*}$ with $\Lambda=\text{diag}\{\lambda_p\}$ and $\boldsymbol{U}$ being an orthogonal matrix. Therefore, (2.26) can be written as:

$$\begin{aligned}
&I(t_n;a_{n-m},...,a_n)\\
&=(R(\left|E_{s,x}(t;a_{n-m},...,a_n)\right|^2+\left|E_{s,y}(t;a_{n-m},...,a_n)\right|^2)\otimes h_e(t))\Big|_{t=t_n}\\
&\quad+\boldsymbol{n}_{xopt}^{T*}\boldsymbol{v}_x(t_n;a_{n-m},...,a_n)+\boldsymbol{n}_{yopt}^{T*}\boldsymbol{v}_y(t_n;a_{n-m},...,a_n)+\boldsymbol{v}_x^{T*}(t_n;a_{n-m},...,a_n)\boldsymbol{n}_{xopt}\\
&\quad+\boldsymbol{v}_y^{T*}(t_n;a_{n-m},...,a_n)\boldsymbol{n}_{yopt}+\boldsymbol{n}_{xopt}^{T}\boldsymbol{U}\boldsymbol{\Lambda}\boldsymbol{U}^{T*}\boldsymbol{n}_{xopt}^{*}+\boldsymbol{n}_{yopt}^{T}\boldsymbol{U}\boldsymbol{\Lambda}\boldsymbol{U}^{T*}\boldsymbol{n}_{yopt}^{*}+n_{th_EF}(t_n)\\
&=I_{sig}(t_n;a_{n-m},...,a_n)+\boldsymbol{z}_{xopt}^{T*}\boldsymbol{b}_x(t_n;a_{n-m},...,a_n)+\boldsymbol{z}_{yopt}^{T*}\boldsymbol{b}_y(t_n;a_{n-m},...,a_n)\\
&\quad+\boldsymbol{b}_x^{T*}(t_n;a_{n-m},...,a_n)\boldsymbol{z}_{xopt}+\boldsymbol{b}_y^{T*}(t_n;a_{n-m},...,a_n)\boldsymbol{z}_{yopt}+\boldsymbol{z}_{xopt}^{T}\boldsymbol{\Lambda}\boldsymbol{z}_{xopt}^{*}+\boldsymbol{z}_{yopt}^{T}\boldsymbol{\Lambda}\boldsymbol{z}_{yopt}^{*}+n_{th_EF}(t_n)
\end{aligned} \tag{2.30}$$

where z_{xopt} (or z_{yopt}) is $\boldsymbol{U}^T\boldsymbol{n}_{xopt}$ (or $\boldsymbol{U}^T\boldsymbol{n}_{yopt}$). $\boldsymbol{b}_x(t_n;\ a_{n-m},\ldots,\ a_n)$ (or $\boldsymbol{b}_y(t_n;\ a_{n-m},\ldots,\ a_n)$) is $\boldsymbol{U}^T\boldsymbol{v}_x(t_n;\ a_{n-m},\ldots,\ a_n)$ (or $\boldsymbol{U}^T\boldsymbol{v}_y(t_n;\ a_{n-m},\ldots,\ a_n)$). As $\boldsymbol{U}$ is an orthogonal matrix, the components of z_{xopt} (or z_{yopt}) are uncorrelated Gaussian variables with zero mean and the variance of their in-phase and quadrature components being $N_0/(2T_0)$. From (2.30), we can derive $P(\varepsilon_c \rightarrow \varepsilon_e)$ in both OSNR-limited and thermal-noise limited operation regions.

A. OSNR Limited Operation Region

The mean and the variance of $I(t_n; a_{n-m},\ldots, a_n)$ are obtained from (2.30) as:

$$I_{ave}(t_n;a_{n-m},...,a_n) = I_{sig}(t_n;a_{n-m},...,a_n) + \frac{2N_0}{T_0}\cdot\sum_{p=1}^{2M+1}\lambda_p \tag{2.31}$$

$$\sigma^2(t_n;a_{n-m},...,a_n) = \sum_{p=1}^{2M+1}(2(\frac{N_0}{T_0})^2\lambda_p{}^2 + 2(\frac{N_0}{T_0})(\left|b_{x,p}(t_n;a_{n-m},...,a_n)\right|^2 + \left|b_{y,p}(t_n;a_{n-m},...,a_n)\right|^2)) \tag{2.32}$$

where $b_{x,p}(t_n; a_{n-m},\ldots, a_n)$ (or $b_{y,p}(t_n; a_{n-m},\ldots, a_n)$) is the p^{th} component of $\boldsymbol{b}_x(t_n; a_{n-m},\ldots, a_n)$ (or $\boldsymbol{b}_y(t_n; a_{n-m},\ldots, a_n)$), $1 \le p \le 2M+1$. The moment generating function (MGF) of $I(t_n;a_{n-m},\ldots, a_n)$ is:

$$\begin{aligned} M(s;a_{n-m},...,a_n) &= \exp(-sI_{sig}(t_n;a_{n-m},...,a_n))\cdot \\ &\prod_{p=1}^{2M+1}\frac{\exp(s^2(\left|b_{x,p}(t_n;a_{n-m},...,a_n)\right|^2 + \left|b_{y,p}(t_n;a_{n-m},...,a_n)\right|^2)N_0/T_0/(1+s\lambda_pN_0/T_0))}{(1+s\lambda_pN_0/T_0)^2} \end{aligned} \tag{2.33}$$

The distribution of $I(t_n; a_{n-m},\ldots, a_n)$ is the inverse Laplace transform of (2.33). Bit-to-bit error probability can be calculated from the MGF by using saddlepoint approximation [131], which is adopted in this section to evaluate TM-induced power penalty without MLSE:

$$\begin{aligned} P_{bit-to-bit} &= \frac{1}{2}E_\delta\{P(I(t_n;a_{n-m},...,a_n) > \alpha_T)\big|_{a_n=0} + P(I(t_n;a_{n-m},...,a_n) < \alpha_T)\big|_{a_n=1}\} \\ &= \frac{1}{2}E_\delta\{\frac{\exp(\psi(s_0;a_{n-m},...,a_n))}{\sqrt{2\pi\psi''(s_0;a_{n-m},...,a_n)}} + \frac{\exp(\psi(s_1;a_{n-m},...,a_n))}{\sqrt{2\pi\psi''(s_1;a_{n-m},...,a_n)}}\} \end{aligned} \tag{2.34}$$

where E_δ is the ensemble average with δ being the set of all possible $[a_{n-m}\ldots a_{n-1}]$. $\psi(s; a_{n-m},\ldots, a_n)=\ln(M(s; a_{n-m},\ldots, a_n))+s\alpha_T-\ln|s|$. s_0 and s_1 are the negative and positive saddlepoints, respectively. The optimal threshold α_T is determined numerically.

Though saddlepoint approximation is accurate in estimating bit-to-bit error probability, it is inconvenient to apply such method to the estimation of sequence-to-sequence error probability $P(\varepsilon_c \rightarrow \varepsilon_e)$. In OSNR limited operation region, such probability is difficult to calculate. Some previous works employed the approximated closed-form expression for the distribution of $I(t_n;\ a_{n-m},\ldots,\ a_n)$ to make the problem solvable [81]-[82]. In this paper, we use Gaussian approximation with signal-dependent mean and variance shown in (2.31) and (2.32):

$$p(I(t_n) \mid a_{n-m},\ldots,a_n) = \frac{1}{\sqrt{2\pi}\sigma(t_n;a_{n-m},\ldots,a_n)} \exp\left(-\frac{(I(t_n) - I_{ave}(t_n;a_{n-m},\ldots,a_n))^2}{2\sigma^2(t_n;a_{n-m},\ldots,a_n)}\right) \quad (2.35)$$

MLSE chooses the error path if:

$$\sum_{p=k}^{k+L-1} -\ln(p(I(t_p) \mid a_{p-m},\ldots,a_p) > \sum_{p=k}^{k+L-1} -\ln(p(I(t_p) \mid b_{p-m},\ldots,b_p) \quad (2.36)$$

Let $\boldsymbol{I}=[I(t_k)\ldots I(t_{k+L-1})]$ and

$$F(\boldsymbol{I};\boldsymbol{\varepsilon}_c) = \sum_{p=k}^{k+L-1} -\ln(p(I(t_p) \mid a_{p-m},\ldots,a_p), F(\boldsymbol{I};\boldsymbol{\varepsilon}_e) = \sum_{p=k}^{k+L-1} -\ln(p(I(t_p) \mid b_{p-m},\ldots,b_p) \quad (2.37)$$

which are the functions with L-dimension variables. Define $B(\boldsymbol{I};\varepsilon_c,\ \varepsilon_e)$ be the locus of all points in L-dimension space such that $F(\boldsymbol{I};\ \varepsilon_c)= F(\boldsymbol{I};\ \varepsilon_e)$. Let $\boldsymbol{I}_{\min}(\varepsilon_c,\ \varepsilon_e) =[I_{\min}(t_k;\ \varepsilon_c,\ \varepsilon_e)\ldots I_{\min}(t_{k+L-1};\ \varepsilon_c,\ \varepsilon_e)]$ be the vector in $B(\boldsymbol{I};\ \varepsilon_c,\ \varepsilon_e)$ that minimizes $F(\boldsymbol{I};\ \varepsilon_c)$, $P(\varepsilon_c \rightarrow \varepsilon_e)$ can be expressed as [81]:

$$P(\boldsymbol{\varepsilon}_c \rightarrow \boldsymbol{\varepsilon}_e) = \exp\left(\frac{\boldsymbol{\eta}^{T*}\boldsymbol{\eta}}{4} - F(\boldsymbol{I}_{\min}(\boldsymbol{\varepsilon}_c,\boldsymbol{\varepsilon}_e);\boldsymbol{\varepsilon}_c)\right) Q\left(\frac{\boldsymbol{\eta}^T\boldsymbol{k}}{\sqrt{2}}\right) \prod_{p=k}^{k+L-1} \left(\frac{\pi}{u_p}\right)^{1/2} \quad (2.38)$$

where

$$u_p = \frac{1}{2} \frac{\partial^2 F(\boldsymbol{I};\boldsymbol{\varepsilon}_c)}{\partial I^2(t_p)} \Bigg|_{\boldsymbol{I}=\boldsymbol{I}_{\min}(\boldsymbol{\varepsilon}_c,\boldsymbol{\varepsilon}_e)} \quad (2.39)$$

η is a column vector with L components of

$$\eta_p = \frac{1}{\sqrt{u_{p+k-1}}} \frac{\partial F(\boldsymbol{I};\boldsymbol{\varepsilon}_c)}{\partial I(t_{p+k-1})}\bigg|_{\boldsymbol{I}=\boldsymbol{I}_{\min}(\boldsymbol{\varepsilon}_c,\boldsymbol{\varepsilon}_e)}, 1 \le p \le L \tag{2.40}$$

and $\boldsymbol{k}$ is

$$\boldsymbol{k} = \frac{\boldsymbol{h}}{\sqrt{\boldsymbol{h}^{T^*}\boldsymbol{h}}}, \boldsymbol{h} = \boldsymbol{u}^T \cdot \nabla(F(\boldsymbol{I};\boldsymbol{\varepsilon}_c) - F(\boldsymbol{I};\boldsymbol{\varepsilon}_e))\big|_{\boldsymbol{I}=\boldsymbol{I}_{\min}(\boldsymbol{\varepsilon}_c,\boldsymbol{\varepsilon}_e)} \tag{2.41}$$

where $\boldsymbol{u}=[u_k^{-1/2}\ u_{k+1}^{-1/2} \ldots\ u_{k+L-1}^{-1/2}]$. When $I(t_p;\ a_{p-m},\ldots,\ a_p)$, $k \le p \le k+L-1$, has the distribution of (2.35), we can achieve a simple result from (2.38) as:

$$P(\boldsymbol{\varepsilon}_c \to \boldsymbol{\varepsilon}_e) = Q(\frac{\boldsymbol{\eta}^T \boldsymbol{k}}{\sqrt{2}}) \tag{2.42}$$

where $\boldsymbol{\eta}$ is a column vector with L components of $2^{1/2} \cdot (I_{\min}(t_{p+k-1};\ \varepsilon_c,\ \varepsilon_e) - I_{ave}(t_{p+k-1};\ a_{p+k-m-1},\ldots,\ a_{p+k-1}))\ /\ \sigma(t_{p+k-1};\ a_{p+k-m-1},\ldots,\ a_{p+k-1})$, $1 \le p \le L$. $\boldsymbol{k}$ satisfies (2.41) with L components of $\boldsymbol{h}$ as:

$$\begin{aligned} &\frac{\sqrt{2}\sigma(t_{p+k-1};a_{p+k-m-1},\ldots,a_{p+k-1})}{\sigma^2(t_{p+k-1};a_{p+k-m-1},\ldots,a_{p+k-1})}(I_{\min}(t_{p+k-1};\boldsymbol{\varepsilon}_c,\boldsymbol{\varepsilon}_e) - I_{ave}(t_{p+k-1};a_{p+k-m-1},\ldots,a_{p+k-1})) \\ &-\frac{\sqrt{2}\sigma(t_{p+k-1};a_{p+k-m-1},\ldots,a_{p+k-1})}{\sigma^2(t_{p+k-1};b_{p+k-m-1},\ldots,b_{p+k-1})}(I_{\min}(t_{p+k-1};\boldsymbol{\varepsilon}_c,\boldsymbol{\varepsilon}_e) - I_{ave}(t_{p+k-1};b_{p+k-m-1},\ldots,b_{p+k-1})) \end{aligned} \tag{2.43}$$

B. Thermal-noise Limited Operation Region

Because $n_{\text{th\_EF}}(t_n)$ has signal-independent Gaussian distribution, $P(\varepsilon_c \to \varepsilon_e)$ is derived to be:

$$P(\boldsymbol{\varepsilon}_c \to \boldsymbol{\varepsilon}_e) = Q(\sqrt{\frac{\delta(\boldsymbol{\varepsilon}_c,\boldsymbol{\varepsilon}_e)^2}{4R_{n_{th\_EF}}(0)}}) = Q(\sqrt{\frac{\delta(\boldsymbol{\varepsilon}_c,\boldsymbol{\varepsilon}_e)^2}{2N_{th\_EF}}}) \tag{2.44}$$

where $N_{\text{th\_EF}}=2\,R_{n_{th\_EF}}(0)$ and

$$\delta(\boldsymbol{\varepsilon}_c,\boldsymbol{\varepsilon}_e)^2 = \sum_{p=k}^{k+L-1}(I_{sig}(t_p;b_{p-m},\ldots,b_p) - I_{sig}(t_p;a_{p-m},\ldots,a_p))^2 \tag{2.45}$$

Therefore, the BER of MLSE is obtained from (2.23), (2.44) and (2.45) as

$$P_e \approx Q(\sqrt{\frac{f_{both}^2(f_0^2+f_{-1}^2+f_{-2}^2)}{2N_{th\_EF}}})+$$
$$\sum_{L=4}^{+\infty} Q(\sqrt{\frac{f_{both}^2(f_0^2+(f_{-1}-f_0)^2+(L-4)(f_{-1}-f_{-2}-f_0)^2+(f_{-1}-f_{-2})^2+(f_{-2})^2)}{2N_{th\_EF}}})(L-2)(\frac{1}{2})^{L-3} \tag{2.46}$$

where the coefficients f_0, f_{-1}, and f_{-2} are determined from (2.22). As a special case of (2.46), it is derived that when PMD is the worst or TM is the worst only, $P_e = 4Q((f_{both}^2/4N_{th\_EF})^{1/2})$. Notice that for ISI free, $P_e= Q((f_{both}^2/2N_{th\_EF})^{1/2})$. Therefore, the receiver power penalty for the worst PMD or the worst TM is equal to 1.9 dB at BER of 10^{-4}. In contrast, when both PMD and TM are the worst, $P_e=3Q((f_{both}^2/8N_{th\_EF})^{1/2})$ and the receiver power penalty is 3.3 dB. Such receiver power penalty can be reduced further at lower BER with the asymptotic value of around 3 dB for error free, due to the decreasing influence of the coefficient 3 for small P_e.

2.2.4. Performance of MLSE for TM Compensation

To verify the developed theory, Monte Carlo simulations as well as analytical calculations were performed. An optical RZ pulse train $E_{pulse}(t)$, consisting of 500,000 bits with 40 samples per bit, was modulated by 10-Gbit/s data and launched into a piece of fiber. $h_x(\gamma^{1/2}E_s(t))$ and $h_y((1-\gamma)^{1/2}E_s(t))$ emulated the effect of PMD with variable γ and DGD. The OBPF was Gaussian shaped with the bandwidth of 50 GHz. The EF was a 4^{th}-order Butterworth filter with the optimized bandwidth in the absence of TM and PMD. The metric of (2.19) for different MLSE states in the look-up table was obtained using non-parametric histogram method by a 200,000-bit training sequence. The performance was evaluated in terms of E_b/N_0 (dB) penalty in OSNR limited operation region or receiver power penalty in thermal-noise limited operation region at BER of 10^{-4}, where E_b was the average power in one bit slot. Fig. 2.32 depicts the back-to-back OSNR-limited performance of the RZ signal under matched filter (solid line) and the adopted practical filter (dashed line). It is show that the required photons per bit to achieve 10^{-9} by using the matched filter are 38 (~16 dB). The adopted system exhibits 0.8-dB E_b/N_0 penalty compared to that under matched filter. Such penalty can be reduced by the optimization of the OBPF's bandwidth [132].

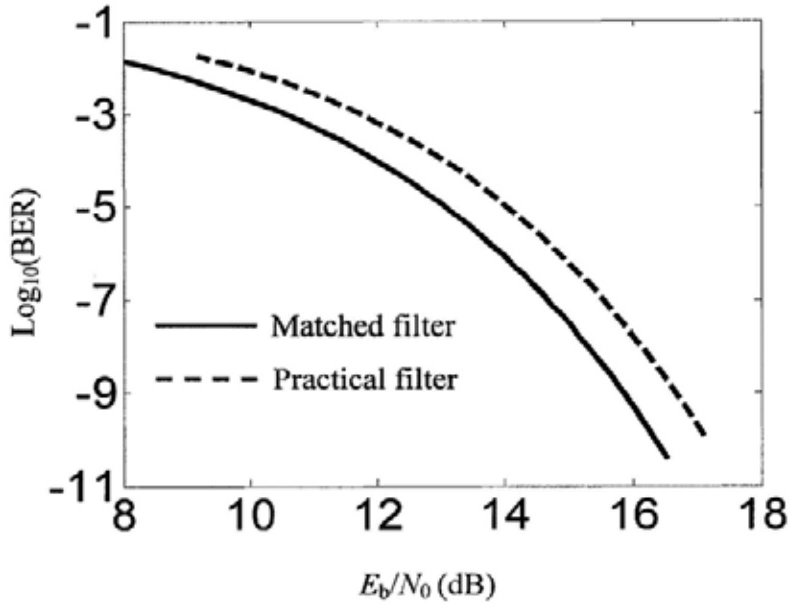

Fig. 2.32: BER versus E_b/N_0 for the matched filter (solid line) and the adopted system (dashed line).

First, the performance of MLSE for compensation of TM in the absence of PMD is investigated. Fig. 2.33 depicts E_b/N_0 penalty (OSNR limited) versus t_{TM} under conventional optimal threshold detection (solid) and MLSE (dashed) when α (the parameter controlling the edge sharpness of the input signal pulse shape) is (a) 0, (b) 0.4, and (c) 0.8. Circles and triangles represent analytical and numerical results, respectively. From Fig. 2.33, we can find that the analytical results agree well with the simulation results. In the case of conventional detection, E_b/N_0 penalty increases rapidly when $|t_{TM}|$ exceeds 30 ps. The E_b/N_0 penalty profile depends on the α parameter. The reason is twofold. First, the temporally less confined NRZ data with larger α value would experience more ISI. Second, when timing is misaligned, much energy leaks into the data transition time region, which enhances the performance sensitivity to α. Slight asymmetric profiles in the figures are due to the asymmetric impulse response of EF. By employing MLSE, E_b/N_0 penalty is significantly reduced for $|t_{TM}|$ >30 ps. The performance of MLSE is also dependent on the parameter α. For

α=0.4 and 0.8 where TM is linear, the E_b/N_0 penalty caused by the worst TM is limited around 6 dB in OSNR limited operation region. On the other hand, when α=0 where TM is nonlinear, the E_b/N_0 penalty for the worst TM has 2-dB reduction compared to that for linear TM.

Fig. 2.34 depicts the received power penalty (thermal noise limited) versus t_{TM} under conventional optimal threshold detection (solid) and MLSE (dashed) when α (the parameter controlling the edge sharpness of the input signal pulse shape) is (a) 0, (b) 0.4, and (c) 0.8. Circles and triangles represent analytical and numerical results, respectively. From the figure, it is found that similar to Fig. 2.33, the analytical results agree well with the simulation results. The received power penalty increases dramatically as $|t_{TM}|$ increases under optimal threshold detection. By employing MLSE, the power penalty can be largely reduced. The performance of MLSE is dependent on the parameter α. For α=0.4 and 0.8 where TM is linear, the E_b/N_0 penalty caused by the worst TM is limited around 1.9 dB. On the other hand, when α=0 where TM is nonlinear, additional 0.4-dB power penalty is exhibited.

We have also shown the capability of MLSE to achieve simultaneous compensation of PMD and TM. Fig. 2.35 depicts the E_b/N_0 penalty (OSNR limited) for (a) α=0.8, γ=1/2 and variable DGD; (b) α=0.8, DGD=100 ps and variable γ. Circles and triangles represent analytical and simulation results respectively. From the figure, it is shown that in the worst case of both PMD and TM where the eye is completely closed, MLSE limits the E_b/N_0 penalty within 9 dB.

Fig. 2.36 depicts the receiver power penalty (thermal noise limited) for (a) α=0.8, γ=1/2 and variable DGD; (b) α=0.8, DGD=100 ps and variable γ. Circles and triangles represent analytical and simulation results respectively. Similar to Fig. 2.35, MLSE can compensate TM and PMD with shared electrical devices. From the figure, it is shown that in the worst case of both PMD and TM, MLSE bounds the receiver power penalty to around 3.3 dB in thermal noise limited operation region.

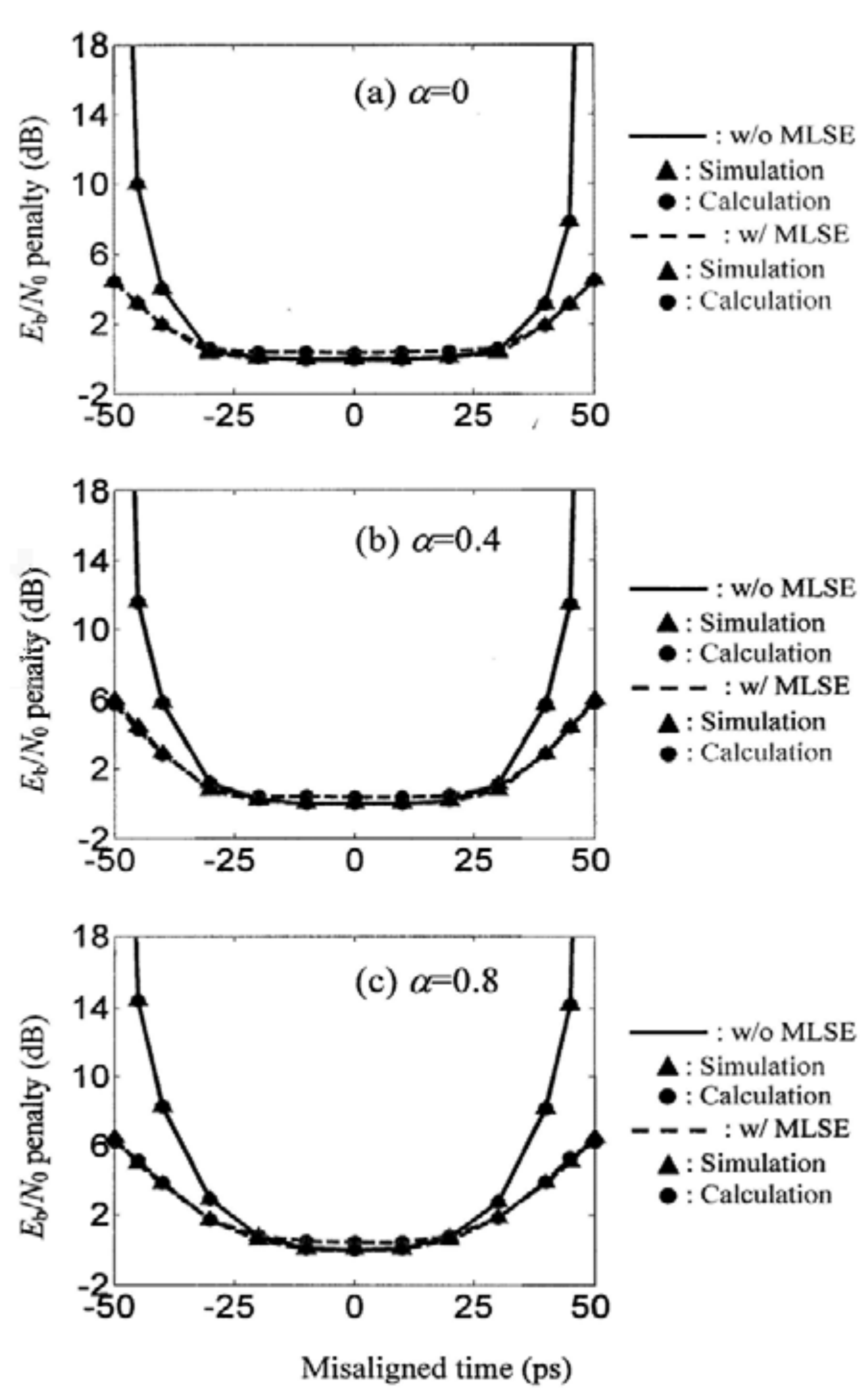

Fig. 2.33: E_b/N_0 penalty (OSNR limited) versus t_{TM} under conventional optimal threshold detection (solid) and MLSE (dashed) when α (the parameter controlling the edge sharpness of the input signal pulse shape) is (a) 0, (b) 0.4, and (c) 0.8. Circles and triangles represent analytical and numerical results, respectively.

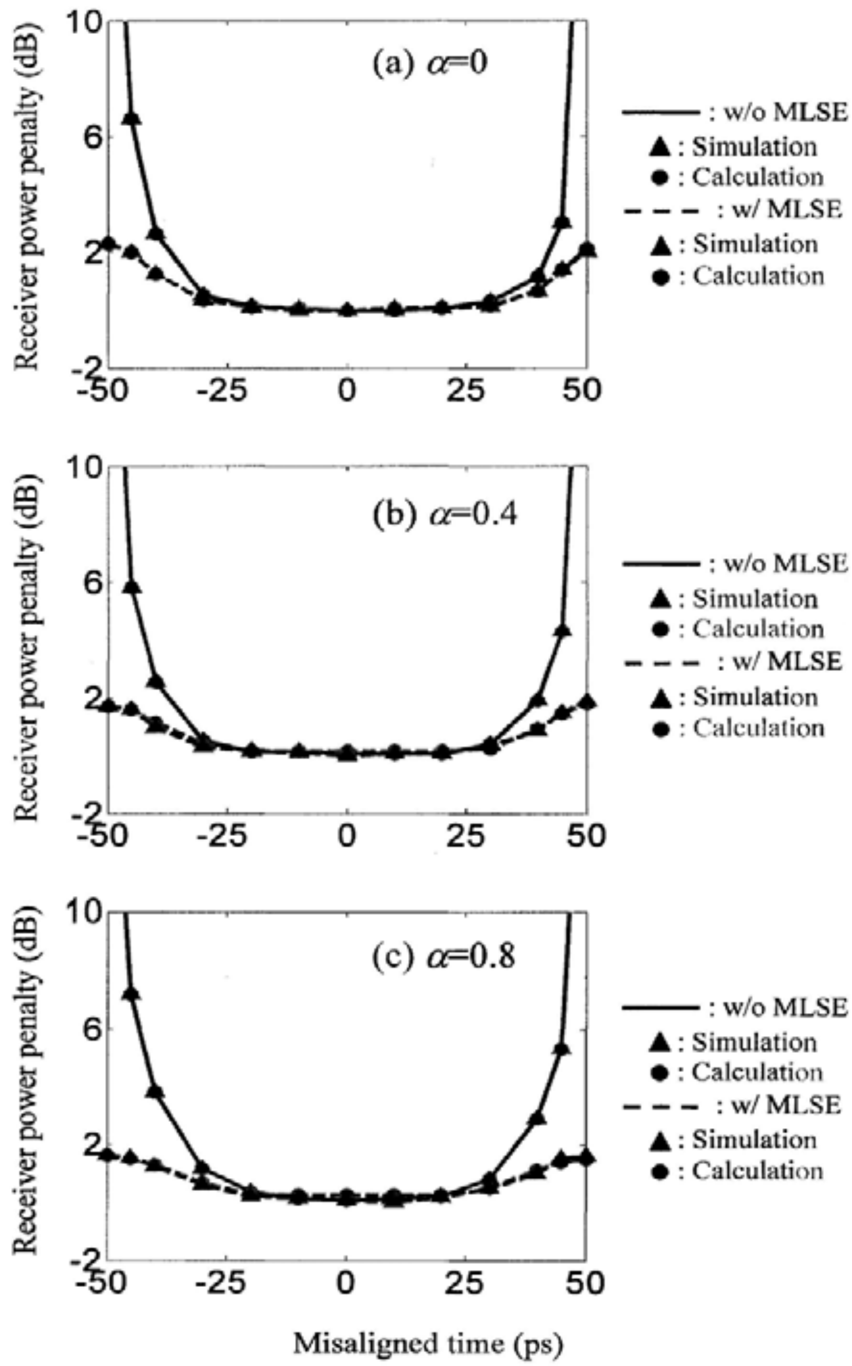

Fig. 2.34: received power penalty (thermal noise limited) versus t_{TM} under conventional optimal threshold detection (solid) and MLSE (dashed) when α is (a) 0, (b) 0.4, and (c) 0.8. Circles and triangles represent analytical and numerical results, respectively.

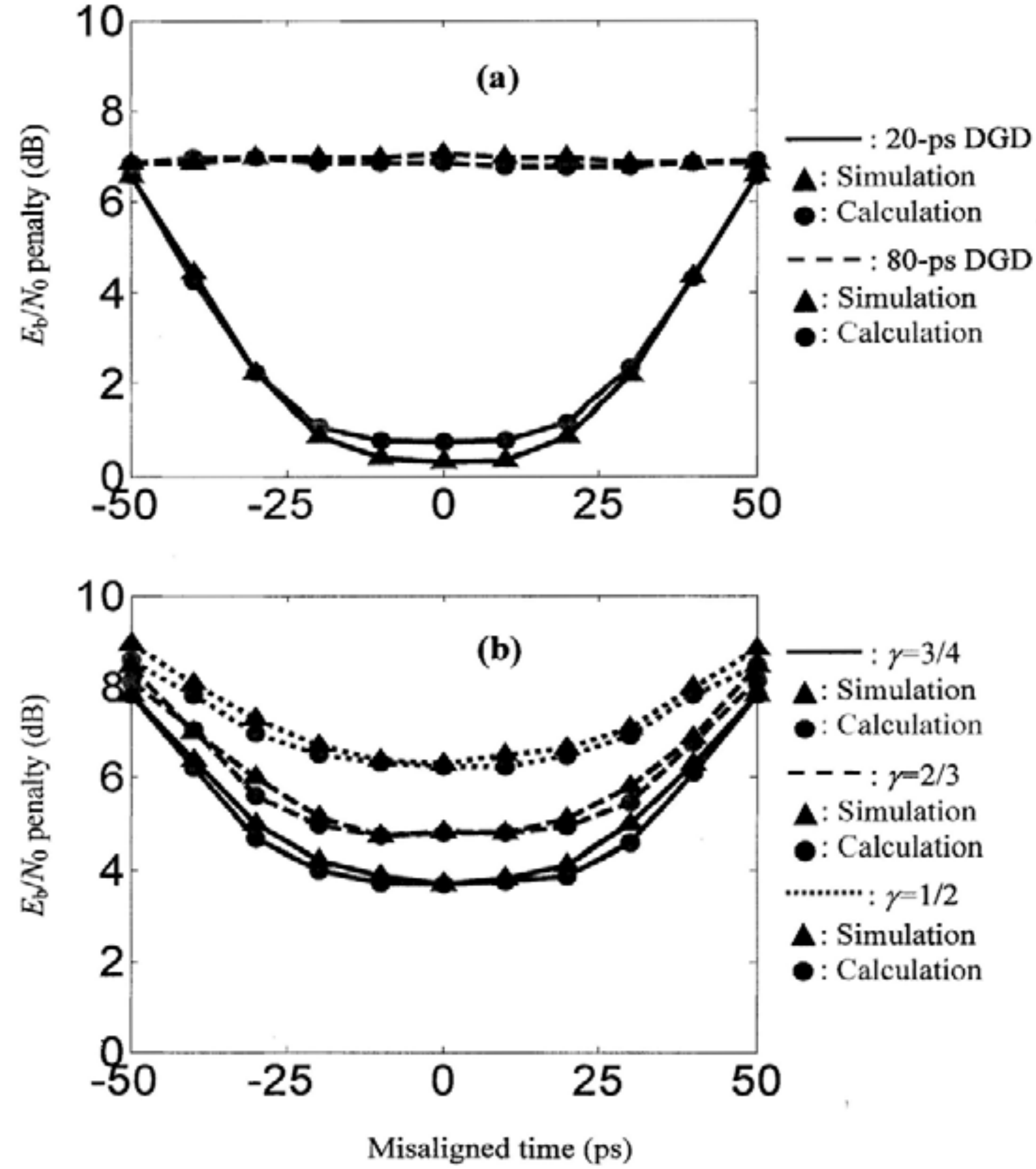

Fig. 2.35: E_b/N_0 penalty (OSNR limited) for (a) α=0.8, γ=1/2 and variable DGD; (b) α=0.8, DGD=100 ps and variable γ. In (a) and (b), circles and triangles represent analytical and simulation results respectively. In (a), solid lines and dashed lines represent DGD of 20 and 80 ps respectively. In (b), solid lines, dashed lines and dotted lines represent γ of 3/4, 2/3 and 1/2 respectively.

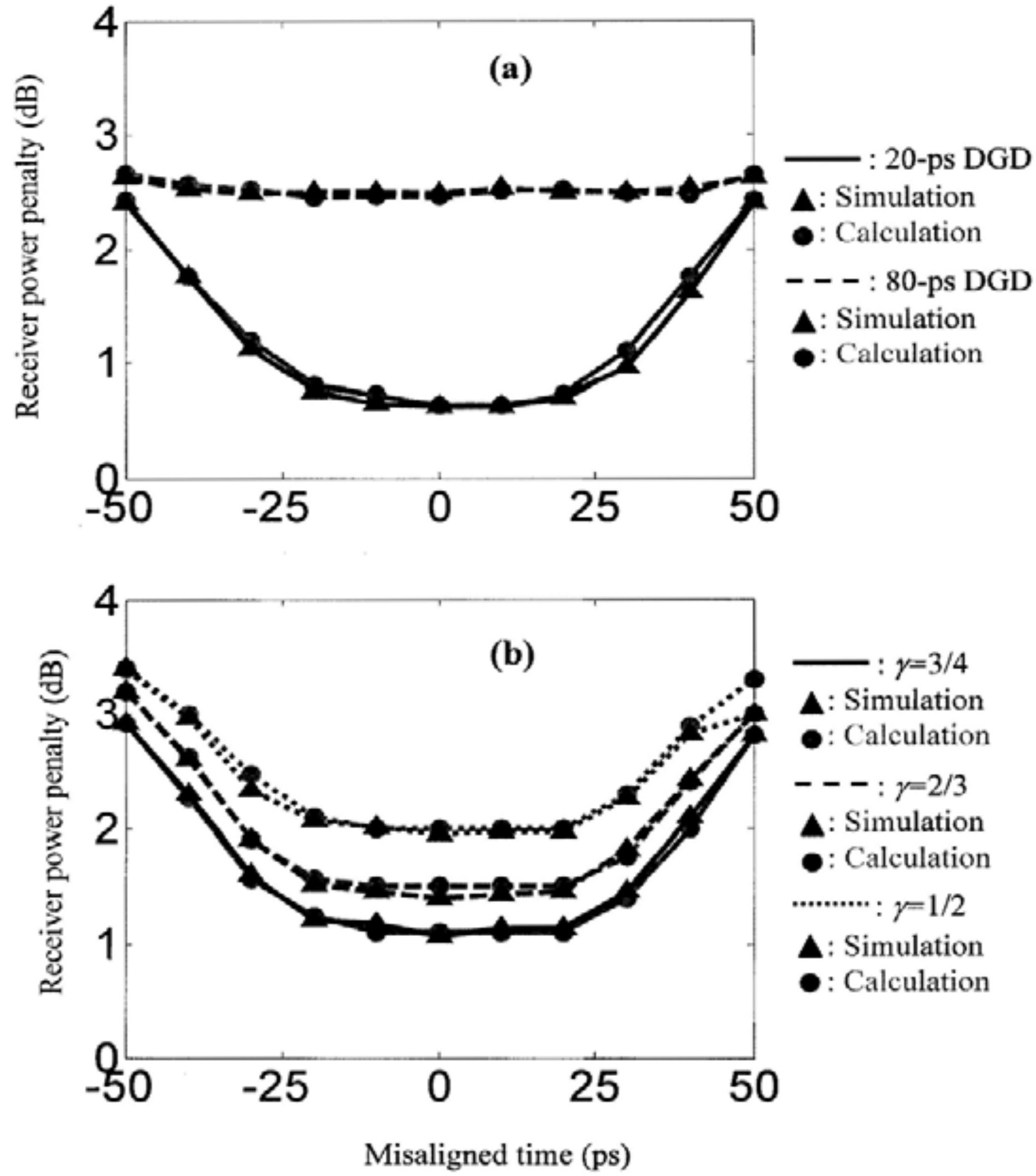

Fig. 2.36: Receiver power penalty (thermal noise limited) for (a) α=0.8, γ=1/2 and variable DGD; (b) α=0.8, DGD=100 ps and variable γ. In (a) and (b), circles and triangles represent analytical and simulation results respectively. In (a), solid lines and dashed lines represent DGD of 20 and 80 ps respectively. In (b), solid lines, dashed lines and dotted lines represent γ of 3/4, 2/3 and 1/2 respectively.

2.2.5. Summary

In summary, we generalize the impairment from TM between the pulse carver and the NRZ data modulator in RZ systems as ISI. We show that MLSE is a simple and cost-effective solution for TM mitigation without increasing additional compensating components. We develop a theory to evaluate the performance of MLSE for compensation of TM without and with PMD in both OSNR limited and thermal-noise limited operation regions. The theory, employing decorrelation of noise components and the steepest decent method as well as Karhunen-Loeve expansion and saddlepoint approximation, is applicable to arbitrary input signal pulse shape, optical and electrical filtering. Monte Carlo simulations are performed and agree with the prediction of the theory well. The results show that the bandwidth of OBPF and the input data pulse shape determine the linear/nonlinear characteristic of TM. The power penalty caused by the worst TM is limited by MLSE to 6 dB in OSNR limited operation region and 1.9 dB in thermal-noise limited operation region. The results also validate the effectiveness of MLSE for simultaneous compensation of TM and PMD with shared electrical devices.

2.3. Summary

In summary, we have conducted an in-depth study on MLSE for impairment compensation. We have proposed and investigated several novel MLSE techniques/structures for advanced modulation formats, including DPSK, ASK/DPSK orthogonal modulation, DQPSK, and 4-ASK. Electronic equalization of advanced modulation formats further extends the transmission reach and relaxes the speed limitation of electronic devices for high-speed optical transmission. We also propose novel applications of MLSE for mitigation of TM between the pulse carver and data modulator in RZ systems and develop a simple and effective theory for the performance evaluation of MLSE for TM compensation.

3. Impairment Mitigation to Achieve High-Speed Centralized Light Source (CLS) WDM-PON

Wavelength division multiplexing passive optical network (WDM-PON) has aroused much attention for next-generation broadband access architecture, due to its large bandwidth and upgrade flexibility [71]-[72]. Centralized light source (CLS) is desirable in WDM-PON because such source at central office (CO) features well-controlled wavelength spacing and management-cost reduction by eliminating wavelength-specific transmitters at optical network units (ONUs) [73]-[79]. The primary objective of my work is to achieve high-speed colorless CLS WDM-PON with data rate of 10 Gbit/s for both downstream and upstream signals.

In the existing CLS schemes, re-modulation technique is promising to achieve a high-speed CLS WDM-PON with upstream transmission capacity up to 10 Gbit/s. By reusing the downstream wavelength, WDM-PON using re-modulation method saves the wavelengths and transmitters for the upstream signals. Several re-modulation schemes have been proposed, including the use of downstream differential phase shift keying (DPSK) signal and upstream on-off keying (OOK) signal, downstream frequency shift keying (FSK) signal and upstream OOK signal, downstream inverse return-to-zero (IRZ) signal and upstream OOK signal, and downstream DPSK signal and upstream DPSK signal [76]-[79]. However, these schemes have one or more of the following disadvantages: 1. color ONUs; 2. poor CD tolerance for 10-Gbit/s upstream transmission; 3. need of re-modulation synchronization. In practice, it is much desirable to operate a high-speed WDM-PON without CD compensation and alignment monitoring for re-modulation synchronization at ONUs, which reduces the cost, maintenance complexity, and power consumption of the network.

The one using supercontinuum (SC) generation is another method to realize a high-speed WDM-PON. By feeding a pulse train into a nonlinear fiber for spectral broadening, SC generation is an effective way to obtain a BLS with more than one hundred high-quality and well wavelength-managed upstream optical carriers [133]. Broadband SC spectrum also has higher OSNR compared to that generated by conventional BLS such as light-emitting diode. Therefore, it can support larger number of channels with higher data rate (10 Gbit/s) and longer transmission distance. In SC-BLS WDM-PON, to properly achieve upstream data modulation, it is essential to locate the pulse peak of upstream carriers in the middle of the upstream data bit slot. However, because the optical pulse carriers are generated at CO but modulated at ONUs, the synchronization between upstream pulse carriers and upstream data is difficult. Furthermore, CD becomes an important issue for upstream signals due to high transmission data rate of 10 Gbit/s and wide spectral width, as wide as the bandwidth of the arrayed waveguide grating (AWG) for channel slicing. Therefore, both CD compensation components and alignment monitors for upstream modulation synchronization at ONUs are required. As a result, the operation complexity of ONUs as well as the implementation and maintenance cost of the network is increased.

In this chapter, we review our recently proposed solutions for these two CLS WDM-PON architectures to mitigate the impairments from CD and asynchronous re-modulation. By eliminating the modulation synchronization module and all-optical CD compensation module, the cost and complexity of WDM-PON is greatly reduced.

i) We propose a novel re-modulation scheme with enhanced tolerance to CD and asynchronous upstream re-modulation. By using this technique, a 30-km-range high-speed colorless CLS WDM-PON without CD compensation and re-modulation synchronization is achieved within 1-dB penalty for both 10-Gbit/s downstream and 10-Gbit/s upstream transmission.

ii) We generalize asynchronous modulation at ONUs as ISI and propose MLSE for upstream signal detection in SC-BLS WDM-PON. MLSE effectively compensate the impairments from 1) asynchronous modulation of upstream pulse carriers at ONUs; and 2) CD in the fibers. Compared to the conventional method, the proposed method features significant cost saving, higher power budget for upstream signals, and lower operation complexity for ONUs in SC-BLS-based WDM-PON.

3.1. A Novel Re-Modulation Scheme with Enhanced Tolerance to CD and Re-Modulation Misalignment at 10 Gbit/s

Fig. 3.1 shows the principle of re-modulation schemes. The downstream wavelength is re-used as the upstream carrier. Several re-modulation schemes have been proposed. In this section, we firstly show that the previous schemes are sensitive to CD or re-modulation misalignment. Then we will propose a novel re-modulation scheme and experimentally show that the proposed method is robust to CD and asynchronous upstream re-modulation.

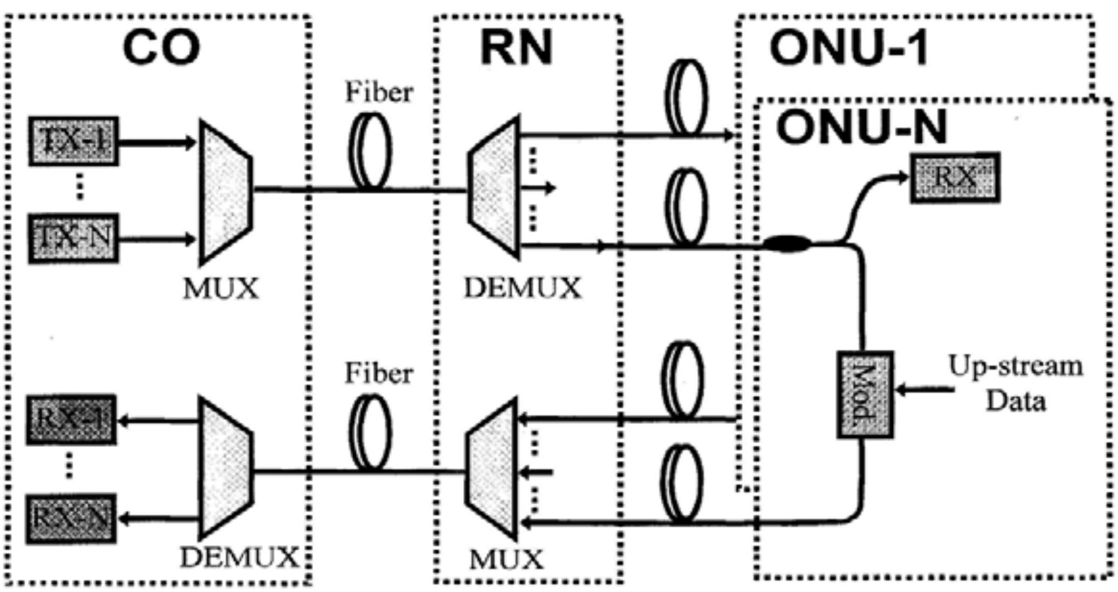

Fig. 3.1: Principle of re-modulation schemes

3.1.1. Tolerance to CD and Re-modulation Misalignment in the Previous Re-modulation Schemes

The first previous scheme is to use downstream constant-intensity FSK signal and upstream re-modulated OOK signal [77]. However, in this scheme, when the downstream FSK signals transmit though the fiber with CD, the two FSK frequency components have different transmission speed. As a result, the downstream FSK signals are highly degraded. After re-modulation by 10-Gbit/s OOK data, the upstream signals are also distorted. Furthermore, in this scheme, the ONUs are color because optical bandpass filters are required at ONUs to convert the downstream FSK signal into OOK signal for detection.

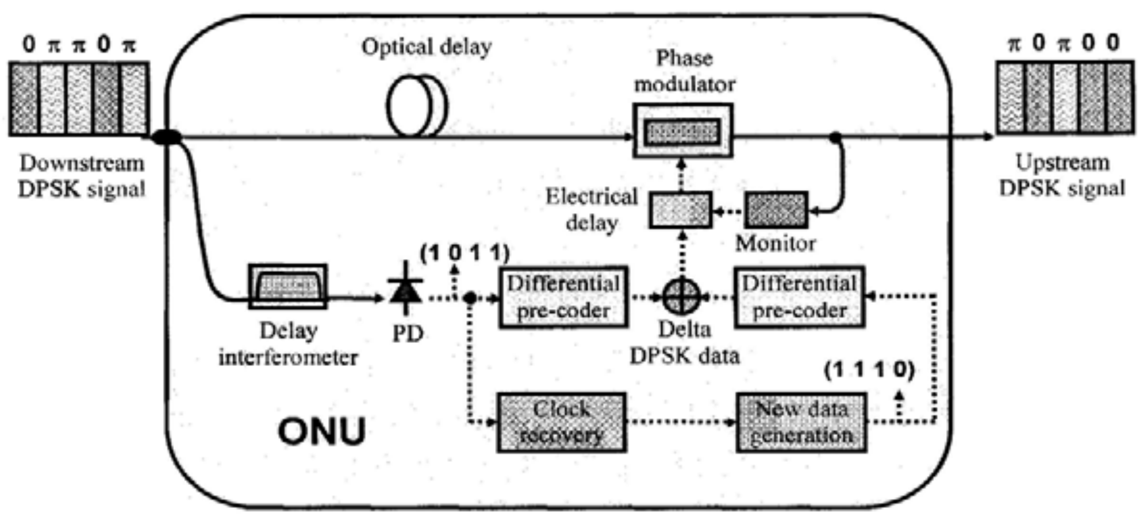

Fig. 3.2: Principle of the re-modulation scheme using downstream DPSK signal and upstream DPSK signal

The second scheme is to use downstream DPSK signal and upstream DPSK signal [79]. In this scheme, at ONUs, the downstream DPSK signals are re-modulated by a delta DPSK data, which is obtained by performing exclusive OR operation between the detected downstream DPSK signals and the upstream DPSK data in electrical domain, as shown in Fig. 3.2. However, for proper operation of this scheme, the electrical delta DPSK data should synchronize with the downstream DPSK signal.

The third scheme by using downstream IRZ signal and upstream OOK signal also needs re-modulation synchronization [78]. The upstream OOK signal is severely degraded by the dips of downstream IRZ signal if re-modulation is not synchronized.

Another scheme is to use downstream DPSK and upstream OOK [76]. However, the inferior tolerance to CD and re-modulation misalignment might not be intuitive and needs experimental verification. Therefore, we will firstly focus on the investigation of this scheme. Fig. 3.3 shows the experimental setup for the investigation. A CW light from distributed feedback (DFB) laser was phase modulated by driving a phase modulator (PM) with 10.61-Gbit/s 2^7-1 PRBS data. The generated downstream signal was transmitted through the feeder and distribution fibers. At ONU, a portion of the downstream data was tapped off by a 50/50 coupler, demodulated by a DI, and fed into a 10-Gbit/s photo-detector for detection. The rest of the optical power was re-modulated by a 10.61-Gbit/s 2^7-1 data in an intensity modulator with extinction ratio (ER) > 20 dB. An electrical delay was used in the experiment to adjust the misalignment between the phase-modulated downstream optical signal and the upstream electrical data. The re-modulated upstream signal was transmitted back to the CO and detected for BER measurement.

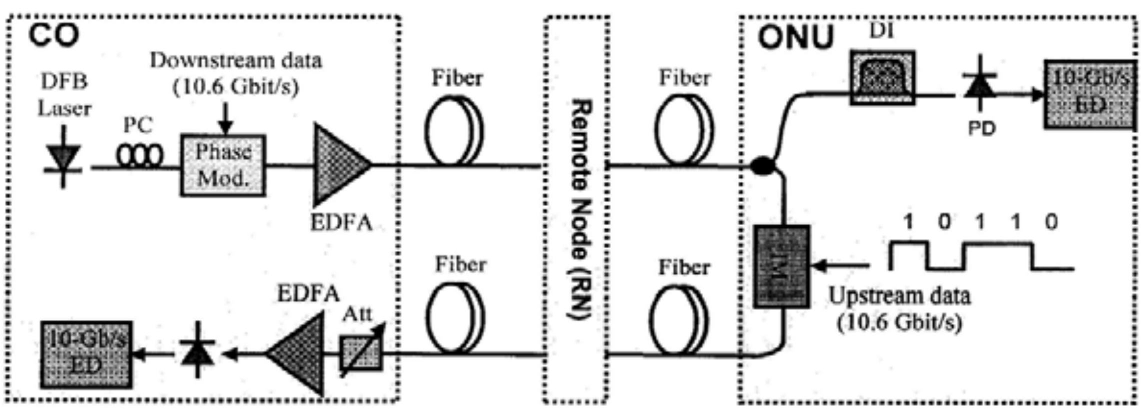

Fig. 3.3: Experimental setup for the investigation of the previous re-modulation scheme using downstream DPSK and upstream OOK

Firstly, we investigate the performance of the upstream signal under synchronized re-modulation. We consider four cases: I) back-to-back case; II) 20-km single-mode feeder fiber with CD compensation and 10-km single-mode distribution fiber without CD compensation; III) 20-km single-mode feeder fiber without CD compensation; (IV)

20-km single-mode feeder fiber without CD compensation and 10-km single-mode distribution fiber without CD compensation. Fig. 3.4 shows the BER curves of 10-Gbit/s re-modulated upstream signals for case I (circles), II (triangles), and III (diamonds) with re-modulation synchronization. The eye diagrams of the upstream signal for case II, III and IV are also shown in the figure. From the figure, it is found that the performance of the upstream signal degrades rapidly as the CD increases. The eye is completely closed for case IV even though the re-modulation is synchronized. This is because the presence of phase modulation induces chirps, which largely reduces the CD tolerance of the OOK signal even for synchronized re-modulation.

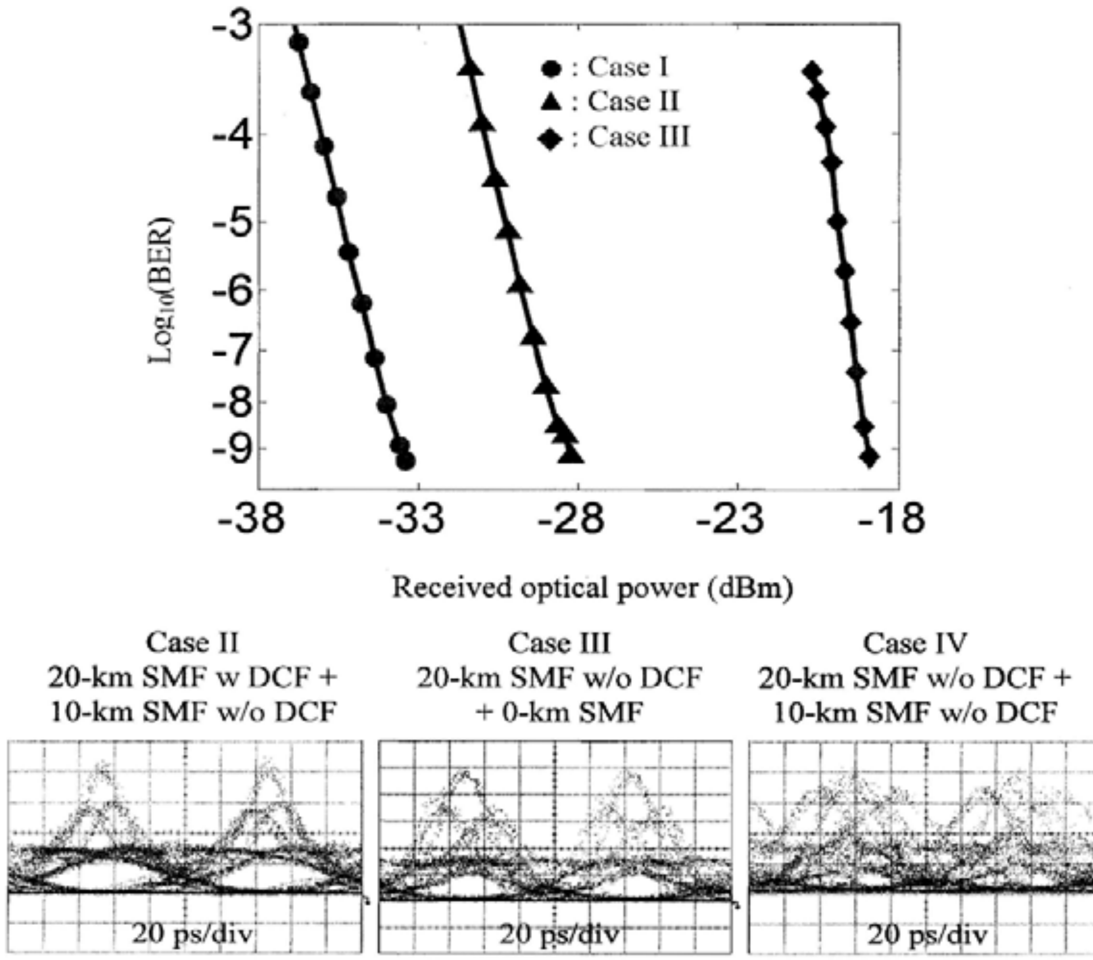

Fig. 3.4: BER curves of 10-Gbit/s re-modulated upstream signals for case I (circles), II (triangles), and III (diamonds) with re-modulation synchronization. Insets show the eye diagrams of the upstream signal for case II, III and IV.

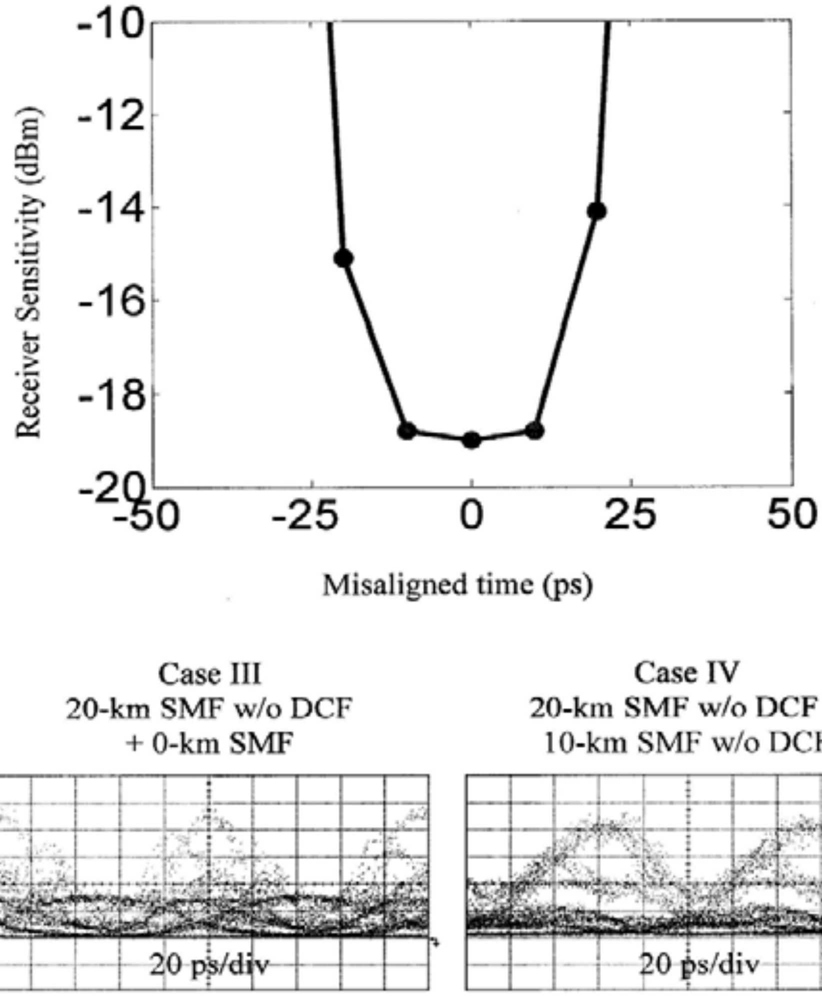

Fig. 3.5: Performance of the re-modulated upstream OOK signal versus misaligned time for case III. Insets show the eye diagrams of the upstream OOK signal with the worst misaligned time for case III and case IV.

Next, we investigate the performance sensitivity of the upstream signal to the re-modulation misalignment. Fig. 3.5 shows the performance of the re-modulated upstream OOK signal versus misaligned time for case III. Insets show the eye diagrams of the upstream OOK signal with the worst misaligned time for case III and case IV. In the experiment, different misaligned time was obtained by adjusting the relative time delay between the phase modulator at CO and the intensity modulator at ONU. Because the worst misaligned time leads to chirp in the middle rather than at the edge of the time slot of the upstream OOK signal, compared to the case of synchronized re-modulation, the CD tolerance of the upstream OOK is further reduced. Therefore, as shown in Fig. 3.4 & 3.5, for case III, the eye with modulation synchronization is still open while the one with the worst misaligned time is completely closed. For case IV, no matter the modulation is synchronized or not, the eyes are both closed.

3.1.2. Proposed Re-modulation Scheme with Enhanced Tolerance to CD and Re-modulation Misalignment

In our work, we propose a novel re-modulation scheme with reduced extinction-ratio (ER) downstream OOK signal and upstream DPSK signal. We show that, despite its back-to-back penalty, such scheme can support a colorless WDM-PON of 30-km CO-ONU distance without CD compensation and re-modulation synchronization within 1-dB penalty for both 10-Gbit/s downstream and 10-Gbit/s upstream transmission.

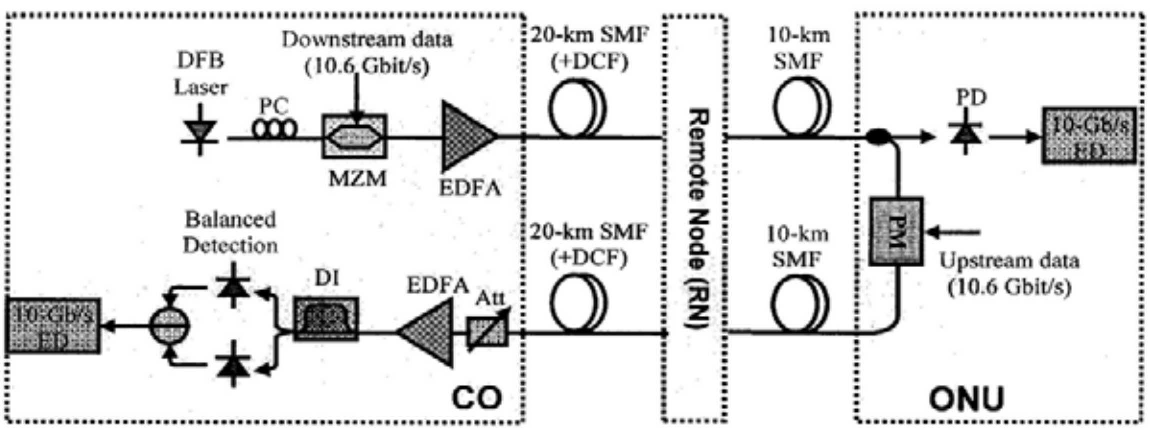

Fig. 3.6: Experimental setup

Fig. 3.6 shows the experimental setup of the proposed scheme. A CW light from DFB laser was intensity modulated with finite ER by driving an MZM with 10.61-Gbit/s 2^7-1 PRBS data. The ER was 4.9 dB. The generated downstream signal was transmitted through 20-km feeder fiber and 10-km distribution fiber. The feeder fiber was usually CD compensated by a piece of DCF in the previous schemes. In contrast, the distribution fiber cannot be CD compensated in practice because its distance varies for different ONU. In our experiment, two cases were considered: I) a DCF for the feeder fiber and no DCF for the distribution fiber; II) no DCF for both feeder and distribution fibers. At the RN, an optical bandpass filter (~ 1 nm) was used to simulate the effect of optical filtering. At ONU, a portion of the downstream data was tapped off by a 50/50 coupler and fed into a 10-Gbit/s photo-detector. The rest of the optical power was re-modulated by a 10.61-Gbit/s 2^7-1 data in a PM. An electrical delay was used in the experiment to adjust the misalignment between the intensity-modulated downstream optical signal and the upstream electrical data. Since ONU is wavelength independent, it is colorless. Furthermore, the use of DPSK format as upstream data relaxes the power budget of the network because the PM has 3 dB less power loss than the MZ intensity modulator and even much less power loss than the electro-absorption modulation (EAM). The re-modulated upstream signal was transmitted back to the CO, demodulated by a DI and detected by a 45-Gbit/s balanced detector for BER measurement. The use of 45-Gbit/s balanced detector for 10-Gbit/s data detection was only restricted by our equipment availability. 45-Gbit/s balanced detector was not optimized for 10-Gbit/s detection and had poor back-to-back receiver sensitivity of around -14 dBm for pure DPSK signal. Therefore, an optical pre-amplifier was used before the detector to investigate the OSNR penalty.

Fig. 3.7 shows performance of 10-Gbit/s pure OOK signal (circles), 10-Gbit/s downstream OOK signal of back-to-back (triangles), case I (diamonds), and case II (squares). Insets show the eye diagrams of the downstream OOK signal for case I and case II. From the figures, it is shown that due to the finite ER (4.9 dB), 3.5-dB back-to-back penalty is exhibited for the downstream OOK signal. However, the downstream signal is robust to CD, with 0.4-dB and 0.6-dB penalty for case I and II respectively.

Fig. 3.8 shows the performance of 10-Gbit/s pure DPSK signal (circles), 10-Gbit/s re-modulated upstream DPSK signal of back-to-back (triangles), case I (diamonds), and case II (squares) with re-modulation synchronization. Insets show the eye diagrams of the upstream DPSK signal of back-to-back, case I, and case II. From this figure, we can find that the downstream OOK signal causes 3.9-dB back-to-back penalty to the re-modulated upstream DPSK signal. However, despite such penalty, the presence of intensity modulation has little impact on the CD tolerance of the re-modulated DPSK signal. Therefore, only 0.5-dB and 0.9-dB penalties are observed for case I and case II, respectively.

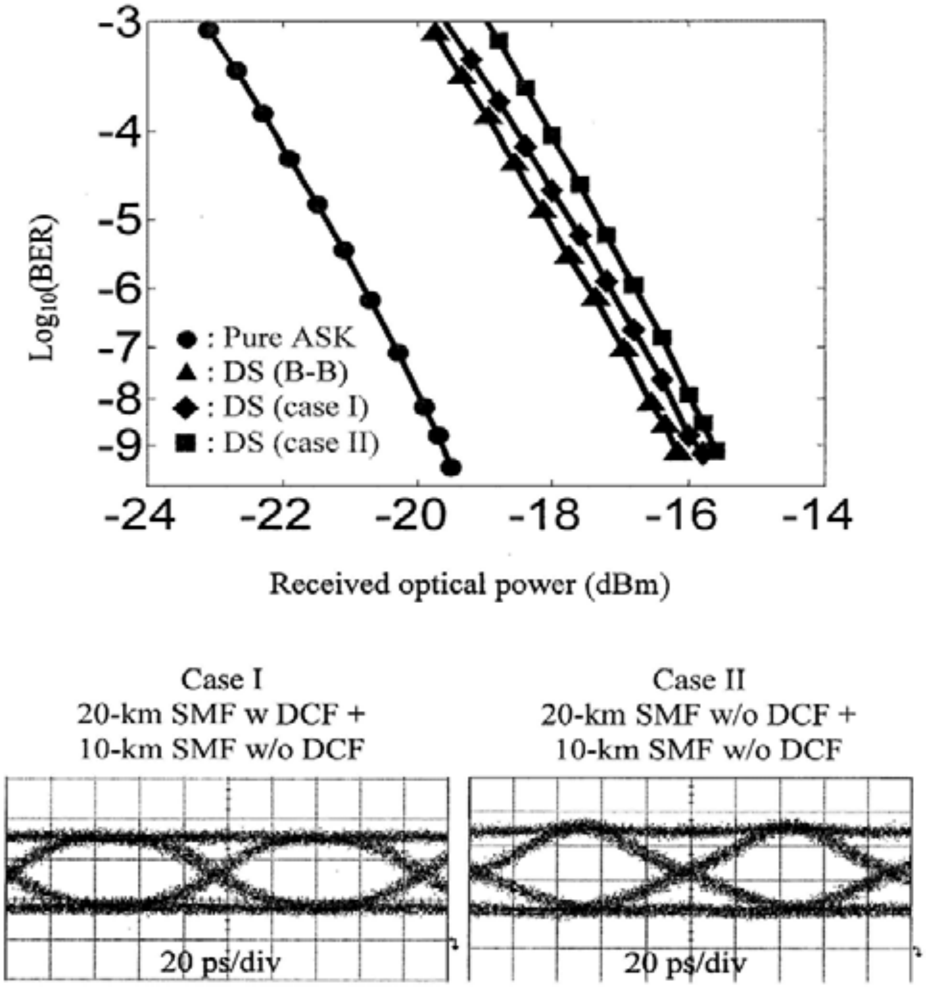

Fig. 3.7: Performance of 10-Gbit/s pure OOK signal (circles), 10-Gbit/s downstream OOK signal of back-to-back (triangles), case I (diamonds), and case II (squares). Insets show the eye diagrams of the downstream OOK signal for case I and case II.

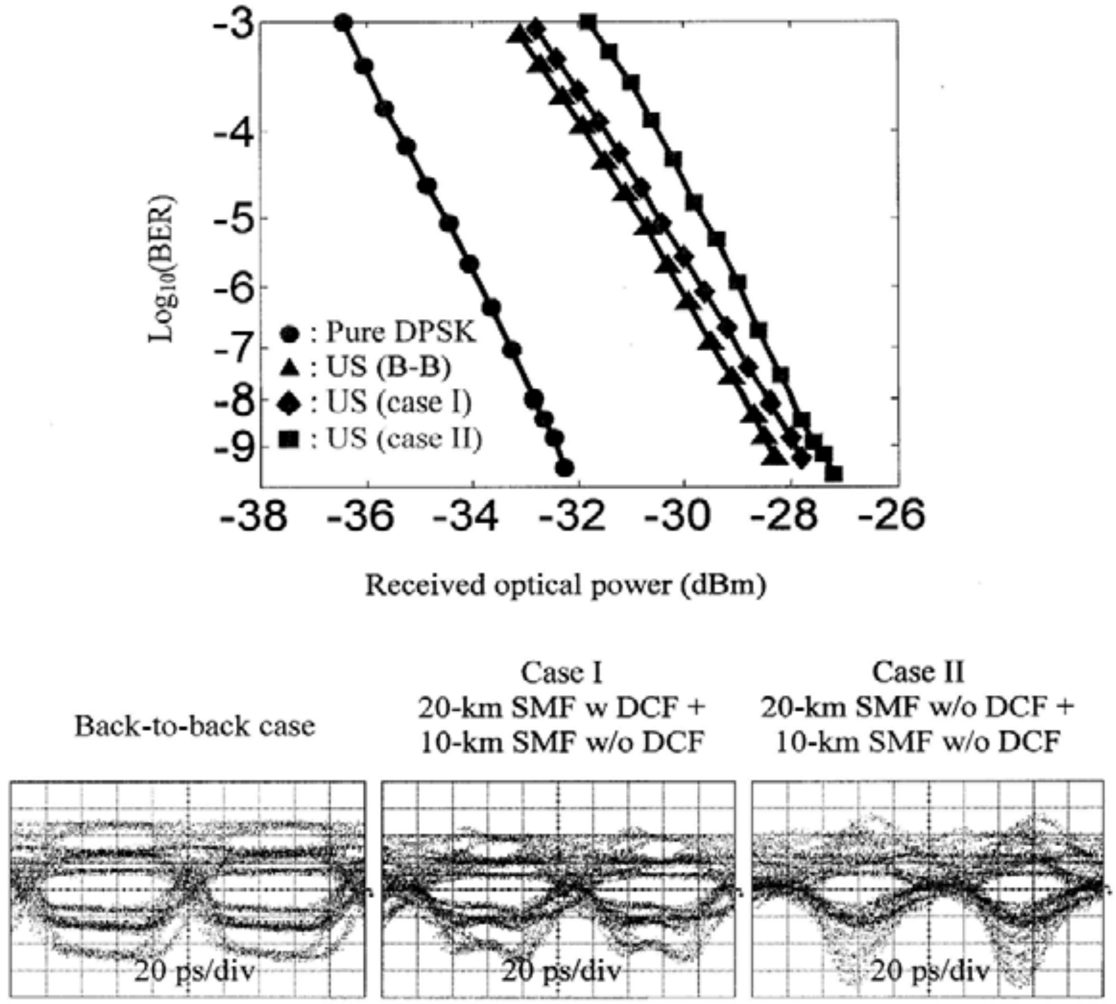

Fig. 3.8: Performance of 10-Gbit/s pure DPSK signal (circles), 10-Gbit/s re-modulated upstream DPSK signal of back-to-back (triangles), case I (diamonds), and case II (squares) with re-modulation synchronization. Insets show the eye diagrams of the upstream DPSK signal of back-to-back, case I, and case II.

Next, we investigate the tolerance of the proposed scheme to re-modulation misalignment, as shown in Fig. 3.9. Circles and triangles represent case I and case II, respectively. Insets show the eye diagrams of the upstream DPSK signal of case I and case II under 0-ps misaligned time and 50-ps misaligned time. From the figure, it is observed that the proposed scheme is robust to re-modulation misalignment. The sensitivity fluctuation is within 0.6 dB for both cases.

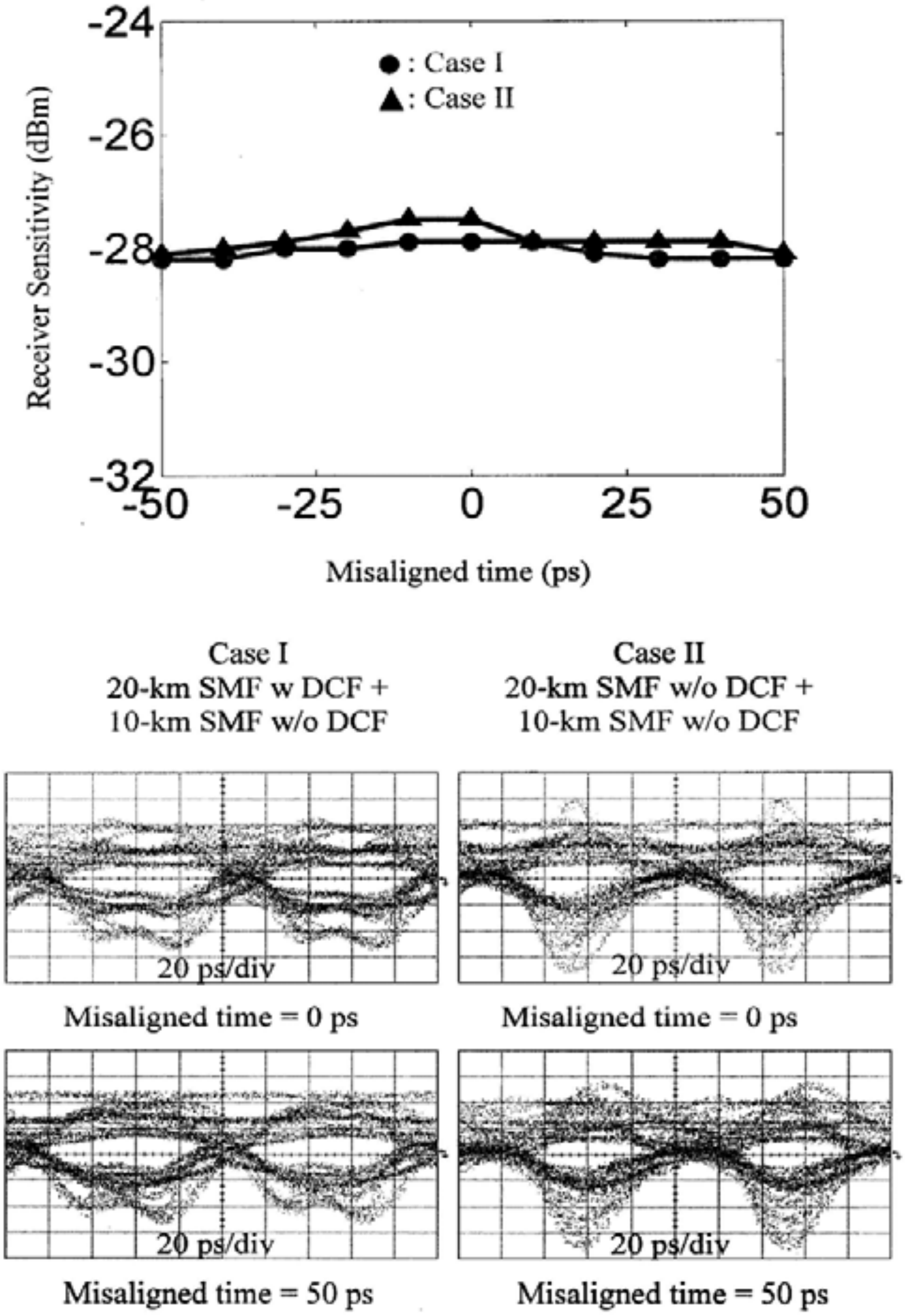

Fig. 3.9: Tolerance to re-modulation misalignment. Circles and triangles represent case I and case II, respectively. Insets show the eye diagrams of the upstream DPSK signal of case I and case II under 0-ps misaligned time and 50-ps misaligned time.

3.1.3. Summary

In summary, we experimentally showed that for the previous scheme using downstream DPSK signal and upstream OOK signal, despite its better back-to-back sensitivity, closed eye was exhibited for the upstream signal for CO-ONU of 20-km SMF without CD compensation and re-modulation synchronization. A novel re-modulation scheme using finite-ER downstream OOK and upstream DPSK was proposed. By using this technique, a 30-km-range high-speed colorless CLS WDM-PON without CD compensation and re-modulation synchronization was achieved within 1-dB penalty for both 10-Gbit/s downstream and 10-Gbit/s upstream transmission.

3.2. MLSE of Upstream Signals for Asynchronous Modulation and CD Compensation in High-Speed Centralized SC BLS WDM-PON

SC generation by feeding a pulse train into an SC nonlinear fiber is an effective way to obtain a BLS with more than one hundred high-quality and well wavelength-managed upstream carriers [133]. Broadband SC spectrum also has higher OSNR compared to that generated by conventional BLS such as light-emitting diode. Therefore, it can support larger number of channels with higher data rate (10 Gbit/s) and longer transmission distance [75]. In SC-BLS WDM-PON, to achieve proper upstream data modulation, it is essential to locate the pulse peak of the upstream carriers in the middle of the upstream data bit slot. However, because the optical pulse carriers are generated at CO but modulated at ONUs, the synchronization between upstream pulse carriers and upstream data is difficult. Furthermore, CD becomes an important issue for upstream signals due to high transmission data rate of 10 Gbit/s and wide spectral width, as wide as the bandwidth of the AWG for channel slicing. Therefore, both CD compensation components and alignment monitors at ONUs for upstream modulation synchronization are required. As a result, the operation complexity of ONUs as well as the cost of the network is increased.

Recently, electronic impairment compensation has attracted considerable interest because of its significant cost saving and adaptive compensation capability. In this paper, we propose MLSE for upstream signal detection in SC-BLS WDM-PON. We analytically show that MLSE at CO can effectively compensate the impairments from not only CD in the fibers but also asynchronous upstream modulation at ONUs. Compared to the conventional method by using alignment monitors at ONUs and all-optical CD compensation components, the proposed method features significant cost saving, lower power requirement for upstream signals, and lower maintenance cost for ONUs in SC-BLS WDM-PON.

3.2.1.Principle

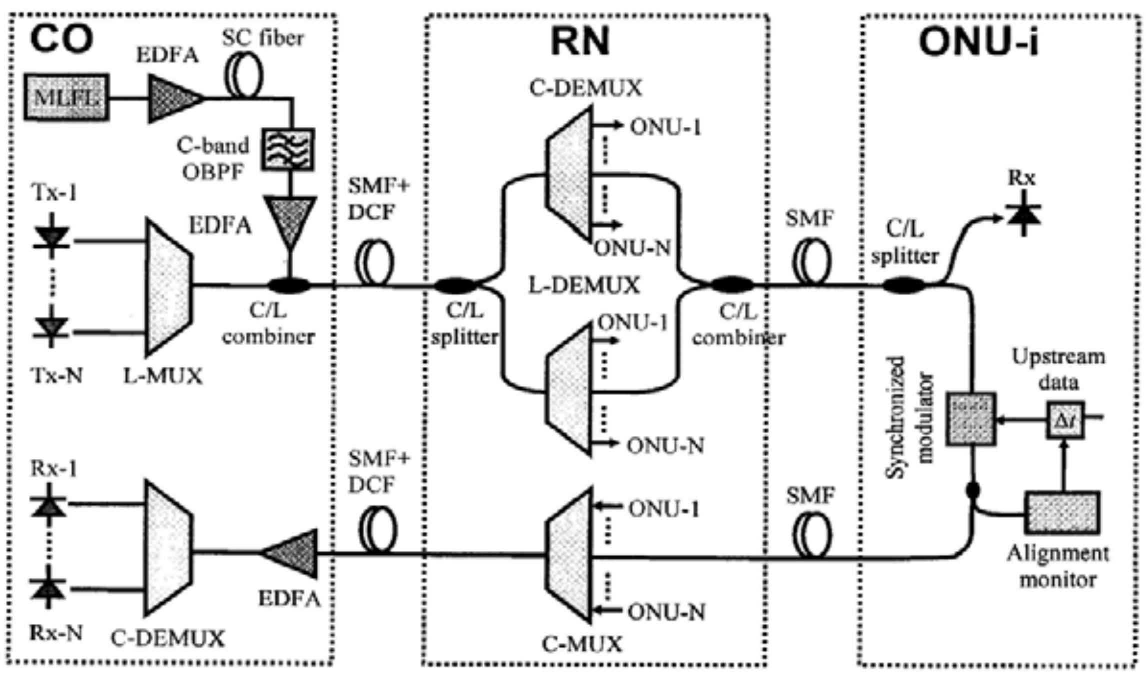

Fig. 3.10: Architecture of SC-BLS WDM-PON.

Fig. 3.10 shows the general architecture of SC-BLS WDM-PON [3]. A C-band 10-Gbit/s SC light source and L-band 10-Gbit/s DFB transmitters are located at CO for the generation of upstream carriers and downstream signals, respectively. The SC spectrum is generated by launching an optical pulse train from a mode-locked fiber laser (MLFL) into a nonlinear SC fiber. The broadened SC spectrum is then filtered by a C-band OBPF and combined with the downstream signals by a C/L band combiner. The combined upstream carriers and downstream signals are fed into a piece of SMF with CD compensation by a DCF in conventional architecture [75]. At the remote-node (RN), the upstream carriers and downstream signals are separated by a C/L band splitter, and demultiplexed by C-band and L-band demultiplexers (DEMUXs) respectively. Each ONU consists of a receiver for downstream signal detection and a synchronized modulator for upstream data modulation. The 10-Gbit/s upstream signals from ONUs are multiplexed by a C-band multiplexer (MUX) at RN and sent back to CO, where they are demultiplexed for detection. In this WDM-PON with colorless ONUs, both downstream and upstream signals can operate at 10 Gbit/s. In principle, SC-BLS can generate more than one hundred high-quality upstream carriers by spectrum slicing. However, CD becomes an issue for upstream signals due to high data rate of 10 Gbit/s and wide spectral width which is determined by the bandwidth of the C-band MUX/DEMUX. Furthermore, the upstream pulse carriers generated from SC-BLS needs to synchronize with the upstream data at ONUs.

To solve these problems, MLSE is proposed for upstream signal detection. Fig. 3.11 depicts the analytical model of the proposed method. In the figure, downstream link is omitted because it is not the bottleneck of the network and can be neglected. The SC spectrum is generated by feeding an optically amplified 1545-nm 3.5-ps 10-Gbit/s pulse train into a normal-dispersive dispersion-flattened fiber. The use of such kind of fiber is essential to enable the SC generation with a flat and stable spectrum [134]. The pulse evolution in the SC fiber is governed by the following equation [90]:

$$\frac{\partial A(z,t)}{\partial z} + i\frac{\beta_2}{2}\frac{\partial^2 A(z,t)}{\partial t^2} = i\gamma \left|A(z,t)\right|^2 A(z,t) \tag{3.1}$$

where $A(z, t)$ is the slowly varying pulse envelope. The nonlinear coefficient γ and the group velocity dispersion parameter β_2 are 2.2 W^{-1}/km and 0.24 ps^2/km respectively. Dispersion slope and fiber loss of the dispersion flattened fiber are negligible for practical consideration. The peak power of the optical pulses into the SC fiber, P, is 6 W. Split-step Fourier method is used to calculate (3.1).

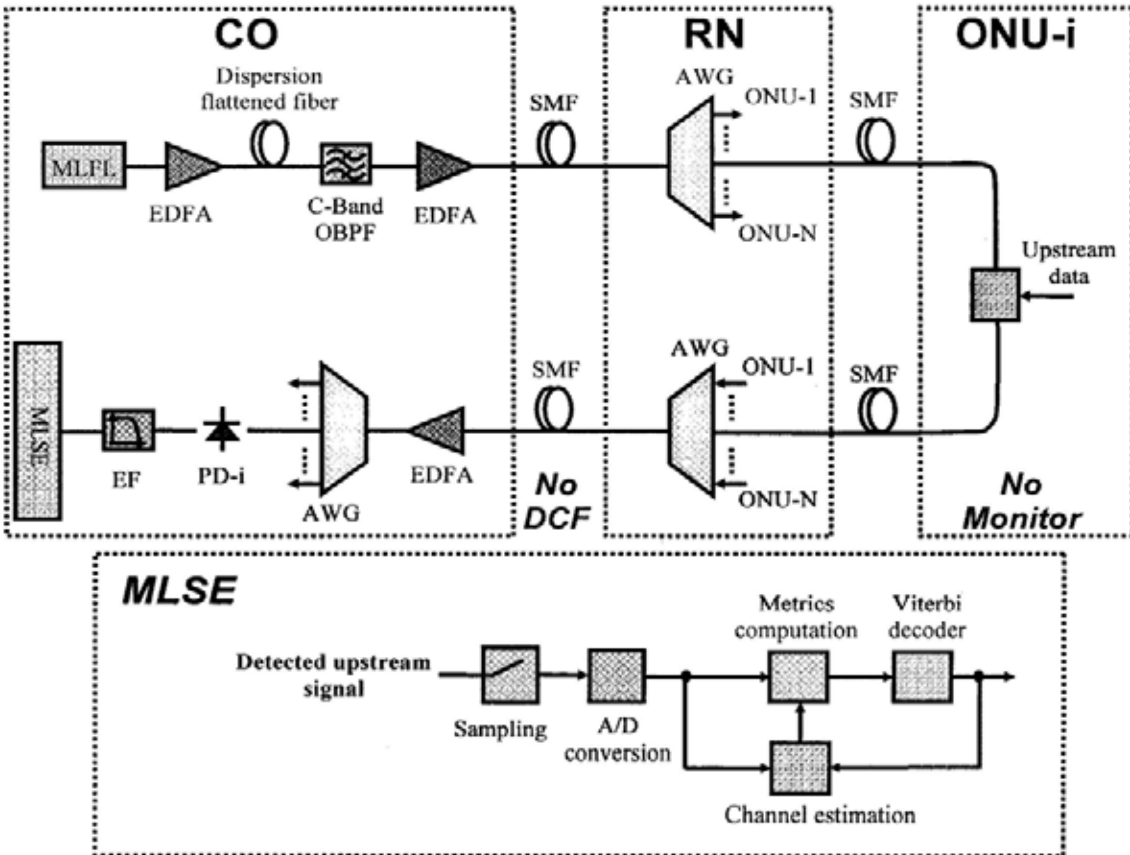

Fig. 3.11: Analytical model of the proposed method.

Fig. 3.12(a) shows the 3-dB bandwidth of broadened SC spectrum versus SC fiber length. In the figure, the two spectral broadening processes are due to self-phase modulation (SPM) and four-wave mixing (FWM), respectively. $L_m = \rho \cdot (L_d \cdot L_n)^{1/2}$ in the figure denotes the fiber length when the spectral width reaches its first maximum, where the dispersion length L_d is T_0^2/β_2 and the nonlinear length L_n is $1/(\gamma P)$ [135]. T_0 is the input pulse width. ρ is a proportional factor and is pulse-shape dependent. To achieve optimal SC spectrum in terms of broadened SC spectral bandwidth and sliced upstream pulse quality, the SC fiber length L is chosen to be $L_m < L = 3$ km $< 2L_m$ [135]. Fig. 3.12(b) shows the spectral profile at L=3 km. From the figure, it is shown that slight power fluctuation is exhibited for the SC spectrum from -800 to 800 GHz, which will lead to different sliced power for different channels as discussed later.

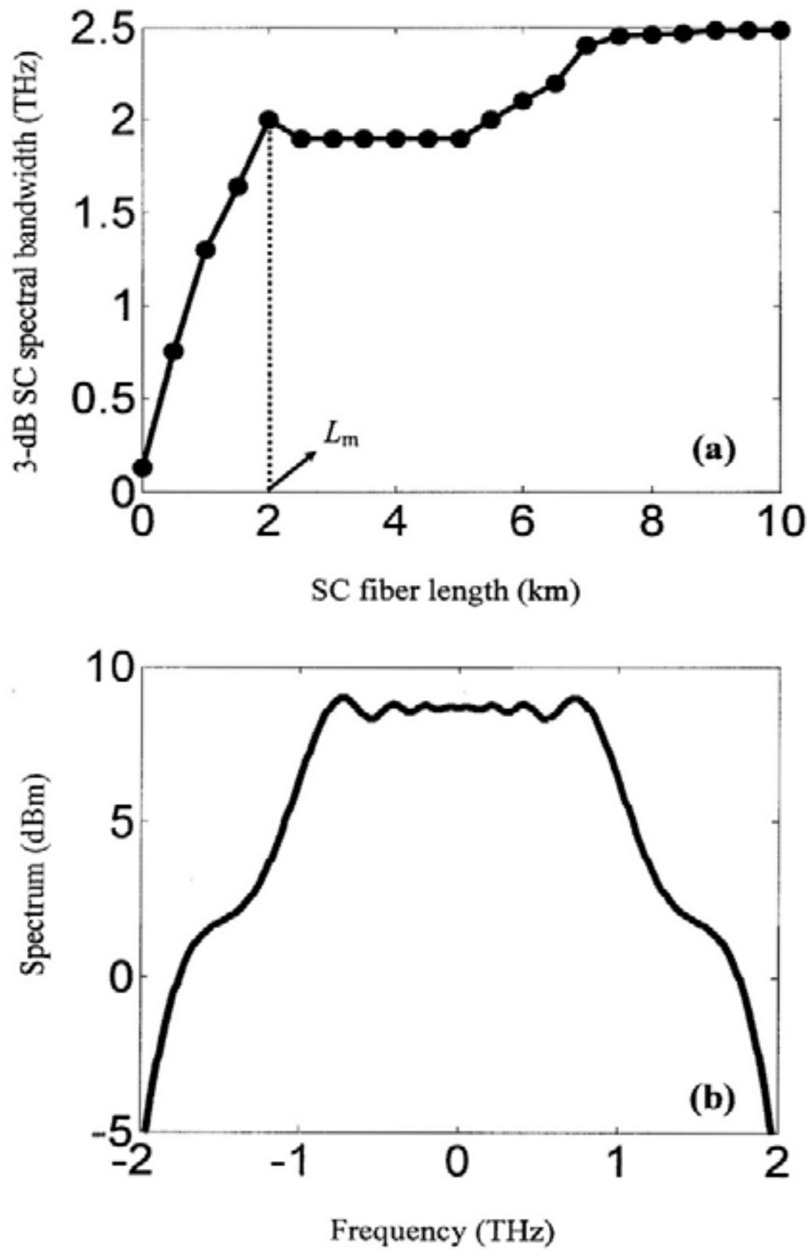

Fig. 3.12: (a) 3-dB bandwidth of broadened SC spectrum versus SC fiber length. (b) The spectral profile at the optimal SC fiber length.

In the transmission link of the proposed scheme (Fig. 3.11), all fiber sections, feeder fibers CO-to-RN and RN-to-CO, and distribution fibers RN-to-ONUs and ONUs-to-RN, have no CD compensation. The CD of the SMF at 1545 nm is assumed to be 16 ps/km/nm. The SC spectrum is sliced into 16 channels with 100-GHz channel spacing by an AWG at RN. The bandwidth of the AWG determines the spectral width, thus the CD tolerance, of the sliced upstream channels. In the paper, two types of AWGs are used for investigation: (1) Gaussian-shaped AWG with 35-GHz 3-dB bandwidth and (2) 2nd-order Gaussian-shaped AWG with 50-GHz 3-dB bandwidth. The sliced upstream carriers are modulated by modulators at ONUs without alignment monitors. The modulated signals are multiplexed at RN and sent back to CO.

At CO, the upstream signals are demultiplexed for detection. The detected signals are filtered by 7-GHz 4th-order Bessel EFs, sampled, A/D converted, and equalized by MLSE. The metric of MLSE, $PM(a_n)$ is

$$PM(a_n) = PM(a_{n-1}) - \sum_j \log(p(I(t_j) \mid a_{n-m}, \ldots, a_n)) \tag{3.2}$$

For one sample per bit, $j=n-m/2$. For two samples per bit, $j=n-m/2$ or $n+1/2-m/2$. a_n and $p(I(t_j) \mid a_{n-m},\ldots,a_n)$ are the nth upstream logical data and the probability of the sampled upstream signal value at time t_j given the logical data $a_{n-m},\ldots,a_n$, respectively. m is the memory length and is assumed to be 4. Assuming that in the sequence estimation using Viterbi algorithm, the estimated path ($b_0\ b_1 \ldots b_{n-1}\ b_n$) diverges from the correct path ($a_0\ a_1 \ldots a_{n-1}\ a_n$) at state k and remerges with the correct path at state $k+L$. Define two vectors to evaluate the error event in the estimation as $\varepsilon_c=[a_{k-m}\ a_{k-m+1} \ldots a_{k+L-2}\ a_{k+L-1}]$ and $\varepsilon_e=[b_{k-m}\ b_{k-m+1} \ldots b_{k+L-2}\ b_{k+L-1}]$. The BER of MLSE is:

$$P_e = \sum_{\varepsilon_e \neq \varepsilon_c} P(\varepsilon_c \rightarrow \varepsilon_e) w(\varepsilon_c, \varepsilon_e) (\frac{1}{2})^{L+m} \tag{3.3}$$

where $P(\varepsilon_c \rightarrow \varepsilon_e)$ is the probability of the error event of transmitting ε_c but receiving ε_e. $w(\varepsilon_c, \varepsilon_e)$ is the number of nonzero components in the vector of $[(b_k-a_k)\ (b_{k+1}-a_{k+1}) \ldots (b_{k+L-m-1}-a_{k+L-m-1})]^T$.

The power budget for the upstream signals in Fig. 3.11 can be calculated. We find that the loss from the spectrum slicing is around 18 dB and 16 dB for 35-GHz Gaussian-shaped AWG and 50-GHz 2nd-order Gaussian-shaped AWG respectively. Assume that the output power of the SC-BLS from CO, the fiber loss, the feeder-fiber length, the distribution-fiber length, and the insertion loss of the AWGs are 30 dBm, 0.2 dB/km, 20 km, 10 km, and 5 dB, respectively. The optical power entering the ONUs can be calculated to be 1 dBm and 3 dBm for 35-GHz Gaussian-shaped AWG and 50-GHz 2nd-order Gaussian-shaped AWG, respectively. We further assume that the loss for modulation at ONUs is 9 dB. Therefore, the power of the upstream signals before detection is calculated to be -26 dBm and -23 dBm for these two AWGs, respectively. Since the receiver sensitivity with pre-amplification is -38 dBm at 10 Gbit/s [75], there is more than 10-dB power margin for both AWGs. Note that compared to the conventional method using alignment monitors at ONUs and DCFs for CD compensation, the proposed method has around 8-dB power saving.

Because for a fixed SC-BLS output power, the received power of the upstream signals varies for different channels and different types of AWGs. Therefore, the performance is evaluated in terms of the SC-BLS output power penalty rather than the received upstream signal power penalty. The SC-BLS output power penalty is with respect to the required SC-BLS output power for the 9th upstream channel to achieve BER of 10^{-9} in the absence of asynchronous modulation and CD under 50-GHz 2nd-order Gaussian-shaped AWG.

3.2.2. MLSE for Asynchronous-Modulation Compensation

Firstly, the performance of MLSE to compensate asynchronous modulation of upstream pulse carriers is investigated. Fig. 3.13 depicts the SC-BLS power penalty (dB) versus misaligned time for the 9th upstream channel by using conventional optimal threshold detection (solid) and one-sample per bit MLSE with the sampling phase at the center of eyes (dashed). Triangles and circles represent 35-GHz Gaussian-shaped AWG and 50-GHz 2nd-order Gaussian-shaped AWG, respectively. Insets show the eye diagrams of the upstream signal under 35-GHz Gaussian-shaped

AWG when the misaligned time is 0 ps and 50 ps. In the figure, feeder-fiber length and distribution-fiber length are assumed to be 0 km. From the figure, it is shown that when the misaligned time is 0 ps, 35-GHz Gaussian-shaped AWG (triangles) has around 3.2-dB SC-BLS power penalty increase compared to 50-GHz 2nd-order Gaussian-shaped AWG (circles). It is because for 35-GHz Gaussian-shaped AWG, larger SC-BLS power is required to compensate the larger power loss from narrower-band optical spectrum slicing. When the upstream pulse carriers and the upstream data are not synchronized, the modulated upstream signals are highly degraded under conventional optimal threshold detection irrespective of the types of AWGs. For the misaligned time of -50 ps or 50 ps, the eyes are completely closed due to ISI, as shown in the insets of Fig. 3.13. By employing MLSE, however, the penalty is largely reduced. For misaligned time of -50 ps or 50 ps, the SC-BLS power penalties are bounded by 4.8 dB and 1.6 dB for 35-GHz Gaussian-shaped AWG and 50-GHz 2nd-order Gaussian-shaped AWG respectively. Notice that for 35-GHz Gaussian-shaped AWG, the penalty caused by asynchronous modulation is also 4.8-3.2=1.6 dB. These results can be interpreted as follows. In the absence of CD, the impairment from asynchronous modulation is generalized as ISI with memory length $m \leq 2$. We can derive BER of one-sample per bit MLSE from (3.3) as:

$$\begin{aligned} P_e \approx\ & Q\Big(\Big(\frac{f(0,0,1)^2 + f(0,1,0)^2 + f(1,0,0)^2}{2N_0}\Big)^{1/2}\Big) \\ & + \sum_{L=4}^{+\infty} (L-2)\Big(\frac{1}{2}\Big)^{L-3} \cdot Q\Big(\Big(\frac{f(0,0,1)^2 + (f(0,0,1) - f(0,1,0))^2}{2N_0} \\ & + \frac{(L-4)(f(0,1,0) - f(1,0,1))^2 + (f(1,0,0) - f(0,1,0))^2 + f(1,0,0)^2}{2N_0}\Big)^{1/2}\Big) \end{aligned} \tag{3.4}$$

where $f(p, q, r)$, $p, q, r \in \{0, 1\}$, is the sampled signal value given the prior, the present, and the posterior upstream logical data of p, q, and r respectively. N_0 is the noise power spectral density. For synchronized upstream modulation, $f(0, 1, 0)=f(1, 1, 1)$, $f(1, 0, 0)=f(0, 0, 1) = 0$, therefore,

$$P_e \approx Q\Big(\Big(\frac{f(1,1,1)^2}{2N_0}\Big)^{1/2}\Big) \tag{3.5}$$

For misaligned time of -50 ps, $f(0, 1, 0)=f(1, 0, 0)=f(1, 1, 1)/2$, $f(0,0,1)=0$. For misaligned time of 50 ps, $f(0, 1, 0)=f(0, 0, 1)=f(1, 1, 1)/2$, $f(1,0,0)=0$. Therefore,

$$P_e \approx 4Q\left(\left(\frac{f(1,1,1)^2}{4N_0}\right)^{1/2}\right) \tag{3.6}$$

From (3.5) and (3.6), the penalty caused by asynchronous modulation can be found to be 1.6 dB. Although the result is obtained under one sample per bit, additional calculation shows that the increase of sample number per bit cannot improve the MLSE's performance. It is because the energy of the upstream RZ signals is concentrated at the center of eyes and additional sample between eyes is unable to provide more information.

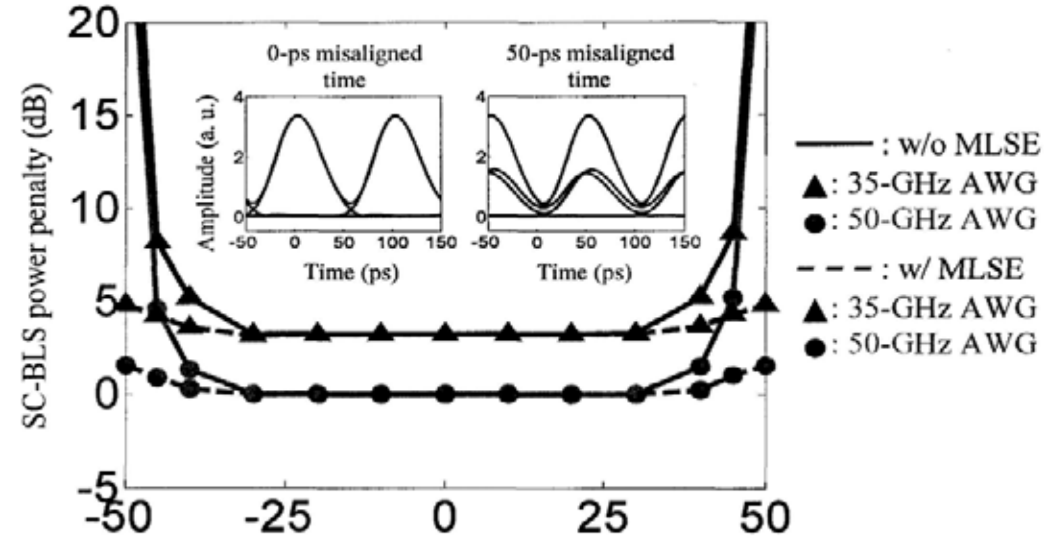

Fig. 3.13: SC-BLS power penalty (dB) versus misaligned time for the 9th upstream channel by using conventional optimal threshold detection (solid) and one-sample per bit MLSE (dashed). Triangles and circles represent 35-GHz Gaussian-shaped AWG and 50-GHz 2nd-order Gaussian-shaped AWG respectively. Insets show the eye diagrams of the upstream signal under 35-GHz Gaussian-shaped AWG when the misaligned time is 0 ps and 50 ps.

Fig. 3.14 shows the SC-BLS power penalty (dB) by using two-sample per bit

MLSE for 16 upstream channels when the misaligned time is 50 ps. Triangles and circles represent 35-GHz Gaussian-shaped AWG and 50-GHz 2nd-order Gaussian-shaped AWG respectively. From the figure, it is shown that the power penalty varies with the upstream channels irrespective of the types of AWGs. However, such variation is due to the different sliced power from SC-BLS for different channels, as shown in Fig. 3.12(b). Additional results show that the penalty caused by asynchronous modulation is independent of the upstream channels as well as the types of AWGs and is bounded by 1.6 dB.

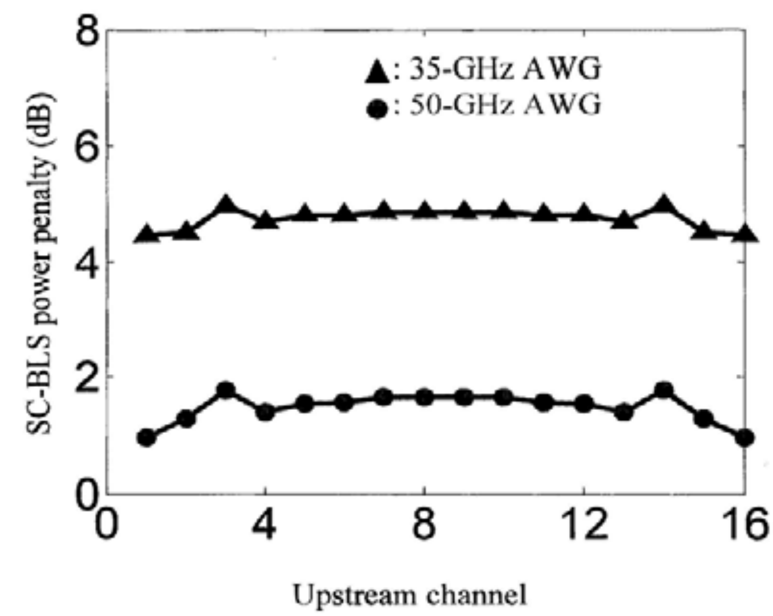

Fig. 3.14: SC-BLS power penalty (dB) under MLSE for 16 upstream channels when the misaligned time is 50 ps. Triangles and circles present 35-GHz Gaussian-shaped and 50-GHz 2nd-order Gaussian-shaped AWGs respectively.

3.2.3.MLSE for CD Compensation

Fig. 3.15(a) shows the SC-BLS power penalty (dB) versus the feeder-fiber length for the 9th upstream channel by using conventional optimal threshold detection (circles), one-sample per bit MLSE with the sampling phase at the center of the bit slot (triangles), one-sample per bit MLSE with the sampling phase between the bit slot (squares), and two-sample per bit MLSE (diamonds). In the figure, 50-GHz 2nd-order

Gaussian-shaped AWG and 0-km distribution-fiber length are assumed. From the figure, it is shown that the penalty increases rapidly under optimal threshold detection (circles). For one-sample per bit MLSE (triangles and squares), when the feeder-fiber length is less than 15 km, the optimal sampling phase is at the center of the bit slot. One-sample per bit MLSE with optimal sampling phase provides limited performance improvement compared to optimal threshold detection. It is because for short feeder-fiber length, CD does not broaden the RZ pulses to the adjacent bits and causes ISI. The SC-BLS power penalty of the upstream signals is mainly from the pulses' peak power reduction. In contrast, when the feeder-fiber length is larger than 15 km, CD-induced pulse broadening transfers the pulse energy from the center of the bit slot to the edge of the bit slot or even the adjacent bits. Therefore, the performance of MLSE with the sampling phase between eyes is comparable to that with the sampling phase at the center of eyes. One-sample per bit MLSE with optimal sampling phase can largely reduce the SC-BLS power penalty. By using two-sample per bit MLSE, the CD tolerance of the upstream signals is further improved. The SC-BLS power penalty for 30-km feeder-fiber length is limited to around 3.6 dB. To investigate the effects of AWGs on the CD tolerance of the upstream signals, Fig. 3.15(b) shows the SC-BLS power penalty (dB) versus the feeder-fiber length for the 9th upstream channel by using conventional optimal threshold detection (solid) and two-sample per bit MLSE (dashed) when the AWG is Gaussian shaped with 35-GHz bandwidth (triangles) and 2nd-order Gaussian shaped with 50-GHz bandwidth (circles). The distribution-fiber length is assumed to be 0 km. From the figure, it is shown that without MLSE (solid), despite its 3.2-dB back-to-back penalty increase, 35-GHz Gaussian-shaped AWG has comparable or better CD tolerance compared to 50-GHz 2nd-order Gaussian-shaped AWG when the feeder-fiber length is larger than 15 km. It is because by using 35-GHz Gaussian-shaped AWG, the sliced upstream channels have narrower spectral bandwidth, resulting in better CD tolerance. By using MLSE, the penalty is largely reduced irrespective of the types of AWGs. At feeder-fiber length of 30 km, the SC-BLS power penalties caused by CD under two-sample per bit MLSE are around 5.7-3.2=2.5 dB and 3.6 dB for 35-GHz Gaussian-shaped AWG and 50-GHz 2nd-order Gaussian-shaped AWG respectively.

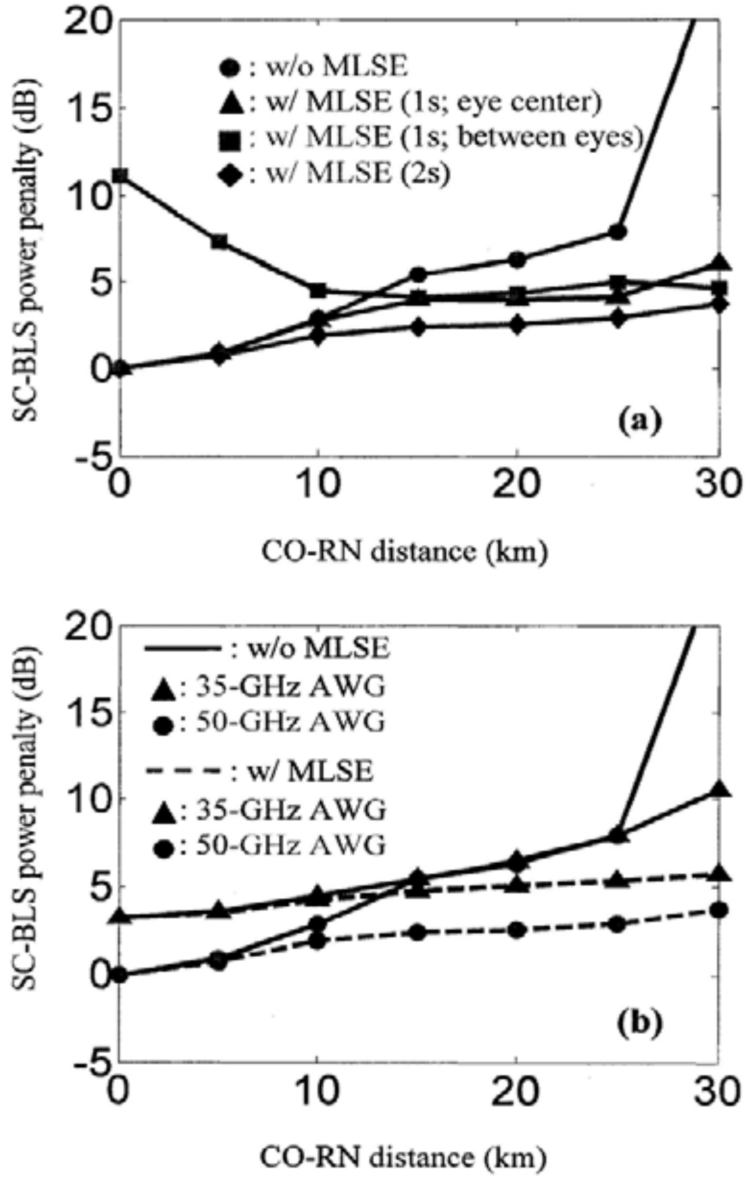

Fig. 3.15: (a) SC-BLS power penalty (dB) versus the feeder-fiber length by using conventional optimal threshold detection (circles), one-sample per bit MLSE with the sampling phase at the center of (triangles) and between the bit slot (squares), and two-sample per bit MLSE (diamonds). (b) SC-BLS power penalty (dB) versus the feeder-fiber length when the AWG is Gaussian shaped with 35-GHz bandwidth (triangles) and 2nd-order Gaussian shaped with 50-GHz bandwidth (circles).

Fig. 3.16 depicts the SC-BLS power penalty (dB) by using two-sample per bit MLSE for 16 upstream channels when the feeder-fiber length is 30 km. Triangles and circles present 35-GHz Gaussian-shaped AWG and 50-GHz 2nd-order Gaussian-shaped AWG respectively. From the figure, it is shown that similar to Fig. 3.14, the SC-BLS power penalty varies with different upstream channels irrespectively of the types of AWGs. However, such variation is due to the different sliced power from SC-BLS for different channels. The penalties caused by CD are channel independent and bounded by 2.5 dB and 3.6 dB for 35-GHz Gaussian-shaped AWG and 50-GHz 2nd-order Gaussian-shaped AWG respectively.

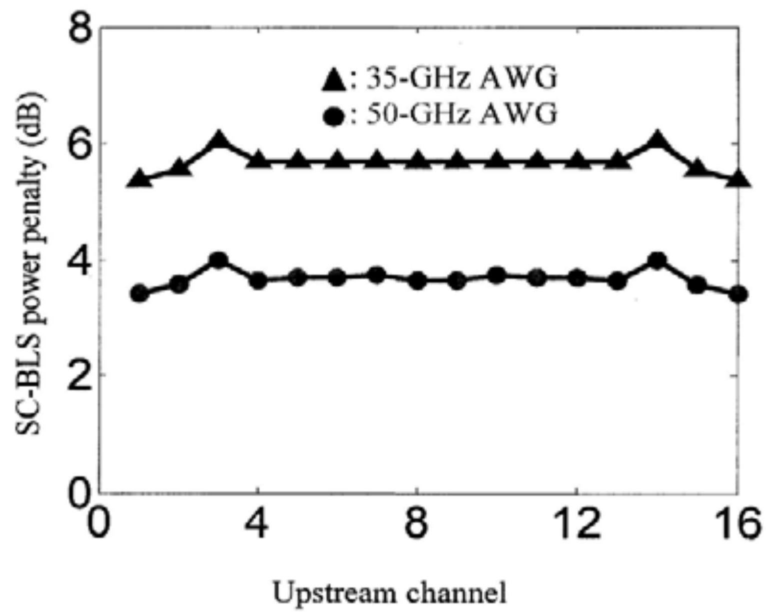

Fig. 3.16: SC-BLS power penalty (dB) under MLSE for 16 upstream channels when the feeder-fiber length is 30 km. Triangles and circles present 35-GHz Gaussian-shaped AWG and 50-GHz 2nd-order Gaussian-shaped AWG respectively.

3.2.4. MLSE for Simultaneous Asynchronous-Modulation and CD Compensation

Next, an SC-BLS WDM-PON with feeder-fiber length of 20 km and distribution-fiber length ranging from 0 km to 10 km is investigated. Fig. 3.17 shows the SC-BLS power penalty (dB) versus misaligned time for the 9th upstream channel by using optimal threshold detection (solid) and two-sample per bit MLSE (dashed) when the AWG is (a) Gaussian shaped with 35-GHz bandwidth; (b) 2nd-order Gaussian shaped with 50-GHz bandwidth. Circles, triangles, and squares represent the distribution-fiber length of 0 km, 5 km, and 10 km respectively. In Fig. 3.17(b), the curve for 10-km distribution-fiber length and by using optimal threshold detection is not plotted due to its SC-BLS power penalty larger than 20 dB as shown in Fig. 3.15. From Fig. 3.17 (a) & (b), it is shown that under optimal threshold detection (solid), the SC-BLS power penalty increases dramatically for asynchronous upstream modulation irrespective of the types of AWGs. The increase of distribution-fiber length also leads to the increase of the SC-BLS power penalty. By using MLSE (dashed), the penalty is largely reduced. To facilitate the description, we define a maximal SC-BLS power penalty, which is the maximal SC-BLS power penalty for varying misaligned time and distribution-fiber length. From Fig. 3.17, it is shown that the maximal SC-BLS power penalties by using two-sample per bit MLSE are bounded by 5.7 dB and 3.6 dB for 35-GHz Gaussian-shaped AWG and 50-GHz 2nd-order Gaussian-shaped AWG respectively. Note that for 35-GHz Gaussian-shaped AWG, there is 3.2-dB back-to-back penalty. Therefore, the penalty caused by asynchronous modulation and CD is 5.7-3.2=2.5 dB. From Fig. 3.17, it is also found that under MLSE detection (dashed), the penalty for asynchronous modulation is comparable to or even smaller than that for synchronized modulation irrespective of the types of AWGs. Such phenomenon is caused by the presence of CD and can be interpreted by Fig. 3.18. Fig. 3.18 depicts the upstream signal evolution for 50-ps misaligned time. (a) and (b) represent the cases in the absence of CD, i. e. feeder-fiber and distribution-fiber lengths of 0 km, and in the presence of CD, respectively. In (a), the pulse center is at the edge of the upstream data bit slot. Thus ISI is induced after upstream modulation. In (b), the CD in the fiber sections CO-to-RN and RN-to-ONUs introduces chirps to the upstream pulses, with positive frequency at the leading edge and negative frequency at the trailing edge. As a result, when the pulses are modulated at ONUs and transmitted back to CO through the fiber section ONUs-to-RN and RN-to-CO, not only pulse broadening effect but also pulse shifting effect are exhibited. The energy of the pulse shifts to the bit slot center, which alleviates ISI.

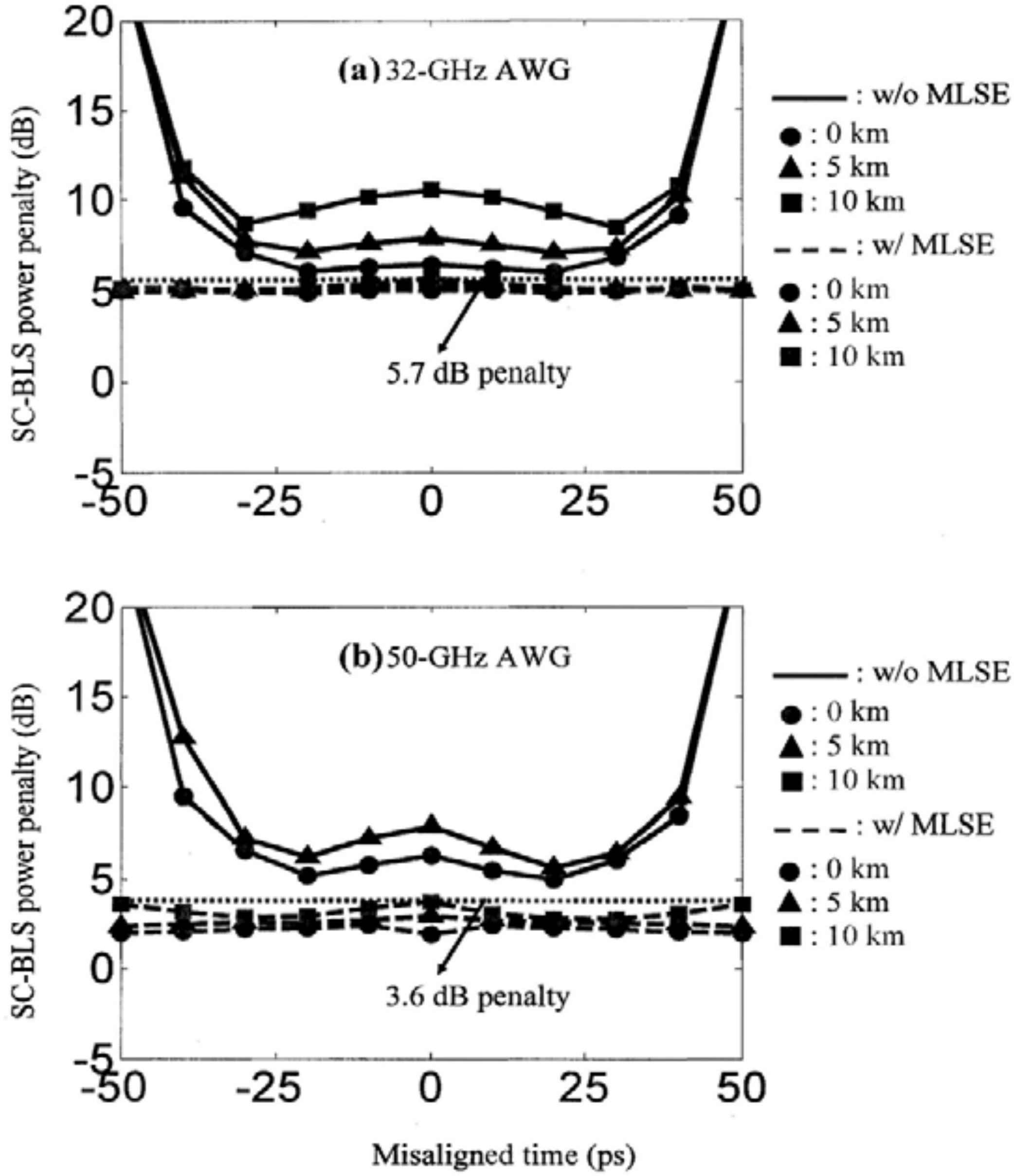

Fig. 3.17: SC-BLS power penalty (dB) versus misaligned time for the 9th upstream channel by using optimal threshold detection (solid) and two-sample per bit MLSE (dashed) when the AWG is (a) Gaussian shaped with 35-GHz bandwidth; (b) 2nd-order Gaussian shaped with 50-GHz bandwidth. Circles, triangles, and squares represent the distribution-fiber length of 0 km, 5 km, and 10 km respectively.

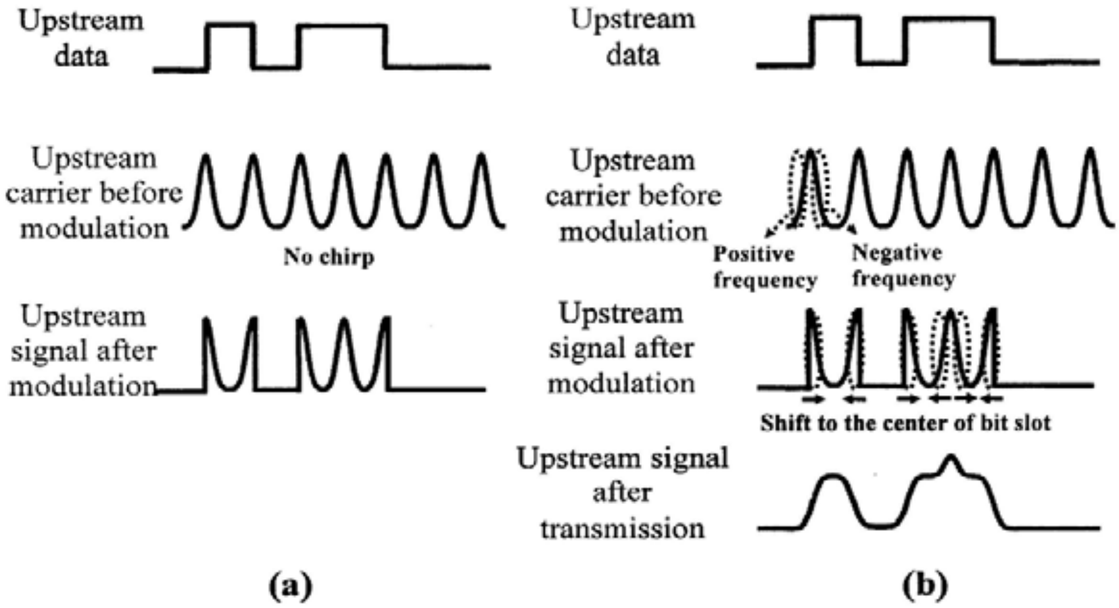

Fig. 3.18: Upstream signal evolution for 50-ps misaligned time. (a) and (b) represent the cases without and with CD respectively.

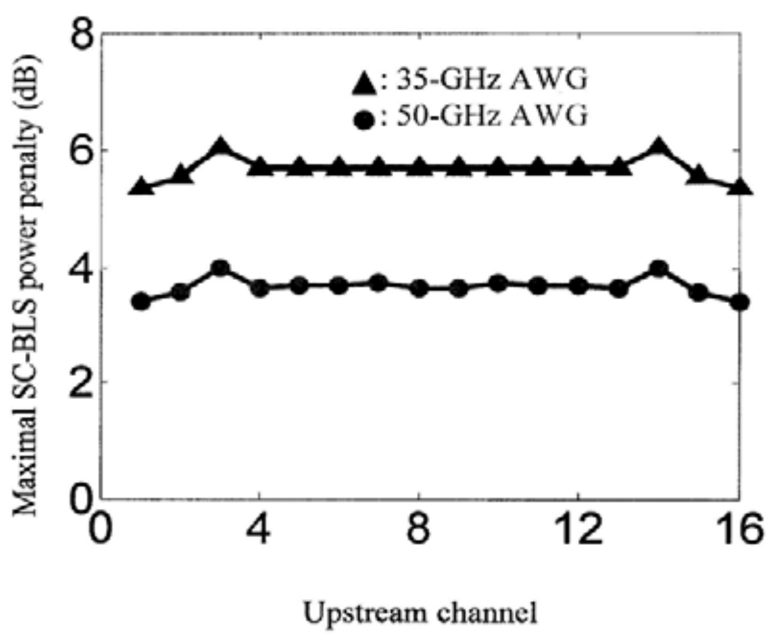

Fig. 3.19: Maximal SC-BLS power penalty (dB) by using two-sample per bit MLSE for 16 upstream channels. Triangles and circles present 35-GHz Gaussian-shaped AWG and 50-GHz 2nd-order Gaussian-shaped AWG respectively.

To evaluate the performance of MLSE for different upstream channel detection, Fig. 3.19 depicts the maximal SC-BLS power penalty (dB) by using two-sample per bit MLSE for 16 upstream channels. Triangles and circles present 35-GHz Gaussian-shaped AWG and 50-GHz 2nd-order Gaussian-shaped AWG respectively. Considering the facts (1) different channels have different sliced power from SC-BLS; (2) there is 3.2-dB back-to-back penalty for 35-GHz Gaussian-shaped AWG, we can conclude from Fig. 10 that the maximal SC-BLS power penalties caused by asynchronous modulation and CD are channel independent and are bounded by 2.5 dB and 3.6 dB for 35-GHz Gaussian-shaped AWG and 50-GHz 2nd-order Gaussian-shaped AWG respectively.

3.2.5.Summary

In summary, we have proposed MLSE for 10-Gbit/s upstream signal detection to compensate asynchronous upstream modulation at ONUs and CD in the fibers in SC-BLS WDM-PON. Analytical calculations show that MLSE bounds the penalty from asynchronous modulation by 1.6 dB for all upstream channels and different types of channel-slicing AWGs. We have investigated a 10-Gbit/s SC-BLS WDM-PON with feeder-fiber length of 20 km and distribution-fiber length ranging from 0 km to 10 km. We show that irrespective of the variation of distribution-fiber length, MLSE enables 10-Gbit/s upstream data transmission, with penalties caused by asynchronous modulation and CD bounded by 2.5 dB and 3.6 dB for 35-GHz Gaussian-shaped and 50-GHz 2nd-order Gaussian-shaped channel-slicing AWGs respectively. By eliminating alignment monitors at ONUs and all-optical CD compensation components, such technique features significant cost saving, lower power requirement for upstream signals, and lower operation complexity for ONUs in SC-BLS WDM-PON.

3.3. Summary

In summary, for the first time, we investigated the tolerance of the high-speed CLS WDM-PONs to asynchronous upstream modulation at ONUs and CD in the fibers. We showed that the previous CLS WDM-PON schemes at 10 Gbit/s suffer from CD and/or asynchronous upstream modulation. We proposed two solutions to mitigate these impairments. Firstly, we proposed a novel re-modulation scheme with enhanced tolerance to CD and asynchronous upstream modulation. Secondly, we applied MLSE for upstream signal detection in SC-based CLS WDM-PON and showed that MLSE can effectively mitigate the impairments from asynchronous upstream modulation and CD. By eliminating the modulation synchronization module and all-optical CD compensation module, the proposed methods can greatly reduce the cost and operation complexity of high-speed CLS WDM-PON.

4. High-Speed All-Optical Signal Processing of Advanced Modulation Formats

The future optical networks will be all-optical such that O-E-O conversion is eliminated, and the bit rate, format, and protocol are transparent. To achieve this goal, a lot of signal processing in network intermediate node must be implemented all optically, such as all-optical label swapping and routing. Furthermore, the recent increasing bandwidth demands constantly drive the increase of the transmission capacity of the all-optical networks. However, the data rate of networks is severely hindered by the maximal operation speed of optical and electrical components as well as the rapidly increasing signal degradation effects, such as CD and PMD.

Advanced optical modulation formats are one of the most promising technologies to significantly alleviate the transmission impairments and increase the capacity of the optical communication systems. They are also capable for enabling various high-speed operation functions in all-optical networks. For example, orthogonal modulation format has attracted a lot of interest to carry optical payload / label in optical networks concurrently.

To freely enable the employment of advanced modulation formats for high-speed optical communication in all-optical networks, all-optical signal processing of advanced modulation formats, such as all-optical format conversion and all-optical coding/decoding, are essential.

In this chapter, we will investigate high-speed all-optical signal processing of advanced modulation formats for applications in all-optical networks:

(i) We propose an all-optical format conversion from 40-Gbit/s RZ signal to 40-Gbit/s inverse RZ (IRZ) / 10-Gbit/s DPSK orthogonal modulation signal to interface high-speed transmission system using RZ format with networks using orthogonal modulation format. The proposed method firstly employs the effect of cross-gain modulation (XGM) in semiconductor optical amplifier (SOA) to convert RZ signal to IRZ signal. A DI following the SOA suppresses the pattern effect in SOA and enhances the operation data rate of the scheme up to 40 Gbit/s. Then a 10-Gbit/s DPSK signal is successfully superimposed on the 40-Gbit/s IRZ signal. Error-free 40-km SMF transmission of the converted 40-Gbit/s IRZ/10-Gbit/s DPSK orthogonal modulation signal was demonstrated.

(ii) We propose an all-optical multilevel 4-ASK coding and decoding technique. The proposed scheme encodes two input on-off-keying signals all optically into a 4-ASK signal using cross absorption modulation in an electro-absorption modulator (EAM) and employs fiber-based all-optical approach for 4-ASK data decoding. The proposed encoding method provides an effective contention resolution in the network intermediate node to maximize the network capacity while the decoding method enables the 4-ASK signal detection by using conventional OOK receiver.

4.1. 40-Gbit/s RZ Signal to 40-Gbit/s IRZ/10-Gbit/s DPSK Orthogonal Signal Conversion

RZ format has been widely used in long-haul transmission due to its several-decibel improvement in receiver sensitivity and better tolerance against PMD compared to NRZ format. On the other hand, orthogonal modulation format is an attractive multi-bit per symbol modulation format to enable high-speed spectral efficient optical transmission and to carry optical payload / label concurrently in optical networks. The format conversion of RZ format into orthogonal modulation format is a key process to interface the long-haul transmission systems with networks.

IRZ modulation format has recently aroused much attention for its applications in spectral-efficient all-optical orthogonal modulation [136]-[138]. Among the existing IRZ generation approaches, the method using the dips generated by a dual-driven MZM is simple [136]. However, in addition to the complex pre-coding, the IRZ signal is electronically generated. Thus it cannot be employed in the intermediate node of networks for all-optical format conversion. In this section, we propose an effective SOA-based format conversion from 40-Gbit/s RZ signal to 40-Gbit/s IRZ / 10-Gbit/s DPSK orthogonal signal. The transmission performance of the converted IRZ / DPSK orthogonal modulation is characterized.

4.1.1. Principle and Experimental Setup

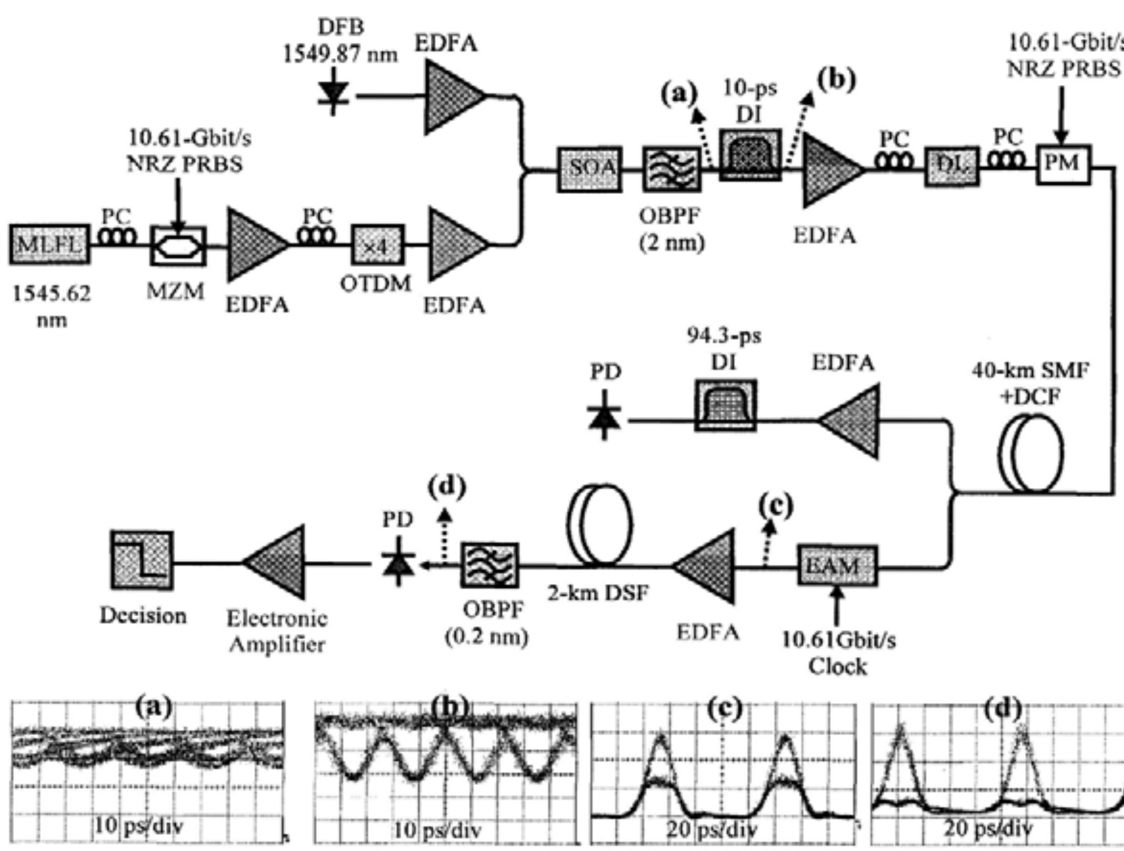

Fig. 4.1: Experimental setup. Insets show the eye diagrams at the points (a) before 10-ps DI, (b) after 10-ps DI, (c) before re-shaping, and (d) after re-shaping.

Fig. 4.1 depicts the experimental setup. A 10.61-Gbit/s 2.5-ps pulse train with the wavelength centered at 1545.62 nm was generated by the mode-locked fiber laser (MLFL) and modulated in the MZM. Then the RZ signal was optically amplified and time-division multiplexed, via fiber delay lines, to an aggregate data rate of 42.44 Gbit/s. For conversion of RZ format into IRZ format, the effect of XGM in a SOA was adopted. A CW probe beam and the 42.44-Gbit/s RZ signals were injected into the SOA. The SOA was driven by a dc bias current of 110 mA. The input power of the CW into the SOA was 13 dBm and that of the OTDM RZ signal varied from 7 dBm to 13 dBm to control the IRZ signal's ER. A 2-nm OBPF was employed to select the converted IRZ pulses. Because of the slow carrier recovery time of SOA, the resulted IRZ signal had a long tail, as shown in the inset (a) of Fig. 4.1. However, the carrier depletion in the SOA also induced cross-phase-modulation (XPM) to the IRZ signal. By properly controlling the phase of the 10-ps DI following the SOA, the IRZ dips was enhanced while the tails was suppressed through optical field interference, as shown in the inset (b) of Fig. 4.1. The generated IRZ was then phase modulated by a 10.61-Gbit/s DPSK signal to generate the IRZ/DPSK orthogonal modulation signal. The choice of 10.61-Gbit/s DPSK signal was only due to our equipment availability. 40-Gbit/sIRZ/40-Gbit/s DPSK orthogonal modulation was also possible. In practical applications, the DPSK signal can be used for carrying label or carrying another data. The optical delay (OD) before the PM was used to adjust the alignment between the IRZ pulses and the DPSK data. The generated IRZ/DPSK orthogonal signal was fed into a piece of 40-km SMF and a matched DCF. At the receiver, an EAM driven by a 10.61-Gbit/s clock provided a gating window and demultiplexed IRZ signal to 10.61-Gbit/s RZ pulses, as shown in the inset (c) of Fig. 4.1. Before detection, a re-shaping stage, consisting of a 4-km dispersion-shifted fiber (DSF) and a 0.2-nm OBPF, was employed to improve the ER. In principle, re-shaping before detection can not improve the BER. However, without the use of the re-shaping, the eye is small and is sensitive to the threshold level. Such degradation was augmented in our experiment because the electronic amplifier had a nonlinear transfer function, which squeezed the eye opening of the low-ER signal further. On the other hand, DPSK signal was demodulated by a DI with the relative delay of 94.3 ps and detected for BER measurement.

4.1.2. Performance of the Converted 40-Gbit/s IRZ Signal

Firstly, we investigate the performance of the converted 40-Gbit/s IRZ signal in the absence of DPSK modulation. Fig. 4.2 shows the BER performance of the four demultiplexed channels from the IRZ signal when the IRZ signal has the ER of 2 dB. The insets depict the eye diagrams of all four channels after the re-shaping stage. The biased dc voltage of EAM was set to be -2.49 V and the signal power into the DSF was 23 dBm. From Fig. 4.2, it is seen that clear eye opening is observed and the receiver sensitivity at a BER of 10^{-9} is around -17 dBm for all four channels.

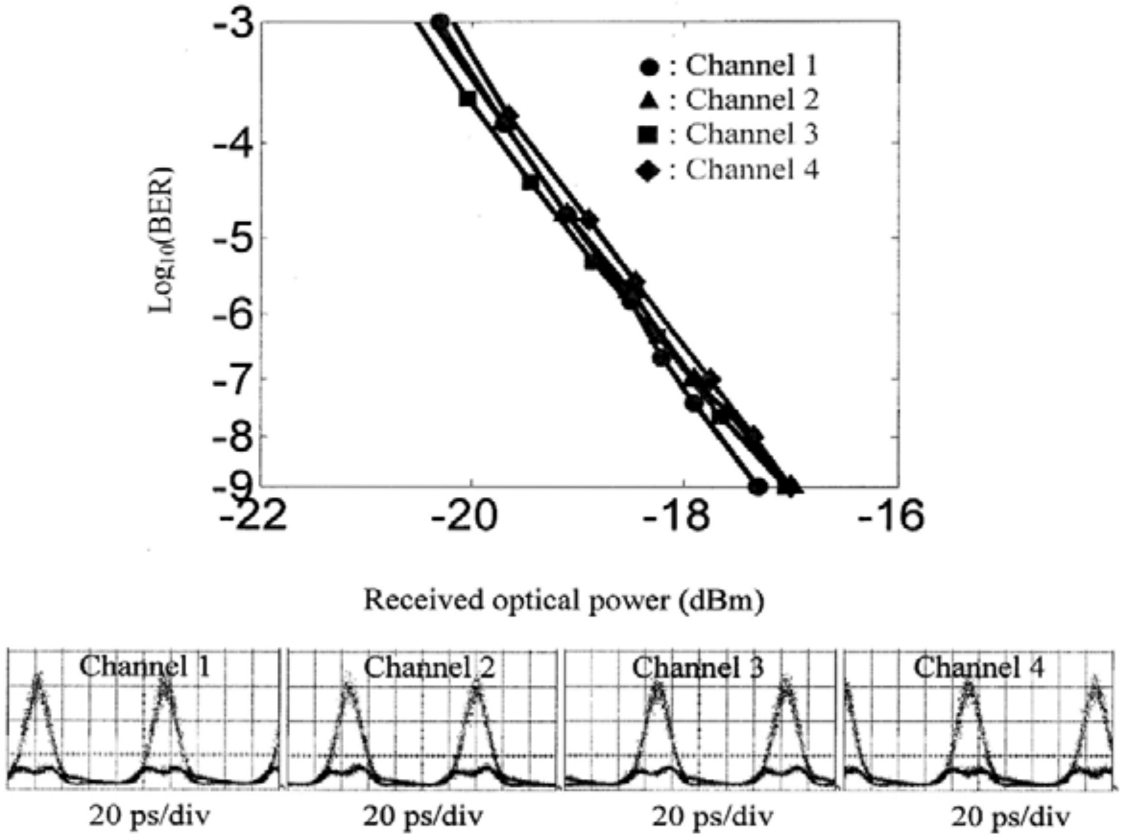

Fig. 4.2: BER performance of four demultiplexed channels from 40-Gibt/s IRZ signal. Insets show the eye diagrams of four demultiplexed channels.

To further investigate the performance sensitivity to the ER, we adjusted the bias current of the SOA and the input power of the RZ control pulses and the CW light into the SOA. Fig. 4.3 shows the BER measurement of the worst demultiplexed channel from the IRZ signal for ER of 2.6 dB (circles), 2 dB (triangles), and 1.6 dB (squares). Solid lines and dashed lines represent the back-to-back case and the case after 40-km SMF transmission respectively. From the figure, it is shown that the receiver sensitivity of -16 dBm can be achieved for all ERs in back-to-back case, indicating excellent performance of the proposed conversion method. After the 40-km SMF transmission, less than 2-dB power penalty is induced for the ER of 2.6 dB and 2 dB. At lower ER of 1.6 dB, the signal suffers from around 3-dB power penalty due to its relative vulnerability to the OSNR degradation.

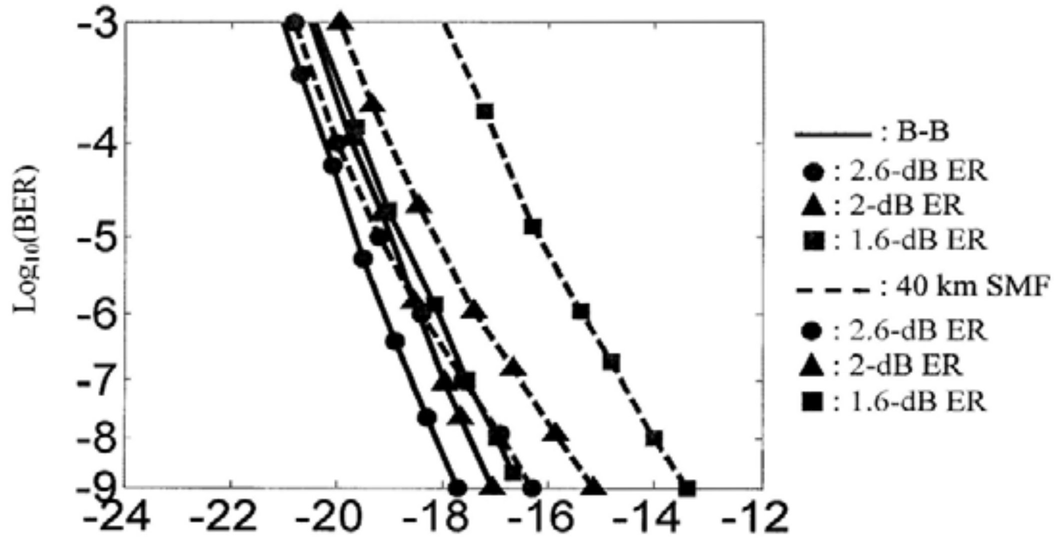

Fig. 4.3: BER measurement of the worst demultiplexed channel from the IRZ signal for ER of 2.6 dB (circles), 2 dB (triangles), and 1.6 dB (squares). Solid lines and dashed lines represent the back-to-back case and the case after 40-km SMF transmission respectively.

4.1.3.Performance of the Converted IRZ/DPSK Orthogonal Modulation Signal

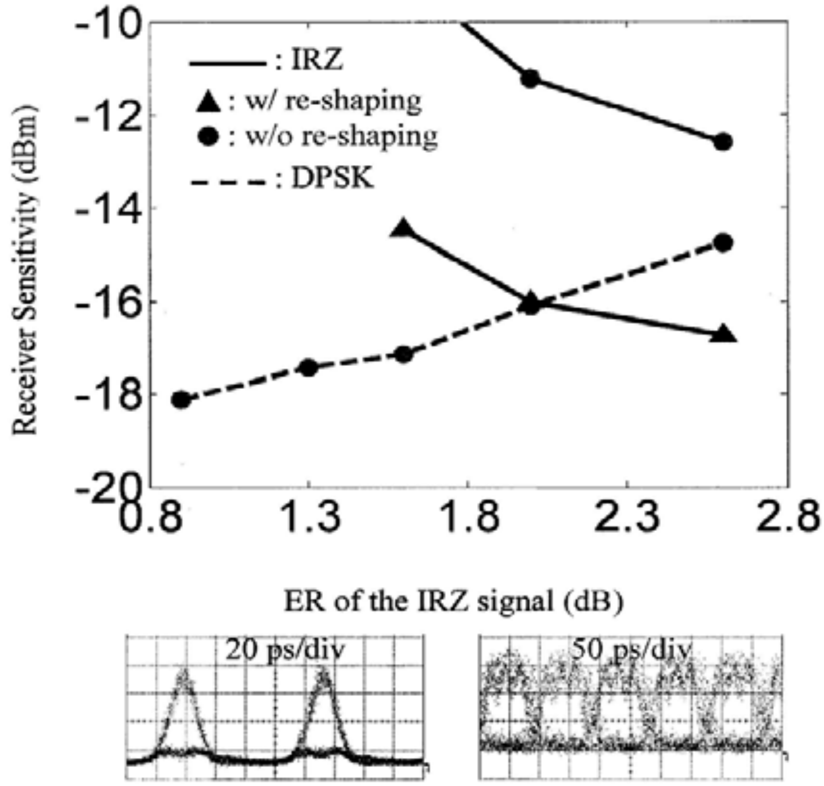

Fig. 4.4: Receiver sensitivity of the DPSK tributary and the IRZ tributary without (circles) and with (triangles) reshaping versus the ER of the IRZ tributary. Solid lines and dashed lines represent the IRZ and the DPSK tributaries of the IRZ/DPSK orthogonal modulation signal respectively. Insets show the eye diagrams of the DPSK and the IRZ tributaries at the optimal ER

For orthogonal modulation, the dependence of the receiver sensitivity of the DPSK tributary and the IRZ tributary without and with reshaping on the ER of the IRZ tributary was investigated for the back-to-back case and the results were shown in Fig. 4.4. Solid lines and dashed lines represent the IRZ and the DPSK tributaries of the IRZ/DPSK orthogonal modulation signal respectively. The OD between the DPSK tributary and the IRZ tributary is set to the value at which the performance of the DPSK is the worst for varying OD values. The insets show the eye diagrams of the

DPSK and the IRZ tributaries at the optimal ER. From the figure, it is seen that by using reshaping, the performance of IRZ signal is improved, leading to a lower optimal ER at around 2 dB, where optimal ER is defined as the ER where IRZ and DPSK tributaries have the same receiver sensitivity. Therefore, less crosstalk is introduced and the performance of the DPSK tributary is improved as well.

Fig. 4.5 shows the performance sensitivity of the DPSK tributary to the timing misalignment between the DPSK tributary and the IRZ tributary. From the figure, it can be seen that the receiver sensitivity fluctuation within 1 dB is achieved. Therefore, the DPSK tributary is robust to such timing misalignment.

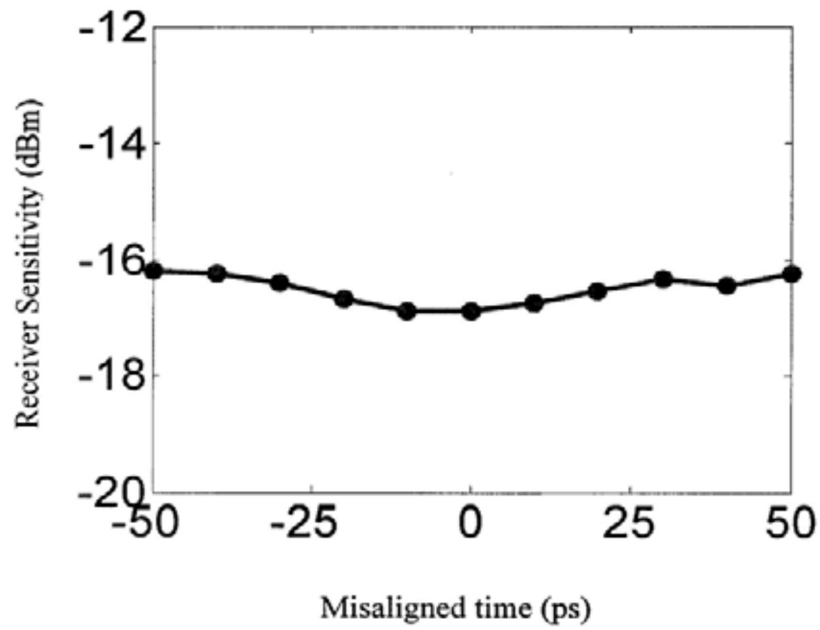

Fig. 4.5: Performance sensitivity of the DPSK tributary to the timing misalignment between the DPSK tributary and the IRZ tributary.

Fig. 4.6 depicts the BER performance of the DPSK tributary (solid) and the IRZ tributary (dashed) of the IRZ/DPSK orthogonal modulation signal in the back-to-back case (triangles) and in the case of 40-km SMF transmission (squares) at ER of 2 dB. The BER curves of the pure DPSK signal without the IRZ tributary (solid and circles) and the pure IRZ signal without the DPSK tributary (dashed and circles) are also shown in the figure for comparison. From the figure, it is shown that the DPSK tributary and the IRZ tributary experience 3-dB and 1-dB power penalties compared to the pure DPSK and IRZ signals without orthogonal modulation, respectively. The possible sources for the 1-dB penalty of the IRZ tributary include the imperfection of polarization stability and the OSNR degradation owing to the loss in the optical delay and the phase modulator. After 40-km transmission, the DPSK and the IRZ tributaries both achieve error free with the receiver sensitivity of -15 dBm and -14 dBm, respectively. Such performance, we believe, can be improved by using a DI with a short delay in the IRZ generation, which is able to generate narrower IRZ pulses and offers less crosstalk to the DPSK signal further.

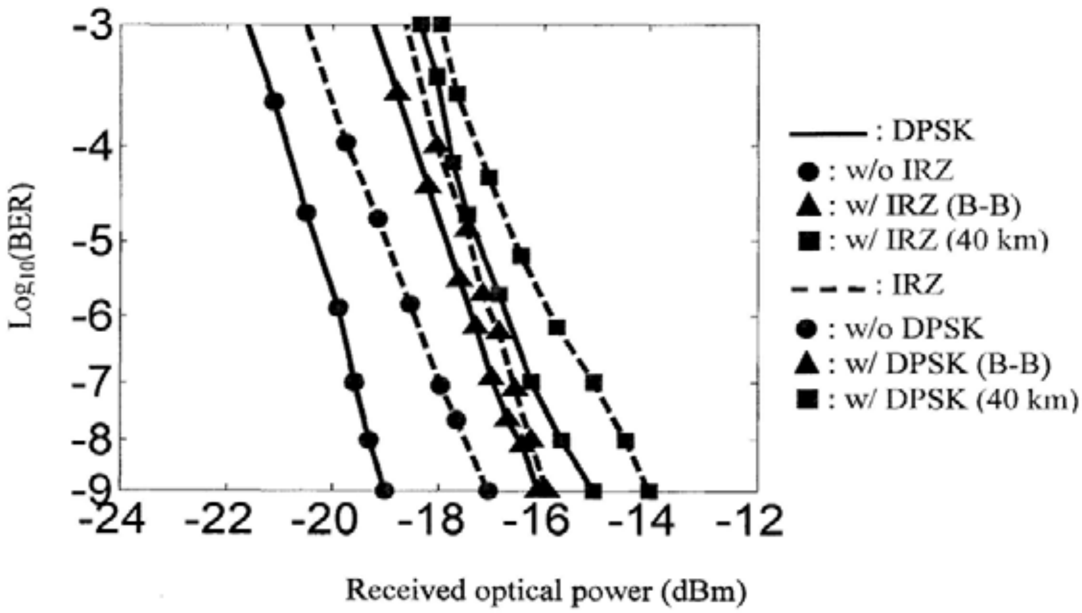

Fig. 4.6: BER performance of the DPSK tributary (solid) and the IRZ tributary (dashed) of the IRZ/DPSK orthogonal modulation signal in the back-to-back case (triangles) and in the case of 40-km SMF transmission (squares) at ER of 2 dB. Circles represent the pure DPSK signal without the IRZ tributary (solid and circles) and the pure IRZ signal without the DPSK tributary (dashed and circles).

4.1.4. Summary

In summary, we proposed a SOA-based all-optical format conversion from RZ format into IRZ/DPSK orthogonal modulation. A DI following the SOA was employed to suppress the pattern effect of the SOA and enhance the operation speed of the scheme to 40 Gbit/s. Error-free performance was achieved for the converted 40-Gbit/s IRZ/10-Gbit/s DPSK orthogonal modulation signal after 40-km SMF transmission.

4.2. A Novel All-Optical 4-ASK Coding and Decoding Scheme

4-ASK is a promising cost-effective spectral-efficient modulation format to extend the transmission capacity. By operating at only half of the bit rate, 4-ASK not only improves the tolerance to CD compared to OOK [13], but also alleviates the speed limitation of electrical and optical components. 4-ASK signal only requires one optical modulator and receiver for signal generation and detection. Therefore, such format is more cost effective than DQPSK and ASK/DPSK orthogonal modulation. The coding and decoding of 4-ASK are usually achieved in electronic domain. However, the control of the level spacing in such scheme is not flexible. As discussed in Chapter 2, the CD tolerance of the 4-ASK is sensitive to the level spacing and improper level spacing would lead to large CD tolerance reduction. Therefore, it is desirable in practice to generate 4-ASK signal with variable level spacing.

On the other hand, it is also desirable to achieve 4-ASK coding and decoding all optically to facilitate high-speed signal processing at intermediate nodes of the all-optical network, e. g. the operation of encoding two OOK signals into a 4-ASK signal to avoid contention. Furthermore, by implementing coding and decoding scheme in optical domain, optical fiber can connect two terminal equipments flexibly without the need to modify the circuit board inside of them. Basic supporting technologies of 4-ASK signal generation, such as power adjustment and data alignment, are more cost-effective and compact in optics.

In this section, we demonstrate an all-optical 4-ASK coding and decoding technique. It is shown that such coding method can easily achieve arbitrary level spacing by tuning a variable ratio coupler and the bias voltage of the EAM. The highly nonlinear fiber (HNLF) with the subsequent narrowband filtering before the receiver can effectively enlarge the desired eye opening to facilitate the BER detection even when a conventional OOK receiver is employed. The proposed scheme has the potential applications in format conversion and contention avoidance in future all-optical networks.

4.2.1. Experimental Setup

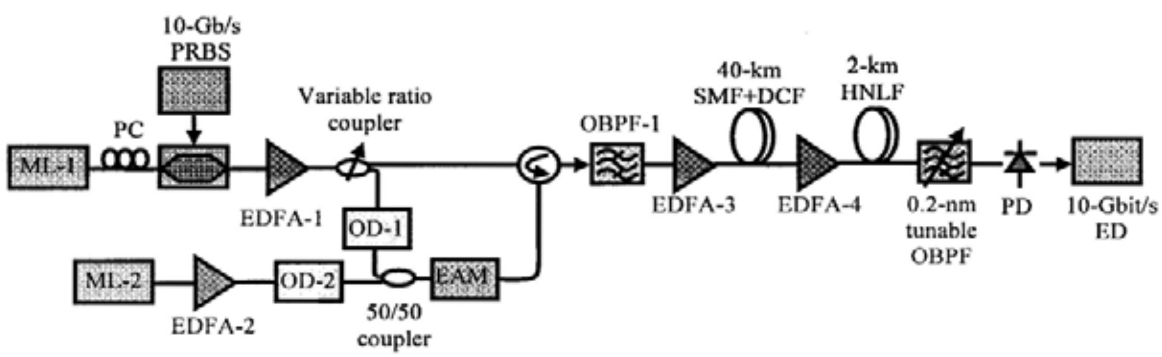

Fig. 4.7: Experimental setup

Fig. 4.7 depicts the experimental setup. A 10-GHz, 3-ps pulse train with the wavelength centered at 1545 nm was generated by the mode-locked laser-1 (ML-1) and modulated by the MZM. Then the signal was amplified using the erbium-doped fiber amplifier-1 (EDFA-1) and split by a variable ratio optical coupler (VROC) into two branches to emulate the two OOK input signals. The two signals were de-correlated by the optical delay-1 (OD-1) and launched into the -3V reversely biased EAM from the opposite directions to avoid the homodyne interference. The optical powers of the two OOK signals injected into the two sides of EAM were 10 dBm (OOK signal 1) and 13 dBm (OOK signal 2), respectively. OD-1 was adjusted to make pulses from the opposite sides collide in the EAM. Because there were totally 4 in-chip optical power level combinations, a 4-level time window in EAM was created through cross-absorption modulation (XAM). Therefore, when a second pulse train from the ML-2 at 1550 nm entered EAM, 4-level information was re-written to the new wavelength and 4-ASK coding function was realized. The output power of EDFA-2 was 7 dBm. The optical delay-2 (OD-2) was used to make the pulses peak in the middle of the time window of the EAM. The generated 4-ASK signal was filtered out from the circulator with a 2-nm OBPF-1 centered at 1550 nm and amplified by the EDFA-3. The 4-ASK signal was transmitted along the 40-km SMF and 8-km DCF. At the receiver end, 4-ASK signal should be converted into three separated 2-level patterns for data reconstruction. In the experiment, it was found that the capability of a conventional OOK receiver which consists of a photo-detector and an electrical limiting amplifier to differentiate these levels was quite limited. We found that such procedure could be implemented in the optical domain by using the HNLF with the subsequent optical filtering. After the amplification using the EDFA-4, a 2-km HNLF with the nonlinear coefficient of γ=10W/km^{-1} and zero dispersion of 1543 nm was employed to broaden the spectrum of the signal through the self-phase modulation effect. As the broadened spectrum width for different 4-ASK levels were different, by tuning the wavelength position of the 0.2-nm bandwidth OBPF-2, the desired eye opening was significantly enlarged while other eyes were compressed so that 4-ASK detection could be achieved even using the conventional OOK receiver.

4.2.2. Experimental Results and Discussions

Experiment was demonstrated at 10 Gsym/s and the resultant bit rate of 4-ASK signal was 20 Gbit/s. Fig. 4.8(a) shows the output waveforms of the coding scheme when (a) only OOK signal 1 (10 dBm input power) is injected into the EAM; (b) only OOK signal 2 (13 dB input power) is injected into the EAM; and (c) both OOK signals are injected into the EAM. From the figure, it is shown that when only one 10-Gbit/s data is injected into the EAM, the mark level induced by the OOK signal 2 is higher than that induced by OOK signal 1. When both of the two data signals are injected, an even higher XAM level appear if the two '1' pulses collide in the EAM. Fig. 4.8(b) is the corresponding eye diagram. It is found the level spacing can be easily adjusted by tuning the variable ratio optical coupler and the bias voltage of the EAM. In OSNR limited back-to-back case, the optimal level spacing is around 0:1:4:9 [13]. However, the practical optimal levels deviate from those values because the low eye is very sensitive to ISI. In our experiment, the level spacing is set to be around 0:1:2:4.

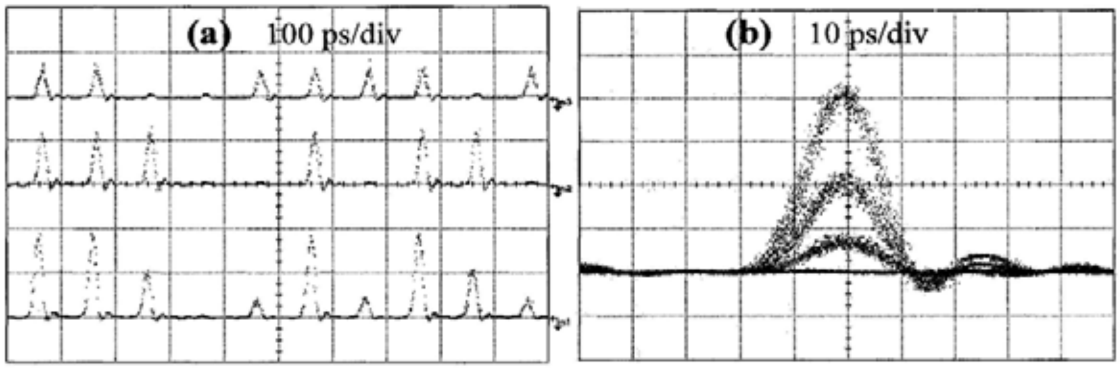

Fig. 4.8: (a) The waveform (lower trace of (a)) and (b) eye diagram of 4-ASK signal. XAM output signals when only 10 dBm (upper trace) and 13 dBm (middle trace) data was injected are also shown in (a).

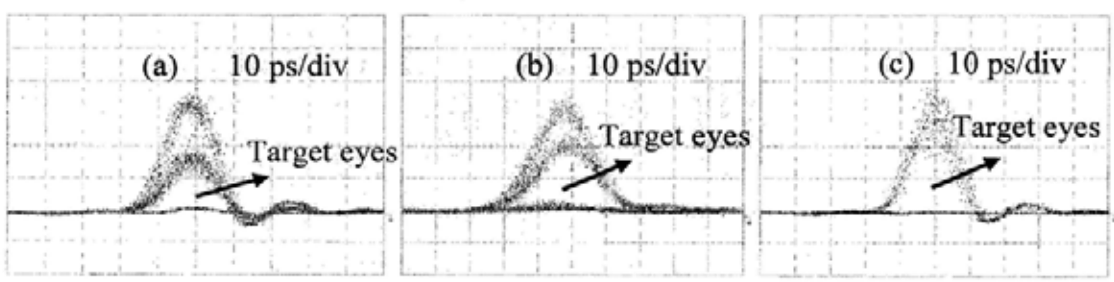

Fig. 4.9: Eye diagrams of the three separated 2-level eye patterns after the OBPF-2. (a), (b), and (c) represent the converted 2-level signals from the lower eye, the middle eye, and the upper eye of the 4-ASK signal, respectively.

Fig. 4.9 shows the eye diagrams of the three separated 2-level eye patterns after the OBPF-2. (a), (b), and (c) represent the converted 2-level signals from the lower eye, the middle eye, and the upper eye of the 4-ASK signal, respectively. The residual eye penalty is due to the lack of optimal operation condition for the decoding in our lab. The optimal operation with respect to the input power of EDFA-4, the characteristics of HNLF, the wavelength position and the bandwidth of OBPF-2 depends on the pulse width and the level spacing of the input 4-ASK signal. At the anomalous dispersion operation region of the HNLF, though higher input power broadens the spectrum more, the noise is amplified as well due to modulation instability effect [134]. Therefore, the power of EDFA-4 in the experiment was limited to be around 9 dBm, resulting in the residual eye penalty. The employment of the narrow-band OBPF-2 help to differentiate different eyes (upper, middle, and low), but it is also sensitive to the noise and the amplitude jitter. Therefore, we believe that after further optimization of the operation parameters, more reduction of the residual eye penalty can be obtained.

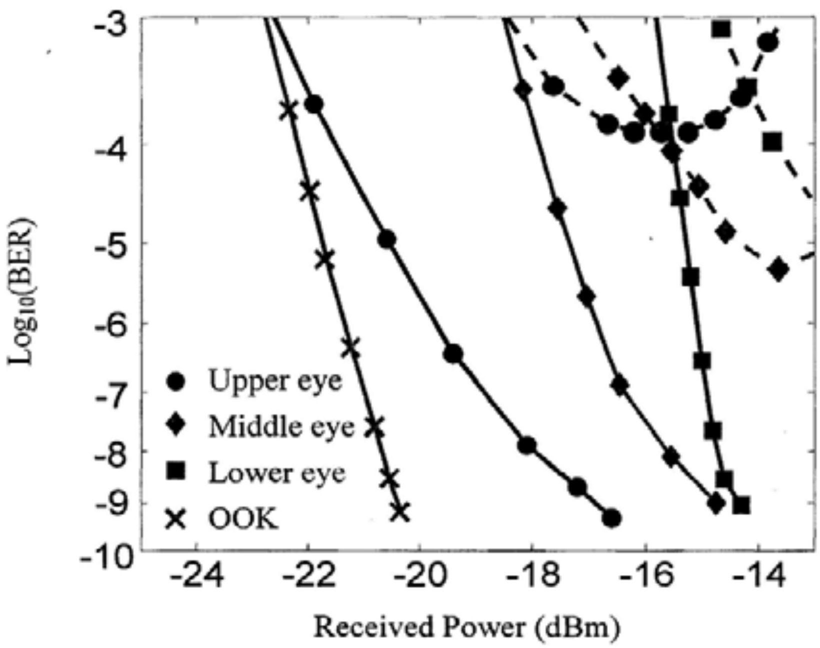

Fig. 4.10: BER curves for the upper eye (circle), the middle eye (diamond), and the lower eye (square) of the 4-ASK signal without (dashed) and with (solid) the all-optical decoding processing. Crosses represent the B-B performance of the two-level OOK signal.

Fig. 4.10 shows the BER curves for the three separated 2-level data patterns without (dashed) and with (solid) the use of the all-optical decoding scheme after the transmission. The back-to-back performance of the OOK signal is also shown in the figure for reference. From the figure, it is shown that the conventional OOK receiver cannot properly detect the 4-ASK signal. In conventional OOK detection, an electrical limiting amplifier is generally used after the photo-detector to enlarge the OOK eye opening and facilitate the threshold determination in BER detection. When a 4-ASK signal is launched into such detector, the lower eye between level-0 and level-1 can be properly detected although large power penalty is induced due to the additional power consumption of other two levels. However, the middle eye between level-1 and level-2 and the upper eye between level-2 and level-3, are compressed and cannot be detected, because level-1, level-2, and level-3 operate at the saturation region of the electrical amplifier. Therefore, there are error floor for the middle and the upper eyes. By using the all-optical decoding method, however, error free operation can be achieved with receiver sensitivity better than -14 dBm for all the three eyes, as shown in Fig. 4.10. From the figure, it is also shown that the sensitivity is the best for the upper eye, while it is worst for the lower eye. Such result, however, does not imply that the upper eye has the highest OSNR. The main reason for such phenomena is that after the decoding, the probability for level-1 of the converted OOK signal is only 1/4 for the upper eye, but is 3/4 for the lowest eye. As far as the OSNR is concerned, from the slope of the curve, we can assert that the OSNR for the low eye is the highest.

4.2.3. Summary

In summary, we experimentally demonstrated, for the first time, a novel all-optical 4-ASK coding and decoding technique. The coding scheme converts two optical OOK signals into a 4-ASK signal using EAM while the decoding scheme employs the HNLF with the subsequent tunable narrowband filtering to extract the different eyes from the 4-ASK signal. Performance was verified by 40-km error-free transmission of 20-Gbit/s 4-ASK signal. Such technique features easy implementation and the flexibility of level spacing optimization. The scheme provides a new way to upgrade the speed of legacy systems. It has the potential applications in format conversion and contention avoidance in future all-optical networks.

4.3. Summary

In summary, we proposed two all-optical signal processing techniques of advanced modulation formats to freely enable the employment of advanced modulation formats for high-speed optical communication in all-optical networks. Firstly, we proposed an all-optical format conversion from 40-Gbit/s RZ signal to 40-Gbit/s IRZ / 10-Gbit/s DPSK orthogonal modulation signal to interface high-speed transmission system using RZ format with networks using orthogonal modulation format. Error-free 40-km SMF transmission of the converted 40-Gbit/s IRZ/10-Gbit/s DPSK orthogonal modulation signal was demonstrated. Secondly, we proposed an all-optical multilevel 4-ASK coding and decoding technique. The proposed scheme encodes two input on-off-keying signals all optically into a 4-ASK signal using cross absorption modulation in an EAM and employs fiber-based all-optical approach for 4-ASK data decoding. This technique can be applied for format conversion and contention avoidance in future all-optical networks.

5. Performance Monitoring for Impairment Compensation

Monitoring is an essential element to enable time varying equalization and distortion compensation. For example, besides the MLSE method, the impairment from CD and PMD can also be eliminated by a monitoring embedded feedback control. Besides, the performance monitors can be used to anticipate major degradations of components like EDFA and optical add-drop multiplexer (OADM), as well as changes in working conditions after the initial service rollout. Protection and restoration mechanisms will be triggered within timing limits when necessary [139].

In this chapter, we demonstrate a simple and polarization-insensitive monitoring scheme for synchronized phase re-modulation (SPRM) by using a narrowband OBPF. SPRM is a crucial signal processing technique to erase the original and write the new phase information simultaneously for phase-encoded modulation formats. Applications include optical label swapping in optical networks, the re-modulation of the downstream signal for upstream transmission in WDM-PON, and the generation of spectral efficient orthogonal modulation format [88], [89], [136]. Experiments show that with the optimal central wavelength of the OBPF, -1.2-dB and 3.8-dB monitoring power dynamic ranges are obtained for NRZ-DPSK and RZ-DPSK formats respectively, thus achieving high monitoring sensitivity.

5.1. Simple Monitoring Technique for Synchronized Phase Re-modulation Using Narrowband Optical Filtering

Fig. 5.1 illustrates the principle of SPRM. The old DPSK signal is re-modulated by a delta DPSK data, which is obtained by performing exclusive OR operation between the detected old DPSK data and the new DPSK data in electrical domain. In binary phase-encoded signal, a π phase change applied to either symbol will swap the original symbol to the other symbol, as shown in the inset of Fig. 5.1. Therefore, by using SPRM, the old DPSK signal is erased and the new DPSK signal is written simultaneously. To properly achieve SPRM, the electrical delta DPSK data should be superimposed onto the time slot center of the old optical DPSK signal. However, the relative time delay between the incoming DPSK signal and the delta DPSK data drifts over time due to temperature variation and imperfect clock recovery in the SPRM module, which increases the difficulty of SPRM and hinders its practical applications.

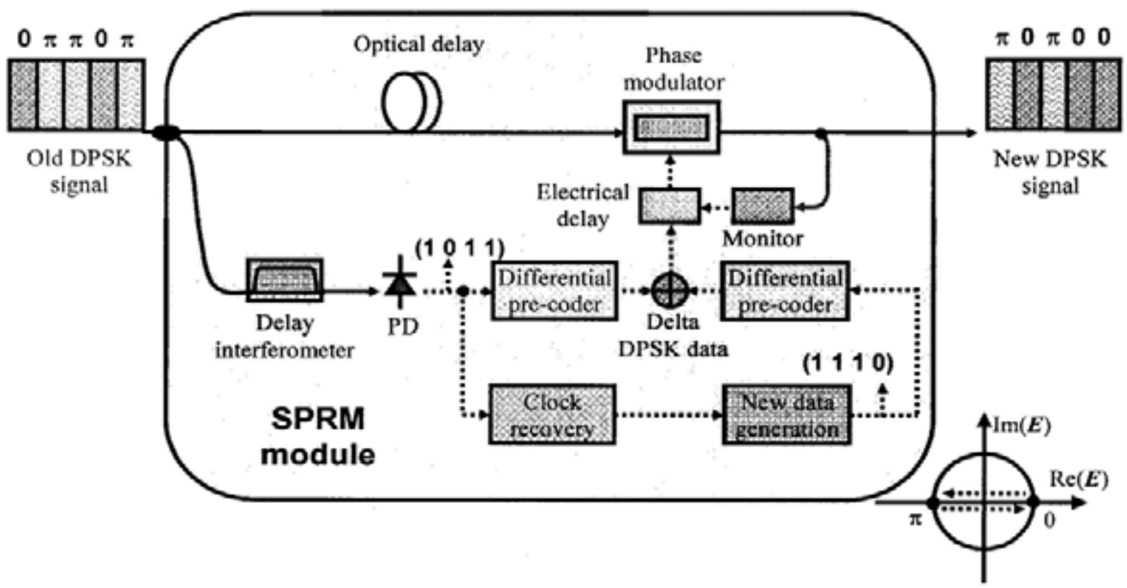

Fig. 5.1: *Principle of SPRM to simultaneously erase old DPSK data and write new DPSK data. Inset: constellation diagram for DPSK.*

To solve this problem, we propose a simple technique using a narrowband OBPF to monitor unsynchronized phase re-modulation. The obtained monitoring signal is fed back to control the delay between the incoming DPSK signal and the electrical delta DPSK data for automatic SPRM. We experimentally show that the proposed method is applicable to both NRZ-DPSK and RZ-DPSK formats. With the optimal central wavelength of the OBPF, -1.2-dB and 3.8-dB monitoring power dynamic ranges (MPDRs), defined as the ratio of the monitoring power for the worst case of phase re-modulation to that for the best case, are obtained for NRZ-DPSK and RZ-DPSK formats respectively, therefore achieving high monitoring sensitivity.

5.1.1. Experimental Setup

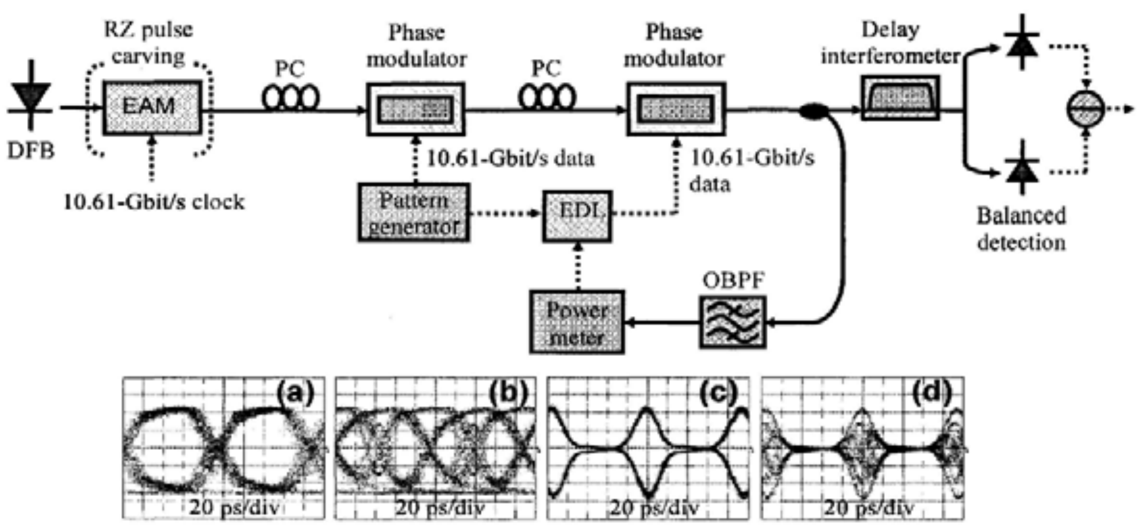

Fig. 5.2: Experimental setup. Insets: the eye diagrams of the new DPSK signal after balanced detection for (a) the best case of phase re-modulation in NRZ-DPSK format; (b) the worst case of phase re-modulation in NRZ-DPSK format; (c) the best case of phase re-modulation in RZ-DPSK format; and (d) the worst case of phase re-modulation in RZ-DPSK format.

Fig. 5.2 shows the experimental setup. The old DPSK signal was generated by modulating a CW light or an optical pulse train by a 10.61-Gbit/s 2^{31}-1 pseudorandom binary sequence (PRBS) in a PM. The optical pulse train was obtained by pulse carving a CW light using an EAM driven by a 10.61-Gbit/s electrical clock. The wavelength of the CW light and the optical pulse train, λ_0, were 1545.83 nm. The old DPSK signal was re-modulated with modulation depth of π by using another PM. An electrical delay line was employed to adjust the time delay between the old DPSK signal and the delta DPSK data. The new DPSK signal was demodulated by a delay interferometer with the relative delay of 94.3 ps and detected by a balanced detector. The monitor consisted of a 0.2-nm OBPF with tunable central wavelength, and a power meter. Insets of Fig. 5.2 show the eye diagrams of the new DPSK signal after balanced detection for (a) the best case of phase re-modulation in NRZ-DPSK format; (b) the worst case of phase re-modulation in NRZ-DPSK format; (c) the best case of phase re-modulation in RZ-DPSK format; and (d) the worst case of phase re-modulation in RZ-DPSK format. From the figure, it is shown that unsynchronized phase re-modulation causes severe eye closure, thus greatly degrades the performance.

5.1.2. Experimental Results and Discussions

Unsynchronized phase re-modulation causes power variation across the new DPSK signal's spectrum. Fig. 5.3 depicts the spectrums of the new DPSK signal versus the wavelength offset with respect to the central wavelength of the DPSK signal under the best case (solid) and the worst case (dashed) of phase re-modulation in (a) NRZ-DPSK and (b) RZ-DPSK formats. From the figure, it is shown that in NRZ-DPSK format, unsynchronized phase re-modulation causes spectral power decrease for the spectrum $|\lambda-\lambda_0|<0.05$ nm and $|\lambda-\lambda_0|>0.15$ nm, and spectral power increase for the spectrum 0.05 nm$<|\lambda-\lambda_0|<0.15$ nm. It is because when the phase re-modulation is asynchronous, re-modulation induced chirps are not superimposed on the edge but on the middle of the time slot. On the other hand, because RZ-DPSK format has no energy at the edge of the time slot, unsynchronized phase re-modulation causes spectral power decrease only for the spectrum $|\lambda-\lambda_0|<0.08$ nm. The spectrum $|\lambda-\lambda_0|>0.08$ nm exhibits spectral power increase. Such kind of spectral power variation can be extracted by a narrowband OBPF and measured by a power meter.

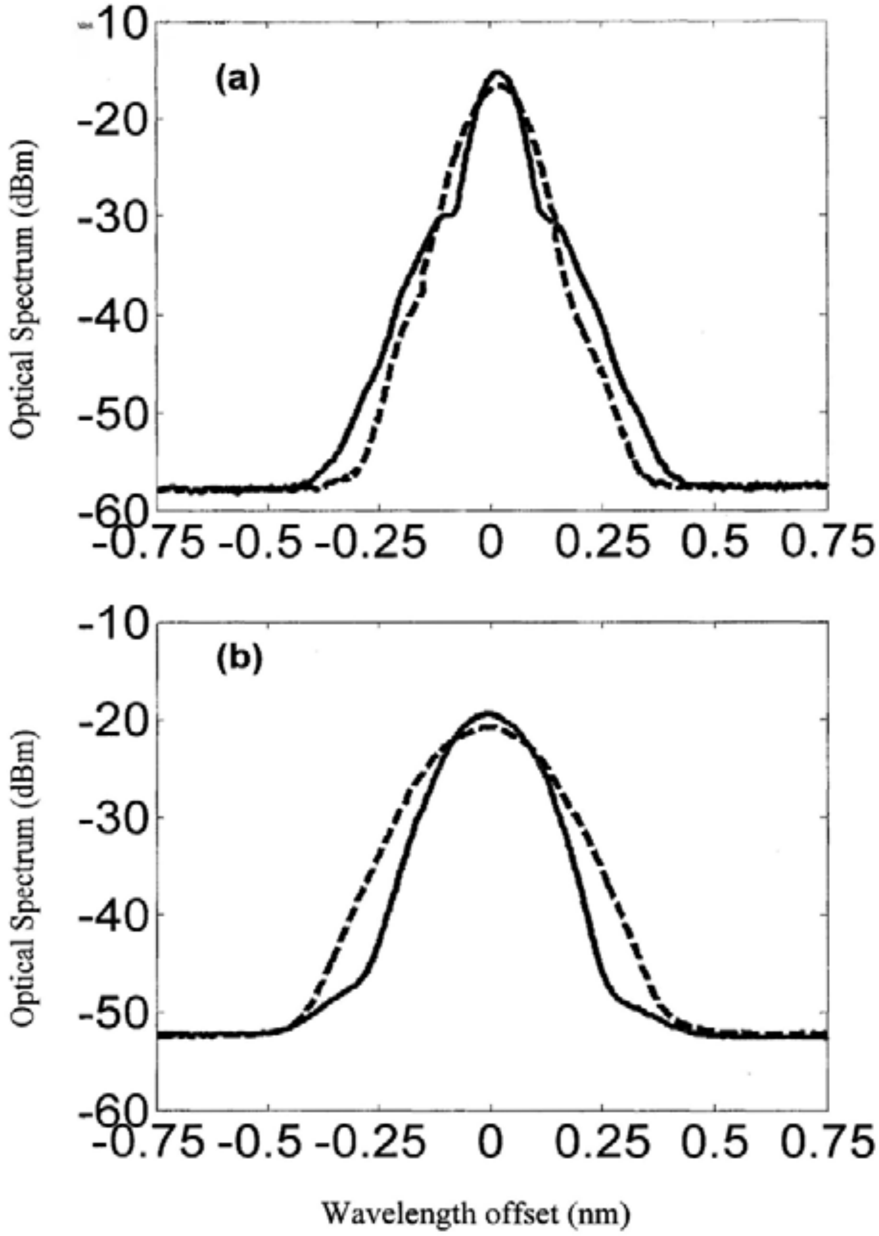

Fig. 5.3: The optical spectrums of the new DPSK signal versus the wavelength offset with respect to the central wavelength of the DPSK signal under the best case (solid) and the worst case (dashed) of phase re-modulation for (a) NRZ-DPSK and (b) RZ-DPSK formats.

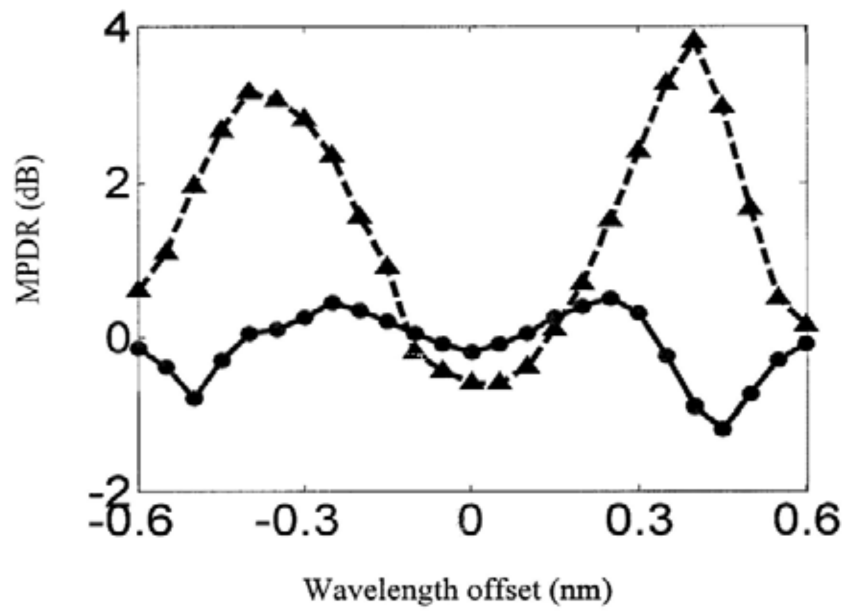

Fig. 5.4: MPDR versus the wavelength offset of the OBPF for NRZ-DPSK (solid) and RZ-DPSK (dashed) formats.

Fig. 5.4 shows the MPDR versus the wavelength offset of the OBPF with respect to the central wavelength of the DPSK signal for NRZ-DPSK (solid) and RZ-DPSK (dashed) formats. Notice that the bandwidth of the OBPF is 0.2 nm and the monitoring power is averaged over the OBPF-filtered spectrum. At small wavelength offset, when the phase re-modulation is unsynchronized, there are both spectral power increase and spectral power decrease across the OBPF-filtered spectrum, resulting in small power difference between the worst case and the best case of phase re-modulation. In contrast, at the wavelength offset of 0.45 nm or 0.4 nm, when the phase re-modulation is unsynchronized, only spectral power decrease or increase exhibits across the OBPF-filtered spectrum for NRZ-DPSK or RZ-DPSK format. As a result, optimal MPDR values of -1.2 dB at the wavelength offset of 0.45 nm and 3.8 dB at the wavelength offset of 0.4 nm are obtained for NRZ-DPSK and RZ-DPSK formats respectively, thus achieving high monitoring sensitivity. Meanwhile, the monitoring module is polarization independent.

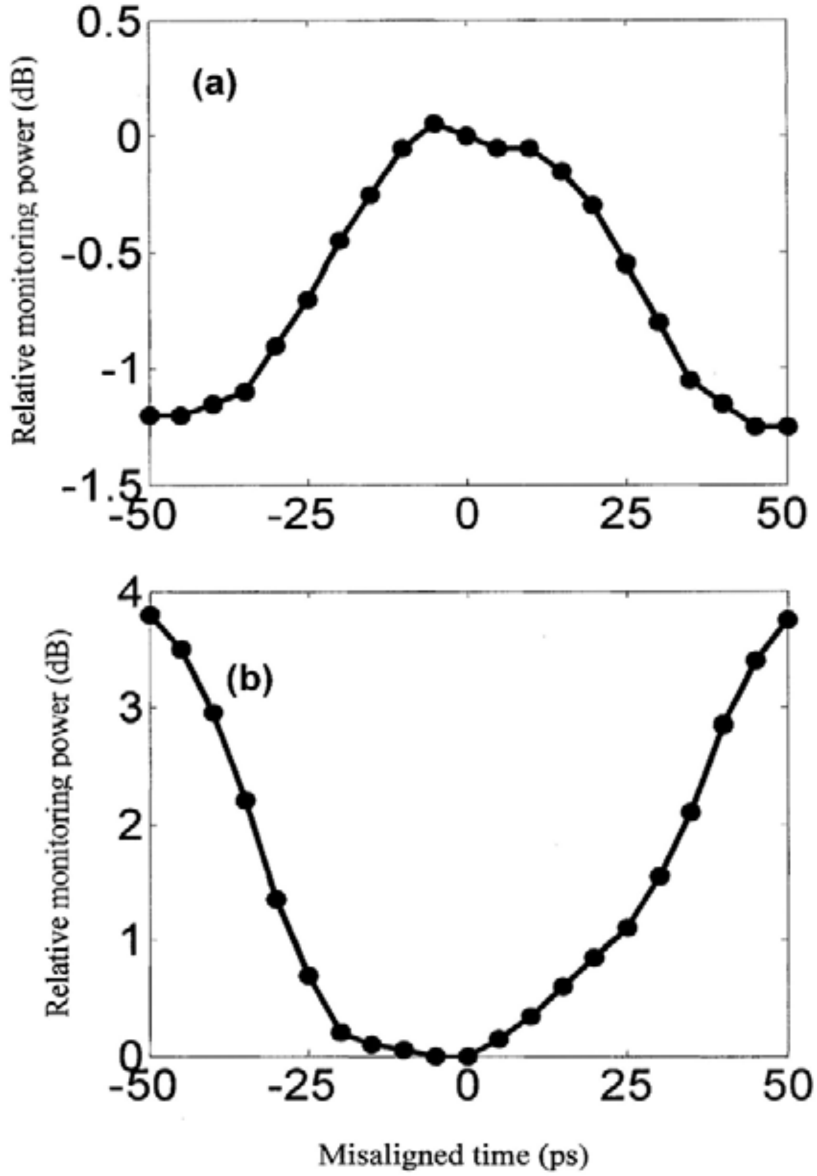

Fig. 5.5: The relative monitoring power versus re-modulation misaligned time for (a) NRZ-DPSK and (b) RZ-DPSK formats. The central wavelength of the OBPF is optimized and the relative monitoring power is with respect to the monitoring power for the best case of phase re-modulation.

Fig. 5.5 shows the relative monitoring power versus re-modulation misaligned time for (a) NRZ-DPSK and (b) RZ-DPSK formats. In the figure, the central wavelength of the OBPF is optimized and the relative monitoring power is with respect to the monitoring power for the best case of phase re-modulation. It is shown that when the misaligned time is larger than +10 ps or less than -10 ps, the relative monitoring power changes significantly. The monitoring signal is fed back to control the EDL for automatic SPRM. As a result, the potential penalty induced by unsynchronized phase re-modulation is avoided.

5.1.3. Summary

In summary, we have proposed and experimentally demonstrated a simple monitoring technique using narrowband optical filtering for SPRM in the applications of label swapping in optical networks, data re-modulation in WDM-PON, and orthogonal modulation generation. By optimizing the central wavelength of the OBPF, the proposed method achieves -1.2-dB and 3.8-dB MPDRs for NRZ-DPSK and RZ-DPSK formats respectively. This simple approach features high monitoring sensitivity and polarization independency.

6. Summary and Future Work

6.1. Summary of the Thesis

The objective of this thesis is to explore novel impairment mitigation approaches which have high compensation performance and/or low operation complexity. As a result, cost-effective high-speed optical transmission systems and optical networks are enabled.

Chapter 2 presented the technologies of MLSE for impairment compensation. In the first part of this chapter, we reviewed our recent work on the design of novel MLSE structures with high impairment compensation performance and low cost for different advanced modulation formats.

(i) In the DPSK format, we discussed our recently proposed multi-chip DPSK MLSE for CD and PMD compensation. We showed that the proposed 3-chip DPSK MLSE can enhance the CD tolerance of 10-Gbit/s DPSK signal to 2.5 times of that by using conventional MLSE and can bound the penalty for 100-ps DGD by 1.4 dB. We further investigated 4-, 5-, and 6-chip DPSK MLSEs and showed that these structures can provide further performance improvement but at the expense of the implementation complexity increase. We suggested that in practice, 3- or 4-chip DPSK MLSE is optimal in terms of the performance and the complexity.

(ii) In ASK/DPSK orthogonal modulation, we determined the fundamental impairment mechanism in CD-limited ASK/DPSK orthogonal modulation format and showed that conventional MLSE which only considers intra-tributary interference of ASK and DPSK tributaries separately fail to improve the overall CD tolerance of the ASK/DPSK signal despite the increase of the MLSE's memory length. J-MLSE exploits the correlation information between the detected ASK and DPSK signals and can improve the CD tolerance of the ASK/DPSK signal significantly. However, a J-MLSE has the implementation complexity compared to conventional MLSE. Therefore, we further proposed a novel DF-J-MLSE. We showed that DF-J-MLSE has the same implementation complexity as a conventional MLSE while preserving the overall CD tolerance of the ASK/DPSK signal by the J-MLSE.

(iii) In DQPSK format, we discussed a novel 3-chip DQPSK J-MLSE. We showed that such scheme significantly outperforms conventional MLSE and J-MLSE in CD and PMD compensation. We showed that the proposed 3-chip DQPSK J-MLSE can enhance the CD tolerance of 20-Gbit/s DQPSK signal to 1.5 times of that by using J-MLSE and exhibits 0.8-dB penalty for 100-ps differential group delay at 10-Gsym/s.

(iv) In 4-ASK format, we showed that due to the increased number of levels, such format is sensitive to ISI from optical filtering, electronic filtering, and CD. We optimized the optical/electronic receiver bandwidth and multilevel spacing of 4-ASK format. We found that the optimal level spacing of the 4-ASK signal changes with the CD values and improper level spacing design leads to significant CD tolerance reduction. As a result, level spacing optimization is difficult in CD-varying 4-ASK optical systems, in which the CD constantly changes due to the time-varying effects of the installed fibers and different routing paths. We proposed 4-ASK MLSE for signal detection. It was shown that 4-ASK MLSE can effectively alleviate the sensitivity of CD tolerance to level spacing, therefore, relax the difficulty of level spacing optimization. By using MLSE, the CD tolerance of the 4-ASK signal is significantly enhanced by a factor of at least two.

We summarized our proposed schemes and compared the proposed schemes with the existing electronic equalization schemes for various advanced modulation formats, as shown in Section 2.1.5. We concluded that the proposed schemes significantly outperform the existing schemes in terms of B-B sensitivity, CD and PMD tolerance, but without much complexity increase.

In the second part of this chapter, we discussed novel applications of MLSE for compensation of other impairments characterized as ISI and investigated a simple analytical method for MLSE performance evaluation. We characterized the impairment from TM between the pulse carver and the data modulator in RZ systems as ISI and proposed to use MLSE for TM mitigation. We also showed that MLSE can achieve simultaneous compensation of TM and PMD. We developed a theory to evaluate the performance of MLSE for compensation of TM without and with the presence of PMD in both OSNR limited and thermal-noise limited operation regions. The developed theory for MLSE's performance evaluation, employing Karhunen-Loeve expansion, saddlepoint approximation, and the steepest decent method, is applicable to arbitrary input signal pulse shape, optical and electrical filtering. We showed that the bandwidth of OBPF and the input data pulse shape determine the linear/nonlinear characteristic of TM. The power penalty caused by the worst TM is limited by MLSE to 6 dB in OSNR limited operation region and 1.9 dB in thermal-noise limited operation region. The results also validate the effectiveness of MLSE for simultaneous compensation of TM and PMD with shared electrical devices.

Chapter 3 investigated the schemes for impairment mitigation in CLS WDM-PON. The primary objective of the work is to achieve high-speed CLS WDM-PON with data rate of 10 Gbit/s for both downstream and upstream signals. However, we showed that in the existing schemes at such high data rate, the upstream signals are sensitive to CD in the fibers and/or asynchronous modulation at ONUs. We reviewed our recently proposed solutions to mitigate the impairments from CD and asynchronous modulation. By eliminating the modulation synchronization module and all-optical CD compensation module, the proposed methods can greatly reduce the cost and operation complexity of high-speed CLS WDM-PON.

(i) In WDM-PON with re-modulation technology, we investigated a novel re-modulation scheme using reduced-ER downstream OOK signal and upstream DPSK signal. We showed that by using this technique, a 30-km-range high-speed colorless CLS WDM-PON without CD compensation and re-modulation synchronization can be achieved within 1-dB penalty for both 10-Gbit/s downstream and 10-Gbit/s upstream transmission.

(ii) In SC-based CLS WDM-PON, we generalized asynchronous modulation at ONUs as ISI and investigated the method using MLSE for upstream signal detection. MLSE effectively compensate the impairments from 1) asynchronous modulation of upstream pulse carriers at ONUs; and 2) CD in the fibers. Compared to the conventional method, the proposed method features significant cost saving, higher power budget for upstream signals, and lower operation complexity for ONUs in SC-BLS-based WDM-PON.

Advanced modulation formats can not only alleviate the transmission impairments and increase the capacity of the optical communication systems but also enable various high-speed optical signal processing in all-optical networks. To freely enable the employment of advanced modulation formats for high-speed optical communication in all-optical networks, all-optical format conversion and coding/decoding for advanced modulation formats are essential. Therefore, Chapter 4 investigated the all-optical signal processing of advanced modulation formats:

(iii) We investigated an all-optical format conversion from 40-Gbit/s RZ signal to 40-Gbit/s IRZ / 10-Gbit/s DPSK orthogonal signal. The method firstly employs the effect of XGM in SOA to convert RZ signal to IRZ signal. A DI following the SOA suppresses the pattern effect in SOA and enhances the operate data rate of the scheme up to 40-Gbit/s. Then a 10-Gbit/s DPSK signal is successfully superimposed on the 40-Gbit/s IRZ signal. Error-free 40-km SMF transmission of the converted 40-Gbit/s IRZ/10-Gbit/s DPSK orthogonal modulation signal was demonstrated.

(iv) We demonstrated an all-optical multilevel 4-ASK coding and decoding technique. The scheme encodes two input on-off-keying signals all-optically into a 4-ASK signal using cross absorption modulation in an EAM and employs fiber-based all-optical approach for 4-ASK data decoding. The proposed encoding method provides an effective contention solution in the network intermediate node to maximize the network capacity while the decoding method enables the 4-ASK signal detection by using conventional OOK receiver.

Chapter 5 investigated a simple and polarization-insensitive monitoring scheme for synchronized phase re-modulation by using a narrowband OBPF. SPRM is a crucial signal processing technique to erase the original and write the new phase information simultaneously for phase-encoded modulation formats. We showed that with the optimal central wavelength of the OBPF, -1.2-dB and 3.8-dB monitoring power dynamic ranges are obtained for NRZ-DPSK and RZ-DPSK formats respectively, thus achieving high monitoring sensitivity.

6.2. Future Work

My future research is to continue the investigation of impairment mitigation to enable cost-effective high-speed optical transmission systems and optical networks.

(i) At the transmitter side, I will propose novel cost-effective generation methods for various modulation formats to reduce the cost while avoiding the ISI during the multilevel generation. I will also develop electronic pre-distortion devices for advanced modulation formats.

(ii) In the fiber link, I will investigate more sophisticated formats such as orthogonal frequency division multiplexing (OFDM) for impairment mitigation.

(iii) At the receiver side, I will investigate more sophisticated detection methods with enhanced tolerance to transmission impairment. My research will focus on two areas. Firstly, I will design electronic equalizer under full-field construction using direct detection. Secondly, I will investigate the electronic equalizer structures for coherent optical detection.

Bibliography

[1] S. Perrin, D. Emberley, A. Harris, and T. S. Valovic, "Worldwide bandwidth end-use forecast and analysis, 2003-2007: more is still not enough", *IDC Report*, Doc #28875, 2003.

[2] T. S. Afferton, "Optical networking – a multi-service global carrier's view", in *the 12th Annual Meeting of the IEEE Lasers and Electro-Optics Society* (LEOS), vol. 2, pp.399-400, 1999.

[3] G. P. Agrawal, *Fiber-Optic Communication Systems*, 3rd edition, John Wiley & Sons.

[4] B. Zhu, L. Leng, L. E. Nelson, Y. Qian, S. Stulz, C. Doerr, L. Stulz, S. Chandtasekar, S. Radic, D. Vengsarkar, Z. Chen, J. Park, K. Feder, H. Thiele, J. Bromage, L. Gruner-Nielsen, and S. Knudsen, "3.08 Tb/s (77×42.7 Gbit/s) transmission over 1200 km of non-zero dispersion-shifted fiber with 100-km spans using C-L-band distributed Raman amplification" *IEEE/OSA Optical Fiber Communication Conference* (OFC), PD23, Anaheim, CA, 2001.

[5] "IEEE 802.3 higher speed study group agenda and general information", http://grouper.ieee.org/groups/802/3/hssg/public/nov06/agenda_01_1106.pdf.

[6] H. Kogelnik, "High-capacity optical communications: personal recollections", *IEEE Journal of Selected Topics in Quantum Electronics*, vol. 6, pp. 1279-1286, 2000.

[7] R. J. Sanferrare, "Terrestrial lightwave systems", *AT&T Technical Journal*, vol. 66, pp.95-107, 1987.

[8] G. Vareille, F. Pitel, and J. F. Marcerou, "3 Tbit/s (300 x 11.6Gbit/s) transmission over 7380 km using C+L band with 25 GHz channel spacing and NRZ format", *IEEE/OSA Optical Fiber Communication Conference* (OFC), PD22, Anaheim, CA, 2001.

[9] R. J. Nuyts, Y. K. Park, and P. Gallion, "Dispersion equalization of a 10 Gb/s repeatered transmission system using dispersion compensation fibers", *IEEE Journal of Lightwave Technology*, vol. 15, pp. 31-42, 1997.

[10] J. H. Winters, and R. D. Gitlin, "Electrical signal processing techniques in long-haul fiber-optic systems", *IEEE Transactions on Communications*, vol. 38, pp.1439-1453, 1990.

[11] J. H. Winters, R. D. Gitlin, and S. Kasturia, "Reducing the effects of transmission impairments in digital fiber optic systems", *IEEE Communications Magazine*, vol. 31, pp. 68-76, 1993.

[12] P. Poggiolini, G. Bosco, "Branch metrics for effective long-haul MLSE IMDD receivers", *European Conference on Optical Communication* (ECOC), We2.5.4, 2006.

[13] S. Walklin, and J. Conradi, "Multilevel signaling for increasing the reach of 10 Gb/s lightwave systems", *IEEE Journal of Lightwave Technology*, vol. 17, pp.2235-2248, 1999.

[14] R. A. Griffin, R. I. Johnstone, R. G. Walker, J. Hall, S. D. Wadsworth, K. Berry, A. C. Carter, M. J. Wale, J. Hughes, P. A. Jerram, and N. J. Parsons, "10 Gb/s optical differential quadrature Phase shift keying (DQPSK) transmission using GaAs/AIGaAs integration", *IEEE/OSA Optical Fiber Communication Conference* (OFC), PD-FD6, Anaheim, CA, 2002.

[15] S. Hayase, N. Kikuchi, K. Sekine, and S. Sasaki, "Proposal of 8-state per symbol (binary ASK and QPSK) 30-Gbit/s optical modulation / demodulation scheme" *European Conference on Optical Communication* (ECOC), Th2.6.4, 2003.

[16] T. Miyazaki, and F. Kubota, "Superposition of DQPSK over inverse-RZ for 3-bit/symbol modulation-demodulation", *IEEE Photon. Technol. Lett.*, vol. 16, pp. 2643-2645, 2004.

[17] M. Serbay, C. Wress, and W. Rosenkranz, "Experimental investigation of RZ-8DPSK at 3×10.7 Gb/s" *the 18th Annual Meeting of the IEEE Lasers and Electro-Optics Society* (LEOS), WE3, 2005.

[18] S. Tsukamoto, K. Katoh, and K. Kikuchi, "Coherent demodulation of optical 8-phase shift keying signals using homodyne detection and digital signal

processing", OThR5, *IEEE/OSA Optical Fiber Communication Conference* (OFC), ThG5, Anaheim, CA, 2006.

[19] K. Sekine, N. Kikuchi, S. Sasaki, S. Hayase, C. Hasegawa, and T. Sugawara, "40 Gbit/s, 16-ary (4 bit/symbol) optical modulation/demodulation scheme", *IEE Electronics Letters*, vol. 41, pp. 430-432, 2005.

[20] T. Tokle, Mo Serbay, Y. Geng, J. B. Jensen, W. Rosenkranz, and P. Jeppesen, "Penalty free transmission of multilevel 240 Gbit/s RZ-DQPSK-ASK using only 40 Gbit/s equipment", *European Conference on Optical Communication* (ECOC), Th4.1.6, 2005.

[21] M. Seimetz, "Performance of coherent optical square-16-QAM systems based on IQ transmitters and homodyne receivers with digital phase estimation", *IEEE/OSA Optical Fiber Communication Conference* (OFC), NWA4, 2006.

[22] H. Yoon, D. Lee, and N. Park, "Performance comparison of optical 8-ary differential phase shift keying systems with different electrical decision schemes", *OSA Optics Express*, vol. 13, no. 2, pp.371-376, 2005.

[23] N. Kikuchi, K. Sekine, and S. Sasaki, "Multilevel signaling for high-speed optical transmission", *European Conference on Optical Communication* (ECOC), Tu3.2.1, Cannes, France, 2006.

[24] N. Kikuchi, K. Sekine, and S. Sasaki, "Proposal of inter-symbol interference (ISI) suppression technique for optical multilevel signal generation", *European Conference on Optical Communication* (ECOC), Tu4.2.1, Cannes, France, 2006.

[25] J. B. Jensen, T. Tokle, C. Peucheret, and P. Jeppesen, "Transmission of multilevel 60 Gbit/s polarization multiplexed RZ-D8PSK using only 10 Gbit/s equipment", *IEEE/OSA Optical Fiber Communication Conference* (OFC), OWM4, Anaheim, CA, 2007.

[26] C. R. S. Fludger, T. Duthel, D. van den Borne, C. Schulien, E-D. Schmidt, T. Wuth, E. de Man, G. D. Khoe, H. de Waardt, "10 x 111 Gbit/s, 50 GHz spaced, polmux-RZ-DQPSK transmission over 2375 km employing coherent equalization", *IEEE/OSA Optical Fiber Communication Conference* (OFC), PDP22, Anaheim, CA, 2007.

[27] A. Leven, N. Kaneda, Ut-Va Koc, and Y. K. Chen, "Coherent receivers for practical optical communication systems", *IEEE/OSA Optical Fiber Communication Conference* (OFC), OThK4, Anaheim, CA, 2007.

[28] D. Ly-Gagnon, S. Tsukamoto, K. Katoh, and K. Kikuchi, "Coherent detection of optical quadrature phase shift keying signals with carrier phase estimation", *IEEE Journal of Lightwave Technology*, vol. 24, pp. 12-21, 2006.

[29] U.-V. Koc, A. Leven, Y. Chen, N. Kaneda, "Digital coherent quadrature phase-shift keying (QPSK)", *IEEE/OSA Optical Fiber Communication Conference* (OFC), OThI1, Anaheim, CA, 2006.

[30] S. Y. Kim, and K. Kikuchi, "1000-km transmission of 20-Gbit/s QPSK-NRZ co-polarized DWDM signals with spectral efficiency of 1 bit/s/Hz using coherent detection" *IEEE/OSA Optical Fiber Communication Conference* (OFC), OThS4, Anaheim, CA, 2007.

[31] S. Tsukamoto, D.-S. Ly-Gagnon, K. Katoh, and K. Kikuchi, "Coherent demodulation of 40-Gbit/s polarization-multiplexed QPSK signals with 16-GHz spacing after 200-km transmission", *IEEE/OSA Optical Fiber Communication Conference* (OFC), PDP29, Anaheim, CA, 2005.

[32] M. Taylor, "Coherent detection for fiber optic communications using digital signal processing", *in Topical Meeting on Coherent Optical Technologies and Applications* (COTA), CThB1, Canada, 2006.

[33] S. Tsukamoto, K. Katoh, and K. Kikuchi, "Unrepeated transmission of 20-Gbit/s optical quadrature phase shift keying signal over 200-km standard single-mode fiber based on digital processing of homodyne-detected signal for group velocity dispersion compensation", *IEEE Photon. Technol. Lett.*, vol. 18, pp. 1016-1018, 2006.

[34] M. G. Taylor, "Accurate digital phase estimation process for coherent detection using a parallel digital processor", *European Conference on Optical Communication* (ECOC), Tu4.2.6, Glasgow, UK, 2005.

[35] D.-S. Ly-Gagnon, K. Katoh, and K. Kikuchi, "Unrepeatered optical transmission of 20 Gbit/s quadrature phase shift keying signals over 210 km using homodyne

phase diversity receiver and digital signal processing", *IEE Electronics Letters*, vol. 41, pp.206-207, 2005.

[36] S. Tsukamoto, D.-S. Ly-Gagnon, K. Katoh, and K. Kikuchi, "Demodulation of co-polarizaed 20-Gbit/s QPSK signls with 16-GHz spacing after 200-km transmission using coherent detection and digital signal processing", *IEEE Conference on Lasers and Electro-Optics* (CLEO), CWO3, 2005.

[37] K. Kikuchi, "Coherent detection of phase shift keying signals using digital carrier-phase estimation", *IEEE/OSA Optical Fiber Communication Conference* (OFC), OTuI4, Anaheim, CA, 2006.

[38] Y. Cai, and A. N. Pilipetskii, "Comparison of two carrier phase estimation schemes in optical coherent detection systems", *IEEE/OSA Optical Fiber Communication Conference* (OFC), OMP5, Anaheim, CA, 2007.

[39] K. Kikuchi, M. Fukase, and S. Y. Kim, "Electronic post-compensation for nonlinear phase noise in a 1000-km 20-Gbit/s optical QPSK transmission system using the homodyne receiver with digital signal processing", *IEEE/OSA Optical Fiber Communication Conference* (OFC), OTuA2, Anaheim, CA, 2007.

[40] K. Kikuchi, "Phase-diversity homodyne detection of multilevel optical modulation with digital carrier phase estimation", *IEEE Journal of Selected Topics in Quantum Electronics*, vol. 12, pp.563-570, 2006.

[41] M. G. Taylor, "Coherent detection for optical communications using digital signal processing", *IEEE/OSA Optical Fiber Communication Conference* (OFC), OMP1, Anaheim, CA, 2007.

[42] S. J. Savory, G. Gavioli, R. I. Killey, and P. Bayvel, "Transmission of 42.8 Gbit/s polarization multiplexed NRZ-QPSK over 6400km of standard fiber with no optical dispersion compensation", *IEEE/OSA Optical Fiber Communication Conference* (OFC), OTuA1, Anaheim, CA, 2007.

[43] A. J. Lowery, and J. Armstrong, "Comparison of power efficient optical orthogonal frequency division multiplexing transmission methods", *Proceedings of the Australian Conference on Optical Fiber Communications* (ACOFT), 2006.

[44] J. Armstrong, and A. J. Lowery, "Power efficient optical OFDM", *IEE Electronics Letters*, vol. 42, pp. 370-372, 2006.

[45] A. J. Lowery, and J. Armstrong, "10 Gbit/s multimode fiber link using power efficient orthogonal-frequency division multiplexing", *OSA Optics Express*, vol. 13, pp. 10003-10009, 2005.

[46] J. Armstrong, B. J. C. Schmidt, D. Kalra, H. A. Suraweera, and A. J. Lowery, "Performance of asymmetrically clipped optical OFDM in AWGN for an intensity modulated direct detection systems", *IEEE Global Telecommunications Conference* (GLOBECOM), SPC07-4, 2006.

[47] A. J. Lowery, and J. Armstrong, "Orthogonal frequency division multiplexing for dispersion compensation of long-haul optical systems", *OSA Optics Express*, vol. 14, pp. 2079-2084, 2006.

[48] A. J. Lowery, L. Du, and J. Armstrong, "Orthogonal frequency division multiplexing for adaptive dispersion compensation in long haul WDM systems", *IEEE/OSA Optical Fiber Communication Conference* (OFC), PDP39, Anaheim, CA, 2006.

[49] I. B. Djordjevic, and B. Vasic, "Orthogonal frequency division multiplexing for high-speed optical transmission", *OSA Optics Express*, vol. 14, 3767-3775, 2006.

[50] I. B. Djordjevic, and B. Vasic, "100 Gbit/s transmission using orthogonal frequency-division multiplexing" *IEEE Photon. Technol. Lett.*, vol. 18, pp.1576-1578, 2006.

[51] W. Shieh, and C. Athaudage, "Coherent optical orthogonal frequency division multiplexing", *IEE Electronics Letters*, vol. 42, pp. 587-588, 2006.

[52] W. Shieh, "Is polarization mode dispersion a detriment or benefit", *European Conference on Optical Communication* (ECOC), Th2.5.2, Cannes, France, 2006.

[53] D. F. Hewitt, "Orthogonal frequency division multiplexing using baseband optical single sideband for simpler adaptive dispersion compensation", *IEEE/OSA Optical Fiber Communication Conference* (OFC), OME7, Anaheim, CA, 2007.

[54] W. Shieh, X. Yi, and Y. Tang, "Experimental demonstration of transmission of coherent optical OFDM systems", *IEEE/OSA Optical Fiber Communication Conference* (OFC), OMP2, Anaheim, CA, 2007.

[55] A. J. Lowery, and J. Armstrong, "Orthogonal frequency division multiplexing for optical dispersion compensation", *IEEE/OSA Optical Fiber Communication Conference* (OFC), OTuA4, Anaheim, CA, 2007.

[56] N. Cvijetic, and Lei Xu, and T. Wang, "Adaptive PMD compensation using OFDM in long-haul 10Gb/s DWDM systems", *IEEE/OSA Optical Fiber Communication Conference* (OFC), OTuA5, Anaheim, CA, 2007.

[57] K. Sticht, H. F. Haunstein, M. Lorang, W. Sauer-Gerff, and R. Urbansky, "Adaptation of electronic PMD equalizer based on BER estimation derived from FEC decoder", *European Conference on Optical Communication* (ECOC), Wep39, Netherlands, 2001.

[58] H. Bulow, W. Baumert, F. Buchali, and W. Keubart, "Adaptation of an electronic PMD mitigator by maximation of the eye opening", *European Conference on Optical Communication* (ECOC), vol. 3, pp.209-210, Germany, 2000.

[59] H. F. Haunstein, K. Sticht, R. Schlenk, W. Sauer-Greff, and R. Urbansky, "Control of 3-tap electrical feed-forward equalizer by conditional error counts from FEC in the presence of PMD", *IEEE/OSA Optical Fiber Communication Conference* (OFC), WQ7, Anaheim, CA, 2002.

[60] H. Bulow, "PMD mitigation techniques and their effectiveness in installed fiber", *IEEE/OSA Optical Fiber Communication Conference* (OFC), vol. 3, pp. 110-112, 2000.

[61] H. F. Haunstein, R. Schlenk, K. Sticht, A. Dittrich, W. Sauer-Greff, and R. Urbansky, "Control of combined electrical feed-forward and decision feedback equalization by conditional error counts from FEC in the presence of PMD", *IEEE/OSA Optical Fiber Communication Conference* (OFC), ThG5, Atlanta, GA, 2003.

[62] B. Franz, D. Roesener, F. Buchali, H. Bulow, G. Veith, "Adaptive electronic feed-forward equalizer and decision feedback equalizer for the mitigation of chromatic dispersion and PMD in 43 Gbit/s optical transmission systems", *European Conference on Optical Communication* (ECOC), We1.5.1, 2006.

[63] B. Franz, F. Buchali, D. Rosener, H. Bulow, "Adaptation techniques for electronic equalizers for the mitigation of time-variant distortions in 43 Gbit/s

optical transmission systems", *IEEE/OSA Optical Fiber Communication Conference* (OFC), OMG1, Anaheim, CA, 2007.

[64]H. Bulow, R. Ballentin, W. Baumert, G. Maisonneuve, G. Thielecke, and T. Wehren, "Adaptive PMD mitigation at 10 Gbit/s using an electronic SiGe equalizer IC", *European Conference on Optical Communication* (ECOC), We C3.4, Nice, France, 1999.

[65]C. Qiao, and M. Yoo, "Optical burst switching (OBS) –A new paradigm for an optical internet", *Journal of High Speed Networks*, vol. 8, pp. 69-84, 1999.

[66]Y. Xiong, M. M. Vandenhoute, and H. Cankaya, "Control architecture in optical burst-switched WDM networks", *IEEE Journal of Selected Areas in Communications*, vol. 18, pp. 1838-1851, 2000.

[67]S. J. B. Yoo, F. Xue, Y. Bansal, J. Taylor, P. Zhong, J. Cao, M. Jeon, T. Nady, G. Goncher, K. Boyer, K. Okamoto, S. Kamei, and V. Akella, "High performance optical label switching packet routers and smart edge routers for the next generation Internet", *IEEE Journal of Selected Areas in Communications*, vol. 21, pp. 1041-1051, 2003.

[68]Z. Rosberg, H. L. Vu, M. Zukerman, and J. White, "Performance analysis of optical burst switching networks" *IEEE Journal of Selected Areas in Communications*, vol. 21, pp. 1187-1197, 2003.

[69]I. Kaminow, and I. Li, *Optical Fiber Telecommunications IVB*, San Diego: Academic Press, 2002.

[70]Y. Lin, and D. Spears, "Passive optical subscriber loops with multi-access", *IEEE Journal of Lightwave Technology*, vol. 7, pp. 1769-1777, 1989.

[71]N. Frigo, P. P. Iannone, P. D. Magill, T. E. Darcie, M. M. Downs, B. N. Desai, U. Koren, T. L. Koch, C. Dragone, H. M. Presby, and G. E. Bodeep, "A wavelength-division multiplexed passive optical network with cost-shared components", *IEEE Photon. Technol. Lett.*, vol. 6, pp. 1365-1367, 1994.

[72]Chang-Hee Lee, Sang-Mook Lee, Ki-Man Choi, Jung-Hyung Moon, Sil-Gu Mun, Ki-Tae Jeong, Jin Hee Kim, and Byoungwhi Kim, "WDM-PON experiences in Korea", *OSA Journal of Optical Networking*, vol. 6, pp. 451-464, 2007.

[73]M. Zirngibl, C. R. Doerr, and L. W. Stulz, "Study of spectral slicing for local access applications", *IEEE Photon. Technol. Lett.*, vol. 8, pp. 721-723, 1996.

[74]K. Akimoto, J. Kani, M. Teshima, K. Iwatsuki, "Gigabit WDM-PON system using spectrum-slicing technologies", *European Conference on Optical Communication* (ECOC), Th2. 4. 6, 2003.

[75]B. Zhang, C. L. Lin, L. Huo, Z. X. Wang, C. K. Chan, "A simple high-speed WDM PON utilizing a centralized supercontinuum broadband light source for colorless ONU", in *Proc. Optical Fiber Communication Conference* (OFC), OTuC6, 2006.

[76]W. Hung, C. K. Chan, L. K. Chen, F. Tong, "An optical network unit for WDM access networks with downstream DPSK and upstream re-modulated OOK data using injection-locked FP laser", *IEEE Photon. Technol. Lett.*, vol. 15, pp. 1476-1478, 2003.

[77]N. Deng, W. Hung, C. K. Chan, L. K. Chen. F. Tong, "A novel wavelength modulated transmitter and its application in WDM passive optical networks", in *Proc. Optical Fiber Communication Conference* (OFC), MF79, 2004.

[78]G. Lu, N. Deng, C. K. Chan, L. K. Chen, "Use of downstream IRZ signal for upstream data re-modulation in a WDM passive optical network", in *Proc. Optical Fiber Communication Conference* (OFC), OFI8, 2005.

[79]Yue Tian, Yikai Su, Lilin Yi, Lufeng Leng, Xiangqing Tian, Hao He, and Xinyu Xu, "Optical VPN in PON based on DPSK erasing/rewriting and DPSK/IM formatting using a single Mach-Zehnder modulator", *European Conference on Optical Communication* (ECOC), Tu4.5.6, Cannes, France, 2006.

[80]D. McGhan, "Electronic dispersion compensation", *in Proc. Optical Fiber Communication Conference* (OFC), OWK1, 2006.

[81]O. E. Agazzi, M. R. Hueda, H. S. Carrer, and D. E. Criveli, "Maximum-likelihood sequence estimation in dispersive optical channels", *IEEE Journal of Lightwave Technology*, vol. 23, pp. 749-763, 2005.

[82]A. J. Weiss, "On the performance of electrical equalization in optical fiber transmission systems", *IEEE Photon. Technol. Lett.*, vol. 15, no. 9, pp. 1225-1227, 2003.

[83] F. Buchali, and H. Bulow, "Adaptive PMD compensation by electrical and optical techniques", *IEEE Journal of Lightwave Technology*, vol. 22, pp. 1116-1126, 2004.

[84] H. Haunstein, R. Urbansky, "Application of electronic equalization and error correction on lightwave systems", *European Conference on Optical Communication* (ECOC), Th1.5.1, 2004.

[85] H. F. Haunstein, W. Sauer-Greff, A. Dittrich, K. Sticht, and R. Urbansky, "Principles for electronic equalization of polarization mode dispersion", *IEEE Journal of Lightwave Technology*, vol. 22, no. 4, pp.1169-1182, 2004.

[86] J. H. Sinsky, "High-speed data and pulse carver alignment in dual Mach-Zehnder modulator optical transmitter using microwave signal processing", *IEEE Journal of Lightwave Technology*, vol. 21, pp. 412-423, 2003.

[87] I. Kang, L. Mollenauer, B. Greene, and A. Grant, "A novel method for synchronizing the pulse carver and electroabsortion data modulator for ultralong-hual DWDM transmission", *IEEE Photonics Technology Letters*, vol. 14, pp. 1357-1359, 2002.

[88] William Shieh, Xingwen Yi, and An V. Tran, "Label swapping for DPSK encoded Labels without wavelength conversion", in *Proc. Optical Fiber Communication Conference* (OFC), OTuC1, Anaheim, CA, 2005.

[89] Xingwen Yi and William Shieh, "On polarization sensitivity of all-optical label swapping using synchronous phase modulation" *IEEE Photonics Technology Letters*, vol. 18, no. 11, pp 1210-1211, Jun. 2006.

[90] G. P. Agrawal, *Nonlinear Fiber Optics*, 3rd Edition, Academic Press.

[91] M. J. Connelly, *Semiconductor Optical Amplifiers*, Kluwer Academic Publishers.

[92] M. M. El Said, J. Sitch, and M. I. Elmarsry, "An electrically pre-equalized 10-Gb/s duobinary transmission system", *IEEE Journal of Lightwave Technology*, vol. 23, pp. 388-400, 2005.

[93] R. I. Killey, P. M. Watts, V. Mikhailow, M. Glick, and P. Bayvel, "Electronic dispersion compensation by signal predistortion using a dual-dirve Mach-Zehnder modulator", *IEEE/OSA Optical Fiber Communication Conference* (OFC), OThJ2, Anaheim, CA, 2005.

[94]P. J. Winzer, and R. J. Essiambre, "Electronic pre-distortion for advanced modulation formats", *European Conference on Optical Communication* (ECOC), Tu4.2.2, Glasgow, UK, 2005.

[95]D. McGhan, C. Laperle, A. Savchenko, C. Li, G. Mak, and M. OSullivan, "5120 km RZ-DPSK transmission over G652 fiber at 10 Gb/s with no optical dispersion compensation", *IEEE/OSA Optical Fiber Communication Conference* (OFC), PDP27, Anaheim, CA, 2005.

[96]T. Sugihara, H. Kubo, T. Mizuochi, and K. Shimizu, "A study on residual distortion equalization in combination with pre-distortion and post-equalizaiton", *IEEE/OSA Optical Fiber Communication Conference* (OFC), OTuH4, Anaheim, CA, 2007.

[97]H. Bulow, B. Franz, F. Buchali, and A. Klekamp, "Electronic mitigation of impairments by signal processing", *European Conference on Optical Communication* (ECOC), We2.5.1, 2006.

[98]H. Bulow, "Electronic dispersion compensation", *IEEE/OSA Optical Fiber Communication Conference* (OFC), OMG5, Anaheim, CA, 2007.

[99]B. Franz, D. Roesener, R. Dischler, F. Buchali, B. Junginger, "43 Gbit/s SiGe based electronic equalizer for PMD and chromatic disperison mitigation", *European Conference on Optical Communication* (ECOC), We1.3.1, 2005.

[100] M. Nakamura, H. Nosaka, M. Ida, K. Kurishima, and M. Tokumitsu, "Electrical PMD equalizer ICs for a 40Gbit/s transmission", in *Proc. Optical Fiber Communication Conference* (OFC), TuG4, 2004.

[101] A. Farbert, S. Langenbach, N. Stojanovic, C. Dorschky, T. Kupfer, C. Schulien, J.-P. Elbers, H. Wernz, H. Griesser, and C. Glingener, "Performance of a 10.7 Gb/s receiver with digital equaliser using maximum likelihood sequence estimation", *European Conference on Optical Communication* (ECOC), Th4.1.5, 2004.

[102] Jin Wang, Joseph M. Kahn, "Performance of electrical equalizers in optically amplified OOK and DPSK systems", *IEEE Photon. Technol. Lett.*, vol. 16, pp.1397-1399, 2004.

[103] V. Curri, R. Gaudino, A. Napoli, and P. Poggiolini, "Electronic equalization for advanced modulation formats in dispersion-limited systems", *IEEE Photon. Technol. Lett.*, vol. 16, pp. 2556-2558, 2004.

[104] H. F. Haunstein, K. Sticht, A. Dittrich, W. Sauer-Greff, and R. Urbansky, "Design of near optimum electrical equalizers for optical transmission in the presence of PMD", *IEEE/OSA Optical Fiber Communication Conference* (OFC), vol. 3, pp. WAA4-1 – WAA4-3, Anaheim, CA, 2001.

[105] H. F. Haunstein, K. Sticht, A. Dittrich, M. Lorang, W. Sauer-Greff, and R. Urbansky, "Implementation of near optimum electrical equalization at 10 Gibt/s", *European Conference on Optical Communication* (ECOC), vol. 3, pp.223-224, Germany, 2000.

[106] M. Cavallari, C. R. S. Fludger, P. J. Anslow, "Electronic signal processing for differential phase modulation formats", *in Proc. Optical Fiber Communication Conference* (OFC), TuG2, 2004.

[107] N. Kikuchi, K. Mandai, S. Sasaki, and K. Sekine, "Proposal and first experimental demonstration of digital incoherent optical field detector for chromatic dispersion compensation", *European Conference on Optical Communication* (ECOC), Th4.4.4, Cannes, France, 2006.

[108] X. Liu, X. Wei, "Electronic dispersion compensation based on optical field reconstruction with orthogonal differential direct-detection and digital signal processing", *IEEE/OSA Optical Fiber Communication Conference* (OFC), OTuA6, Anaheim, CA, 2007.

[109] A. D. Ellis, M. E, McCarthy, "Receiver-side electronic dispersion compensation using passive optical optical field detection for low cost 10 Gbit/s 600 km-reach applications", *IEEE/OSA Optical Fiber Communication Conference* (OFC), OTuE4, Anaheim, CA, 2006.

[110] A. Polley, and S. E. Ralph, "Receiver-side adaptive opto-electronic chromatic dispersion compensation", *IEEE/OSA Optical Fiber Communication Conference* (OFC), JThA51, Anaheim, CA, 2007.

[111] M. Rubsamen, P. J. Winzer, and R.-J Essiambre, "MLSE receivers for narrow band optical filtering", *IEEE/OSA Optical Fiber Communication Conference* (OFC), OWB6, Anaheim, CA, 2006.

[112] C. Xia, and W. Rosenkranz, "Electrical dispersion compensation for different modulation formats with optical filtering", *IEEE/OSA Optical Fiber Communication Conference* (OFC), OWR2, Anaheim, CA, 2006.

[113] F. Buchali, H. Bulow, "Correlation sensitive Viterbi equalization of 10 Gb/s signals in bandwidth limited receivers", in *Proc. Optical Fiber Communication Conference* (OFC), OFO2, 2005.

[114] J. D. Downie, J. Hurley, M. Sauer, S. Lobanov, and S. Raghavan, "Experimental measurements of the effectiveness of MLSE against narrowband optical filtering distortion", *IEEE/OSA Optical Fiber Communication Conference* (OFC), OMG4, Anaheim, CA, 2007.

[115] F. N. Hauske, B. Lankl, C. Xie, E.-D. Schmidt, "Itarative electronic equalization utilizing low complexity MLSEs for 40 Gbit/s DQPSK modulation", *IEEE/OSA Optical Fiber Communication Conference* (OFC), OMG2, Anaheim, CA, 2007.

[116] Moshe Nazarathy, and Erez Simony, "Multichip differential phase encoded optical transmission", *IEEE Photon. Technol. Lett.*, vol. 17, pp. 1133-1135, 2005.

[117] Yoav Yadin, Alberto Bilenca, and Moshe Nazarathy, "Soft detection of multichip DPSK over the nonlinear fiber-optic channel", *IEEE Photon. Technol. Lett.*, vol. 17, pp. 2001-2003, 2005.

[118] Xiang Liu, "Digital implementation of soft detection for 3-chip-DBPSK with improved receiver sensitivity and dispersion tolerance", in *Proc. Optical Fiber Communication Conference* (OFC), OTuI2, 2006.

[119] Michael Ohm and Joachim Speidel, "Quaternary optical ASK-DPSK and receivers with direct detection", *IEEE Photon. Technol. Lett.*, vol. 15, pp. 159-161, 2003.

[120] Xiang Liu, Xing Wei, Yuan-Hua Kao, Juerg Leuthold, C. R. Doerr, and L. F. Mollenauer, "Quaternary differential-phase amplitude-shift-keying for DWDM

transmission", *European Conference on Optical Communication* (ECOC), Th2.6.5, 2003.

[121] Xiang Liu, Yikai Su, Xing Wei, Juerg Leuthold, and Randy C. Giles, "Optical-label switching based on DPSK/ASK modulation format with balanced detection for DPSK payload", *European Conference on Optical Communication* (ECOC), Tu4.4.3, 2003.

[122] Nan Chi, Jianfeng Zhang, Pablo V. Holm-Nielsen, Christophe Peucheret, and Palle Jeppesen, "Transmission and transparent wavelength conversion of an optically labeled signal using ASK/DPSK orthogonal modulation", *IEEE Photon. Technol. Lett.*, vol. 15, pp. 760-762, 2003.

[123] S. L. Jansen, D. Van Den, Borne, C. Climent, M. Serbay, C. J Weiske, H. Suche, P. Krummrich, S. Spaelter, S. Calabra, N. H. Denschlag, P. Leisching, W. Rosenkranz, W. Solher, G. D. Khoe, T. Koonen, and H. Waardt. "10,200 km 22x2x10Gbit/s RZ-DQPSK dense DWDM transmission without inline dispersion compensation through optical phase conjugation", *IEEE/OSA Optical Fiber Communication Conference* (OFC), PDP28, Anaheim, CA, 2005.

[124] X. Wang, K. Kitayama, "Analysis of Beat Noise in Coherent and Incoherent Time-Spreading OCDMA", *IEEE Journal of Lightwave Technology*, vol. 22, pp. 2226-2235, 2004.

[125] B. Zhang, C. L. Lin, L. Huo, Z. X. Wang, C. K. Chan, "A Simple High-Speed WDM PON Utilizing a Centralized Supercontinuum Broadband Light Source for Colorless ONUs", in *Proc. Optical Fiber Communication Conference* (OFC), OTuC6, 2006.

[126] M. Pauer, P. J. Winzer, and W. R. Leeb, "Bit error probability reduction in direct detection optical receivers using RZ coding", *IEEE Journal of Lightwave Technology*, vol. 19, pp. 1255-1262, 2001.

[127] H. Sunnerud, M. Karlsson, and P. A. Andrekson, "A comparison between NRZ and RZ data formats with respect to PMD-induced system degradation", *IEEE Photonics Technology Letters*, vol. 13, pp. 448-450, 2001.

[128] C. Lawetz and J. C. Cartledge, "Performance of optically preamplified receivers with Fabry-Perot optical filters", *IEEE Journal of Lightwave Technology,* vol. 14, pp. 2467-2474, 1996.

[129] J. G. Proakis, *Digital Communications,* 4th ed. New York: McGraw-Hill, 2000.

[130] E. Forestieri, "Evaluating the error probability in lightwave systems with chromatic dispersion, arbitrary pulse shape and pre- and post- detection filtering", *IEEE Journal of Lightwave Technology*, vol. 18, pp. 1493-1503, 2000.

[131] C. W. Helstrom, "Distribution of the filtered output of a quadratic rectifier computed by numerical contour integration", *IEEE Transaction on Information Theory,* vol. 32, pp. 450-463, 1986.

[132] P. J. Winzer, M. Pfennigbauer, M. M. Strasser, and W. R. Leeb, "Optimum bandwidths for optically preamplfied NRZ receivers", *IEEE Journal of Lightwave Technology*, vol. 19, pp. 1263-1273, 2000.

[133] H. Takara, "Supercontinuum multi-carrier source for WDM systems", in *Proc. Optical Fiber Communication Conference* (OFC), WR5, 2002.

[134] K. R. Tamura, H. Kubota, and M. Nakazawa, "Fundamentals of stable continuum generation at high repetition rates", *IEEE Journal of Quantum Electronics*, vol. 36, pp. 773-779, 2000.

[135] S. Taccheo, and K. Ennser, "Investigation of amplitude noise and timing jitter of supercontinuum spectrum-sliced pulses", *IEEE Photon. Technol. Lett.*, vol. 14, pp. 1100-1102, 2002.

[136] Siu-Sun Pun, Chun-Kit Chan, and Lian-Kuan Chen, "Demonstration of a novel optical transmitter for high-speed differential phase shift keying / inverse return-to-zero orthogonally modulated signals", *IEEE Photonics Technology Letters,* vol. 17, no. 12, pp 2763-2765, Dec. 2005.

[137] Mario Zitelli, "Optical phase and intensity modulation using dark pulses," *IEEE Photon. Technol. Lett.*, vol. 16, pp. 1972-1974, 2004.

[138] C. W. Chow, and H. K. Tsang, "Optical label encoding and swapping using half-bit delayed dark RZ payload and DPSK label", *OSA Optics Express*, vol. 13, pp. 5325-5330, 2005.

[139] D. C. Kilper, R. Bach, D. J. Blumenthal, D. Einstein, T. Landolsi, L. Ostar, M. Preiss, and A. E. Willner, "Optical performance monitoring", *IEEE Journal of Lightwave Technology*, vol. 22, pp. 294-304, 2004.

Appendix A-List of Acronyms

A/D	analog to digital
ASE	amplified spontaneous emission
ASK	amplitude shift keying
AWG	arrayed waveguide grating
BER	bit error rate
BT	bit torrent
CD	chromatic dispersion
CLS	centralized light source
CO	central office
DCF	dispersion compensating fiber
DCM	dispersion-compensating module
DEMUX	demultiplexer
DFB	distributed feedback laser
DFE	decision-feedback equalizer
DF-J-MLSE	decision feedback joint maximum likelihood sequence estimation
DGD	differential group delay
DI	delay interferometer
DPSK	differential phase shift keying
DQPSK	differential quadrature phase shift keying
DSF	dispersion shifted fiber
DSP	digital signal processing
DWDM	dense wavelength division multiplexing
EAM	electro-absorption modulator
EDFA	erbium-doped fiber amplifier
EF	electronic filter

ER	extinction ratio
FFE	feedforward equalizer
FM	fast mode
FSK	frequency shift keying
FWM	four-wave mixing
GVD	group velocity dispersion
HNLF	highly nonlinear fiber
IRZ	inverse return to zero
ISI	intersymbol interference
J-MLSE	joint maximum likelihood sequence estimation
KL	Karhunen Loeve
MAN	metropolitan area network
MC-DPSK	multi-chip differential phase shift keying
MGF	moment generation function
MLFL	mode-locked fiber laser
MLSE	maximum likelihood sequence estimation
MPDR	monitoring power dynamic ranges
MUX	multiplexer
MZM	Mach-Zehnder modulator
NRZ	non-return to zero
OADM	optical add-drop multiplexer
OBPF	optical bandpass filter
OD	optical delay
OFDM	orthogonal frequency division multiplexing
ONU	optical network unit
OOK	on-off keying
OSNR	optical signal to noise ratio
PM	phase modulator
PMD	polarization mode dispersion
PON	passive optical network
PRBS	pseudorandom binary sequence
QAM	quadrature amplitude modulation

RN	remote node
RZ	return to zero
SBS	stimulated Brillouin scattering
SC	supercontinuum
SM	slow mode
SMF	single mode fiber
SOA	semiconductor optical amplifier
SPM	self-phase modulation
SPRM	synchronized phase re-modulation
SRS	stimulated Raman scattering
TM	timing misalignment
VROC	variable ratio optical coupler
WDM	wavelength division multiplexing
WDM-PON	wavelength-division-multiplexing passive optical network
XAM	cross absorption modulation
XGM	cross gain modulation
XPM	cross phase modulation

Appendix B-Publications

[1]. **Jian Zhao**, Lian-Kuan, "Electronic Equalization of 10-Gbit/s Upstream Signals for Asynchronous-Modulation and Chromatic-Dispersion Compensation in High-Speed Centralized Supercontinuum Broadband-Light-Source WDM-PON", accepted for publication in *OSA Journal of Optical networking.*

[2]. **Jian Zhao**, Lian-Kuan Chen, Chun-Kit Chan, "Maximum Likelihood Sequence Estimation for Impairment Compensation in Advanced Modulation Formats", *Opto-Electronics and Communications Conference* (OECC), Yokohama, Japan, July, 2007.

[3]. **Jian Zhao**, Lian-Kuan Chen, Chun-Kit Chan, "Maximum Likelihood Sequence Estimation for Chromatic-Dispersion Compensation in 4-ASK Modulation Format", *Opto-Electronics and Communications Conference* (OECC), 13B2-2, Yokohama, Japan, July, 2007.

[4]. **Jian Zhao**, Lian-Kuan Chen, "A novel 3-chip DPSK maximum likelihood sequence estimation for chromatic-dispersion and polarization-mode-dispersion compensation", *OSA Optics Letters,* July, 2007.

[5]. **Jian Zhao**, Yuen-Ching Ku, Lian-Kuan Chen, "A simple monitoring technique for synchronized phase re-modulation using narrowband optical filtering", *Electronics Letters*, vol. 43, pp.363-364, 2007.

[6]. **Jian Zhao**, Lian-Kuan Chen, Chun-Kit Chan, "A novel re-modulation scheme to achieve colorless high-speed WDM-PON with enhanced tolerance to chromatic dispersion and re-modulation misalignment", *IEEE/OSA Optical Fiber Communication Conference* (OFC), OWD2, Anaheim, CA, 2007.

[7]. **Jian Zhao**, Lian-Kuan Chen, Chun-Kit Chan, "Maximum likelihood sequence estimation for chromatic dispersion and polarization mode dispersion

compensation in 3-chip DPSK modulation format", *IEEE/OSA Optical Fiber Communication Conference* (OFC), OMG3, Anaheim, CA, 2007.

[8]. **Jian Zhao**, Lian-Kuan Chen, Chun-Kit Chan, "Joint maximum likelihood sequence estimation for chromatic dispersion compensation in ASK-DPSK modulation format", *IEEE Photonics Technology Letters*, vol. 19, pp. 73-75, 2007.

[9]. **Jian Zhao,** Lian-Kuan Chen, Chun-Kit Chan, "Electronic equalization for unsynchronized modulation and chromatic dispersion compensation in supercontinuum-based WDM-PON", *European Conference on Optical Communication* (ECOC), We3. P. 159, Cannes, France, 2006.

[10].Li Huo, **Jian Zhao**, Chinlon Lin, Chun-Kit Chan, Zhaoxin Wang, "Demonstration of an optical frequency-hopping scheme for secure communications", *IEEE Conference on Lasers and Electro-Optics* (CLEO), CWQ4, LA, CA, 2006.

[11].**Jian Zhao,** Lian-Kuan Chen, Chun-Kit Chan, "40-Gbit/s SOA-based all-optical IRZ generation assisted by DI for orthogonal modulation in OTDM systems", *IEEE Conference on Lasers and Electro-Optics* (CLEO), CFH3, LA, CA, 2006.

[12].Li Huo, **J. Zhao**, Chinlon Lin, Chan-Kit Chan, Zhaoxin Wang, "Experimental demonstration of a novel all-optical multilevel 4 amplitude shift keying coding/decoding scheme", *IEEE/OSA Optical Fiber Communication Conference* (OFC), JThB41, Anaheim, CA, 2006.

[13].**Jian Zhao**, Li Huo, Chun-Kit Chan, Lian-Kuan Chen, Chinlon Lin, "Analytical investigation of optimization, performance bound, and chromatic dispersion tolerance of 4 amplitude shift keying format", *IEEE/OSA Optical Fiber Communication Conference* (OFC), JThB15, Anaheim, CA, 2006.

[14].**Jian Zhao,** Lian-Kuan Chen, Chun-Kit Chan, "Tolerance of misalignment between ASK and DQPSK modulation in ASK/DPSK orthogonal modulation systems", *Opto-Electronics and Communications Conference* (OECC), 5F3-3, Kaohsiung, Taiwan, 2006.

[15].**Jian Zhao,** Lian-Kuan Chen, Chun-Kit Chan, "Maximum likelihood sequence estimation in the presence of timing misalignment and polarization mode dispersion in optically amplified RZ systems", *IEEE International Conference on Communication,* (ICC), CT20-7, Istanbul, Turkey, 2006.

[16].**Jian Zhao**, Lian-Kuan Chen, Chun-Kit Chan, "Performance degradation induced by pulse carver/data modulator misalignment in RZ-DPSK systems", *IEEE Conference on Lasers and Electro-Optics* (CLEO), JThE62, Baltimore, USA, 2005.

[17].**Jian Zhao**, Lian-Kuan Chen, Chun-Kit Chan, "Mitigation of timing misalignment induced distortion using electronic equalizer in RZ/CSRZ systems", *IEEE Photonics Technology Letters*, vol. 17, pp. 1106-1108, 2005.

[18].**Jian Zhao**, Lian-Kuan Chen, Chun-Kit Chan, Chinlon Lin, "Performance sensitivity to system parameters in multi-wavelength super-continuum sources", *IEEE Journal of Quantum Electronics*, vol. 41, pp. 709-716, 2005.

[19].**Jian Zhao**, Lian-Kuan Chen, Chun-Kit Chan, Chinlon Lin, "Analysis of performance optimization in super-continuum sources", *OSA Optics Letters*, vol. 29, pp. 489-491, 2004.